AC Zeeman Force with Ultracold Atoms

Charles T. Fancher

Saginaw, MI

Master of Science, College of William and Mary, 2012
Bachelor of Science, Worcester Polytechnic Institute, 2010

A Dissertation presented to the Graduate Faculty
of the College of William and Mary in Candidacy for the Degree of
Doctor of Philosophy

Department of Physics

The College of William and Mary
January 2017

APPROVAL PAGE

This Dissertation is submitted in partial fulfillment of
the requirements for the degree of

Doctor of Philosophy

Charles T. Fancher

Approved by the Committee, November 2016

Committee Chair
Associate Professor Seth A. M. Aubin, Physics
The College of William and Mary

Associate Professor Enrico Rossi, Physics
The College of William and Mary

Professor Todd D. Averett, Physics
The College of William and Mary

Professor John B. Delos, Physics
The College of William and Mary

Professor Charles I. Sukenik, Physics
Old Dominion University

ABSTRACT

Ultracold atom experiments use a gas of neutral atoms with temperatures less than 100 μK above absolute zero and offer unmatched experimental control of quantum states and coherence, which has allowed ultracold atom-based measurements to be some of the most precise to date. While ultracold atom experiments can control almost all atomic degrees of freedom, spin-dependent trapping and spatial manipulation has remained difficult if not inaccessible. We are developing a method of spin-dependent trapping and spatial manipulation for ultracold neutral atoms using the AC Zeeman force produced by a microwave magnetic near-field gradient generated by an atom chip. We measure the AC Zeeman force on ultracold rubidium atoms by observing its effect on the motion of atoms initially in free-fall and on those confined in a trap. We have studied the force as a function of microwave frequency detuning from a hyperfine transition at 6.8 GHz at several magnetic field strengths and have observed its characteristic bipolar and resonant features predicted by two-level dressed atom theory. We find that the force is several times the strength of gravity in our setup, and that it can be targeted to a specific hyperfine transition while leaving other hyperfine states and transitions relatively unaffected. We find that our measurements are reasonably consistent with parameter-free theoretical predictions.

TABLE OF CONTENTS

ACKNOWLEDGMENTS

It takes a lot of work from a lot of people to plan and build an ultracold atom apparatus as well as run the actual experiments on it. There have been many undergraduate students that have passed through the lab, each with their own contributions to building new equipment or calibrating devices or taking data. I am grateful to former graduate students Megan Ivory and Austin Ziltz for doing the vast majority of the initial apparatus build. I appreciate the contributions that AJ Pyle has made to the team by being dedicated to maintaining and improving the apparatus - especially when it did not directly benefit his research. I am grateful to Drew Rotunno for his enthusiasm in making things in the lab better and Shuangli Du for his work on the K lasers. I thank my advisor Seth Aubin for his help and guidance along the way.

I couldn't have kept my sanity through this process without good friends I have had along the way. Nick Murgolo, Jim Adam, Stefan Oehrlein, and Mike Bayersdorfer were great friends that helped to pass the time in Williamsburg. I would like to say thank you to Will Dickinson for being my constant gym buddy and keeping me level both with my priorities and my squats. Calvin Johnson has been a good role model for being quietly competent in his field.

To Lily, who has made all this work worthwhile.

LIST OF FIGURES

LIST OF TABLES

CHAPTER 1

Introduction

Ultracold atom experiments use a gas of neutral atoms with temperatures in the range of 100 μK above absolute zero and offer a high degree of experimental control of quantum states and coherence. This quantum control has allowed ultracold atom-based measurements to be some of the most precise to date. Atomic clocks are now accurate to 1 part in 10^{18}, equivalent to losing 1 second over the age of the universe [1]. Atom interferometers can measure the acceleration due to Earth's gravity to 1 part in 10^{10} or less [2, 3], and a rotations of one revolution per second to a few parts in 10^8 [4, 5, 6]. Ultracold atom experiments also enable the study of many other physical systems such as quantum magnetism [7, 8], superfluidity and superconductivity [9], and tests of general relativity [10].

These experiments are possible because of the unmatched experimental control available in ultracold atom systems. Atom clouds have been cooled to less than 500 pK above absolute zero [11, 12]. Cold atom sensor systems can also be made spatially compact, with sensing volumes as small as 90 μm^3 [13]. Several experimental systems have been shown to deterministically load a single cold atom [14, 15], as well as address a single cold atom within an optical lattice of hundreds of atoms

spaced less than 1 μm apart [16]. The collisional properties of cold atoms can be changed via an optical [17, 18] or magnetic [19, 20, 21] Feshbach resonance.

While ultracold atom experiments can control almost all atomic degrees of freedom, spatial manipulation that depends on the internal state of an atom ('state-dependent spatial manipulation') has remained difficult if not inaccessible. Magnetic traps based on a static field (DC magnetic traps) produce energy shifts in atoms based on their internal hyperfine state and sub-level created by the DC Zeeman (DCZ) effect. However, these potentials created by the DC Zeeman effect on different sub-levels must be proportional to one another; it is not possible to selectively apply a DC Zeeman potential to one magnetically sensitive state but not others. Optical dipole potentials are produced by the interaction of an atom with an oscillating electric field and are frequently used to trap atoms independent of their spin [22]. When operating near a magic wavelength, where the scalar polarizabilities of the ground and excited states are equal, they can produce spin-dependent potentials that are proportional to one another or must be periodic [23, 24, 25]. We aim to add state-dependent spatial manipulation to the ultracold atom toolbox. More specifically, we aim to demonstrate a fully spin-dependent potential that can have an arbitrary shape and can be applied to one spin state while leaving the others unaffected.

In this thesis, I study the Zeeman effect due to oscillating magnetic fields at microwave frequencies, called the AC Zeeman (ACZ) effect, for spin-dependent spatial manipulation of cold atoms. This effect works as follows: an AC magnetic field is applied with a frequency close to a specifically targeted transition between Zeeman sublevels within different, or the same, hyperfine manifolds. These states are all generally within the electronic ground state of the atom. The interaction between the targeted atomic states and the applied microwave field creates an energy shift similar to the AC Stark effect in an optical dipole trap [22, 26]. Unlike an optical

dipole trap, however, the ACZ effect only shifts the energy of the targeted Zeeman sublevel states and leaves the others unaffected. This spin-dependence assumes that the energy separation between the targeted states and the neighboring Zeeman sublevels is large. This energy separation is dictated by the DC Zeeman shift, which can be modified without affecting the ACZ potential. The ACZ energy shift depends on the strength of the AC magnetic field and on the difference between the applied frequency and the resonant frequency of the atomic transition, called the 'detuning' δ. Stronger AC magnetic fields create larger energy shifts, as do fields with frequency tuned closer to atomic resonance: $\delta \to 0$. The spatial dependence of the applied AC magnetic field creates a spatial dependence in the energy shift (i.e. potential) which in turn gives rise to a force that can be used to spatially constrain the atoms [26, 27].

The use of the ACZ effect as a tool for spatial control of neutral atom experiments was first proposed in 1962 [28] and in 1989 for cold atom experiments [26]. The ACZ effect was shown to deflect the path of a beam of warm K atoms in 1967 [29] and to weakly constrain the positions of cold Cs atoms in 1993 [27]. The 1993 experiment used a macroscopic microwave cavity a few cm across, which required 1 kW of circulating microwave power to constrain the atomic cloud in the horizontal plane but yet was weaker than gravity. The spatial gradient in the applied AC magnetic field was the limiting factor in the experiment. To my knowledge, the ACZ effect as a tool in cold neutral atom experiments has been dormant until recently.

The field is beginning to heat up again with the advent of micro-fabricated atom chips used for trapping and manipulation of cold atoms and ions [30, 31, 32, 33, 34]. The potential due to the ACZ effect was used for atom interferometry with a Bose-Einstein condensate (BEC) of ^{87}Rb in 2009 [33]. The ACZ effect was also recently used in 2011 for the crucial application of quantum gate control in trapped ions [30]. The experimental work in this thesis explores the ACZ force produced by a

microwave magnetic near-field gradient generated by an atom chip. Atom chips are spatially compact circuit boards, roughly the size of a saltine cracker, that weigh only a few grams and contain the current-carrying wires necessary to trap cold atoms [31]. Due to the close proximity of the ultracold atoms to the the current-carrying wires, atom chips can operate with substantially less power (P≈100 mW) than other trapping methods such as macroscopic magnetic traps based on coils (P≈1 kW) or laser-based optical dipole traps (P≈2 W). The atom-chip distance (d=10-500 μm) is much smaller than the wavelength of the 6.8 GHz microwaves used ($\lambda = 4.4$ cm), and thus puts the apparatus squarely in the near-field regime where $d \ll \lambda$. In this regime, the length scale for the AC magnetic field geometry is dictated by the distance to and between the current carrying wires, not the microwave wavelength. If we neglect the skin effect, then the AC magnetic field can be calculated by using Ampère's law and is proportional to $1/d$. The AC magnetic field gradient, which gives rise to the ACZ force, is then proportional to $1/d^2$.

1.1 AC Zeeman Application: Trapped Atom Interferometry

There has been a recent surge in the development of field-deployable devices for precision inertial sensing [35] and time-keeping [36]. This has put a new emphasis on Space, Weight, and Power (SWaP) requirements of ultracold atom systems. The cold atom experiments that first made BECs in the mid-1990s [37, 38] were roughly the size of a room. Our apparatus is shown in figure 1.1 and is still the size of a room two decades later. However, there have been efforts to try to reduce the SWaP requirements of cold atom systems for field applications including a demonstration of a BEC at a physics conference vendor area [39], use in micro-gravity on a parabolic

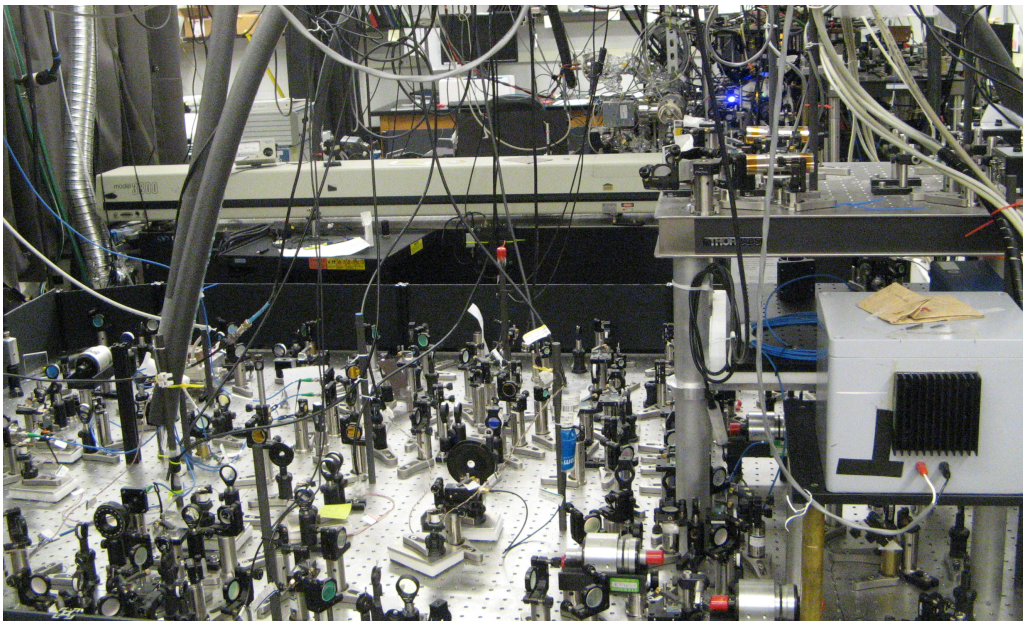

FIG. 1.1: Image of W&M Cold Atom Lab. The two optics tables pictured are 5 feet x 10 feet. The apparatus requires a few kW of electrical power to run. The Spectra Physics laser (white rectangle on far optics table) draws a few more kW of power. Image credit: S. Aubin.

flight [35], a drop tower [40], a sounding rocket [41], and in space [42, 43]. A recently reported science payload capable of producing a BEC with 100,000 atoms every second is a cylinder with height of 1 m and diameter of 0.7 m; it has a mass of 147 kg, and draws 364 W of power [43].

One of the main motivations for miniaturizing cold atom systems is the ability to operate in microgravity for extended periods of time. Current state-of-the-art atom interferometers use a free space configuration where the atoms are in free fall during the experiment [2, 5, 35, 44, 45]. These devices have limits on the integration time imposed by their size, or must operate in a microgravity environment. An interferometer using trapped atoms cooled to quantum degeneracy can ease these constraints. A trapped atom interferometer has been shown to work with BECs using an adiabatic double-well potential [46]. However, the interferometer sensitivity when using a trapped BEC is limited by the relatively strong atom-atom interactions that increase with atomic density, called mean-field interaction. Fermions have

strongly suppressed mean-field interactions, but are of limited use because of their nature; no two fermions can occupy the same spatial and spin state. Each atom in a degenerate Fermi gas (DFG) occupies a different state in the atom trap. If the traditional adiabatic double well potential is used, then each of these trap levels (states) acquires a different splitting phase, which washes out the interference pattern.

The ACZ force would allow for new applications like a trapped atom interferometer with fermions. The spin-dependent force could act equally on all of the trap levels (states) to preserve the interference pattern after splitting the clouds. This experiment could be conducted by using an optical dipole potential to spatially constrain the atoms and the ACZ force as a part of the interferometer. This approach blends the well-studied method of frequency measurement in an atomic clock and the spatial dependence of an atom interferometer, to produce a precise inertial sensor by spatially separating atomic clock states via a spin-dependent force.

The ACZ force could also be used as a trapping potential by using atom chip wires currently being used for trapping using the DC Zeeman effect. Positioning the atoms in the near-field regime should allow for creating AC magnetic fields whose shape follows those of the DC magnetic fields currently used to trap atoms. If the ACZ effect were used as the trapping potential, then it could operate at an arbitrary DC magnetic field. This important capability should allow for precise control of atom-atom interactions through magnetic Feshbach resonances such as in an optical dipole trap (ODT). Furthermore, the hyperfine transitions driven by the AC magnetic field (microwave typically) are essentially immune from spontaneous emission, unlike the electronic transitions targeted by ODTs. Finally, ACZ potentials should also allow forced evaporative cooling with the addition of a second, much weaker, AC magnetic field to spin-flip the atoms from a trapped state to an anti-trapped state, similar to a DC magnetic trap with forced RF evaporation. The ACZ traps would allow the efficient evaporative cooling available in DC magnetic traps

and the tuning of atom-atom interactions possible in ODTs.

1.2 Thesis Structure

In this thesis I report a successful measurement of a spin-dependent, bipolar, and resonant force produced by the ACZ effect. The measurements are in good qualitative agreement with *ab-initio* theoretical predictions. This force is substantially stronger than gravity for 3 W of microwave power, opening up the possibility of future trapping experiments. This thesis is structured in the following manner. Chapter 2 introduces the theory needed for the general operation of the ultracold gas apparatus from laser cooling through magnetic trapping and evaporative cooling to produce a BEC. Chapter 3 discusses theory specific to the ACZ effect including calculations of the Rabi frequency and possible atom traps based on the ACZ effect. I discuss our ultracold gas apparatus in Chapter 4 and talk about how to keep it running reliably on a day-to-day basis. Chapter 5 is devoted to the Spectra Physics 3800 laser (aka 'lasersaurus') and the methods used to create ODTs in our apparatus. The bulk of the experimental results are contained in Chapter 6, which discusses measurements of the ACZ force produced by a microwave magnetic near-field gradient generated by an atom chip that is spin-dependent, stronger than gravity, and consistent with theoretical predictions. Chapter 7 discusses a set of exploratory measurements on the stability of the dressed atom ACZ eigenstates for atoms held in an ODT. In Chapter 8, I present progress on developing a new method of atom chip manufacturing for future work on the ACZ effect in cold atom systems. The thesis concludes with an outlook on future work in Chapter 9.

CHAPTER 2

Ultracold Atom Theory

Ultracold atom experiments rely heavily on the interaction between electromagnetic fields and internal atomic states for most aspects of the experimental sequence including Doppler cooling, magneto-optical trapping, optical molasses, optical pumping, trapping atoms, and imaging the atoms. A good understanding of the different ways light interacts with atoms is essential to understand, run, and improve ultracold atom experiments.

This chapter follows the work of [47]. It starts with an overview of how electromagnetic fields interact with an atom based on its internal states, then will move on to laser Doppler cooling, and will progress through the different techniques in order of increasing complexity.

2.1 2-Level Atom

A two level atom is defined as having a ground state, $|g\rangle$, with energy $E_g = \hbar\omega_g$ and an excited state, $|e\rangle$, with energy $E_e = \hbar\omega_e$. The atomic transition frequency between the two states, ω_0, is defined as $\omega_0 = (\omega_e - \omega_g)$. This can be seen graphically in Figure 2.1. The Hamiltonian that describes this two level system is given by

equation 2.1. The third step subtracts a constant energy offset, ω_g.

$$\mathcal{H}_0 = \begin{pmatrix} E_e & 0 \\ 0 & E_g \end{pmatrix} = \hbar \begin{pmatrix} \omega_e & 0 \\ 0 & \omega_g \end{pmatrix} = \hbar \begin{pmatrix} \omega_0 & 0 \\ 0 & 0 \end{pmatrix} \tag{2.1}$$

If an electromagnetic wave is applied to a two level atom it is useful to define $\delta = \omega_l - \omega_0$ as the detuning of the applied field, where ω_l is the angular frequency of the applied electromagnetic wave. A field is said to be red-detuned for $\delta < 0$ and blue-detuned for $\delta > 0$.

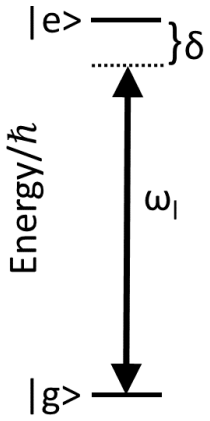

FIG. 2.1: A two level atom with a ground state, $|g\rangle$, and an excited state, $|e\rangle$. The arrow shows the frequency of an applied E-M wave. In this case the E-M wave frequency, ω_l, is slightly lower than the atomic resonance ω_0.

2.2 2-level Atom Interacting with an E-M Field

Much of atomic, molecular, and optical (AMO) physics deals with the interaction of atoms with electromagnetic fields. The Stark effect is used to describe the effects of electric fields and the Zeeman effect is used to describe the effects of magnetic fields. These effects are generally broken up by looking at the AC and DC effects separately. The DC Zeeman effect will be described later in Section 2.5 on magnetic trapping. The AC Stark effect is commonly used for AMO physics and

will be described in more detail shortly. The AC Zeeman effect is the topic of much of this work and will be described in detail in its own chapter.

We will start by considering a single frequency laser field applied to a two level atom. We will simplify this even more by considering only the electric field of the laser and neglect the magnetic field. We define our coordinate system as follows: the atom is at the origin and the electric field is polarized along $\hat{z}$. We will define the electric field operator by:

$$\vec{E}(t) = E_0 \cos(\omega_l t)\hat{\epsilon} \tag{2.2}$$

where E_0 is the maximum strength of the electric field in the plane wave, $\hat{\epsilon}$ is a unit vector defining the polarization, ω_l is the similar angular frequency of the applied E-M wave, and t is time. This applied electric field induces an electric dipole interaction with the two level atom given by: [47]

$$\hat{\mathcal{H}}_{edip} = -e\vec{E}(\vec{r}, t) \cdot \vec{r} = -eE_0 \cos(\omega_l t) r(\hat{\epsilon} \cdot \hat{r}) \tag{2.3}$$

where e is the charge of the electron, and $\vec{r}$ is the position operator. This interaction Hamiltonian adds off-diagonal terms by mixing the ground and excited states of the original two level atom. These off diagonal terms are given by equation 2.4.

$$\mathcal{H}_0 = \langle e| \mathcal{H}_{edip}|g\rangle \tag{2.4}$$

Substituting equation 2.3 into equation 2.4 we can simplify to get equation 2.5 for the interaction Hamiltonian in terms of the applied electric field.

$$\langle e| \mathcal{H}_{edip}|g\rangle = -eE_0(\vec{r}, t) \cos(\omega_l t) \langle e| r\hat{\epsilon} \cdot \hat{r}|g\rangle \tag{2.5}$$

We will now make the *electric dipole approximation* and ignore the spatial variation of the applied electric field over the extent of the electron wave function. We can then make a further simplification by introducing a new term, called the Rabi frequency, Ω, in equation 2.6. This Rabi frequency is commonly used as a metric for the strength of the atom-field interaction and is proportional to the square root of the intensity of the applied field, I.

$$\Omega = -\frac{eE_0}{\hbar} \langle e| r|g\rangle \propto \sqrt{I} \tag{2.6}$$

Using this definition for the Rabi frequency we can simplify equation 2.5 to equation 2.7.

$$\langle e| \mathcal{H}_{edip} |g\rangle = \hbar\Omega \cos(w_l t) \tag{2.7}$$

Working with this $\langle e| \mathcal{H}_{edip}|g\rangle$ allows us to solve the time-dependent Schrödinger equation for the coefficients c_g and c_e of a state $\Psi = c_g e^{-i\omega_g t}|g\rangle + c_e e^{-i\omega_e t}|e\rangle$. The time-dependent Schrödinger equation gives the coupled equations 2.8 [47].

$$i\hbar \frac{dc_g(t)}{dt} = c_e(t) \langle g| \mathcal{H}_{edip} |e\rangle e^{-i\omega_0 t} \tag{2.8a}$$

$$i\hbar \frac{dc_e(t)}{dt} = c_g(t) \langle e| \mathcal{H}_{edip} |g\rangle e^{i\omega_0 t} \tag{2.8b}$$

Plugging in equation 2.7 to equation 2.8 leads to the solution given in equation 2.9.

$$c_g(t) = [\cos(\frac{\Omega' t}{2}) - i\frac{\delta}{\Omega'} \sin(\frac{\Omega' t}{2})] e^{+i\delta t/2} \tag{2.9a}$$

$$c_e(t) = -i\frac{\Omega}{\Omega'} \sin(\frac{\Omega' t}{2}) e^{-i\delta t/2} \tag{2.9b}$$

This solution includes the introduction of the generalized Rabi frequency, Ω' defined

in equation 2.10.

$$\Omega^{'} = \sqrt{\Omega^2 + \delta^2} \tag{2.10}$$

Now that we have solved for the c_e and c_g terms under the effects of an applied E-M field, let's figure out what happens to the eigenenergies of the system in the presence of this coupling light field. We will neglect the effects of spontaneous emission for now and will discuss it more later. We will follow the dressed atom method for solving for the eigenenergies, which requires two approximations to work. The first is the aforementioned *electric dipole approximation*. The second is called the *rotating wave approximation* (RWA) that says that the laser oscillation frequency is much greater than the detuning, and terms of $1/\omega_l$ should be neglected in favor of terms of $1/\delta$. Another way to state this is that $\delta \ll \omega_l$ in figure 2.1. This approximation takes equation 2.7 and gives the much simpler effective Hamiltonian, $\mathcal{H}_{int}$, in equation 2.11:

$$\mathcal{H}_{int} = \frac{\hbar}{2} \begin{pmatrix} 0 & \Omega \\ \Omega & 0 \end{pmatrix} \tag{2.11}$$

2.2.1 Dressed Atom

The dressed atom approach incorporates the atomic Hamiltonian from equation 2.1, $\mathcal{H}_0$, the Hamiltonian for the laser field with N+1 photons, $\mathcal{H}_{laser}$, and the interaction Hamiltonian from 2.11, $\mathcal{H}_{int}$, into one combined Hamiltonian. From here on, we refer to the applied electromagnetic wave as a laser field, but the applied field can be produced from any source. Equation 2.12 gives the combined dressed atom

Hamiltonian, $\mathcal{H}_{dressedatom}$, in the $\{|e, N-1\rangle|g, N\rangle\}$ basis.

$$\mathcal{H}_{dressedatom} = \mathcal{H}_0 + \mathcal{H}_{laser} + \mathcal{H}_{int} \tag{2.12}$$

$$= \hbar \begin{pmatrix} \omega_e & 0 \\ 0 & \omega_g \end{pmatrix} + \hbar\omega_{laser} \begin{pmatrix} N-1 & 0 \\ 0 & N \end{pmatrix} + \frac{\hbar}{2} \begin{pmatrix} 0 & \Omega \\ \Omega & 0 \end{pmatrix} \tag{2.13}$$

Now we subtract a constant energy offset $\hbar\omega_{laser}N + \hbar\omega_g$ from equation 2.13 and simplify with the definition of the detuning $\delta = \omega_{laser} - \omega_0$ to arrive at the final dressed atom Hamiltonian in equation 2.14:

$$\mathcal{H}_{dressedatom} = \frac{\hbar}{2} \begin{pmatrix} -\delta & \Omega \\ \Omega & \delta \end{pmatrix} \tag{2.14}$$

Diagonalizing this matrix to solve for the eigenenergies of the new combined laser plus atom system gives the eigenenergies $E_\pm$ in equation 2.15 [48].

$$E_\pm = \pm\frac{\hbar}{2}\Omega' \tag{2.15}$$

where Ω' is defined in equation 2.10 as $\Omega' = \sqrt{\delta^2 + \Omega^2}$. The new eigenstates of the system are given by equation 2.16 where $\sin(2\theta) \equiv \Omega/\Omega'$ and $\cos(2\theta) \equiv -\delta/\Omega'$.

$$|+\rangle = \sin(\theta)|g, N\rangle + \cos(\theta)|e, N-1\rangle \tag{2.16}$$

$$|-\rangle = \cos(\theta)|g, N\rangle - \sin(\theta)|e, N-1\rangle \tag{2.17}$$

If we now assume the limit of large detuning, or $|\delta| >> |\Omega|$, we arrive at a much easier result in equation 2.18.

$$E_\pm = \pm\frac{\hbar\Omega^2}{4\delta} \tag{2.18}$$

2.2.2 Spontaneous Emission and Optical Bloch Equations

Until now we have neglected the effects of spontaneous emission and have relied solely on the effect that the applied field has on the atomic states. Spontaneous emission plays a critical role in much of the preparation of ultracold atom samples. We start with the spontaneous emission rate of a 2 level atom [47]. The dipole moment, $\vec{\mu}$, is defined as $\vec{\mu} \equiv e \langle e | \vec{r} | g \rangle$. ϵ_0 is the permitivity of free space and c is the speed of light in vacuum.

$$\gamma \equiv \frac{\omega_0^3 \mu^2}{3\pi\epsilon_0 \hbar c^3} \tag{2.19}$$

This γ is the rate at which an atom in the excited state will emit a photon and transition to the ground state. The lifetime of the atom in the excited state is therefore given by $\tau = 1/\gamma$. For the commonly used $5P_{3/2}$ excited state of ^{87}Rb, $\tau = 27$ ns.

With this spontaneous emission rate in hand, we can work with a density matrix formalism to add in the effects of spontaneous emission to the dressed atom states we derived in section 2.2.1 to come to a quantity called the scattering rate, which will be useful when describing laser Doppler cooling. We will start with the time-dependent Schrödinger equation for a density matrix in equation 2.20.

$$i\hbar \frac{d\rho}{dt} = [\mathcal{H}, \rho] \tag{2.20}$$

Here the Hamiltonian, $\mathcal{H} = \mathcal{H}_{dressedatom}$ from equation 2.14. The density matrix ρ is defined for an arbitrary state $|\psi\rangle$ as $\rho = |\psi\rangle \langle\psi|$, i.e. $\rho_{ee} = |e\rangle \langle e|$ and gives the excited state population. Expanding out equation 2.20 for each term of the density

matrix gives equation 2.21 [47]. Here we have defined $\tilde{\rho}_{ge} \equiv \rho_{ge} e^{i\delta t}$.

$$\frac{d\rho_{ee}}{dt} = -\gamma\rho_{ee} + \frac{i\Omega}{2}(\tilde{\rho}_{ge} - \tilde{\rho}_0)) \tag{2.21a}$$

$$\frac{d\rho_{gg}}{dt} = +\gamma\rho_{ee} + \frac{i\Omega}{2}(\tilde{\rho}_0 - \tilde{\rho}_{ge})) \tag{2.21b}$$

$$\frac{d\tilde{\rho}_{ge}}{dt} = -(\frac{\gamma}{2} + i\delta)\tilde{\rho}_{ge} + \frac{i\Omega}{2}(\rho_{ee} - \rho_{gg}) \tag{2.21c}$$

$$\frac{d\tilde{\rho}_0}{dt} = -(\frac{\gamma}{2} - i\delta)\tilde{\rho}_0 + \frac{i\Omega}{2}(\rho_{gg} - \rho_{ee}) \tag{2.21d}$$

Here the terms with the spontaneous emission rate from equation 2.19 are added in manually to account for the spontaneous emission of the 2 level atom from the excited state to the ground state. Spontaneous emission decreases the population of the excited state, ρ_{ee}, and adds to the population of the ground state, ρ_{gg}. At first glance this appears to be an intractable problem. However, we can leverage a few known quantities to solve for the scattering rate, $\gamma_s = \gamma\rho_{ee}$. First, we can use normalization to enforce $\rho_{ee} + \rho_{gg} = 1$ and define the state population difference as $\rho_{dif} \equiv \rho_{ee} - \rho_{gg}$. Second, we know that $\rho_0 = \rho^*_{ge}$. Third, we will solve for the steady state, i.e. $\frac{d\rho_0}{dt} = \frac{d\rho_{dif}}{dt} = 0$. These three knowns allow us to solve for the scattering rate in equation 2.22 [47]:

$$\gamma_s = \gamma\rho_{ee} = \frac{s_0}{1 + s_0 + (\frac{2\delta}{\gamma})^2}(\frac{\gamma}{2}) \tag{2.22}$$

where we define the saturation parameter as $s_o = I/I_{sat}$. The saturation intensity, I_{sat}, is the laser intensity of resonant light where the scattering rate is half of its maximum value, $\gamma/2$, and is defined in equation 2.23 [47].

$$I_{sat} = \frac{\pi hc}{3\lambda_0^3\tau} \tag{2.23}$$

Here $\lambda_0 \equiv 2\pi c/\omega_0$ is the resonant wavelength.

2.3 Laser Doppler Cooling

Laser Doppler cooling is a widely used method for cooling atoms to ultracold temperatures, tens to hundreds of μK. We will start with classical physics of the Doppler effect, then move on the explain how the Doppler effect can be used in laser cooling to create a velocity-dependent retarding force.

The non-relativistic Doppler formula for a wave traveling at velocity v_{wave} through a medium is given by equation 2.24, where $f^{'}$ is the frequency as measured by the observer [49]. Here f is the frequency of the wave emitted by the source in its rest frame, $v_{observer}$ is the velocity of the observer, v_{source} is the velocity of the source, and the upper sign means motion towards each other. The measured frequency goes up when the source and observer move towards each other and goes down when they move away from each other.

$$f^{'} = f\frac{v_{wave} \pm v_{observer}}{v_{wave} \mp v_{source}} \tag{2.24}$$

We can take equation 2.24 and apply it to an atom and a traveling laser beam to derive laser Doppler cooling. Laser Doppler cooling of ultracold atoms works by leveraging the change in frequency of a laser, as seen in the moving frame of the atom, as a function of the velocity of the atom, see figure 2.2. We can simplify

FIG. 2.2: Simplified picture of laser Doppler cooling. The atom travels to the right at some velocity, v. The laser propogates to the left.

equation 2.24 by using the laboratory frame, where the source of the laser light is stationary. Using c as the speed of light in vacuum, we obtain equation 2.25 for the

frequency observed by the atom, $f^{'}$ as a function of the laser frequency, f_l.

$$f^{'} = f_l \frac{c \pm |v_{atom}|}{c} \tag{2.25}$$

This shift in laser frequency, as observed by the atom, can be treated as a change in the detuning δ of the laser from the atomic resonance. By rearranging equation 2.25 and introducing $\vec{k_l}$ as the wave vector of the laser and $\vec{v}$ as the velocity of the atom we arrive at equation 2.26 for the change in detuning due to the Doppler effect [47].

$$\delta_{doppler} = \delta - \vec{k_l} \cdot \vec{v} \tag{2.26}$$

Now that we have an equation in hand for dealing with the Doppler frequency shift from an atom with finite velocity, we will move on and further discuss the physics of laser Doppler cooling. We can treat absorption and spontaneous emission events as independent momentum transfers between the laser light field and the atom. Each absorption event transfers $|\Delta p_{abs}| = \hbar\omega_l/c$ of momentum between the laser light field to the atom, where $\omega_l \equiv 2\pi f_l$. Each spontaneous emission event produces a momentum kick of $|\Delta p_{emit}| = \hbar\omega_0/c$ in a random direction.

In an absorption event, the momentum transferred from the laser light field to the atom is in the direction of the propagation of the laser field. In a spontaneous emission event, momentum is transferred from the atom to the laser light field in a random direction, see figure 2.3. With repeated absorption and spontaneous emission events entropy is thus transferred from the atom to the laser light field.

Taking one more step we can derive a force from the absorption of photons from a single laser light field by the atom as the momentum transfer divided by the time between scattering events, Δt, in equation 2.27. The emission of photons should sum to zero momentum transfer taken as an average over many scattering events.

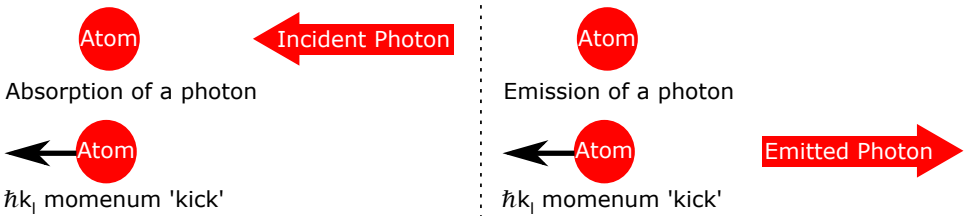

FIG. 2.3: Diagram of momentum transfer during photon absorption (left) and emission events (right). The momentum kick from absorption is in the same direction as the momentum of the incident laser light field. The momentum kick from spontaneous emission is in a random direction.

The effect of momentum jitter due to spontaneous emissions will be discussed in more detail in section 2.3.1.

$$\vec{F}_l = \frac{\Delta \vec{p}_{abs}}{\Delta t} = \gamma_s \frac{\hbar \omega_l}{c} \hat{k}_l \tag{2.27}$$

This single laser could only cool the atom if the atom is moving anti-parallel to the propagation direction of the laser field. To ensure cooling for an arbitrary atom velocity, we add in a second counter-propagating laser beam and define the direction of motion as $\vec{x}$. This brings us to equation 2.28 [47].

$$\vec{F}_{total} = \vec{F}_1 + \vec{F}_2 = \gamma_{s1} \frac{\hbar \omega_l}{c} \hat{x} - \gamma_{s2} \frac{\hbar \omega_l}{c} \hat{x} \tag{2.28}$$

The scattering rate, γ_s defined in equation 2.22, is the only piece of equation 2.28 that is dependent on the velocity of the atom, through the velocity-dependent detuning. Combining equations 2.28, 2.26, and 2.22 we can arrive at 2.29, the total velocity-dependent scattering force for an atom with two counter-propagating laser light fields (in one-dimension) [47]. Here we have made the assumption that the two lasers have equal intensity such that $s_1 = s_2 = s_0$.

$$\vec{F}_{total} = \frac{\hbar \omega_l}{c} \frac{s_0 \gamma}{2} \left[\frac{1}{1 + s_0 + (\frac{2}{\gamma}(\omega_l - \frac{v_a}{c}\omega_l - \omega_0))^2} - \frac{1}{1 + s_0 + (\frac{2}{\gamma}(\omega_l + \frac{v_a}{c}\omega_l - \omega_0))^2} \right] \tag{2.29}$$

We can now make an assumption that the detuning of the laser field is large, or more precisely that $(2\delta/\gamma)^2 >> 1$. This assumption leads to a much cleaner form of the velocity-dependent scattering force in equation 2.30 [47].

$$\vec{F}_{total} \approx \frac{4\hbar k^2 s_0 (2\delta/\gamma)}{(1 + s_0 + (2\delta/\gamma)^2)^2}\vec{v} = -\beta\vec{v} \tag{2.30}$$

2.3.1 Doppler Limit

There is an inherent limit to the laser Doppler cooling process created by the heating associated with a single photon recoil from an atom [47]. When an atom emits a photon it gets a momentum 'kick' in the opposite direction to the emitted photon. This momentum 'kick' provides a lower bound for the momentum that can be achieved through laser Doppler cooling. It has an associated recoil velocity of $v_r = \hbar k_l/M = \hbar\omega_l/Mc$. Here M is the mass of the atom. Taking this one step further we can define a recoil energy, E_r, associated with the recoil velocity.

$$E_r = \frac{Mv_r^2}{2} = \frac{\hbar^2\omega_l^2}{2Mc^2} = \hbar\omega_r \tag{2.31}$$

In the last step of equation 2.31 we have defined the recoil frequency as $\omega_r \equiv E_r/\hbar$.

We can use a simple conservation of energy method to determine the heating that is associated with a single photon scattering (absorption and spontaneous emission) event. Figure 2.3 is a good reference for visualization of this process. For absorption we have $\hbar\omega_{absorb} = \hbar\omega_0 + \hbar\omega_r$ and for emission we have $\hbar\omega_{emit} = \hbar\omega_0 - \hbar\omega_r$. Thus, one photon scattering event increases the energy of the atom, or heats it, by $E_{heat} = \hbar(\omega_{absorb} - \hbar\omega_{emit}) = 2\hbar\omega_r$. This process can be envisioned as a random walk in momentum space. Using the previously derived scattering rate in equation 2.22 we can determine the heating rate of two laser beams, $R_{heating}$, in equation 2.32 in the low scattering rate limit, $\gamma_s \ll \gamma/2$. Here the factor of two in front of the

scattering rate γ_s represents the presence of two laser beams.

$$R_{heating} = 2\hbar\omega_r(2\gamma_s) \tag{2.32}$$

Now that we have the heating rate in equation 2.32 we can combine it with the cooling rate given in 2.30 to solve for the steady state kinetic energy of the atom by setting the two rates equal to each other. The result is equation 2.33 [47].

$$KE = \frac{\hbar\gamma}{8}(\frac{2\delta}{\gamma} + \frac{\gamma}{2\delta}) \tag{2.33}$$

This steady state kinetic energy is minimized for a laser detuning of $\delta = -\gamma/2$. Plugging in this optimal detuning and using $1/2k_BT_D = \langle E \rangle$ we can arrive at the lower limit for the Doppler temperature, T_D, in equation 2.34.

$$T_D = \frac{\hbar\gamma}{2k_B} \tag{2.34}$$

The on-resonance spontaneous emission rate for the $5P_{3/2}$ state of ^{87}Rb is $(2\pi)6.075$ MHz [22]. This gives a Doppler temperature limit of $T_D = 146$ μK.

2.3.2 Sub-Doppler Cooling (Optical Molasses)

Optical molasses is a laser cooling technique that can be used to cool atoms below the Doppler limit discussed in section 2.3.1 [50]. Optical molasses uses the transfer of energy from the atoms to the laser light field by selective absorption of lower frequency photons and spontaneous emission of higher frequency photons to accomplish cooling of the atoms, similar to traditional laser Doppler cooling.

Optical molasses accomplishes selective absorption of lower frequency photons by using two red-detuned counter-propagating laser beams to create a standing

wave of changing polarization. The standing wave creates an AC Stark shift that is different for the different ground level atomic spin states. For simplicity we will work with a system with a ground level with $F = 1/2$ and two ground states $m_f = \pm 1/2$. We will define the $\sigma^-(\sigma^+)$ light as circularly polarized, rotating around the propagation axis in the positive(negative) sense. Figure 2.4 shows a cartoon

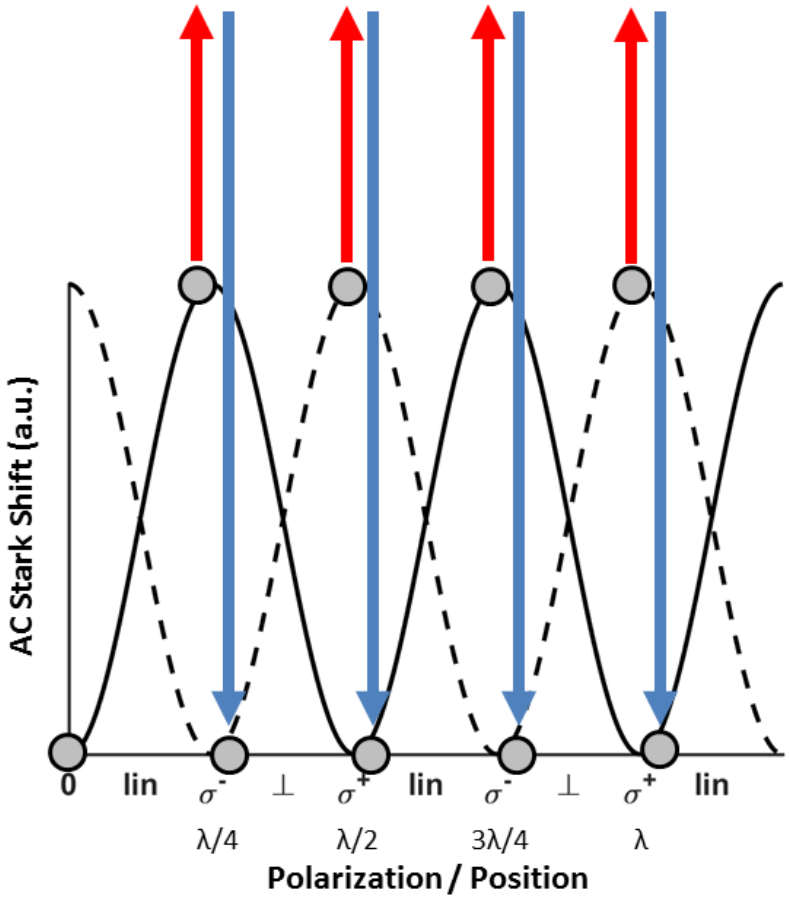

FIG. 2.4: Plots of two different electronic spin states +1/2 (solid) and -1/2 (dashed) vs. position of the atom which corresponds to a changing standing wave polarization for a lin-⊥-lin lattice configuration. The atom (black circle) starts at x = 0 and 'climbs' a potential energy hill until reaching σ^- light, $z = \lambda/4$, where it undergoes absorption (red arrow) and spontaneous emission (blue arrow) to be transferred from +1/2 into -1/2. This process then repeats in another $\lambda/4$ of distance where the standing wave polarization changes to σ_+ and the atom gets optically pumped from -1/2 to +1/2.

of the varying polarizations for these two laser light fields and their effect on the energy levels of the atoms. When the light is σ^- polarized at $\lambda/4$ the +1/2 state gets AC Stark shifted closer to resonance and is more likely to absorb a photon and

get pumped into the excited state. When the atom undergoes spontaneous emission afterwards it can decay into the -1/2 state which at that position is AC Stark shifted to the blue (away) from resonance. The atom then 'climbs' the potential energy hill again until it enters a region of σ^+ light at $\lambda/2$ where it undergoes an absorption process again. This continual climbing up a potential hill and optical pumping back to the bottom again cools the atoms by transferring energy to the laser light field. The limit for cooling with optical molasses is related to the momentum jitter due to a single photon emission event, $\Delta p = \hbar\omega_0/c$. The optical molasses cooling limit is given by equation 2.35. For light cooling on the D_2 line of ^{87}Rb the $T_{OM} = 360$ nK.

$$T_{OM} = \frac{(\Delta p)^2}{mk_B} = \frac{\hbar^2\omega_0^2}{mc^2k_B} \tag{2.35}$$

Optical molasses is also commonly referred to as "Sisyphus Cooling" owing to the similarity to the greek myth of King Sisyphus whose punishment for bad deeds during his life was to roll an enchanted boulder uphill only to have it roll back down before he could make it to the top.

2.3.3 Optical Pumping

Optical pumping is a term that is used to describe the changing of internal atomic states by the scattering of photons. Deliberate optical pumping can be employed to preferentially populate any 'stretched' atomic state, those with $|m_F| = F$, that is advantageous for an experiment. The optical pumping light pulse employed in our experiment is a short (1 ms), relatively weak, pulse of σ_+ light that drives the ^{87}Rb transition from $5^2S_{1/2} \rightarrow 5^2P_{3/2}$, as seen in figure 2.5. The σ_+ light drives atoms to the right of figure 2.5, or $m_f^{'} = m_F + 1$. The atoms in the excited $5^2P_{3/2}F^{'} = 2$ state can undergo spontaneous emission with any light polarization with probabilities given in the circles connecting the two states in figure 2.5. Over

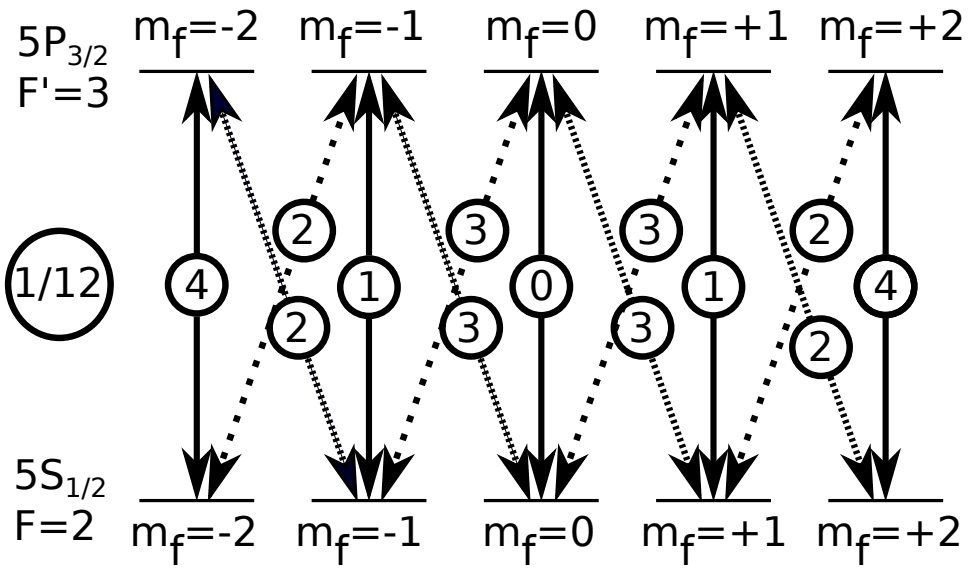

FIG. 2.5: Optical Pumping in ^{87}Rb between the $5^2S_{1/2} \rightarrow 5^2P_{3/2}$ states (D2 line) with $F = 2, F^{'} = 2$. Solid lines represent π transitions, closely dashed lines represent σ_- transitions, and loosely dashed lines represent σ_+ transitions. Numbers within the lines correspond to the transition probability, the square of the dipole matrix elements, in units of $|\langle J = 1/2| er |J = 3/2\rangle|^2$ with a total factor of 1/12 [51].

a large enough number of scattering events, all of the atoms will eventually work their way over to the $5^2S_{1/2}|F = 2, m_F = +2\rangle$ state. There is no σ^+ transition for this state so the atoms there go 'dark' and no longer absorb the optical pumping light. This leaves a spin-polarized atomic sample in $5^2S_{1/2}|F = 2, m_F = +2\rangle$.

Optical pumping has its drawbacks and imperfections such as: heating from multiple photon scattering events, dense atomic samples shadowing the inner atoms from OP light, polarization impurities, and misalignment between laser light $\vec{k_l}$ and the quantizing magnetic field direction. Polarization impurities in the laser light field and misalignment of the laser light field propagation direction manifest by driving unwanted π and σ_- transitions. This leads to atomic samples that have a finite population in unwanted spin states, $m_F \neq +2$ for our experiment. These problems can be mitigated by ensuring the purity of the circular polarization of the pumping light and the alignment between the light propagation vector and the quantization magnetic field.

Optical pumping is particularly useful during the transition from laser cooled atoms to magnetic trapping. Magnetically trapping straight from optical molasses without optically pumping atoms into $m_F = +2$ would lead to a magnetic trap with 1/5 as many atoms as are available. During the MOT and optical molasses stage of the experiment, there are large populations of atoms in each of different m_F states of ^{87}Rb $5^2S_{1/2}F = 2$. The only magnetically trappable states are $m_F = +2, +1$ and we specifically run the magnetic field gradient large enough to trap $m_F = +2$ against gravity, but not $m_F = +1$. After a proper optical pumping sequence there is a spin-polarized atomic sample ready for efficient loading into the magnetic trap.

2.4 Magneto-Optical Trapping (MOT)

Magneto-Optical Traps (MOTs) are a standard experimental starting point used in cold atom experiments. They combine the cooling effects of red-detuned laser light with the spatial dependence and confinement of a magnetic field. A typical MOT set up is seen in figure 2.6. Atoms in the state $m_F = -1$ experience $U_{DCZeeman} < 0$ to the right of the center of the coils, and are shifted closer to resonance with the σ_- light incident from the right hand side. This preferential light absorption from the right hand side pushes the atoms to the left (towards the center). Atoms in the state $m_F = +1$ experience $U_{DCZeeman} < 0$ to the left of the center of the coils, and are shifted closer to resonance with the σ_+ light incident from the left hand side. This preferential absorption also pushes them towards the center of the coils.

The red-detuned light cools the atoms and the spatially varying magnetic field creates a spatially varying detuning. This spatially varying detuning provides a restoring force towards the center of the coils creating the MOT due to preferential light absorption from the laser beams. Typical MOT numbers in our apparatus

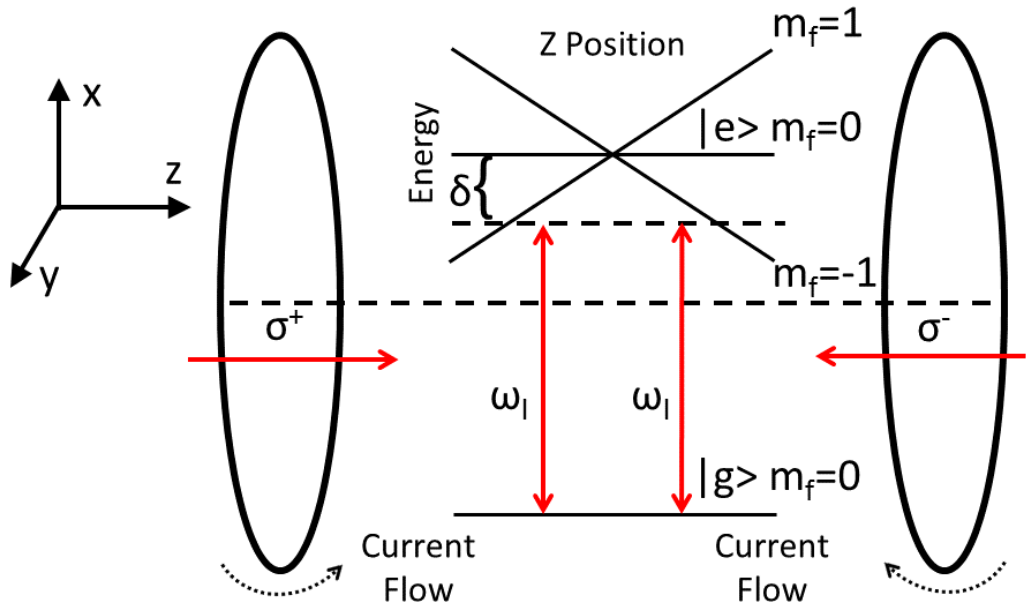

FIG. 2.6: Cartoon schematic of a Magneto-Optical Trap. A pair of coils in Anti-Helmholtz configuration, as seen in figure 2.7, produce a linear magnetic field gradient along $\hat{z}$. A pair of counter-propagating laser beams with opposite circular polarization are incident from the left and the right with a frequency ω_l at a detuning of δ below the $|g, m_F = 0\rangle \rightarrow |e, m_F = 0\rangle$ resonance. The atoms experience a restoring force towards the center $z = 0$ from the combined magnetic and optical forces. This is shown with a $J_g = 0, J_e = 1$ transition, but is applicable for any $J_e = J_g + 1$ transition [47].

have $N \approx 5 \times 10^8$ and $T \approx 100\mu K$, note the Doppler Temperature $T_D = 146\mu K$.

2.5 Magnetic Trapping

Magnetic traps are used primarily for spatial confinement and evaporative cooling of atoms that have already gone through the laser cooling and optical pumping processes [52, 47]. Magnetic trapping relies on the energy shift of internal atomic states by an externally applied DC magnetic field, called the DC Zeeman effect. In the low-field limit the DC Zeeman effect shifts the energy of the atomic levels as given in equation 2.36. Here, $\vec{\mu}$ is the dipole magnetic moment of the atomic state, m_f is a 'good' quantum number giving the projection of the total angular momentum, $\vec{\boldsymbol{F}} = \vec{\boldsymbol{I}} + \vec{\boldsymbol{L}} + \vec{\boldsymbol{S}}$, along the magnetic quantization axis, $\hat{\boldsymbol{B}}$. g_F is the

Landé g-factor and μ_B is the Bohr magneton.

$$U_{Zeeman} = -\vec{\mu} \cdot \vec{B} = m_f g_f \mu_B |\vec{B}| \tag{2.36}$$

States with $m_f g_f > 0$ are low-field seekers, while states with $m_f g_f < 0$ are high-field seekers. Local maxima are forbidden for magnetostatic fields in free space [47, 53]. This leaves only magnetic field minima, and thus only states with $m_f g_f > 0$ are trappable in a DC magnetic field.

2.5.1 DC Quadrupole Magnetic Traps

A simple method for creating a quadrupole magnetic trap for cold atoms is a pair of coils in anti-Helmholtz configuration. This has several advantages and disadvantages. These traps are relatively cheap and easy to assemble, can trap large clouds of atoms, and enable good optical access. These traps typically suffer from poor confinement for evaporation, require large amounts of current (50-150 A), and have $|\vec{B}| = 0$ at the center which can lead to Majorana spin-flip losses.

The magnetic field on-axis in the middle of the two coils is given by: $|B| = A\sqrt{x^2 + y^2 + 4z^2}$ where the coils are separated in the z-direction, called the strong axis. A is a parameter defined by the exact geometry of the system and current running through the coils. The magnetic field gradient produced by these coils is given by equation 2.37. The gradient is twice as strong along the strong (z) axis as the other two axes.

$$\nabla \vec{B} = B'(\frac{\hat{\boldsymbol{x}}}{2} + \frac{\hat{\boldsymbol{y}}}{2} + \hat{\boldsymbol{z}}) \tag{2.37}$$

A useful calculation to make is to determine the magnetic field gradient that produces a force equal to gravity on the atoms. A magnetic trap can be used to spin-distill samples by applying a magnetic field gradient that will only hold

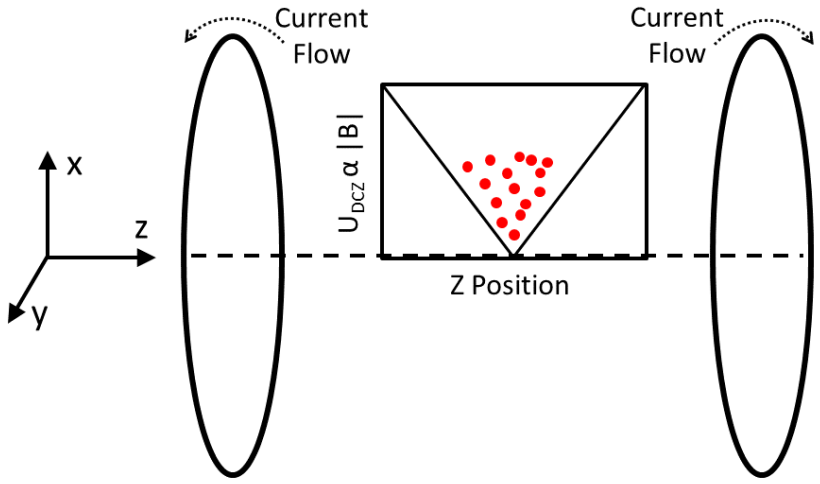

FIG. 2.7: Magnetic trap created by two coils in anti-Helmholtz configuration. The red dots represent atoms in the trapping potential created by running current through the coils.

$|F = 2, m_f = +2\rangle$ against gravity, but not $|F = 2, m_f = +1\rangle$. If we set $F_{zeeman} = \mu \nabla B$ equal to the force due to gravity, $F_{gravity} = Mg$, we can solve for $B^{'}$ in equation 2.38. Here M is the mass of the atom and g is the acceleration due to gravity.

$$B^{'} = \frac{Mg}{m_f g_f \mu_B} \tag{2.38}$$

Magnetic quadrupole traps suffer a distinct disadvantage in that atoms passing through or near the center of the trap experience a zero or very small magnetic field and can experience Majorana spin-flips. This process occurs when the atoms pass through changing magnetic fields faster than the spin of the atoms can keep up. This creates a non-adiabatic condition where the spin of the atoms no longer follows the local magnetic field, which leads to changes in the m_f Zeeman sub level of the atoms. In order to maintain adiabaticity the Larmor precession frequency, ω_z, must be much greater than the orbital frequency of the atoms in the magnetic trap, ω_T.

Equation 2.39 gives the necessary conditions for the velocity of the atom, $\vec{v}$ [47].

$$\begin{aligned} &\omega_z \gg \omega_T \\ \Leftrightarrow &\frac{\mu B}{\hbar} \gg \frac{d\vec{B}/dt}{\vec{B}} = \frac{|\vec{v} \cdot \nabla \vec{B}|}{\vec{B}} \end{aligned} \tag{2.39}$$

Majorana spin-flips are detrimental to the experiment for three reasons. First, the spin flips can cause the atoms to go into a different magnetically trappable state, causing an impure sample and atom number losses during evaporation. Second, the atoms can spin flip to a state that is not magnetically trappable, leading to atom number loss. Finally, the atoms that are more likely to get spin-flipped are those that spend the most time orbiting near the center of the trap, or the coldest atoms. When these colder atoms get spin-flipped to a non-trappable atomic state it leads to heating in addition to atom number loss as colder atoms are preferentially removed from the cloud. These ejected atoms get accelerated out of the trap and may collide with trapped atoms while exiting, leading to additional heating.

2.5.2 Atom Chip Magnetic Trap

The atom chip used in our apparatus uses a Ioffe-Pritchard type trap to magnetically confine atoms such that $|B| \neq 0$ everywhere to prevent spin-flop losses. This is accomplished by using a Z-shaped wire on the atom chip in combination with two external homogeneous magnetic fields: B_{Ioffe} and B_{Hold}, as seen in figure 2.8. The magnetic field magnitude produced by the chip wire is given by equation 2.40. Here I is the current running through the chip wire, d is the distance from the chip wire, and μ_0 is the vacuum permeability. In the thin wire limit, Ampère's law gives the magnetic field produced by the chip wire.

$$|B_{chip}| = \frac{\mu_0 I}{2\pi d} \tag{2.40}$$

As shown in Figure 2.8, B_{Chip} and B_{Hold} cancel at a distance, d, directly above the Z-wire given by equation 2.41. The B_{Ioffe} pointing out of the page perpendicular to the B_{Hold} and B_{Chip} maintains a minimum $|B| \neq 0$ to prevent spin flip losses. Ideally B_{Ioffe} is homogeneous and does not play a role in the spatial manipulation or trapping of the atoms and only serves to preserve the $|B|$ floor.

$$d = \frac{\mu_0 I}{2\pi |B_{Hold}|} \tag{2.41}$$

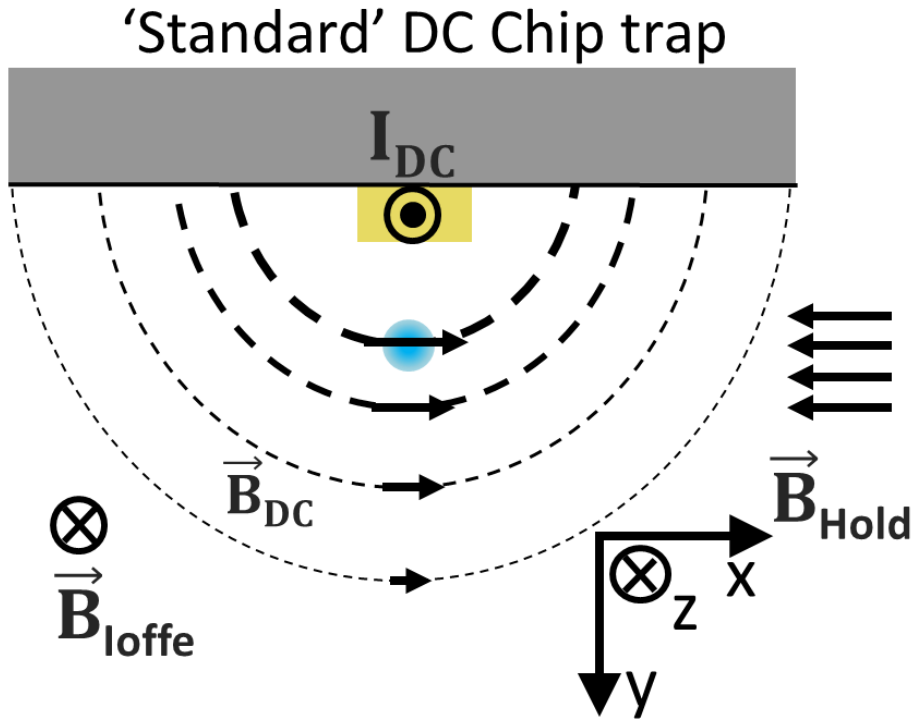

FIG. 2.8: Schematic of the chip magnetic trap. The Z-wire (gold rectangle) carries a current running out of the page which produces $\vec{B_{DC}}$. The other magnetic fields, $\vec{B_{Hold}}$ and $\vec{B_{Ioffe}}$, are produced by two pairs of external coils in Helmholtz configuration. The blue dot gives the location of the magnetic field minimum where the weak field seeking atoms are trapped.

The wire geometry shown provides for 'radial' confinement along $\hat{x}$ and $\hat{y}$, but do not provide any confinement into $\delta_{exp}$and out of the page along $\hat{z}$. The 'endcap' wire segments of the Z-wire in figure 2.8 run along $\hat{x}$, but are not shown for simplicity.

These 'endcap' wire segments provide the axial confinement along $\hat{z}$ necessary for a trapping potential in all three dimensions. These endcap wires are shown in the top view of figure 4.12.

2.6 Imaging

All of the data presented in this thesis starts from taking pictures of atom clouds with a CCD camera. These images can be analyzed to give the size, shape, position, and number of atoms present in a cloud. There are two types of imaging that are used, each with their own benefits and drawbacks: fluorescence imaging and absorption imaging.

Fluorescence imaging is the simplest method to apply to an atom cloud, and is often the first method learned for a new graduate student. Fluorescence imaging is conducted by shining a resonant, or near-resonant, laser field to the atomic cloud to be measured and collecting the resulting fluorescence from the atoms on a CCD camera. The atoms absorb the resonant light and emit it into a random direction. This entire scattering process occurs at a rate given in Equation 2.22, repeated here for convenience.

$$\gamma_s = \frac{s_0}{1 + s_0 + (\frac{2\delta}{\gamma})^2}(\frac{\gamma}{2}) \tag{2.42}$$

Here $s_0 = I/I_{sat}$ is a measure of the intensity of the laser beam, δ is the detuning from resonance, and γ is the natural linewidth of the targeted transition.

The big advantage of this method is that it is has a low background and can be used to image small atom numbers, even down to a single atom in other groups [54]. Fluorescence imaging can also be used to image a MOT while it is operating simply by turning on the camera. This real-time feedback can be extremely useful when first aligning a MOT and trying to get all of the beams aligned and correctly

balanced in power. The disadvantage of fluorescence imaging is that at high atomic densities, the incident light interacts with atoms close to the surface before being able to probe those further in. This loses information about atoms on the inside of the cloud and generally leads to undercounting the atom number. It is also more difficult to get an atom number from the fluorescence counts on a CCD camera because you need to know the collection solid angle of the imaging system, the quantum efficiency of the CCD sensor, the gain of the analog-to-digital converter in the camera, the exposure time of the image, and the power of the applied laser beam.

More quantitative measurements of the atom number in our apparatus are conducted with absorption imaging using resonant or near-resonant light. Absorption imaging takes an image 'head-on' of a laser beam aimed through the atomic cloud into the camera imaging system. The atomic cloud absorbs some of the light in the first 'shadow' image. There is a wait time of about 1/2 of a second and another picture is taken without any atom present, the 'laser' image. The atom number can then be extracted from these two images by using a method based on Beer's law [47].

$$I(z)/I_0 = e^{-OD} \tag{2.43}$$

Here $I(z)$ is the measured light intensity in each camera pixel in the 'shadow' image with atoms, and I_0 is the intensity in the 'laser' image. The optical depth can then be solved for by: $OD = ln(\frac{I_o}{I(z)})$. This optical depth (OD) of a column of cold atoms along the direction of travel, $\hat{z}$, of a low intensity intensity laser beam $I_0 \ll I_{sat}$ is given by:

$$OD = \sigma_0(1 + (\frac{2\delta}{\gamma})^2)^{-1} nz \tag{2.44}$$

where n is the atomic density, typically measured in $atoms/cm^3$ and $\sigma_0 = \frac{3\lambda}{2\pi}$ is the on-resonance atomic cross section. If we multiply each side by the area of the CCD

pixel, A_{pixel}, then we get to:

$$nzA = N = \frac{A_{pixel}}{\sigma_0}(1 + (\frac{2\delta}{\gamma})^2)ln(\frac{I_o}{I(z)}) \tag{2.45}$$

In Equation 2.45 N is the measured atom number. The only experimental parameters that need to be known are the area of the CCD pixel, A_{pixel}, (make sure to account for any imaging system magnification) and the digital counts in each pixel, I_0 for the 'laser' image and $I(z)$ for the 'shadow' image.

The biggest benefit of absorption imaging is this ability to obtain quantitative measures of the atom number using only the data measured by the camera and the known pixel size and laser detuning. Absorption imaging also gives accurate information about atoms present in the center of the cloud, that fluorescence imaging does not. A drawback of absorption imaging is that the constant background created by the laser. It is difficult to image low atom numbers with absorption imaging as a result. Figure 2.9 shows an example image of absorption imaging of the MOT cell magnetic trap.

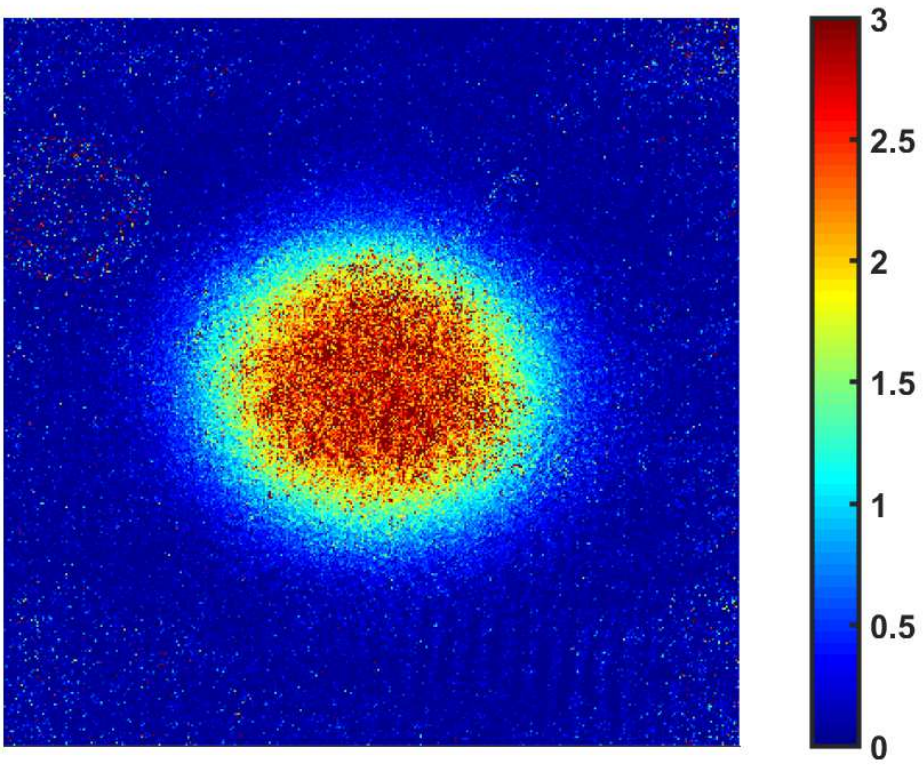

FIG. 2.9: ^{87}Rb MOT cell magnetic trap absorption imaging. The color axis is optical depth (OD) and the entire image is 9.7mm x 7.3 mm. This cloud is loaded from a 3 second MOT load with a time-of-flight of 7 ms. The imaging light is on resonance ($\delta = 0$). There are about 6×10^7 atoms at a temperature of 100μK.

CHAPTER 3

AC Zeeman Theory

This chapter describes the theory behind the ACZ effect that is demonstrated experimentally in later chapters. This chapter follows the first proposal of using the ACZ effect to trap and manipulate ultracold atoms [26] as well as a general text on two-level atom theory [47].

This chapter is arranged as follows. Section 3.1 uses a two-level atom approximation to derive the energy shifts and the dressed atom eigenstates of the ACZ effect. Section 3.2 discusses how to calculate the Rabi frequency given a specific transition and applied AC magnetic field, as well as how to experimentally measure the Rabi frequency. Section 3.3 describes numerical simulations done to test the effect of adding a second microwave field to use as a method of forced evaporation. The chapter finishes with section 3.4 which describes how to create trapping potentials using the ACZ effect with an AC magnetic near-field generated close to an atom chip.

3.1 Dressed Atom Theory

The AC Zeeman effect can be well understood using a standard two-level atom with states $|g\rangle$ and $|e\rangle$ interacting with an applied E-M field with frequency ω_{RF}, introduced in section 2.1. Now, however, the transition being driven is an M1 hyperfine transition at the RF/microwave frequency level instead of the previous optical transitions with an applied laser field. In our experiments we typically work with the $|F = 2, m_F = +2\rangle \leftrightarrow |F = 1, m_F = +1\rangle$ M1 hyperfine transition within the $5S_{1/2}$ level manifold in ^{87}Rb. However, the theory presented in this section is valid for any M1 hyperfine transition.

The dressed atom theory for this new system is the same as in section 2.2.1 for optical transitions, and is repeated for ease of reading. The dressed atom approach incorporates the bare atomic Hamiltonian, $\mathcal{H}_0$, the Hamiltonian for an RF field with N+1 photons, $\mathcal{H}_{RF}$, and the interaction Hamiltonian, $\mathcal{H}_{int}$, into one combined Hamiltonian. Equation 3.1 gives the combined dressed atom Hamiltonian, $\mathcal{H}_{dressedatom}$, in the $|e, N-1\rangle|g, N\rangle$ basis.

$$\mathcal{H}_{dressedatom} = \mathcal{H}_0 + \mathcal{H}_{RF} + \mathcal{H}_{int} \tag{3.1}$$

$$= \hbar \begin{pmatrix} \omega_e & 0 \\ 0 & \omega_g \end{pmatrix} + \hbar\omega_{RF} \begin{pmatrix} N & 0 \\ 0 & N+1 \end{pmatrix} + \frac{\hbar}{2} \begin{pmatrix} 0 & \Omega \\ \Omega & 0 \end{pmatrix} \tag{3.2}$$

Next, we subtract a constant energy offset $\hbar\omega_{RF}(N+1) + \hbar\omega_g - \hbar\frac{\delta}{2}$ from equation 3.2 and simplify with the definition of the detuning $\delta = \omega_{RF} - \omega_{eg}$ to arrive at the final dressed atom Hamiltonian in equation 3.3:

$$\mathcal{H}_{dressedatom} = \frac{\hbar}{2} \begin{pmatrix} -\delta & \Omega \\ \Omega & \delta \end{pmatrix} \tag{3.3}$$

Here the Rabi frequency is defined the same as before. When written in terms of the strength of the AC magnetic field, $\vec{B}_{AC}$, and the magnetic moment $\vec{\mu} = (2\mu_B/\hbar)\vec{S}$, the Rabi frequency becomes the following:

$$\Omega = \frac{1}{\hbar}\langle e| - \vec{\mu}\cdot\vec{B}|g\rangle = -\frac{\mu_B}{\hbar^2}\langle e|\, 2\vec{S}\cdot\vec{B}|g\rangle \tag{3.4}$$

Here $\vec{S}$ is the spin operator for the valence electron and $\mu_B = h \times 1.3996$ MHz/G is the Bohr magneton. This equation is examined in more detail in section 3.2.

3.1.1 ACZ Energy Shift

Diagonalizing the matrix in equation 3.3 gives the eigenenergies $E_{dressedatom\pm}$ below [48].

$$E_{dressedatom\pm} = \pm\frac{\hbar}{2}\Omega' \tag{3.5}$$

The generalized Rabi frequency is $\Omega' = \sqrt{\delta^2 + \Omega^2}$. The eigenenergies in equation 3.5 are plotted below in figure 3.1 in red and blue. The black lines represent the energies of the bare atom plus photon states, $|g, N\rangle$ and $|e, N-1\rangle$. The energy

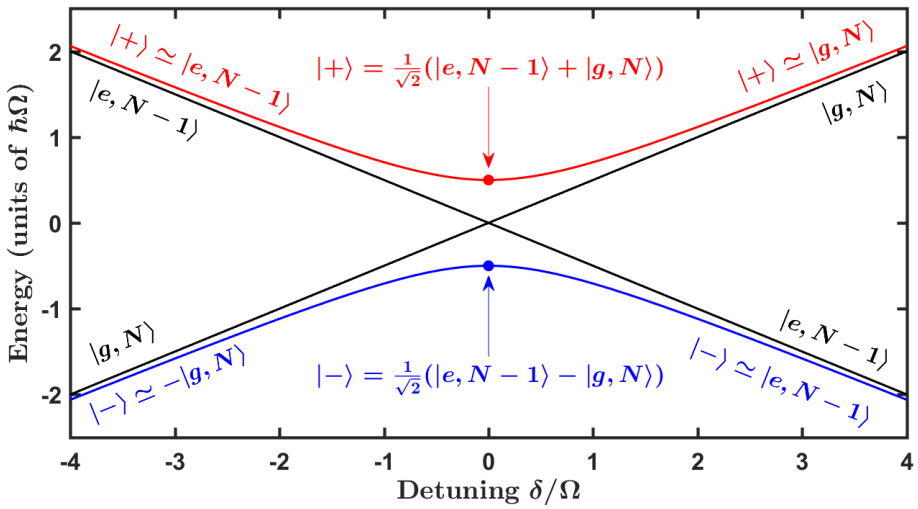

FIG. 3.1: Avoided Level Crossing. Plot of the eigenergies $E_{dressedatom\pm}$ for the μw-dressed atom eigenstates $|\pm\rangle$ versus detuning δ in red and blue. The bare atom plus photon states $|g, n\rangle$ and $|e, N-1\rangle$ are plotted in black.

shift due to the ACZ effect, E_{ACZ}, can be found by taking the difference in energy between the $|\pm\rangle$ states (red and blue) and the bare states shown (black) in Figure 3.1. The resulting ACZ energy shift [26] is given by:

$$E_{\pm} = \pm\frac{\hbar}{2}(-|\delta| + \Omega') \tag{3.6}$$

The energy shift $E_{\pm}$ is largest in magnitude on resonance ($\delta = 0$) where it has a value $E_{\pm} = \pm\frac{\hbar\Omega}{2}$. As the detuning increases, this energy shift decreases and the energies of the dressed atom eigenstates $|\pm\rangle$ get closer to those of the bare states $|g, N\rangle$ and $|e, N-1\rangle$. The difference between the energy of the $|\pm\rangle$ states and the bare atomic states $|g, N\rangle$ and $|e, N-1\rangle$ can be used as a rough measure of the relative population: the closer the energies are the more relative population in each state. For example, for $\delta = +4\Omega$, the population of the $|-\rangle$ state is mostly the $|e, N-1\rangle$ bare atomic state. This is discussed in more detail in section 3.1.3.

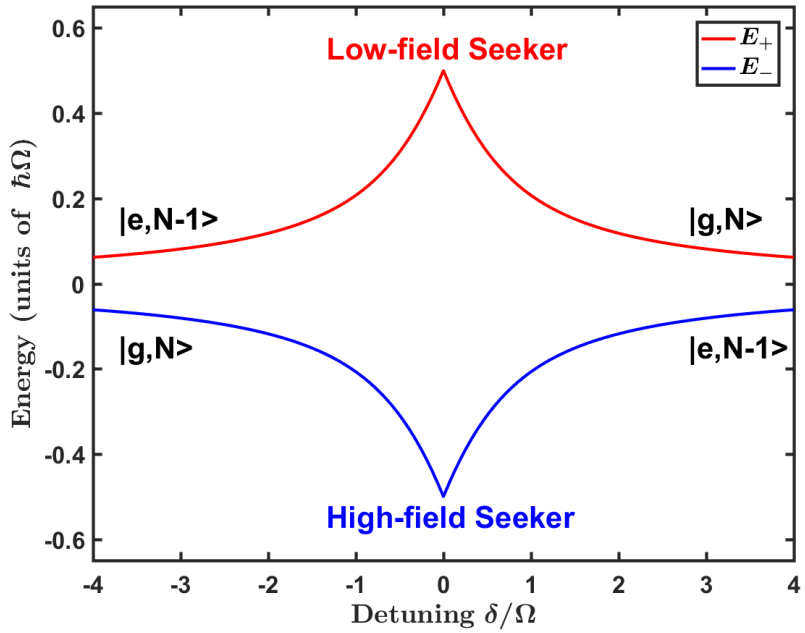

FIG. 3.2: ACZ Energy Shift. The red(blue) lines plot the energy shift due to the ACZ effect, $E_{\pm}$ for the $|+\rangle(|-\rangle)$ states given in equation 3.6. The $|\pm\rangle$ states are equal superpositions of $|g, N\rangle$ and $|e, N-1\rangle$ on resonance, but are well described by one or the other far off resonance.

The ACZ energy shifts from equation 3.6 are plotted in figure 3.2 in red for the $|+\rangle$ state and blue for the $|-\rangle$ state. The $|+\rangle$ state has a positive energy shift for all detunings δ and is thus a low-field seeker. Similarly, the $|-\rangle$ state has a negative energy shift for all detunings δ and is therefore a high-field seeker. In the experiments of this thesis, we work in the near-field regime where the AC magnetic field shape closely follows that of the DC field. Local maxima are not allowed for static magnetic fields [47, 53] so it follows that they are not allowed in the near-field regime for AC magnetic fields. The $|-\rangle$ can then by trapped by a local minimum in the AC magnetic field while the $|+\rangle$ state is not trappable in this near-field regime.

It is useful to take the limit of equation 3.6 in the case of large detuning, $|\delta| \gg |\Omega|$, and small detuning , $|\delta| \ll |\Omega|$. For the large detuning case the ACZ energy shift is given in equation by:

$$E_{\pm} \approx \pm \frac{\hbar \Omega^2}{4\delta} , \quad |\delta| \gg |\Omega| \tag{3.7}$$

This energy shift in the large detuning limit can be seen graphically in figure 3.3.

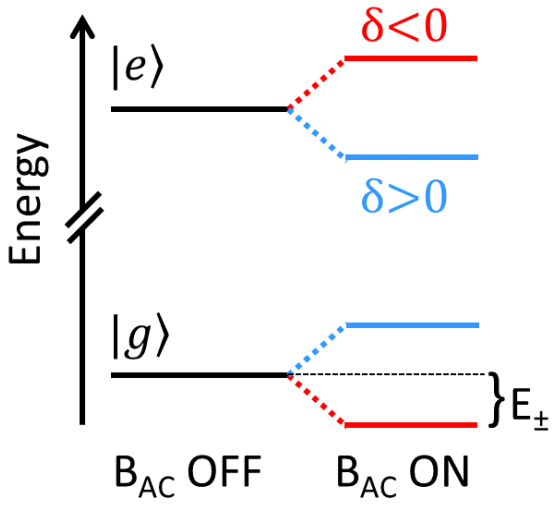

FIG. 3.3: ACZ Energy Level Shift. This shows the energy shifts of the ground and excited states in the limit of large detuning $\delta \gg |\Omega|$ from the ACZ effect.The energy in the AC magnetic field has been removed. The black lines represent the energy of the bare atomic states without the AC magnetic field while the red(blue) lines represent the energy of these states with the AC magnetic field turned on for $\delta < (>)0$.

The energy shift is mathematically the same as that of an optical dipole trap seen in figure 5.1. The limit of small detuning is given by:

$$E_{\pm} \approx \pm\frac{\hbar}{2}(-|\delta| + \Omega) \ , \quad |\delta| \ll |\Omega| \tag{3.8}$$

Figure 3.4 plots these two limits along with the full energy of the trappable $|+\rangle$ state, $E_+ = \frac{\hbar}{2}\sqrt{\delta^2 + \Omega^2}$ given in equation 3.6. The small detuning limit is only close to the full value of $E_{\pm}$ for $\frac{|\delta|}{|\Omega|} < 0.5$. The large detuning limit matches well for $\frac{|\delta|}{|\Omega|} > 1.5$. It is only in the intermediate case where $\frac{|\delta|}{|\Omega|} \simeq 1$ that the full energy is not well described by one of the limits.

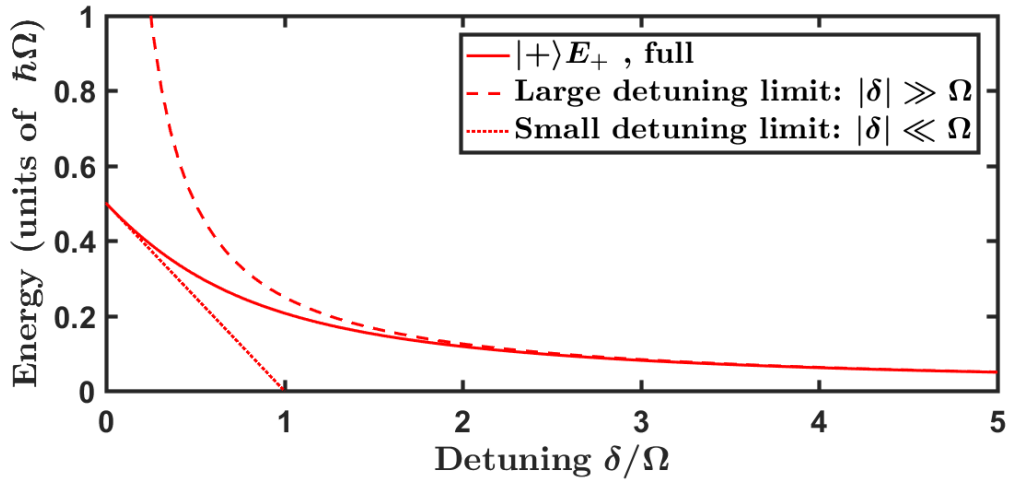

FIG. 3.4: ACZ energy shift including limits for large and small detunings. The solid red line plots the full energy of the trappable $|+\rangle$ state, $E_+ = \frac{\hbar}{2}\sqrt{\delta^2 + \Omega^2}$ given in equation 3.6. The dashed and dotted lines plot the limits of large and small detunings given in equations 3.7 and 3.8, respectively.

3.1.2 AC Zeeman Force vs. DC Zeeman Force

The on-resonance AC Zeeman effect is very similar in strength to the DC Zeeman effect. To demonstrate this we will consider the relative forces, in one-dimension, of a thin-wire with current I_{DC} acting on atoms that are a distance r away. Ampère's law gives a magnetic field with magnitude $|B_{DC}| = \frac{\mu_0 I_{DC}}{2\pi r}$ and gra-

dient $|\frac{dB_{DC}}{dr}| = \frac{\mu_0 I_{DC}}{2\pi r^2}$ Using equation 2.36 we can get the force from the DC Zeeman effect as:

$$F_{DCZ} = -\frac{d}{dr}U_{DCZ} = m_f g_F \mu_B \frac{dB_{DC}}{dr} = m_f g_F \mu_B \frac{\mu_0 I_{DC}}{2\pi r^2} \tag{3.9}$$

For the near-field of a thin-wire, the AC magnetic field has the same magnitude as the DC magnetic field, so that $|B_{AC}| = \frac{\mu_0 I_{AC}}{2\pi r}$ and $|\frac{dB_{AC}}{dr}| = \frac{\mu_0 I_{AC}}{2\pi r^2}$ We can also find a similar equation for the AC Zeeman force using the spatial gradient in the AC magnetic field and equation 3.6. The detuning is generally constant in space.

$$F_{ACZ\pm} = -\frac{d}{dr}E_{\pm} = \mp\frac{\hbar}{2}\frac{\Omega}{\Omega'}\frac{d\Omega}{dr} \tag{3.10}$$

We consider the on-resonance case where the force is the largest and the easiest to calculate. We will assume that the radiated field is polarized perpendicular to the quantization DC magnetic field such that we lose 1/2 of the amplitude of the driving field and $B_- = B_{AC}/2$. We will also assume that we are driving the transition $|2,2\rangle \leftrightarrow |1,1\rangle$ in ^{87}Rb so that the Rabi frequency is $\Omega = \frac{\mu_B B_- \sqrt{3}}{2\hbar}$. Plugging these values into equation 3.10 we get the following.

$$F_{ACZ\pm} = \pm\frac{\mu_B\sqrt{3}}{4}\frac{dB_-}{dr} = \pm\frac{\mu_B\sqrt{3}}{4}\frac{\mu_0 I_{AC}}{2\pi r^2} \tag{3.11}$$

For this case we will assume experimental parameters of $I_{DC} = 37$ mA and $I_{AC}(RMS) = I_{AC}(amplitude)/\sqrt{2} = 37$ mA at a distance of $r = 100$ μm from the wire to the atom location. This assumption means that equal power is dissipated in the two cases, assuming equal impedance. Plugging these values into equations 3.9 and 3.11 we get $F_{DCZ} = 4.82\ mg$ and $F_{ACZ} = 2.95\ mg$ where m is the mass of an ^{87}Rb atom and g is the acceleration due to gravity.

3.1.3 ACZ Eigenstates $|\pm\rangle$

The interaction between the RF field and atomic states 'dresses' these atomic states so that the eigenstates of the system, $|\pm\rangle$, are no longer equal to those of the bare atom plus photon field states $|g, N\rangle$ and $|e, N-1\rangle$. The new eigenstates of the system are given by equation 3.12 where $\sin(2\theta) \equiv \Omega/\Omega'$ and $\cos(2\theta) \equiv -\delta/\Omega'$ [26].

$$|+\rangle = \sin(\theta)|g, N\rangle + \cos(\theta)|e, N-1\rangle \tag{3.12}$$

$$|-\rangle = \cos(\theta)|g, N\rangle - \sin(\theta)|e, N-1\rangle \tag{3.13}$$

This relation can be simplified to find the relative populations in the $|g, N\rangle$ and $|e, N-1\rangle$ states for a given $|\pm\rangle$ state.

$$|\langle e, N-1|\pm\rangle|^2 = \frac{1}{2}(1 \mp \frac{\delta}{\Omega'}) \tag{3.14}$$

$$|\langle g, N|\pm\rangle|^2 = \frac{1}{2}(1 \pm \frac{\delta}{\Omega'}) \tag{3.15}$$

The relative population of these states is determined by the sign of the detuning, δ, as well as the size of the detuning relative to the Rabi frequency Ω. On-resonance, $\delta = 0$, the $|\pm\rangle$ states are equal superpositions of the bare atomic states $|g, N\rangle$ and $|e, N-1\rangle$. Off resonance, $|\delta| \gg |\Omega|$, the $|\pm\rangle$ states are well defined by one or the other of the bare atomic states $|g, N\rangle$ and $|e, N-1\rangle$. Figure 3.5 shows this relation by plotting the relative population of $|\langle e, N-1||\pm\rangle|^2$ from equation 3.14 as a function of the detuning δ.

An important tool that we employ in the experiment in section 6.2 is a procedure called an Adiabatic Rapid Passage (ARP). An ARP starts by applying a microwave field far off resonance ($|\delta_0| \gg |\Omega|$) in a region where the bare atomic states are approximately the same as the dressed states. The detuning of the microwave field is then swept to the desired value to keep the atomic state in either the $|+\rangle$ or the

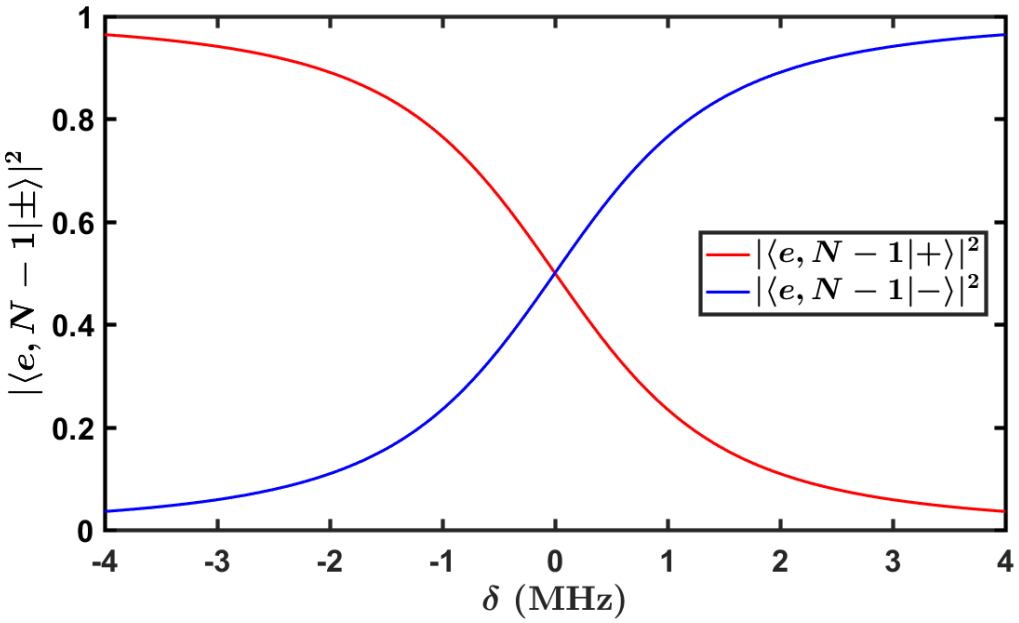

FIG. 3.5: Dressed Atom Eigenstate Relative Populations. Relative population of dressed atom eigenstates $|\langle e, N-1|\pm\rangle|^2$ vs. detuning δ. The red(blue) lines plot the relative population of the $|+\rangle(|-\rangle)$ eigenstates in the $|e, N-1\rangle$ state from equations 3.14 and 3.15.

$|-\rangle$ states. This frequency sweep is performed slowly (adiabatically) with respect to Rabi frequency Ω, but rapidly with respect to the decoherence of the system [47]. Hence the strange ability for the sweep to be both adiabatic and rapid.

This process can be visualized in figures 3.1 and 3.5. The detuning starts far to the left or right of the plot where the $|\pm\rangle$ states are well defined by only one of the bare atomic states $|g, N\rangle$ and $|e, N-1\rangle$. Slowly varying the detuning with respect to the Rabi frequency constrains the atomic states along either the red or blue $|\pm\rangle$ curves. Sweeping the detuning too quickly can cause the states to 'hop' from one dressed state to the other. With an ARP procedure, either bare atomic state, $|g, N\rangle$ or $|e, N-1\rangle$, can be made into the untrappable high-field seeking $|-\rangle$ state or the trappable low-field seeking $|+\rangle$ state by selection of the sign of the initial detuning δ_0 and then stopping the sweep at the desired final detuning δ.

3.2 Rabi Frequency

The Rabi frequency plays an important role in the ACZ effect by determining the energy shift and force, and how fast ARP sweeps can be applied. This section focuses on determining how to calculate the Rabi frequency and matrix elements for a given M1 hyperfine transition. We will assume a transition between the hyperfine manifolds $F = 2 \leftrightarrow F = 1$ because it describes the ground electronic state of ^{87}Rb, used in these experiments, as well as ^{39}K and ^{41}K that are available with our apparatus. This procedure should work for any other M1 hyperfine transition, though the exact numbers should change. The Rabi frequency for a RF or microwave field applied to a two-level atom is repeated from earlier in the chapter.

$$\Omega = \frac{1}{\hbar} \langle e| - \vec{\mu} \cdot \vec{B}_{AC}|g\rangle = -\frac{\mu_B}{\hbar^2} \langle e| 2\vec{S} \cdot \vec{B}_{AC}|g\rangle \tag{3.16}$$

We can substitute in $\vec{\mu} = (2\mu_B/\hbar)\vec{S}$, neglecting the nuclear spin (a 0.1% effect). Expanding the dot product of $\vec{S} \cdot \vec{B}_{AC}$ gives $\vec{S} \cdot \vec{B}_{AC} = S_x B_x + S_y B_y + S_z B_z$. We will assume that the DC magnetic quantization axis is along $\hat{z}$ and spatially uniform. We can then change to the basis of the ladder operators, $S_\pm = S_x \pm iS_y$ and $B_\pm = B_x \pm iB_y$, that represent the $\sigma^\pm$ transitions for circularly polarized AC magnetic fields. Substituting in the definitions for $S_\pm$ and $B_\pm$ we arrive at $S_x B_x + S_y B_y = \frac{1}{2}(S_+ B_- + S_- B_+)$. B_z stays the same and represents the π-polarized AC magnetic field oriented along the same direction as the quantization DC magnetic field. We can plug these into equation 3.16 to get the following.

$$\Omega = -\frac{\mu_B}{\hbar^2} \langle e| B_- S_+ + B_+ S_- + 2B_z S_z|g\rangle \tag{3.17}$$

It is useful here to make an assumption that the energy separation between the hyperfine manifolds is much greater than the energy separation within the manifolds

for the different m_F states. In our experiment the level splitting between the $F = 2$ and $F^{'} = 1$ hyperfine levels of ^{87}Rb is 6834.7 MHz. The largest quantization magnetic field used in this experiment is $B_{DC} = 52$ G. This gives a DC Zeeman separation between neighboring m_F levels of 36 MHz. The matrix elements on the right-hand side of equation 3.17 can then be calculated by finding the Clebsch-Gordan coefficients for the transitions [55] and are listed in equations 3.18 and 3.19.

$$\langle F, m_f | S_{\pm} | F^{'}, m_F^{'} \rangle = \pm\hbar \frac{\sqrt{(F \pm m_F)(F \pm m_F^{'})}}{2I+1} \delta_{m_F, m_F^{'} \pm 1} \tag{3.18}$$

$$2\langle F, m_f | S_z | F^{'}, m_F^{'} \rangle = \pm 2\hbar \frac{\sqrt{(F + m_F)(F - m_F^{'})}}{2I+1} \delta_{m_F, m_F^{'}} \tag{3.19}$$

It is assumed in equations 3.18 and 3.19 that $F > F^{'}$. With the assumption that $F = 2$ and $F^{'} = 1$ then we can calculate the matrix elements from 3.18 and 3.19, shown in table 3.1. The strongest transitions are the π transitions that have $\Delta m_F = 0$. It is interesting that of these, the strongest is for the 'clock' state $|F = 2, m_F = 0\rangle \leftrightarrow |F^{'} = 1, m_F^{'} = 0\rangle$ that is insensitive to first order DC Zeeman shifts. The next strongest transitions are for the 'stretched states' $|F = 2, m_F = +2\rangle \leftrightarrow |F^{'} = 1, m_F^{'} = +1\rangle$ and $|F = 2, m_F = -2\rangle \leftrightarrow |F^{'} = 1, m_F^{'} = -1\rangle$. The experiment described in chapter 6 primarily uses the $|F = 2, m_F = +2 \leftrightarrow |F^{'} = 1, m_F^{'} = +1\rangle$ σ^+ transition.

3.2.1 Rabi Flopping

Applying a RF or microwave field to an atom causes it to undergo Rabi oscillations where the state of the atoms oscillates with time as measured in the bare atomic state $|e, N-1\rangle$ and $|g, N\rangle$ basis [47, 56]. This is a byproduct of transforming the eigenstates of the system into the $|\pm\rangle$ basis, as described earlier in this section. As an example, we will start with atoms initialized in the $|g\rangle$ state, apply a field with

F	m_F	$F^{'}$	$m_F^{'}$	S_+ $(\hbar/4)$	S_- $(\hbar/4)$	$2S_z$ $(\hbar/4)$
2	2	1	+1	$\sqrt{12}$	0	0
2	+1	1	+1	0	0	$\sqrt{12}$
2	+1	1	0	$\sqrt{6}$	0	0
2	0	1	+1	0	$\sqrt{2}$	0
2	0	1	0	0	0	$\sqrt{16}$
2	-1	1	0	0	$\sqrt{2}$	0
2	0	1	-1	$\sqrt{6}$	0	0
2	-1	1	-1	0	0	$\sqrt{12}$
2	-2	1	-1	0	$\sqrt{12}$	0

TABLE 3.1: Matrix elements for the $|F, m_f\rangle \leftrightarrow |F^{'}, m_F^{'}\rangle$ transitions on the right-hand side of equations 3.18 and 3.19. There is a factor of $(\hbar/4)$ that must be applied to each that comes from the $\hbar/(2I+1)$ term. The values listed here are for a nuclear spin $I = \frac{3}{2}$ found in ^{87}Rb, ^{39}K, and ^{41}K. Here we assume that the $F = 2$ hyperfine level is the $|e\rangle$ state and the $F^{'} = 1$ hyperfine level is the ground state $|g\rangle$. Note that the factor of 2 on the S_z transitions is 'baked in' to the number under the square root on the right-most column.

detuning δ from the atomic resonance, and measure the population in the excited state as a function of time. If we take equation 2.9 and take $|c_e|^2 = |\langle \pm|e, N-1\rangle|^2$, then we can get the population in the $|e\rangle$ state as a function of time [47].

$$|c_e|^2 = |-i\frac{\Omega}{\Omega^{'}}\sin(\frac{\Omega^{'}t}{2})e^{-i\delta t/2}|^2 = \frac{1}{2}|\frac{\Omega}{\Omega^{'}}|^2(1-\cos(\Omega^{'}t)) \tag{3.20}$$

Figure 3.6 shows how the population in the excited state, $|c_e|^2$, changes with time. As the detuning is increased, the amplitude of the oscillations, $\frac{1}{2}|\frac{\Omega}{\Omega^{'}}|^2$, decreases while the frequency, $\Omega^{'} = \sqrt{\delta^2 + \Omega^2}$, increases. When we measure the ACZ force in chapter 6 we experimentally measure the Rabi frequency in subsection 6.2.3 as a means to double-check the measured ACZ force against predictions. This Rabi frequency was measured by applying an on-resonance microwave field and measuring the excited state population $|c_e|^2$ as a function of time. The Rabi frequency can be found by fitting the measured $|c_e|^2$ data to a sinusoidal function.

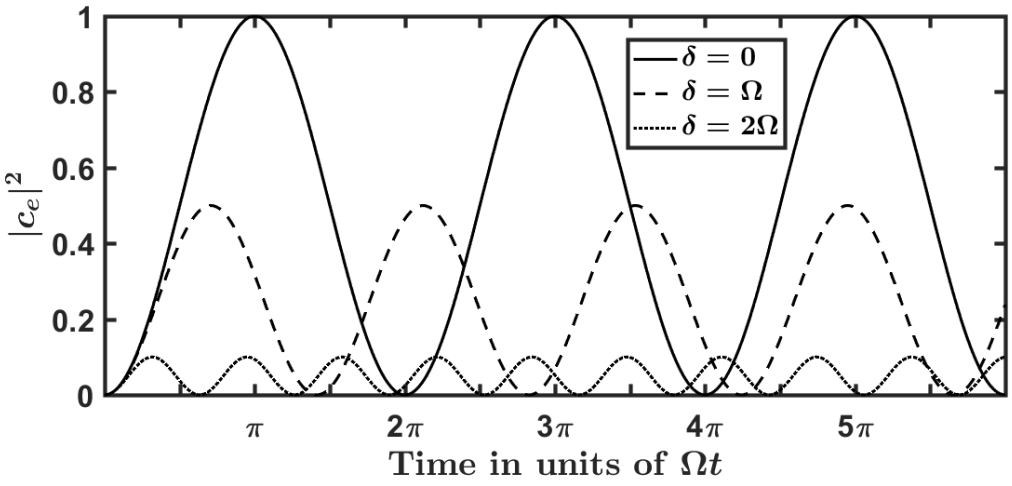

FIG. 3.6: Rabi flopping at varying detunings. The excited state population from 3.20 is plotted as a function of time in units of Ωt. As the detuning is increased, the amplitude of the oscillations, $\frac{1}{2}|\frac{\Omega}{\Omega'}|^2$, decreases while the frequency $\Omega' = \sqrt{\delta^2 + \Omega^2}$ increases.

3.3 2-Level Atom Driven by Two Microwave Fields

If an ACZ potential is used to trap ultracold atoms, then an important question is whether one can perform forced evaporation through spin-flipping from the trappable $|+\rangle$ state to the to the anti-trapped $|-\rangle$ state, similar to a DC magnetic trap. The Hamiltonian for this system is similar to the one studied for laser cooling with two laser fields of different frequencies, often referred to as the 'bichromatic force' [57, 58, 59]. The analytical treatments of the bichromatic force may be of use to future students, however we take a different approach here. To start, we chose to do simple numerical simulations of adding a weak second field to a 2-level atom dressed with a strong microwave field. These simulations were done with a stronger 'trap' field with Rabi frequency Ω_1 and detuning δ_1 and a weaker 'evap' field which had Rabi frequency Ω_2 and detuning δ_2. The results of this effort are contained in this section and show the expected ability to spin-flip the ACZ eigenstates ($|\pm\rangle$) with the introduction of a weak second field. These results also show that changing the strength of the 'trap' field shifts the center and width of the resonance of these spin-flips.

We will start the derivation from the time-dependent Schrödinger equation $\mathcal{H}_{2field}|\Psi\rangle = i\hbar\frac{d}{dt}|\Psi\rangle$ where $\mathcal{H}_{2field}$ is the Hamiltonian for the two-field system. We will assume a state

$$|\Psi\rangle = c_g e^{-i\omega_g t}|g\rangle + c_e e^{-i\omega_e t}|e\rangle \tag{3.21}$$

Applying the time-dependent Schrödinger equation gives the coupled equations below [47]:

$$i\hbar\frac{dc_g(t)}{dt} = c_e(t)\,\langle g|\,\mathcal{H}_{2field}\,|e\rangle\,e^{-i\omega_{eg}t} \tag{3.22a}$$

$$i\hbar\frac{dc_e(t)}{dt} = c_g(t)\,\langle e|\,\mathcal{H}_{2field}\,|g\rangle\,e^{i\omega_{eg}t} \tag{3.22b}$$

Now we diverge from the single field case. The two-field interaction term is given below where $\omega_{1,2}$ are the frequencies of the applied fields.

$$\langle e|\,\mathcal{H}_{2field}\,|g\rangle = \hbar\Omega_1\cos(w_1 t) + \hbar\Omega_2\cos(w_2 t) \tag{3.23}$$

The next step is to take the time derivative of both sides in equation 3.23 to get a second-order differential equation. We can also apply the *rotating wave approximation* to discard terms with $e^{-i(\omega_1+\omega_2)t}$ which oscillate too quickly compared to terms with $e^{-i(\omega_1-\omega_2)t}$. This gives the coupled second order differential equations below.

$$\frac{d^2c_g}{dt^2} - i\left(\frac{\Omega_1\delta_1 e^{i\delta_1 t} + \Omega_2\delta_2 e^{i\delta_2 t}}{\Omega_1 e^{i\delta_1 t} + \Omega_2 e^{i\delta_2 t}}\right)\frac{dc_g}{dt} + \frac{1}{4}(\Omega_1^2 + \Omega_2^2 + 2\Omega_1\Omega_2\cos((\delta_1-\delta_2)t))c_g = 0 \tag{3.24}$$

$$\frac{d^2c_e}{dt^2} + i\left(\frac{\Omega_1\delta_1 e^{-i\delta_1 t} + \Omega_2\delta_2 e^{-i\delta_2 t}}{\Omega_1 e^{-i\delta_1 t} + \Omega_2 e^{-i\delta_2 t}}\right)\frac{dc_e}{dt} + \frac{1}{4}(\Omega_1^2 + \Omega_2^2 + 2\Omega_1\Omega_2\cos((\delta_1-\delta_2)t))c_e = 0 \tag{3.25}$$

The second order coupled differential equations 3.24 and 3.25 can be fed into a numerical solver (ode45 function in MATLAB®) to get a sense for the time dependence of the wave function. Figure 3.7 shows the results of using a numerical

solver for these equations with a state that starts in $|g\rangle$ with $c_g^2(t=0)=1$. The

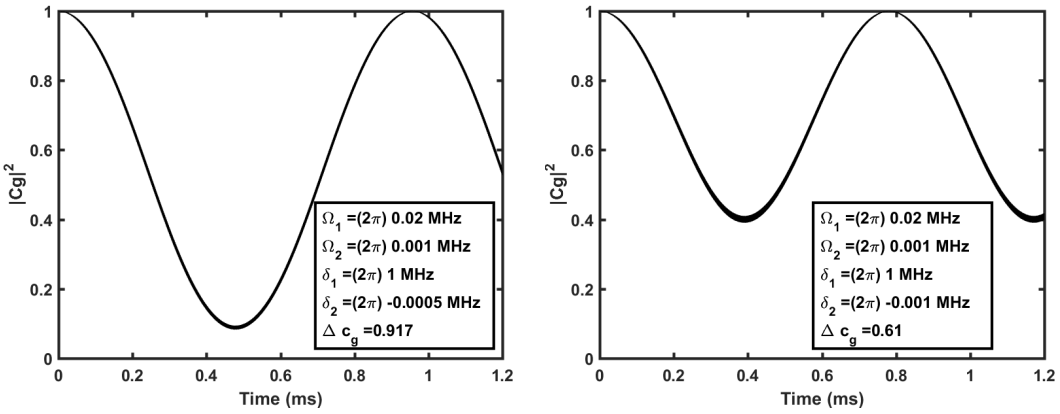

FIG. 3.7: 2-level Dressed Atom $|c_G|^2$ vs. Time. (left) Shows Rabi oscillations for $\delta_2 = -\frac{1}{2}\Omega_2$ and (right) shows Rabi oscillations for $\delta_2 = -\Omega_2$. The peak-to-peak amplitude of the oscillations decreases from $|\Delta c_g|^2$ from 0.917 to 0.61.

system undergoes fast and slow Rabi oscillations with frequencies $\Omega_1' = \sqrt{\Omega_1^2 + \delta_1^2}$ and $\Omega_2' = \sqrt{\Omega_2^2 + \delta_2^2}$, respectively. The fast oscillations show up as the thickness of the lines in Figure 3.7 while the slow oscillations are clearly visible. Figure 3.7(a) shows these oscillations for a $\delta_2 = -\frac{1}{2}\Omega_2$ while figure 3.7(b) has $\delta_2 = -\Omega_2$. The large (visible) Rabi oscillations get faster, with a smaller amplitude, as the magnitude of δ_2 is increased.

If we define a quantity $\Delta c_g^2 = (\max(c_g) - \min(c_g))$ we can get a sense for how the system behaves to a change in the 'evap' field detuning δ_2. Figure 3.8(a) shows a plot of Δc_g^2 as a function of δ_2. There is clearly a peak at $\delta_2 \approx 0$ MHz. If the Rabi frequency of the 'trap' field Ω_1 is increased, then the location of this peak shifts, as seen in Figure 3.8(b). This resonance shift is what we expect as the 'trap' field shifts the energy of the system in the single field case by: $E_\pm = \pm\frac{\hbar}{2}(-|\delta_1| + \sqrt{\Omega_1^2 + \delta_1^2})$, first derived in equation 3.6.

If we continue to make plots similar to those in figure 3.8 at varying values of the strength of the 'trap' field, Ω_1, then we can measure how the resonance peak location and width change. Figure 3.9(a) shows how the peak center location changes with

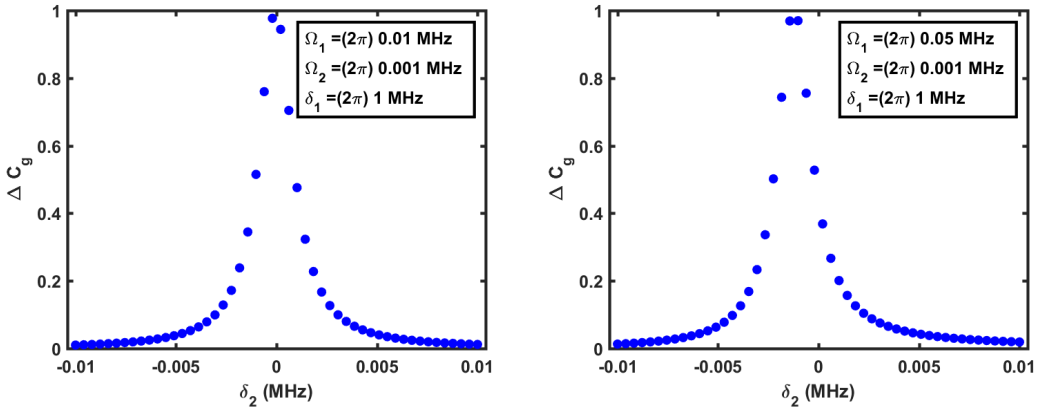

FIG. 3.8: 2-level Two Photon Resonance Peak vs. δ_2. (left) Shows a plot of $|\Delta c_g|^2$ as a function of δ_2 for a 'strong field' Rabi frequency of $\Omega_1 = (2\pi)0.001$ MHz. (right) Shows the same for a 'strong field' Rabi frequency of $\Omega_1 = (2\pi)0.005$ MHz.

Ω_1. The center of each was measured by hand to get the diamonds shown. The 'theory' for the shift of the resonance center for a single field case is plotted as the solid black line as $\Delta_{center} = |\delta_1| - \sqrt{\Omega_1^2 + \delta_1^2}$. These two agree well and suggest that taking the contributions of the two fields separately may be a valid approximation for future work. Figure 3.9(b) shows how the resonance width changes with Ω_1. The

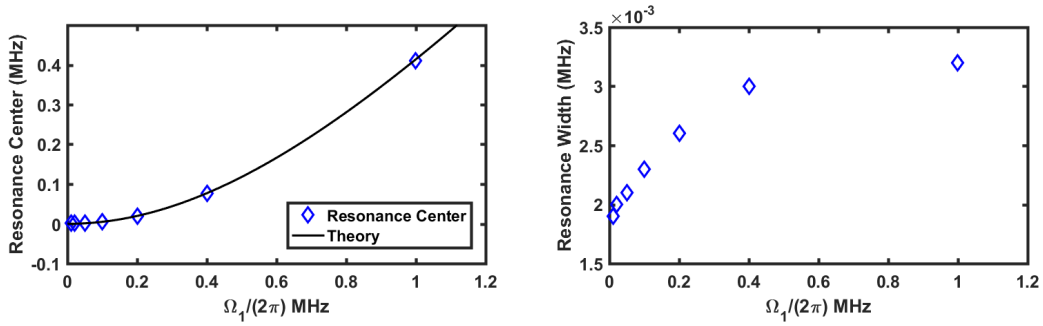

FIG. 3.9: 2-level Two Photon Resonance Peak vs. Ω_1. (left) Shows a plot of the shift in the center of the resonance in figure 3.8 as a function of the 'strong field' Rabi frequency of Ω_1 as measured by hand in blue diamonds. The black line shows the expected energy shift (divided by $\hbar$) created by a single field: $\Delta_{center} = |\delta_1| - \sqrt{\Omega_1^2 + \delta_1^2}$. (left) Shows a plot of the width of the resonance in figure 3.8 as a function of the 'strong field' Rabi frequency of Ω_1.

width here is defined as the full width at half maximum. The resonance peak for large $\Omega_1 = (2\pi)1$ MHz was distorted and asymmetric.

These initial efforts at modeling a two-level atom subject to two separate mi-

crowave fields demonstrate a couple of important things. First, there were not any surprises in the data like a separate resonance peak for different values of δ_2 in figure 3.8. Second, we were able to change the resonance peak location by varying the strength of the 'trap' field Ω_1 in figure 3.9. This gives us some confidence that studying the effects of the two fields separately as a 'trap' and as an 'evap' may be a valid assumption, similar to a DC magnetic trap plus an RF 'evap' field.

3.4 Trapping using the AC Zeeman effect

One of the long-term goals of the ACZ project is to create a trap for atoms using only the ACZ effect. There are several unique advantages to creating a trap using the ACZ effect. First, these traps are compatible with an arbitrary DC magnetic field, limited only by the frequency range of the microwave source: this allows for tuning of atom-atom interactions via a DC magnetic Feshbach resonance [60]. Second, these traps are compatible with forced evaporation with the addition of a second microwave field, discussed in section 3.3, which allows for efficient evaporative cooling. Third, the M1 hyperfine transitions on which ACZ traps would operate do not suffer from spontaneous emission. Finally, the trap would be inherently spin-dependent, which would add a unique experimental tool that is currently missing from the cold atom toolbox.

The shape of these traps is dependent on the shape of the AC magnetic near-field, which is dictated by the physical geometry and phase of the current-carrying wires. These wires are typically on the order of 100 μm center-to-center (as in our apparatus [61]), but can be made to be 10 μm or less [62]. It is advantageous to create a trap in a location where the AC magnetic field gradient is as large as possible so that the trap constrains the atoms with a large trapping frequency. The ideal scenario is to trap very close to wires that are very closely spaced together

(neglecting engineering challenges associated with capacitive or inductive coupling between neighboring wires). The quality of the ACZ trapping potential is dependent on the quality of the wire trace; the smoother the wire traces the less distortion in the AC magnetic field and the closer the atoms can be, vice-versa for wires with internal defects and rough surfaces. In order to trap atoms against gravity, we must create an AC magnetic field minimum and trap the low-field seeking $|+\rangle$ state with energy $E_+ = \frac{\hbar}{2}(-|\delta| + \sqrt{\delta^2 + \Omega^2})$. For the remainder of this section, we will employ $|e\rangle$=$|F = 2, m_F = +2\rangle$ and $|g\rangle$=$|F = 1, m_F = +1\rangle$. The Rabi frequency from equation 3.17 is then proportional to the strength of the B_- AC magnetic field that drives the σ^+ transitions, $\Omega \propto B_- = B_x - iB_y$. The potential energy, and thus the force, from the ACZ effect depends on $|\Omega|^2$.

Our first simulation is shown in Figure 3.10 for a simple 2-wire configuration that we can use with our current apparatus. Here we have used the thin-wire approximation given below where $r = \sqrt{x^2 + y^2}$ and assume a current $+I_{AC}$ along $+\hat{z}$, directed out of the page in figure 3.10.

$$\vec{B}_{AC} = \frac{\mu_0 I}{2\pi r}(-\frac{y}{r}\hat{x} + \frac{x}{r}\hat{y}) \tag{3.26}$$

The two wires in figure 3.10 drive RMS currents of $I = 40$ mA (the largest that we are currently capable of) that are exactly in phase. This creates a trapping potential directly in between the wires. This is the problem with this configuration; the trap is centered on a location where there is a currently a wire. Trapping with this method would require milling out the central section of our chip. This approach is conceivable, but inconvenient, and also limits the optical access to the trapped atoms.

Figure 3.11 shows a feasible trapping potential located above the chip, in free space, created by adding a third current-carrying wire. This third wire in the middle

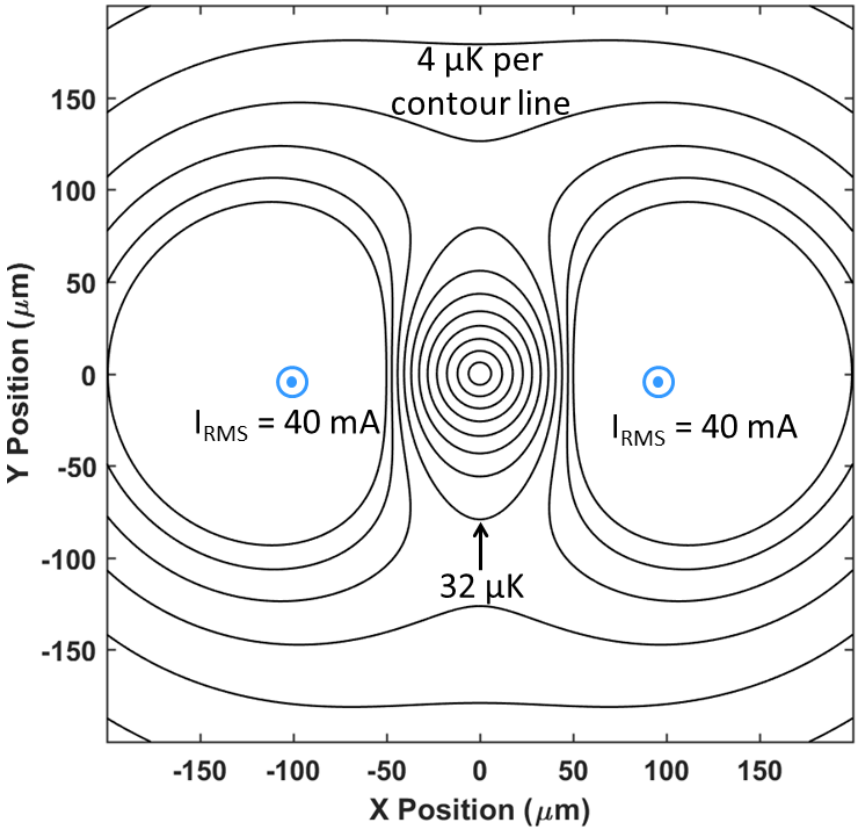

FIG. 3.10: 2-Wire ACZ Trapping Potential. The trapping wires are spaced 200 μm apart, the same as the two U-wires on either side of the central Z-wire in our current chip. The wires drive currents of $I_{AC}(RMS) = 40$ mA that are exactly in phase and create a trap with depth of $U_{ACZ}/k_B \approx 32\mu$K.

drives current exactly out of phase with the other two to 'push' the center of the trap in the $+\hat{y}$ direction. This creates a trap that is centered at $x = 0, y = 72$ μm. This trap was calculated for a larger current of $I = 100$ mA so that the trap depths would be comparable. This larger current is necessary because the trap is located farther from the current-carrying wires where the AC magnetic field, and its gradient, are weaker. Figure 3.11(b-c) show the ACZ potential along slices in the $\hat{x}$ and $\hat{y}$ directions, respectively. These slices are centered on the trap center $x = 0, y = 100$ μm. Both of these simulations use an on-resonance ACZ effect with $\delta = 0$ to maximize the trapping potential. They can be run with a larger detuning to limit the state mixing at the cost of running larger currents, or having a lower trap depth.

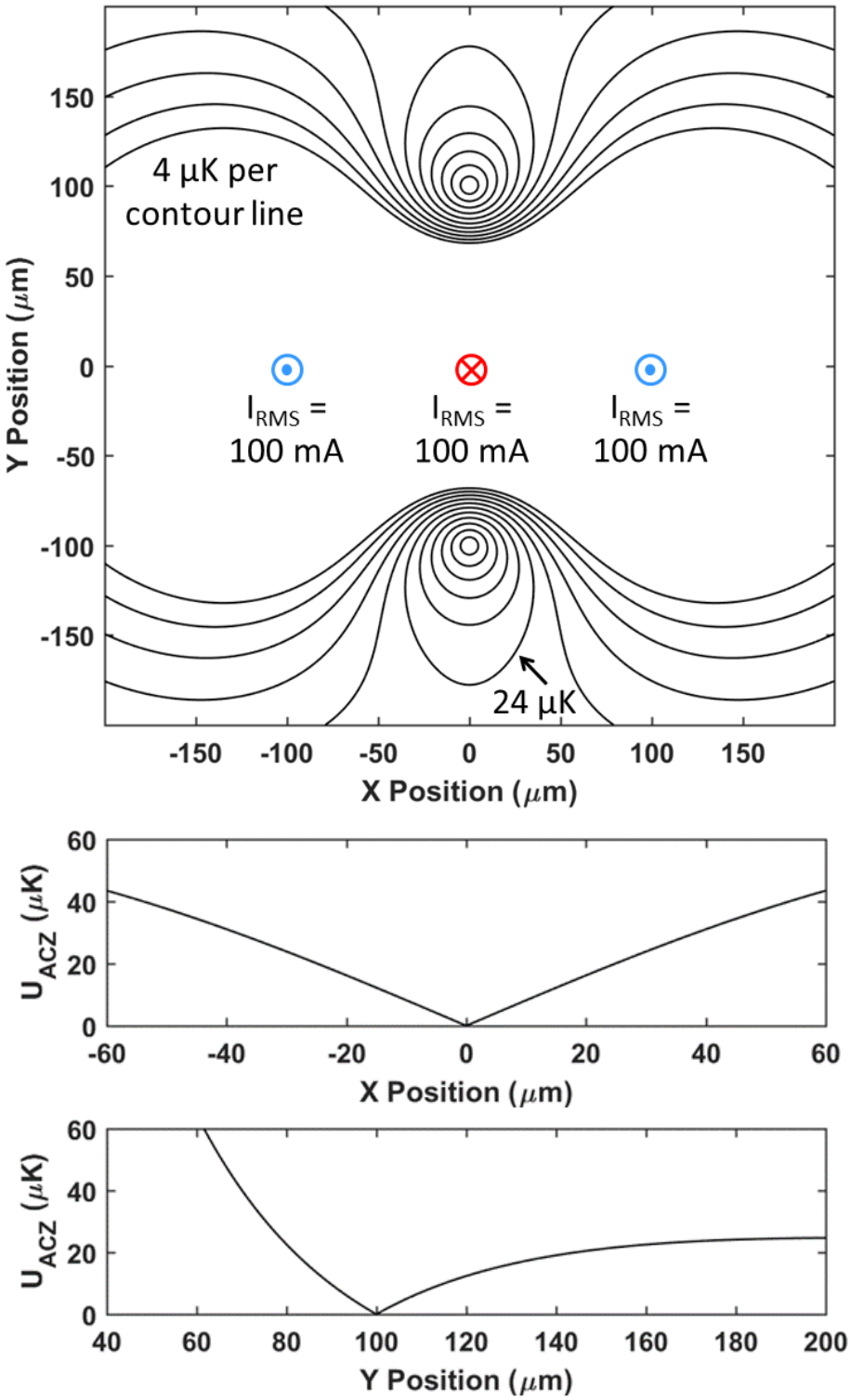

FIG. 3.11: 3-Wire ACZ Trapping Potential. (left) This scheme uses the two U-wires driving currents in phase with each other and exactly out of phase with the current in the central Z-wire. The wires drive currents of $I_{AC}(RMS) = 100$ mA and create a trap with depth of $U/k_B \approx 24\mu$K. (right) The two plots on the right show slices of the potential taken at the center of the trap: $x = 0, y = 100$ μm.

Creating an atom trap using only the ACZ effect is possible with the atom chip that is currently installed in our apparatus. In order to make this trap we would have to install new microwave hardware to drive the three wires with larger currents and with the correct phases. This is a problem with a well established solution that requires adding a more powerful microwave amplifier and some electronics to measure, and correct, the relative phases of the three currents. In addition to creating a trap with the atom chip currently installed in the apparatus, it is possible to create new atom chips with different wire sizes and shapes, and possible better impedance matching. Atom chip manufacturing is described in more detail in chapter 8.

CHAPTER 4

Apparatus

Ultracold atom apparatuses are typically complex, take a long time to build, and pass through multiple students during their lifetime. Our apparatus is no different; it has been under construction in some way or other since 2007 and I am the third graduate student to perform experiments with this apparatus. Details of the construction of the apparatus can be found in our apparatus paper [61] and in the theses of M. K. Ivory [63] and A. R. Ziltz [64] available on the cold atom group website [65]. In this chapter I will describe my contributions to the apparatus and measurements that I have made of its performance. I will also include methods that I have found useful to improve its day-to-day performance in an effort to pass my institutional knowledge on to future students.

This chapter is laid out as follows: Section 4.1 describes how to optimize the MOT, optical molasses, and optical pumping. Section 4.2 describes issues that may arise with the magnetic trap and the magnetic transport to the chip. Section 4.3 describes the Rb tapered amplifier and the rebuild that we performed on it. Section 4.4 describes day-to-day operation and maintenance of the lasers used in Rb experiments. Section 4.5 describes the method by which we resurrected the BEC

and increased the atom number to as high as $N_{BEC} = 4 \times 10^4$. Finally, Section 4.6 describes the lab-built microwave system used in the ACZ experiments.

4.0.1 Overall Apparatus Operation

This section contains a brief overview of the cold atom apparatus described in this chapter to help give context when describing different parts in detail. The Dual-Chamber apparatus is shown in Figure 4.1. The experimental procedure to make a

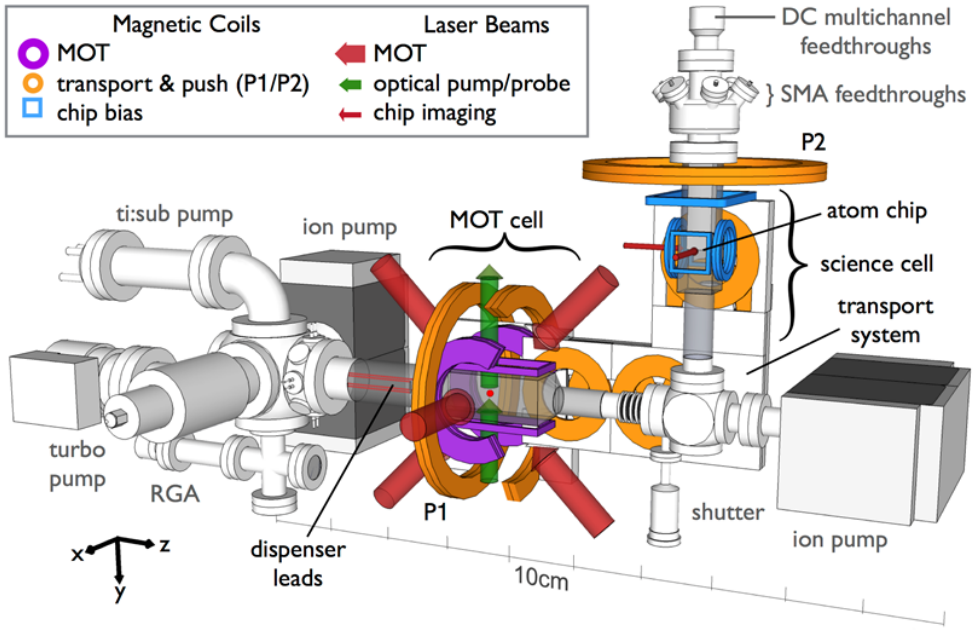

FIG. 4.1: Diagram of the main parts of the dual-chamber ultracold atom apparatus. Image credit: A. Ziltz [61]. The MOT is the red sphere in the center of the MOT cell. The magnetic trapping and transport system that moves the atoms from the MOT cell to the science cell is shown in orange. The coils on the near side of the vacuum cell are not shown. The atom chip is mounted upside down on the gray chipstack. The red laser beams near the atom chip are used for imaging.

Bose-Einstein Condensate (BEC) starts by collecting atoms from background vapor in the MOT cell for 10-25 seconds. Then, the MOT quadrupole coils are quickly turned off and an optical molasses (OM) pulse is applied to cool the atoms. This is followed by a quick turn on of the vertical bias coils and an optical pumping (OP)

Stage	Atom Number	T (μK)	Note
MOT	$5-6\times10^8$	100	Hard to estimate exact N
Optical Molasses	$5-6\times10^8$	16	Long tof
MOT cell B-Trap	3×10^8	60	9 ms tof
Chip Load	2.5×10^6	90	Comp. then Decomp.
BEC	2.5×10^4	0.4	Typical BEC

TABLE 4.1: Typical apparatus performance benchmarks. This list is meant to be self-consistent and a means of trouble-shooting the apparatus. The MOT and optical molasses atom numbers should be taken as estimates as they are challenging to measure independently. The MOT cell B-Trap numbers correspond to approximately 2500 ADC counts in the middle of 'Btrapopt' ADwin sequencer panel with 8×10^7 total ADC counts and a temperature of about 85 μK with 9 ms time of flight (tof) between turning the trap off and imaging.

pulse to spin-polarize the cloud into the $|F=2,m_F=2\rangle$ 'stretched' state. The MOT quadrupole coils are then quickly turned on to create a magnetic trap, often referred to as a B-trap, for the atoms. This magnetic trap is then moved to the right in Figure 4.1 to the corner, then up to the atom chip. A. R. Ziltz designed and built the interleaved magnetic transport system used on our experiment [64]. The atoms are loaded onto a DC micro-magnetic trap created by the atom chip, and forced RF evaporation is applied to evaporate to BEC. Table 4.0.1 provides a guide for typical atom numbers and temperatures for each stage of the procedure from the MOT to the BEC.

4.0.2 ADwin Sequencer

The experiments described in this thesis require simultaneous and precise control of many analog and digital signals in order to function. These are different methods of performing this task including systems based on open source software [66, 67, 68]. Our system uses an ADwin sequencer to control the experiment through 32 analog channels with the ability to output -10V to +10V. In addition, there are 64 digital outputs that can drive either 0V or +3.3V. The sequencer is programmed

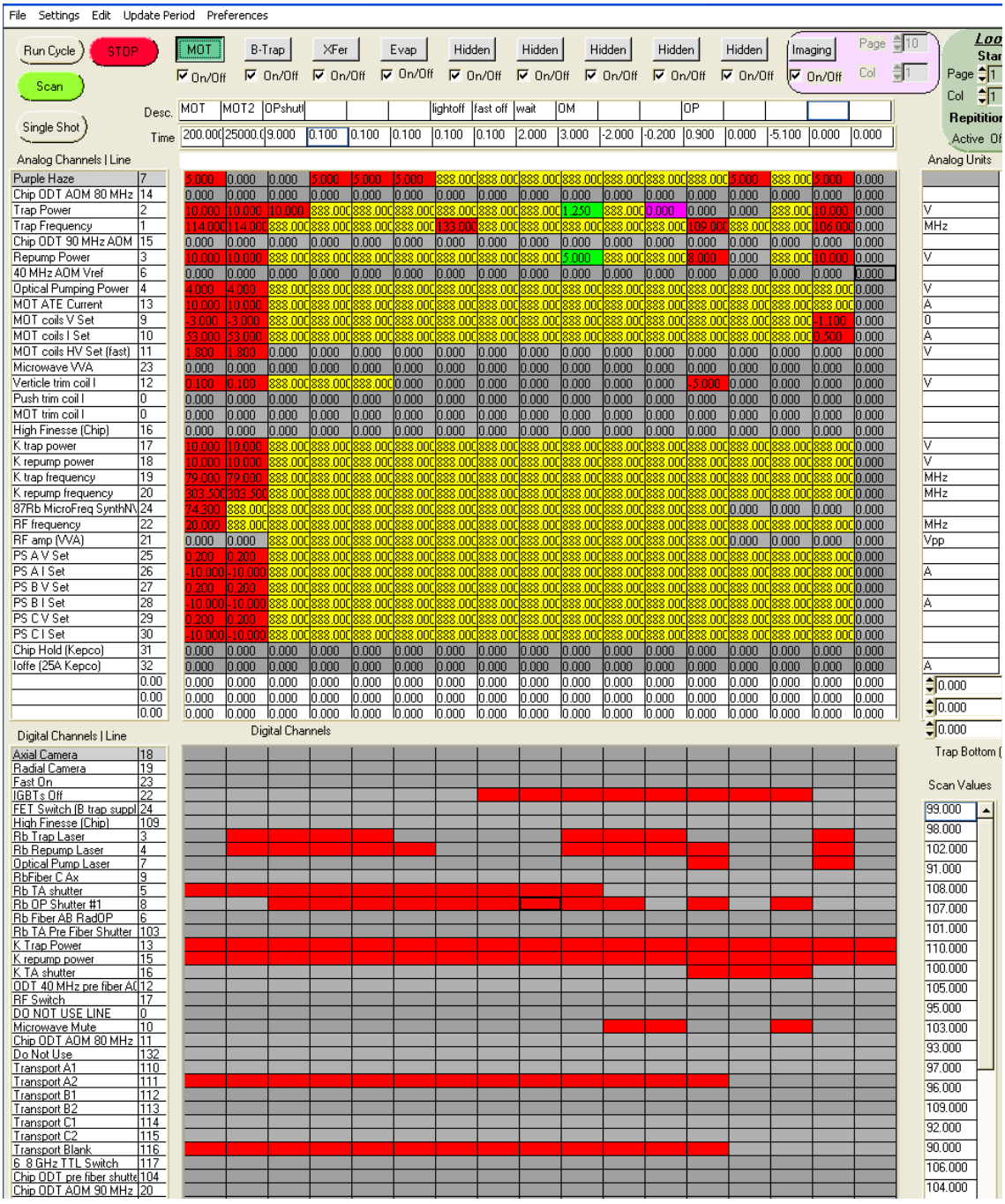

FIG. 4.2: Example of and ADwin sequencer panel. This specific panel starts the experiment and runs through to optical pumping for ^{87}Rb.

as shown in figure 4.2. There are 17 columns per page and up to 10 pages per experiment. The time of each column can be set (in ms) as well as the value of each

analog and digital output. The analog controlled channels are on top. If desired, a linear mapping can be made from the units entered into an output voltage. The MOT coils *Iset* is a good example of this. The user can input a desired current and the user interface converts it to an output voltage based on a previously entered conversion. The red squares represent a step to a requested analog output value, the yellow squares copy the previous set value, and the green squares perform a linear ramp from the previous value to the set value. The digital controls are set to 0V for a gray square and +3.3V for a red square. This specific panel starts the experiment and runs through to optical pumping for ^{87}Rb.

4.1 ^{87}Rb Magneto-Optical Trap Optimization

The overall performance of the system, generally measured in ^{87}Rb BEC atom number, is most frequently affected by the performance of the MOT, Optical Molasses, and to a lesser degree, optical pumping. If these are all working well then apparatus generally produces reliable, high atom number, and cold MOT cell magnetic trap clouds. This is crucial ingredient for good loading onto the chip, which is in turn the crucial ingredient for efficient cooling to a large atom number BEC. Figure 4.3 shows a representative false-color fluorescence image taken of an ^{87}Rb MOT.

4.1.1 Laser Configuration

In this thesis there are many references to the trap and repump lasers that are used to cool and image ^{87}Rb. Figure 4.4 defines what these two lasers are and the transitions that they drive. The trap laser drives the $\left|5S_{1/2}, F=2\right\rangle \rightarrow \left|5P_{3/2}F'=3\right\rangle$ cycling transition. Atoms in $\left|5P_{3/2}, F=3\right\rangle$ can only decay into $\left|5S_{1/2}, F=2\right\rangle$ due to selection rules. Occasionally, the trap light accidentally drives the $\left|5S_{1/2}, F=2\right\rangle \rightarrow \left|5P_{3/2}F'=2\right\rangle$

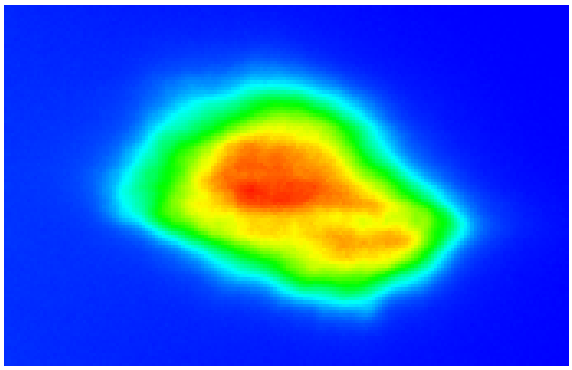

FIG. 4.3: False-color fluorescence image of an ^{87}Rb MOT. The red represents more photon counts corresponding to more atoms while the blue represents less of each.

transition. The $\left|5P_{3/2}, F=2\right\rangle$ state can decay into either $\left|5S_{1/2}, F=2\right\rangle$ or $\left|5S_{1/2}, F=1\right\rangle$. The atoms that fall into $\left|5S_{1/2}, F=2\right\rangle$ continue in the cycling transition. However, the atoms that fall into $\left|5S_{1/2}F=1\right\rangle$ are too far detuned from the trap laser to absorb any more photons and go 'dark' to the light. The repumper light drives the $\left|5S_{1/2}, F=1\right\rangle \rightarrow \left|5P_{3/2}, F^{'}=2\right\rangle$ transition. The atoms then decay from $\left|5P_{3/2}, F^{=}2\right\rangle$ into $\left|5S_{1/2}, F=2\right\rangle$ or $\left|5S_{1/2}F^{=}1\right\rangle$. This process continues until the atoms fall into $\left|5S_{1/2}F^{=}2\right\rangle$ and get back into the cycling transition driven by the trap light.

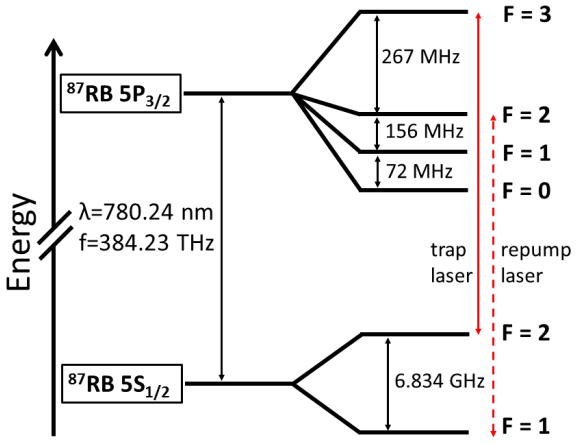

FIG. 4.4: Energy level and laser diagram for ^{87}Rb. The trap laser drives the $\left|5S_{1/2}, F=2\right\rangle \rightarrow \left|5P_{3/2}F^{'}=3\right\rangle$ cycling transition. The repumper light drives the $\left|5S_{1/2}, F=1\right\rangle \rightarrow \left|5P_{3/2}F^{'}=2\right\rangle$ transition to repump atoms back to the cycling transition. Figure adapted from [51].

4.1.2 Magneto-Optical Trap

The MOT in our apparatus is loaded from background gas. We use a light induced atom desorption (LIAD) system [69, 61] built in house by A.J. Pyle to dynamically vary the background pressure of the Rb and K atoms. This system works by directing up to 1.8 W of 405nm light onto the MOT cell glass by using high power LEDs. We use separate SAES dispenser to preferentially supply the MOT cell with Rb or K. This light desorps the Rb and K atoms that get stuck to the glass walls and allows for experimental control of the background pressure of up to three orders of magnitude. This light is left on during the MOT loading stage to enhance the MOT loading rate and turned off during the rest of the experimental cycle to limit losses from collisions with background atoms. Figure 4.5 shows the

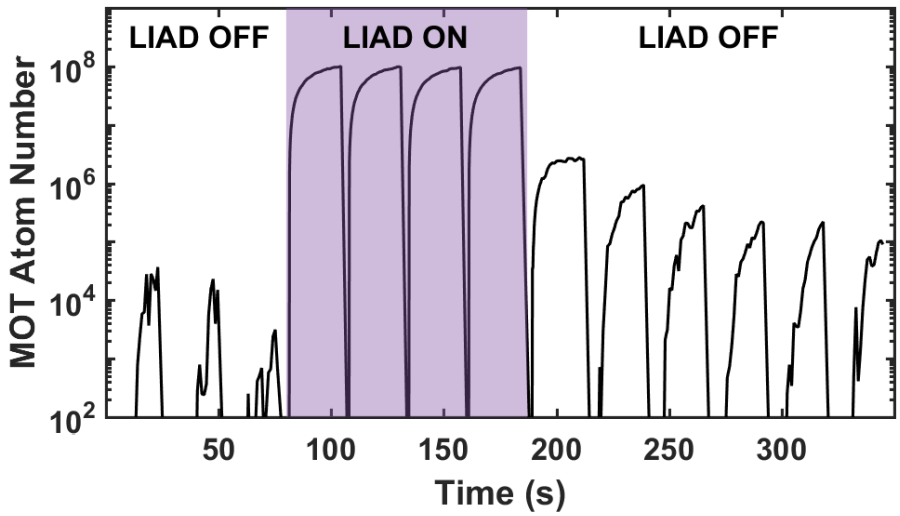

FIG. 4.5: LIAD effect on ^{87}Rb MOT atom number. Each MOT load was 25 sec. Fluorescence imaging was used to measure the intensity of the scattered light to get real-time imaging. This scattered light power was referenced to atom numbers measured previously with absorption images [61]. Data was taken on 17Jan2013 in Bk. 1 pg. 151.

effects of using this LIAD technique by plotting the MOT atom number as a function of time with the LIAD on and off. Fluorescence imaging was used to measure the amount of light scattered by running the MOT. This was compared to previously taken absorption images to get a real-time measurement of the MOT atom number.

However, it is difficult to get an accurate atom number measurement using this technique for large clouds, as discussed in section 2.6. The background Rb pressure in the MOT cell drops by almost two order of magnitude shortly after turning off the LIAD LEDs and decays another order of magnitude in about two minutes.

The performance of the MOT is generally dictated by three things: laser power balancing, overall laser power, and MOT beam alignment. Power balancing can be achieved by small rotations of the red-labeled wave plates for 780 nm light. This should be done before each experimental run. Overall laser power is generally dictated by the light power coming through the fiber that feeds the Rb tapered amplifier (TA). There should be 20-25 mW of light (trap + repump) coming through the fiber into the TA, which results in 370 mW of usable light out of the TA, as measured with a focusing lens just before the light gets split by the first polarizing beam-splitter (PBS) cube to the different MOT axes.

The MOT can benefit from a realignment once or twice per year, depending on how frequently mirrors get bumped and the quality of the laboratory temperature and humidity control. A complete realign starts by optimizing the alignment into the TA by playing off the spatial mode and the total output power to increase the usable power. The next step after the TA input alignment is to align individual MOT beam axes. This is accomplished by aligning the beams to the black 2" telescopes. It is assumed that these telescopes are properly aligned to overlap at the center of the magnetic trap and that they do not move.

It is useful to work with one axis at a time, by blocking the light to the other axes, and to iterate back and forth between the two directions in that axis. Repeat the steps for each axis independently. Start with the 'terrible axis' that is the hardest to get to and finish with the horizontal axis that is the easiest to get to. The TA current should be set to 1A. Take extreme care not to bump the black telescopes! It is useful to have a security camera located underneath the MOT cell so that

light scattered by all four sides of the MOT cell are visible. The general alignment procedure takes about half a day and is as follows:

1. Block the light to one of the paths as close as possible to the PBS cube that splits the light.

2. Watch the security camera on the T.V. and close down the iris until a diffraction pattern with a nice dark central spot is visible.

3. Close down the iris on the first telescope that the traveling beam hits and check whether the dark spot is centered.

4. Use a mirror far away from the first telescope to center the beam on the iris.

5. Open both irises.

6. Repeat steps 1-5 for the counter-propagating path. This gives the translation part of walking the beam.

7. Open all of the irises and put a piece of paper by where the light is split at the PBS to block one of the counter-propagating beams and allow the other to propagate through and (hopefully) hit the paper.

8. Steer the propagating beam to line up with the blocked beam by using a mirror as close as possible to the first black telescope that the propagating beam goes through. This gives the angle portion of the beam walking.

9. Switch which beam is blocked and perform step 8 again.

10. Check the alignment of both beams to the telescopes using steps 1-3. If the alignment is good then the alignment for this axis is complete. If steps 8,9 have altered the alignment, repeat steps 1-9. This back-and-forth ensures that

the beams will be centered on their telescopes and have the correct direction of propagation.

There are a few other minor things that can affect the performance of the MOT. The MOT tends to perform better with the vertical trim coil set to 0.1 A during the MOT stage and turn it off before OM. This helps to align the MOT position to the magnetic trap position along the vertical axis. The amount of trap and repump light that couples into the TA fiber can change over time. It is worthwhile to adjust the mixing waveplate before the TA to change the trap to repumper power ratio while looking at the magnetic trap optimization panel.

4.1.3 Optical Molasses

A well functioning optical molasses stage is the most important part of loading a large N and low T sample of atoms onto the chip. A couple of things to note are:

- The optical molasses needs a well zeroed magnetic field
  - Power balancing of the beams can make up for a non-zero magnetic field.
  - Use a low TA current, 1A or less, and a long tof after OM to check each trim coil individually. Look for a colder, denser cloud.
  - Turn the TA current back up to maximum (1.6A) when done.
- The optical molasses needs to be centered on the location of the magnetic field.
  - Measure the center of the magnetic trap with in-trap fluorescence imaging.
  - Use the wave plates to change the power balancing to produce a cold cloud that is centered at the same location as the magnetic trap.
- After the fast turn-off of the MOT magnetic field (I≈14A) the lasers get knocked out of lock.

  - It generally takes 1-2 ms for the lock to get back as measured by the error signal on the lock box.
  - There should be a 1-2 ms wait between fast off and the start of OM to account for this.
  - A tighter (higher gain) current lock and a looser (lower gain) piezo lock tend to help make the process of re-locking faster.

- I have found that about 3 ms of OM is optimal. Too much time and the cloud expands too much, too little time and there is not enough cooling.

- There was a point where we were getting a lot of trap lock noise at about 134 MHz on the double pass AOM, which is where the OM operates.
  - This was traced to the cable carrying the signal for the repump offset lock at about 792 MHz getting too close to the cable carrying the RF to the double pass AOM.

- The OM generally likes a ramp down in both trap and repump power during the 3 ms. Trap 10V to 1.25 V, repump 10V to 5V of the analog control for the VVA driving the AROM. This equates to a reduction in optical power of approximately 1/4 and 1/2, respectively.

As mentioned in the first bullet point, the power of the counter-propagating beams has to be properly balanced in for the optical molasses to perform optimally. An imbalance in beam power causes a net force on the atoms. This force on the atoms can be mistakenly balanced by using a net force by a non-zero magnetic field. This leads to a situation where changing one parameter individually will make the optical molasses perform worse (hotter atoms), but changing them both in the correct way will make it perform better. Figure 4.6 shows how this issue can be diagnosed by

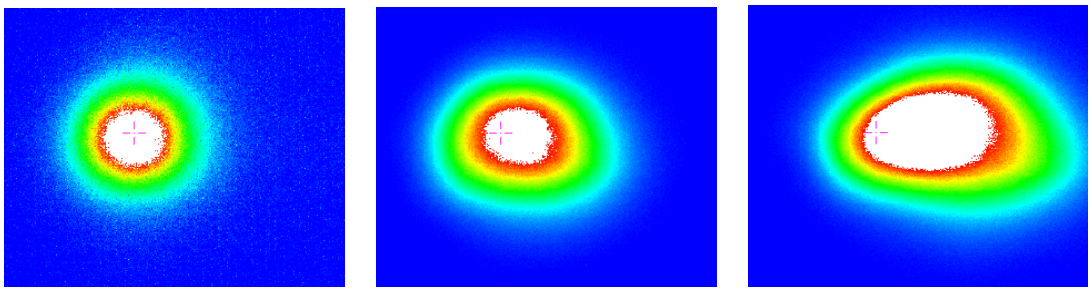

FIG. 4.6: Effect of optical force on optical molasses shape. Fluorescence images of a ^{87}Rb optical molasses for different optical powers. This shows the effect of a well zeroed magnetic field but imbalanced optical powers. From left to right the tapered amplifier has current 1A, 1.3A, 1.6A. The imbalance in the optical power affects the OM shape more as the total optical power is increased. The cursor represents the center of the MOT cell magnetic trap. The images are 5.4 mm wide by 4.2 mm tall.

separating the two forces. The optical force is proportional to the optical power. By decreasing the optical power (force) as much as possible on the left of figure 4.6 we can see that the cloud is small and round, which tells us that the magnetic field is well zeroed. Increasing the optical power (going to the right in figure 4.6) we see that the imbalanced optical force misshapes the cloud. With this knowledge that the magnetic field is well behaved, we can use the waveplates to balance the optical force by looking at the size and shape of the atom cloud.

When the optical molasses is working well, the temperature can be as low as $T \approx 16\mu$K. The temperature depends on the atom number; the more atoms in the optical molasses, the higher the temperature. As the atom number increases the atom density increases. This increases the chance that a photon emitted by an atom will interact with a neighboring atom and heat it. This temperature can be measured by a standard time of flight technique where the atoms are released from the trap and cloud size $\sigma(t)$ is measured as a function of time of flight before imaging, as shown in Figure 4.7. The cloud starts at a size σ_0 and expands at some expansion velocity, v, according to the following equation, where t is the time of flight.

$$\sigma(t) = \sqrt{\sigma_0^2 + (vt)^2} \tag{4.1}$$

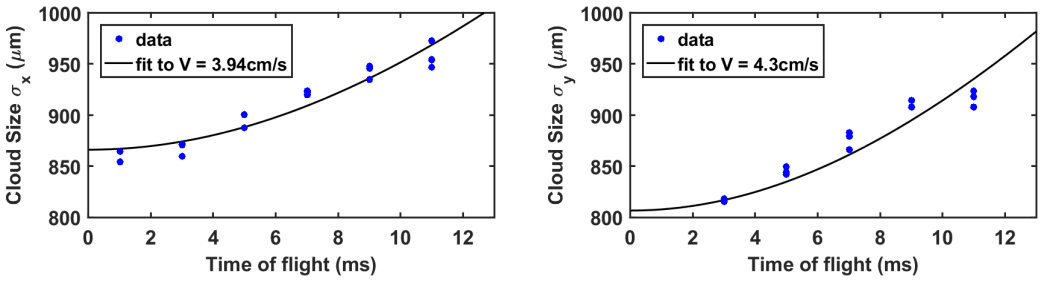

FIG. 4.7: ^{87}Rb optical molasses temperature measurement. The measurement was repeated 3 times for each time-of-flight and the scatter is shown on the plot. The data are fit to $\sigma(t) = \sqrt{\sigma_0^2 + (vt)^2}$ where σ_0 is the initial cloud size, t is the time of flight and v is the expansion velocity The measured temperature is $T \approx 15\mu$K for x, 18μK for y. This data was taken on 25 Apr 2014, with the MOT CCD camera. There were 7.4μm per pixel with an imaging system magnification of 0.489.

Here v refers to the velocity in the single dimension that is being measured. Once the cloud size is measured as a function of time, then the data can be fit to equation 4.1 to extract the expansion velocity v and the initial size σ_0. The temperature can then be found by solving for T in $\frac{1}{2}mv^2 = \frac{1}{2}kT$. Plugging in Boltzmann's constant k and the mass of ^{87}Rb we can come at the following useful approximation:

$$T = \frac{m}{k}(v)^2 \approx 1.05\frac{\mu K}{(cm/s)^2} \tag{4.2}$$

This can be a useful conversion for quick calculations of the temperature; the temperature (in μK) is approximately equal to the square of the expansion velocity (in cm/s).

4.1.4 Optical Pumping

The optical pumping step spin-polarizes the atom cloud (after the optical molasses stage) for loading into the MOT cell magnetic trap. In general, the optical pumping is not too finicky: there are many different conditions where it works more or less the same and does not drift much day-to-day. That being said, here are some tips for getting the optical pumping to work well. There should be about 1 mW of

power output from the OP fiber with repump light blocked, single pass trap AOM off, OP AOM full power. With this power level the OP generally likes to be at 1/2 power (3V AOM VVA control) for 0.9 ms. The repump light that helps with optical pumping comes from the MOT beams, not through the OP path. A simple step of the vertical trim coil to -5V is sufficient in the same column. For ^{87}Rb we optically pump on the D2 line with $F = 2 \leftrightarrow F' = 2$. This allows the desired $|F = 2, m_F = 2\rangle$ state to go dark to the applied σ^+ light, see section 2.3.3.

Our OP system, like many systems, is not perfect, and there are two issues that can create σ^- light. The first is misalignment between the incident linear polarization and the $\lambda/4$ wave plate. The second issue that can create σ^- light is misalignment between the light $\vec{k}$ and the quantization magnetic field. The σ^- component of light produced by these misalignments will excite atoms in the $|F = 2, m_F = 2\rangle$ state to the undesired $\left|F' = 2, m_F^{'} = 1\right\rangle$ state, which can decay into $|F = 2, m_F = 0, 1, 2\rangle$. This leads to heating of the cloud if the optical pumping pulse is too long or too powerful. There is a trade-off between this and sending enough light to adequately polarize the cloud before the magnetic trapping stage. We have found 0.9 ms of light at a detuning of $\delta = -2$ MHz from the $\left|5S_{1/2}, F = 2, m_F = +1\right\rangle \leftrightarrow \left|5P_{3/2}, F^{'} = 2, m_F^{'} = +2\right\rangle$ transition for $B_{DC} = 9.2$ G at about 0.5 mW of optical power to be the optimal mix.

We improved the magnetic trap loading significantly by re-calibrating the vertical trim coil used as the DC quantization magnetic field for the optical pumping. The quoted calibration for the vertical trim coil was about 0.6 G/A. By assuming this to be accurate we spent quite some time tracing down other leads. We finally measured this calibration by measuring the resonance location of the imaging light as a function of I_v, the current in the 'vertical trim' coil. We used absorption imaging at different imaging frequencies to find the center, f_0. The measured magnetic

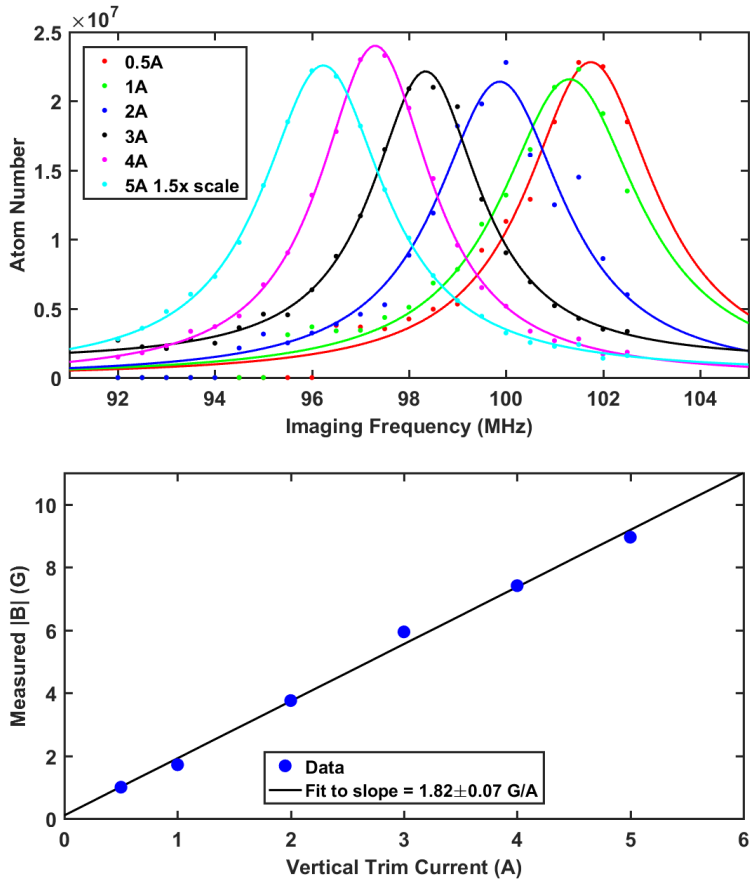

FIG. 4.8: MOT cell vertical trim coil calibration. ^{87}Rb MOT cell magnetic trap absorption imaging. The x-axis is the double-pass AOM frequency. The y-axis is the measured atom number from absorption imaging. The solid lines fits are to lorentzians $N = A - \frac{D}{\pi}\frac{\frac{1}{2}\Gamma}{(f-f_0)^2+(\frac{1}{2}\Gamma)^2}$. The 5A case was taken last and had a lower overall atom number and was scaled by a factor of 1.5 for easy comparison to the other curves. (bottom) Measured magnetic field $|B| = \frac{2(f_0-102.5)}{1.4MHz/G}$ vs. I_v. The data were fit to a line with slope $1.82 \pm 0.07 G/A$ and offset 0.1 ± 0.22.

field was then calculated as: $|B| = \frac{2(f_0-102.5)}{1.4MHz/G}$ vs. I_v. The factor of two comes from the double-pass AOM and the 1.4 MHz/G is from the approximate differential DC Zeeman shift of the $|2,2\rangle \rightarrow |3,3\rangle$ imaging transition [51]. These $|B|$ were plotted vs. I_v and fit to a line with slope $1.82 \pm 0.07 G/A$.

4.2 Magnetic Trap and Transport System

Figure 4.9 shows a representative false-color fluorescence image taken of an ^{87}Rb MOT. The red represents more photon counts corresponding to more atoms while the blue represents less of each.

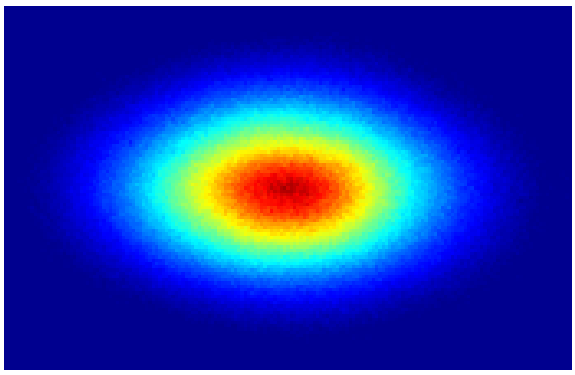

FIG. 4.9: False-color fluorescence image of an ^{87}Rb magnetic trap. The red represents more photon counts corresponding to more atoms while the blue represents less of each.

The vast majority of day-to-day problems that arise with the apparatus can typically be traced back to the MOT and optical molasses. There are also problems that arise from time to time with the MOT cell magnetic trap and the magnetic transport system. However, the MOT cell magnetic trap works reliably and has a long lifetime, as shown in Figure 4.10. We attribute the long lifetime in part to the ability to dynamically vary the background gas pressure using a LIAD system described in section 4.1, and to the vacuum cleaning procedure described in [61].

In the past there have been issues where the MOT-cell magnetic trap has been run at a current that was sufficient to trap the $|F = 2, m_F = 1\rangle$ state against gravity. This led to contamination of the cloud during evaporation and a failed evaporation path to BEC. The I_{set} and V_{set} analog control parameters for the MOT coil power supply dictates the fast and slow, respectively, current output during the MOT cell magnetic trap. These should be set so that the trap runs at a current just below that which will support $|F = 2, m_F = 1\rangle$ against gravity to provide extra confinement for

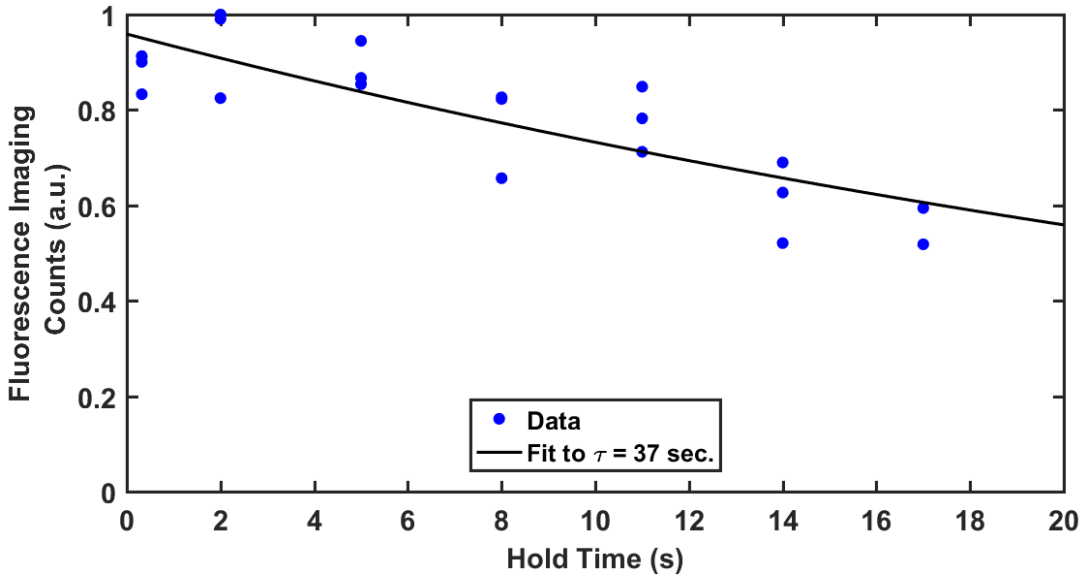

FIG. 4.10: ^{87}Rb MOT cell magnetic trap lifetime from fluorescence imaging. Each hold time was repeated 3 times and the scatter is plotted. The measured ADC counts are roughly proportional to the atom number. The fit is to $N = Ae^{-\frac{t}{\tau}}$ with $A = 0.96$ and $\tau = 37s$ It is hard to claim knowledge of the behavior of the atom cloud at a hold time of longer than 17 seconds, the longest that we measured. Measuring longer in the MOT cell magnetic trap is difficult because of heating of the quadrupole MOT coils.

the $|F = 2, m_F = 2\rangle$ state. The I_{set} and V_{set} should also be adjusted so that there is a smooth transition between voltage control and current control modes on the power supply, or rather that the current vs. time curve is smooth. The '$Fast\ V_{set}$' in the ADwin sequencer dictates the voltage that gets applied to the high voltage capacitor for the fast-on switch, see A.R. Ziltz thesis for details [64]. This can be adjusted in a similar manner to keep a smooth current trace. As always, empirical measurements of atom number and temperature in the MOT cell magnetic trap should be taken as an ultimate measure of success.

The magnetic transport system has performed reliably since it was installed and has had no major issues. There have been two minor issues that are worth noting here. The first is that the terminal block connections that connects the magnetic transport coils to the coil-plexer get loose over time. The solution to this problem is

to go around to all of the terminal connections and tighten them every six months. AJ Pyle and I spent considerable time and effort to rearrange the wire leads and connections so that they are easily accessible for routine tightening.

The magnetic transport from the MOT cell to the atom chip location takes approximately 8 s and can be hampered by stray near-resonant light scattering off the trapped atoms, causing loss and heating. There is a shutter on the laser table that blocks the near-resonant light there from going into an optical fiber to the tapered amplifier (TA) on the apparatus table. Despite our best efforts, the output light of the TA is not perfectly blocked during the magnetic transport and can cause atom loss and heating if seeded with the near-resonant light from the laser table. The second issue that arises during the magnetic transport part of the cycle is that this shutter on the laser table can get stuck open and allow near-resonant light to seed the TA. This light passes through the TA and should be completely blocked by a post-TA shutter installed on the apparatus table. This is not the case, however, and this light ends up heating the atom cloud during magnetic transport, which leads to less atoms being loaded hotter onto the chip, $T \geq 100\mu$K. This can be checked by manually cycling the shutters and can be fixed by reapplying tape layer(s) between the sticky Sorbathane and the shutter arm.

4.2.1 Atom Chip Micro-magnetic Trap

The atom chip that we use in our apparatus is shown in figure 4.11. This chip was built by Dylan Jervis in the Thywissen group at the University of Toronto. The chip is roughly 3 x 2 cm wide and a few mm thick. The electrical connections to the chip are made with conductive epoxy [61]. The substrate that provides the bulk of the chip is made of aluminum nitride (AlN). The wires are made from 3 μm thick silver plated with gold. As discussed late in chapter 8, AlN has excellent thermal

conductivity and silver has excellent electrical conductivity. There are multiple adhesion layers used to get the silver wires to stick to the AlN. The AlN serves as

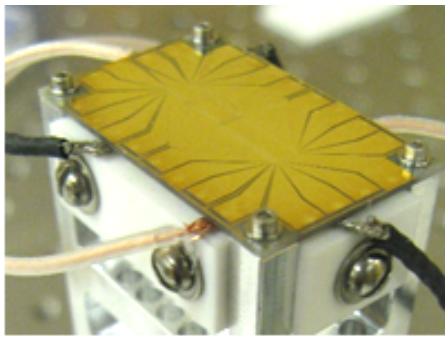

FIG. 4.11: Image of Atom Chip. The atom chip measures approximately 3 x 2 cm. This photo was taken before the chip was put into the vacuum cell. The wires are attached with electrically conductive epoxy [61]. This chip was built by Dylan Jervis in the Thywissen group at the University of Toronto.

a heatsink for the energy dissipated when running current through the wires. Our atom chip is limited to 1 A of DC current through the Z wire shown in figures 4.12 and 4.13 by the heating it experiences.

We use a Ioffe-Pritchard type trap to magnetically confine atoms such that $|B| \neq 0$ everywhere to prevent spin-flop losses [31]. This is accomplished by using a Z-shaped wire on the atom chip in combination with two external homogeneous magnetic fields: B_{Ioffe} and B_{Hold}, as seen in figures 4.12 and 4.13. The B_{Ioffe} and B_{Hold} are created by the blue coils near the chip cell in figure 4.1. In the thin wire limit, Ampère's law gives the magnetic field produced by the chip wire in equation 4.3. Here I is the current running through the chip wire, d is the distance from the chip wire, and μ_0 is the vacuum permeability.

$$|B_{chip}| = \frac{\mu_0 I}{2\pi d} \tag{4.3}$$

As shown in Figure 4.13, B_{Chip} and B_{Hold} cancel at a distance, d, directly below the

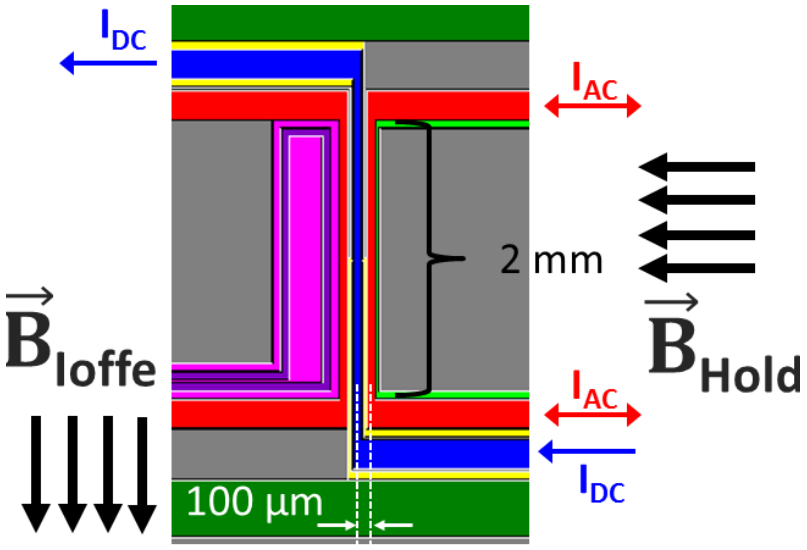

FIG. 4.12: Atom Chip Wire Schematic Top View. The blue wire in the center is the Z-wire used to create the DC micro-magnetic trap. The red wire to the right carries the 6.8 GHz microwave current used in the experiments in chapters 6 and 7.

Z-wire given by equation 4.4. The B_{Ioffe} pointing out of the page perpendicular to the B_{Hold} and B_{Chip} maintains a non-zero DC magnetic field, $|B| \neq 0$, to prevent spin flip losses. Ideally, B_{Ioffe} is homogeneous and does not play a role in the spatial manipulation or trapping of the atoms and only serves to preserve the $|B|$ floor. However, there is a small magnetic field gradient and curvature applied by the *Ioffe* coils.

$$d = \frac{\mu_0 I}{2\pi |B_{Hold}|} \tag{4.4}$$

The wire geometry shown provides for 'radial' confinement along $\hat{x}$ and $\hat{y}$, but do not provide any confinement into and out of the page along $\hat{z}$. The 'endcap' wire segments of the Z-wire in figure 4.13 run along $\hat{x}$, but are not shown for simplicity. These 'endcap' wire segments provide the axial confinement along $\hat{z}$ necessary for a trapping potential in all three dimensions.

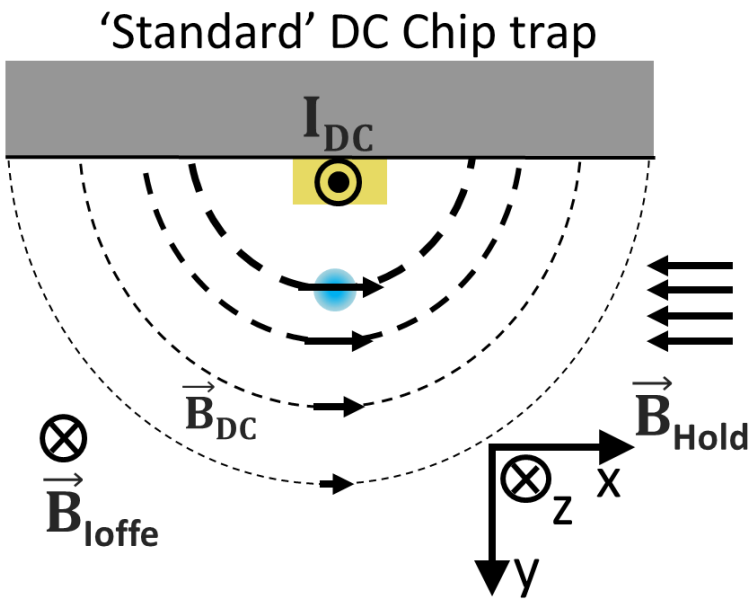

FIG. 4.13: Atom Chip Micro-magnetic Trap Side View. The Z-wire (gold rectangle) carries a current running out of the page which produces $\vec{B}_{DC}$. The other magnetic fields, $\vec{B}_{Hold}$ and $\vec{B}_{Ioffe}$, are produced by two pairs of external coils in Helmholtz configuration. The blue dot gives the location of the magnetic field minimum where the weak field seeking atoms are trapped.

4.3 Rb Tapered Amplifier Repair

4.3.1 Collimating Lens

The original construction of the Rb tapered amplifier (TA) mount had a defect that prevented the input lens from getting close enough to the TA chip. This prevented the input light from being properly mode-matched to the TA chip, which lead to a decrease in the maximum TA output power.

We took apart the copper mounting block and replaced the offending screw with a shorter one. This allowed the collimating lens close enough to the TA chip to focus all of the input light on to the TA chip. This increased the raw amplified output laser power to 850 mW. This also cleaned up the output mode and we increased the 'useful' power in the central beam to 380 mW after spatial filtering

4.3.2 Broken Peltier

There is a Peltier Thermo-Electric Cooler (TEC) sandwiched between the copper block holding the TA chip and the aluminum block attached to the optics table. This regulates the temperature of the TA chip. At some point this TEC broke and ceased regulating the TA temperature. Over the course of 30 minutes of being turned on the TA chip would heat up and cause the output laser power to decrease from 375 mW to 320 mW. There is also evidence that there was some beam steering associated with this temperature drift.

We were able to trace the problem back to a faulty TEC by measuring its resistance with a multimeter. After replacement, the TEC worked properly and kept the TA at a constant temperature, as monitored by the thermistor on the TA control box. The new TEC solved the temperature, laser power, and beam steering drift associated with the TA chip self-heating.

4.4 Trap and Repumper Laser

This section contains information about trouble-shooting the specific lasers used in our apparatus during my tenure. [1]

4.4.1 Trap Multimoding

A known problem of the trap master laser is that it can 'multi-mode', or output more than one frequency at a time. This can be seen by looking at the Fabry-Perot cavity signal with the injection laser properly locked. This can also be seen by looking at the saturation spectroscopy (sat-spec) signal. If the sat-spec signal is fuzzy then the trap laser is probably multi-moding. This can be fixed in most cases

[1] In the summer of 2016, the 'trap' laser died and was replaced, but this information should be generally useful for external cavity diode lasers (ECDLs).

by turning down the trap laser current by a few tenths of a mA.

4.4.2 'Gray Box' Repumper Mode-Hop

The 'gray box' repumper laser (black Thorlabs mount) is a replacement for the former ECDL laser used to drive the $\left|5S_{1/2}, F = 1\right\rangle \rightarrow \left|5P_{3/2}, F' = 2\right\rangle$ transition in ^{87}Rb. The laser tends to mode hop with changes in current or temperature. In general, the output frequency / wavenumber is inversely proportional to both laser current and temperature. The target wavenumber for the repumper transition of $\left|5S_{1/2}, F = 1\right\rangle \rightarrow \left|5P_{3/2}, F' = 2\right\rangle$ is 12816.693 cm^{-1} in vacuum.

If the laser mode hops, then it can generally be reset to the correct optical frequency by increasing the temperature of the laser by 2 °C and then bringing it back down to the original temperature. This can be accomplished in 10-15 minutes if you dynamically change the set point of the TEC so that the overshoots from the feedback circuit brings you to the right temperature. It can also be useful to 'knock' on the gray box with your knuckles when close to the peak temperature to get the laser to hop modes. If the laser is left on at the same current and the same temperature (and not disturbed) ,then it can take on the order of a month before it mode hops.

4.5 Bigger, Better BEC

We went about a year without a BEC in the lab from March 2014 to March 2015. We traced the issue back to too much RF power during the evaporation which created $|F = 2, m_F = 1\rangle$ atoms. We learned of the spin contamination by doing spin-dependent imaging using the DC Stern-Gerlach effect at different points in the evaporation path. This technique is discussed in more detail in section 7.1 The cloud started with no measurable $|2, 1\rangle$ atoms, but their relative population increased as

	RF1	RF2	RF3	DC	RF4	RF5	RF6	RF7	RF8
RF F. (MHz)	12.5	10.5	6.6	3.64	3.585	3.5	3.44	3.425	3.390
VVA (V)	3	3	1.5	1	1	0.5	0.225	0.225	0.225
Duration (ms)	800	800	500	500	400	200	200	200	200

TABLE 4.2: RF frequency and amplitude parameters. This is valid for the evaporation path to BEC as of April 2016. The RF amplitude is given in units of V that are doubled before being sent to a Mini-Circuits $ZX-2500-S+$ variable voltage attenuator (VVA) that controls the RF amplitude. The decompression stage also lowers the value of B_{Ioffe} and B_{Hold} to lower the trap frequency and the minimum trap energy.

the evaporation path proceeded. This caused the evaporation to fail around a phase space density (PSD) of ≈ 0.05, which is about the 'RF 5' column in the ADwin sequencer where the RF knife goes down to 3.5 MHz. Changing other evaporation path parameters like evaporation time, compression, final RF frequency, etc. did not allow for increases in phase space density; it only allowed for atom number loss.

The phase space density of a trapped gas is $PSD = n\lambda_{dB}^3$ where n is the atomic

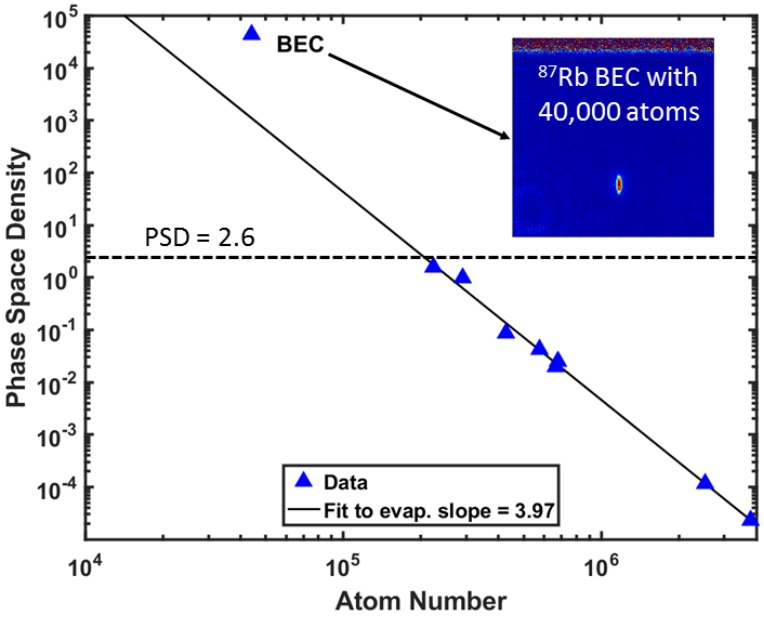

FIG. 4.14: Phase space density as a function of atom number for the ^{87}Rb from the initial chip load (bottom right) to BEC (top left). The data are fit to: $PSD = N^{-m}$ where m is the evaporation slope. This data represents a best-case scenario shortly after optimizing the MOT cell magnetic trap and the evaporation path. Points are larger than error bars. The produces a BEC of $\approx$ 40,000 atoms. All images were taken using the axial camera, with a variable tof, on 04Mar2016 recorded in book 6 page 127.

density and the de Broglie wavelength is given by: [70, 37]

$$\lambda_{dB} = \frac{\hbar}{\sqrt{2\pi m k_B T}} \tag{4.5}$$

The transition from a thermal gas to a BEC occurs at a PSD of 2.612 [70, 37].

Decreasing the RF power during the final part of the evaporation stage limits the production of $|F = 2, m_F = 1\rangle$ and allowed for the creation of BECs. The total atom number in the BEC depends on the exact RF power ramps in columns 'RF5' and 'RF6'. Too much RF power and the $|2, 1\rangle$ state contaminates the sample and the evaporation fails. Too little RF power and the RF knife does not fully eject the hottest atoms and the evaporation fails. Empirical testing of the RF power from the Berkeley Nucleonics RF source (start at +8 dBm) and the final RF power set in the ADwin sequencer are necessary for BEC optimization. Figure 4.14 shows phase space density (PSD) vs. atom number for an optimized evaporation path for a chip-trapped ultracold ^{87}Rb cloud starting at 'RF1' and going all the way to a BEC with $N_{BEC} = 40,000$ atoms.

On a time scale of approximately once every six months it is advisable to tune up the evaporation path to BEC. Table 4.2 describes a typical BEC evaporation path that can be used as a template and gives definitions for the various RF columns. These are the points that are plotted in Figure 4.14. On this time scale the atom number and temperature loading onto the chip generally drift such that the BEC atom number can be re-optimized altering the evaporation path. In general for more, hotter atoms you should use less compression and evaporate quicker. Similarly for fewer, colder atoms you should use more compression and evaporate slower. The most commonly changed parameters of the evaporation path are column time, RF frequency, and RF power. The values of B_{Hold} and B_{Ioffe} during the compression stage can also be changed to change the trapping frequencies.

The most effective way that I have found the tune the evaporation path is to go column-by-column starting with the first columns of loading on the chip and change the times by doubling and halving to see if there are any easy gains the be made with timing. I then work on the RF frequency, and finally the RF power. If there is an increase in both N and PSD then that is a clear win. If one of N and PSD goes up while the other goes down the choice is not as easy. What I have found works well is to use the largest evaporation slope, m, as seen in equation 4.6. Here the starting point is labeled 1 and the test column is labeled 2.

$$m = -\frac{log_{10}(PSD_2) - log_{10}(PSD_1)}{log_{10}(N_2) - log_{10}(N_1)} = -\frac{log_{10}(\frac{PSD_2}{PSD_1})}{log_{10}(\frac{N_2}{N_1})} \tag{4.6}$$

All of the above data are taken with a MOT collection time of 25 seconds, which gives a total cycle time of about 40 seconds to produce a BEC including the approximately 8 second magnetic transport and 6 seconds of chip loading and evaporation. We attempted to reduce this total cycle time by reducing the MOT collection time and the results are shown in figure 4.15. The data are taken at the same point in the evaporation path (the exact point along the evaporation path was not written down, but is probably the 'decompression' stage gauging by the atom number). In addition to the data shown in figure 4.15, we were able to create a BEC for a MOT collection time of 5 s. This is not plotted, however, because the transport coils heat too much to run the apparatus continuously at a 5 s MOT collection time. The ultimate decision of the MOT load time is dependent on the experiment being run; if the experiment requires a large BEC, then a 25 s MOT load is most suitable, but if the experiment does not require a large BEC, then a shorter time can be used to speed up data collection. The main data in section 6.2 were taken with a 10 second MOT collection time.

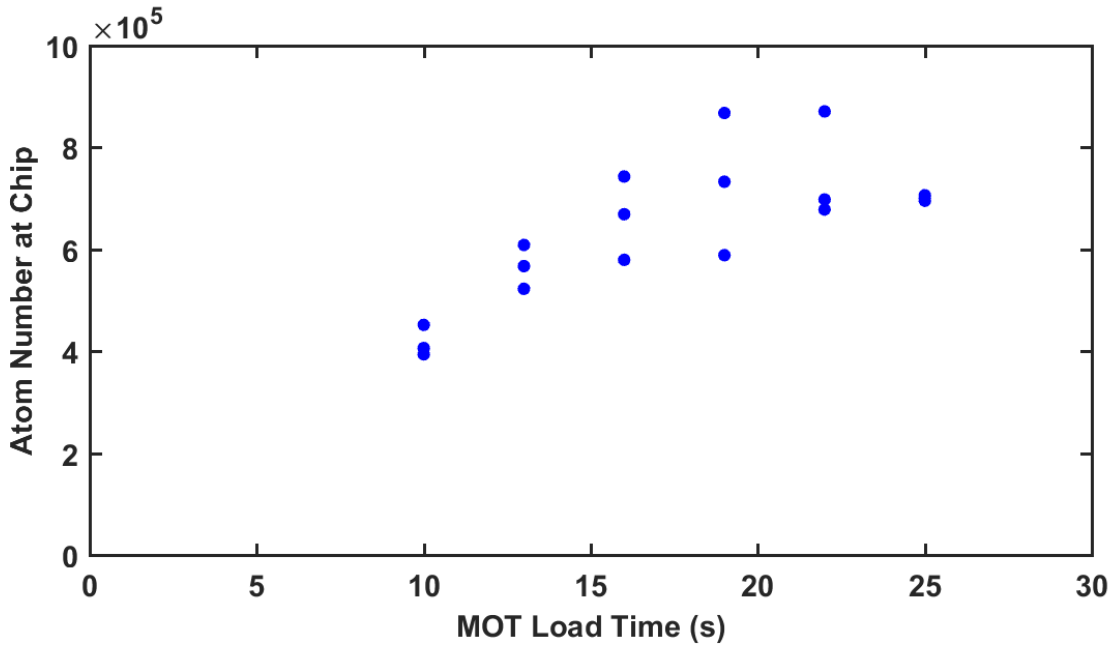

FIG. 4.15: Chip micro-magnetic trap atom number vs. MOT collection time for ^{87}Rb. The exact point in evaporation path was not recorded. The data points repeated 3 times per MOT load time and the scatter is plotted. We were able to create a BEC with a 5 s MOT collection time but it is now shown here.

4.6 Microwave System

The system used to provide high power microwave to the ACZ experiment has three main pieces. An RF signal at about 107 MHz serves as the clock for a SynthNV device that served to multiply up the signal by 32 to 3.4 GHz. The signal then passed from the SynthNV to the 'Dr. Watts' box where it was frequency doubled to 6.8 GHz and amplified before being sent to the chip U-wire.

FIG. 4.16: Microwave System Block Diagram. The clock generates a signal at 107 MHz. The SynthNV multiplies up the signal by 32. 'Dr. Watts' doubles the signal frequency to 6.8 GHz, amplifies the power, and sends the signal to the Chip U-wire.

4.6.1 107 MHz clock

Two different devices can be used as the 107 MHz source that clocks the SynthNV. Originally, we started operating with a HP 8657B signal generator with external DC frequency modulation. This worked to provide a stable frequency source for the initial experiments, including the force measurement experiments. The maximum modulation we could get on a 107 MHz clock signal was ±200kHz. This produced a full range of 13 MHz when multiplied up to 6.8 GHz. This frequency could be controlled with a ±10V analog signal from the ADwin sequencer divided down to ±1.8V to the HP 8657B after a 2700 Ω series resistor. This frequency control system this allows the ADwin sequencer to quickly vary the microwave frequency at 6.8 GHz by ±6.5 MHz through a ±10 V analog control signal.

The main drawback of the HP clock was that the range was limited to 13 MHz. This limited our capabilities of targeting more than one microwave transition when the spacing between the hyperfine levels $|F, m_F\rangle$ is large. The HP clock also had to be calibrated every time the central frequency was moved. The procedure to calibrate the HP clock was to select the central frequency on the HP signal generator, then change the ADwin output voltage while recording the frequency on a frequency counter. Fitting the resulting line of frequency vs. input voltage gave a calibration to put into the ADwin sequencer control program. This calibration was good to ≈1 kHz over a span of 13 MHz at a central frequency of 6.8 GHz.

The solution to both of these problems was to install a new clock source and replace the HP 8657B clock with a Direct Digital Synthesizer-based clock. Figure 4.17 shows an overhead view of the DDS source. An Arduino Due uses an ethernet shield to talk to a lab computer and controls a AD9910 DDS chip on an evaluation board that outputs the desired RF frequency. This DDS source has been worked on by multiple undergraduate students (J. Winkler, L. Paradis, J. Hagee, and H.

Cantor-Cooke) and was completed by graduate student A. P. Rotunno. This DDS source can operate at any frequency <400 MHz without the need for a manual change or a calibration. This allows for targeting different hyperfine transitions subject to large DC Zeeman energy shifts within the the same experimental sequence, which allowed for the three state preparation and spin-selective push pull in chapter 6.2. One downside of using the DDS clock is that it has no interface with the ADwin; frequency changes have to be added manually. However, the Adwin sequencer does provide the TTL pulse that initiates a DDS frequency change.

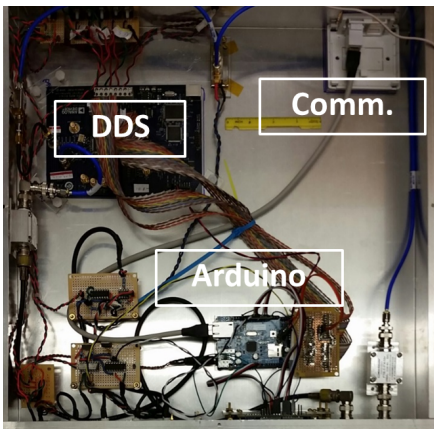

Sweep #	Start Freq (MHz)	End Freq (MHz)	Duration (ms)
1	106.85938	106.83594	400
2	108.50976	108.50976	1
3	107.28640	107.39577	3.5
4	108.50976	108.50976	1
5	107.85902	107.96839	3.5
6	108.30026	108.30026	1
7	108.30026	108.50976	.1

FIG. 4.17: DDS RF clock source. (left) Overhead view of the DDS clock box with the main parts labeled (Image Credit: A. P. Rotunno). The Arduino Due controller is controlled via ethernet (Comm.) and in turn controls the AD9910 DDS chip. (right) Screen capture of the web page served by the Arduino which controls the frequency sweeps of the DDS.

The DDS works by taking a list of frequency sweeps given to it from a web page served by the Arduino and then executing these frequency sweeps when triggered by the ADwin software. The DDS RF source is capable of phase continuous frequency sweeps as short as 10 μs over its full RF range (1-400 MHz) with as little as 100μs of downtime between sweeps. The DDS stays at the first frequency until triggered, then stays at each end frequency until the next frequency sweep is triggered. It is important to start the sweep about 100 μs before turning on the microwave power so the frequency has time to change to the 'start' value from the previous 'finish'

value. A common workaround is to use an dummy sweep while the microwave power is off to set DDS source at the desired start frequency. With this dummy sweep, the 'real' sweep can start at the same time as the fast turn on of the microwave power. A word of caution: if the TTL sweep trigger is left 'high' past the allotted time for a given frequency sweep, then the next sweep will start.

4.6.2 SynthNV

The SynthNV is a programmable phase-lock loop oscillator synthesizer produced by Windfreak Technologies (cost $600 USD) The device can be programmed via a USB cable to set its input clock frequency and the frequency to output. The SynthNV also has an internal 10 MHz clock so that it can be used to generate a static frequency without an external clock. We were advised from the manufacturer that the line width of the output signal is significantly reduced if the output signal is set to a power of 2 of the input signal. We set the device to accept a clock of 107 MHz and output a signal of $107 \times 32 = 3424$ MHz. Once the device is set up through the software it can be run by itself on wall power from the settings stored in the local EEPROM. A trick to getting the device to work properly is to ensure that the clock signal to the SynthNV is turned on before the SynthNV is powered. The SynthNV should be power cycled if the clock signal to it is interrupted.

The output frequency of the SynthNV can be swept by sweeping the input clock frequency. The SynthNV operates in a single frequency band that is selected by the input clock frequency when it gets powered on. These frequency bands are about 150 MHz wide. Once the input clock reaches a frequency corresponding the the edge of the output frequency band, the output power of the SynthNV drops to a point where it is not measurable. These frequency bands overlap which makes it important to power on the SynthNV at the same input clock frequency else it may

select a different than usual band. I have found that powering up the SynthNV at an input clock frequency of 107 MHz keeps it the band used in the experiments in this thesis that stretches below 6834 MHz and above 6960 MHz. A word of warning: using a clock frequency of 107.2 MHz or higher when powering on the SynthNV will cause it to select a higher frequency band that does not stretch down to 6834 MHz.

4.6.3 Dr. Watts

The purpose of the 'Dr. Watts' box is to take the 3.4 GHz signal from the SynthNV, double it to 6.8 GHz, amplify the power, and add the experimental control that we need for the final microwave signal. Figure 4.18 shows an overhead view of the box as well as a block diagram of the entire microwave system. There is slow

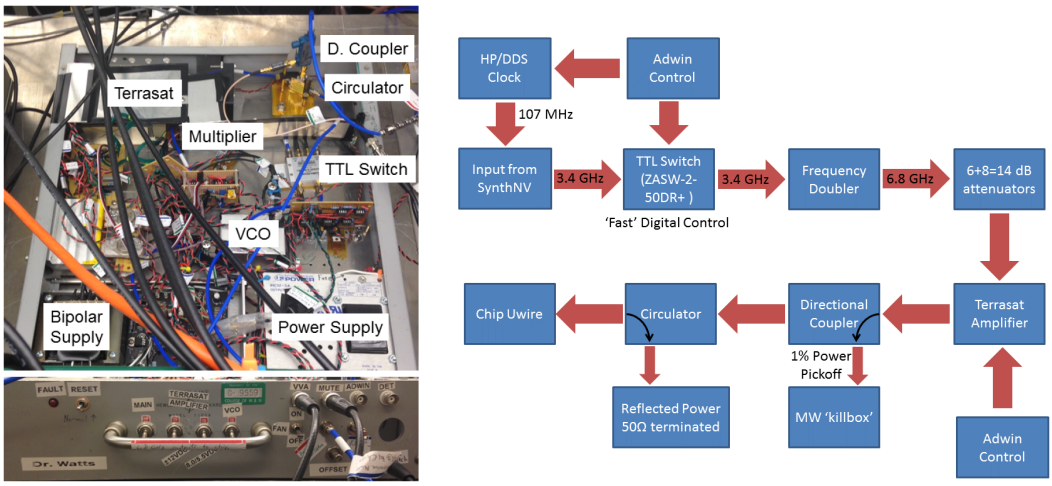

FIG. 4.18: Dr. Watts microwave system. (left) Overhead view of 'Dr. Watts' with major parts labeled (Image credit: A. R. Ziltz). (right) Block diagram of entire microwave system. The microwave 'killbox' intercepts the digital signals to the TTL switch and blocks the microwave current when a fault is triggered. The system is set up to allow maximum power to flow for 0.5 seconds.

(ms-level) analog (0-22.2dB attenuation) and digital control over the power output of the main power amplifier (Terrasat). In addition, there is a fast (10 ns) RF TTL switch on the microwave signal before it reaches the doubler. A. J. Pyle and A. R. Ziltz did a great job building and testing the Dr. Watts box. My contribution to

Dr. Watts was the addition of a microwave 'kill-box' that monitors the power sent to the chip and turns off the microwave signal to the chip if the microwave power is too high or if the microwave are left on for too long (≈ 0.5 seconds at full power.)

The total experimental system allows for digital frequency sweep control and digital and analog power control of the microwave current directed at the U- wire of the atom chip. The chip was designed for operation with DC currents and no special efforts have been made at impedance matching. The maximum microwave power out of Dr. Watts is $P = 3.3$ W. Most of the microwave power is reflected from the chip and is dumped into a 50 Ω load resistor attached to the reflection port of the circulator so that it does not damage the Terrasat amplifier.

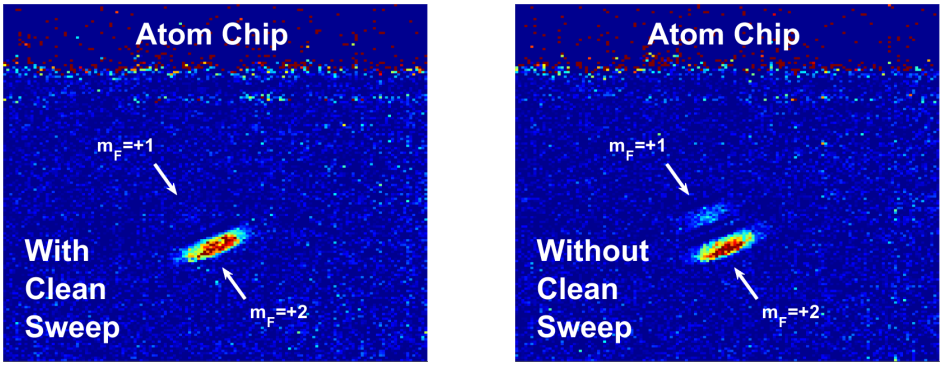

FIG. 4.19: Microwave clean sweep in DC chip trap for ^{87}Rb. This data was taken in an atom chip trap located under the U-wire after the 'RF8' evaporation column. There was a DC Stern-Gerlach pulse applied to spatially separate the $|F = 2, m_F = +2\rangle$ and $|F = 2, m_F = +1\rangle$ states before imaging the clouds on the radial camera.

In addition to performing ACZ experiments, the microwave system has allowed for spin distillation of atoms trapped in the DC chip trap. The evaporation process in the DC chip trap creates a small amount of $|2, 1\rangle$ atoms in the atom cloud ($\approx$ 15%). The $|2, 1\rangle$ atoms contaminate the atomic cloud and causes problems with evaporation, see section 4.5. Figure 4.19 shows DC Stern-Gerlach images with and without a microwave 'clean-sweep' targeting the $|2, 1\rangle \rightarrow |1, 1\rangle$ transition. The microwave field allows for targeted removal of the $|2, 1\rangle$ state via a spin-flip to the

anti-trapped $|1,1\rangle$ state without disturbing the desired $|2,2\rangle$ state. In contrast, the RF field targets all of the m_F levels within $F = 2$ equally, to first order in the DC Zeeman shift, and cannot be targeted to a specific m_F state.

CHAPTER 5

Optical Dipole Traps

An Optical Dipole Trap (ODT) is a versatile tool used in a wide variety of ultracold atom experiments. The trapping potential of an ODT is (mostly) independent of F or m_F states for linearly polarized light [22] and can be used to perform different experiments than are possible with a DC magnetic trap. Vector light shifts that affect different F or m_F states differently can be used for interesting experiments with limited configurations [71, 23, 72], but are beyond the scope of this discussion. In addition, ODTs can be turned on and off quickly without generating stray transient fields like those from eddy currents produced turning off DC magnetic traps. The experiments in Chapter 6 show that the ODT is a crucial tool for measuring an ACZ force stronger than gravity with our atom chip apparatus.

This chapter is organized in four sections. Section 5.1 details the theory for creating a trapping potential using a spatially varying AC Stark shift with a two-level atom. Section 5.2 describes the Spectra-Physics 3800 ND:YAG laser named 'lasersaurus' used to create an ODT in the MOT cell. Section 5.3 describes the process of sending the lasersaurus light through a single-mode fiber. The chapter finishes with Section 5.4 which describes the crossed ODT installed just below the

surface of the atom chip used to aid in the ACZ force measurement in Chapter 6

5.1 ODT Theory

An optical dipole trap (ODT) uses the AC Stark effect with a spatially varying field created by one or more lasers to create a trapping potential for neutral atoms [22]. ODTs were initially proposed for trapping neutral atoms in 1970 with the first experimental realization in 1986 [73]. There are many different configurations for optical dipole traps [47, 22]. This section will derive the general energy shift for a two-level atom in an applied laser field, then apply this to the ODT configuration found in our experiment.

The derivation of the ODT trapping potential for a single frequency laser field starts by assuming that we are working with a two-level atom. For the ^{87}Rb atoms used in our experiments, the ground state is $|g\rangle = |5S_{1/2}\rangle$, the excited state is $|e\rangle = |5P_{3/2}\rangle$ and the states are separated in energy by $E_0 = \hbar\omega_0$. The energy shift produced by the interaction between a two-level atom and a laser field of frequency ω_l can be taken from equation 3.6, repeated here:

$$E_{\pm} = \pm\frac{\hbar}{2}(-|\delta| + \Omega') \tag{5.1}$$

The detuning is defined by $\delta = \omega_l - \omega_0$, and the generalized Rabi frequency is $\Omega' = \sqrt{\delta^2 + \Omega^2}$. The Rabi frequency is $\Omega = -\frac{\langle e|\mu|g\rangle}{\hbar}E_0(\vec{r}) \propto \sqrt{I(\vec{r})}$. Here E_0 is the magnitude of the electric field, r is the position operator, and $I(\vec{r})$ is the intensity of the laser field. The $\langle e|\,\mu|g\rangle$ term is the dipole matrix element where $\mu = er$ and e is the charge of an electron. The $\pm$ in equation 5.1 correspond to the dressed atom eigenstates discussed in section 3.1.3. A more thorough derivation including effects of order Δ_{FS}/δ can be found in [22]; Δ_{FS} is the fine structure splitting.

In the far-detuned limit of $|\delta| \gg \Omega$, the dressed-atom eigenstates $|\pm\rangle$ are well defined by the bare atom plus photon states $|g, N\rangle$ and $|e, N-1\rangle$, as shown in figure 3.1 and figure 3.5. In the far detuned limit, the energy shift in equation 5.1 for the ground state is given below by:

$$E_g = +\frac{\hbar\Omega^2}{4\delta} \tag{5.2}$$

The energy shift for the excited state can be obtained through a simple change in sign.

$$E_e = -\frac{\hbar\Omega^2}{4\delta} \tag{5.3}$$

These energy shifts are shown graphically in figure 5.1.

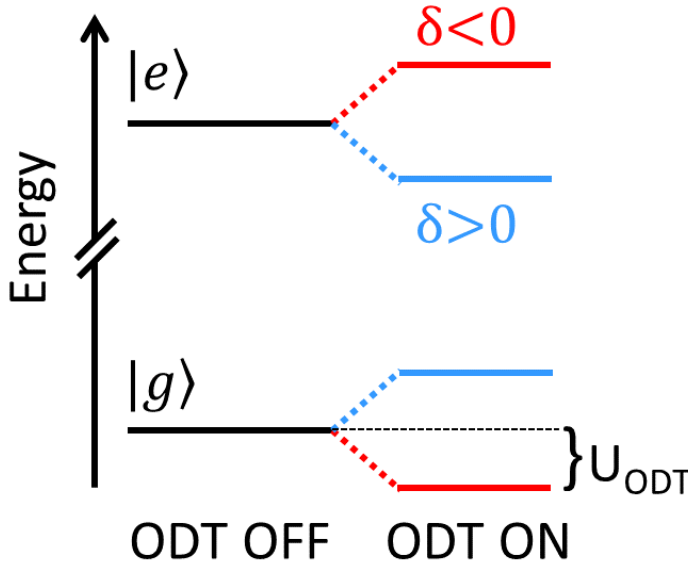

FIG. 5.1: Shift in energy created by turning on the ODT. The energy in the photon field has been removed. The black lines represent the energy of the bare atomic states without the ODT while the red (blue) lines represent the energy of these states with the ODT turned on for $\delta < (>)0$. Ground state atoms, $|5S_{1/2}\rangle$ for ^{87}Rb, experience a negative energy shift for red-detuned light and are strong-field seekers.

A spatially varying Ω, through a spatially varying electric field, in equation 5.2 gives rise to a trapping potential. We can expand equation 5.2 with the definition of Ω to get equation 5.4 for the trapping potential U_{ODT} experienced by the $|g\rangle$ atoms

due to the laser field:

$$U_{ODT} = +\frac{\hbar\Omega^2}{4\delta} = \frac{|\langle e|\,\mu|g\rangle|^2}{4\hbar\delta}E_0^2 = \frac{|\langle e|\,\mu|g\rangle|^2}{2\hbar c\epsilon_0}\frac{I(\vec{r})}{\delta} \tag{5.4}$$

Here the effective off-resonance dipole matrix element $|\langle e|\,\mu|g\rangle| = 2.44ea_0$ for the D_2 line of ^{87}Rb [51], e is the charge of an electron, a_0 is the Bohr radius, c is the speed of light in vacuum, and ϵ_0 is the vacuum permittivity. Equation 5.4 shows that the ground state is attracted towards high intensity light (strong field seeker) for red-detuned light, $\delta < 0$, and away from high intensity light (weak field seeker) for blue-detuned light, $\delta > 0$.

An important feature of ODTs is the scattering rate, or the rate at which atoms in the trap absorb and emit the light used to trap them. The atoms are initialized in the $|g\rangle$ state. However, a photon absorbed from the laser field by an atom will pump it into $|e\rangle$. This state is generally short lived (lifetime of $\tau = 26$ ns in ^{87}Rb), so any atoms pumped into $|e\rangle$ quickly radiate a photon and fall back into $|g\rangle$. The scattering rate for this process in an ODT can be calculated using equation 2.22 and assuming the far-detuned limit $|\delta| \gg \gamma$ [22].

$$\gamma_s = \frac{(I/I_{sat})}{(\frac{2\delta}{\gamma})^2}\frac{\gamma}{2} = \frac{\omega_0^3|\langle e|\,\mu|g\rangle|^4}{6\pi\hbar^3c^4\epsilon_0^2}\frac{I(\vec{r})}{\delta^2} \tag{5.5}$$

The saturation intensity, I_{sat}, is the laser intensity of resonant light where the scattering rate is half of its maximum value, $\gamma/2$, and is defined in equation 2.23 [47]. Comparing equations 5.4 and 5.5 we can see that the trapping potential scales like $1/\delta$ while the scattering rate scales like $1/\delta^2$. This scaling makes it advantageous to work with optical dipole traps with as large a detuning as possible, while still maintaining the necessary trapping parameters. In fact, ODTs are often called FORTs: far-off-resonance optical traps [74].

One of the simplest methods for creating an ODT, and the one used in our apparatus, is to send a red-detuned collimated beam into a converging lens and trap the strong-field seeking ground state atoms at its focus. The ODT used in this experiment uses a red-detuned laser with wavelength, $\lambda_l = 1064$ nm, compared to a resonant wavelength of $\lambda_0 = 780$ nm for the D2 line of ^{87}Rb. A schematic of the experimental setup is shown in figure 5.2. A collimated red-detuned laser beam is incident on a converging lens, with focal length $f > 0$, that focuses the light at a distance f past the lens. The atoms in the ground state are strong-field seekers and are attracted to the focus of the laser beam.

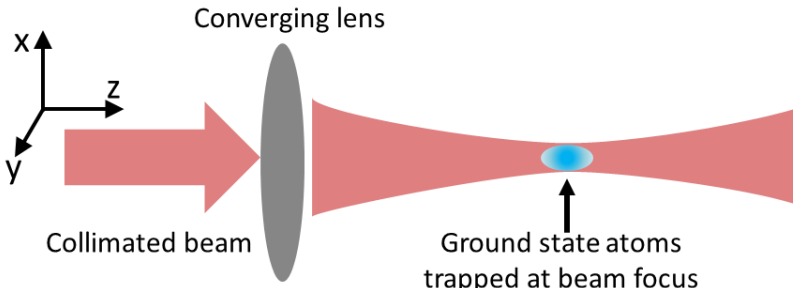

FIG. 5.2: Optical dipole trap schematic. A collimated beam is incident from the left where it goes through a converging lens. The ground state atoms (blue oval) are strong-field seekers for the red-detuned light and are attracted to the focus of the beam.

We can use simple Gaussian optics combined with equation 5.4 to find the trapping potential for the ODT in this configuration. A single lens focuses a collimated beam to a focus with waist radius w_0 and maximum intensity I_0. Equation 5.6 gives the spatial variation in laser light intensity at the focus of the beam as a function of $r = \sqrt{x^2 + y^2}$, the transverse distance from the optical axis of the beam [75, 22].

$$I(\vec{r}) = I_0 e^{-2\frac{r^2}{w_0^2}} \tag{5.6}$$

In the above equation I_0 is the maximum intensity and is can be derived by the normalization condition of the Gaussian to be: $I_0 = 2P/(\pi w_0^2)$ where P is the power of the laser. For small values of r/w_0, equation 5.6 can be well approximated by

performing a Taylor expansion about $r = 0$. By the symmetry in equation 5.6 we can eliminate the terms that are odd in r.

$$I(\vec{r}) = I_0[1 - 2(\frac{r}{w_0})^2 + \mathcal{O}(r^4)]) \approx -2I_0(\frac{r}{w_0})^2 \tag{5.7}$$

If we plug Equation 5.7 into 5.4, and omit the constant term (I_0) since it does not contribute to the trapping potential, then we get an equation for the harmonic trapping potential for the ground atomic state at the focus a red-detuned ODT:

$$U_{ODT}(\vec{r}) = -\frac{|\langle e|\mu|g\rangle|^2}{2\hbar c\epsilon_0\delta}(\frac{4P}{\pi w_0^4})r^2 = \frac{1}{2}m\omega_r^2 r^2 \tag{5.8}$$

where the radial trapping frequency is given by:

$$\omega_r = \frac{|\langle e|\mu|g\rangle|}{w_0^2}\sqrt{\frac{4P}{\pi\hbar\epsilon_0 c|\delta|m}} \tag{5.9}$$

This potential describes trapping in the $\hat{x}$ and $\hat{y}$ directions transverse to the propagation of the beam.

A single beam provides confinement along $\hat{z}$ in addition to the transverse directions. This 'axial' confinement is due to the changing waist radius along $\hat{z}$. The waist is smallest at the focus and expands along $\hat{z}$ as shown below [22].

$$w(z) = w_0\sqrt{1 + (z/z_R)^2} \tag{5.10}$$

Here, the Rayleigh length, z_R, is given by $z_R = \pi\omega_0^2/\lambda_l$. If we plug equation 5.10 in equation 5.6 and assume that $r = 0$, then we get the equation below.

$$I(\vec{z}) = \frac{2P}{\pi w_z^2} = \frac{2P}{\pi w_0^2}(\frac{1}{1 + (z/z_R)^2}) = I_0\frac{1}{1 + (z/z_R)^2} \tag{5.11}$$

We can follow a similar procedure to equation 5.7 and expand equation 5.11 about $z = 0$. The same symmetry argument applies to neglect terms odd in z. Neglecting the constant intensity term and those of $\mathcal{O}(z^4)$ we arrive at the trapping potential along $\hat{z}$.

$$U_{ODT}(\vec{z}) = -\frac{|\langle e|\mu|g\rangle|^2}{2\hbar c\epsilon_0\delta}(\frac{2P}{\pi w_0^2 z_R^2})z^2 = \frac{1}{2}m\omega_z^2 z^2 \tag{5.12}$$

The axial trapping frequency is

$$\omega_z = \frac{|\langle e|\mu|g\rangle|}{(w_0 z_R)}\sqrt{\frac{2P}{\pi\hbar\epsilon_0 c|\delta|m}} \tag{5.13}$$

Combining equations 5.12 and 5.8 we can find a 3-D trapping potential for a single focused Gaussian laser beam

$$U_{ODT}(\vec{r},\vec{z}) = \frac{1}{2}m\omega_r^2 r^2 + \frac{1}{2}m\omega_z^2 z^2 \tag{5.14}$$

This equation assumes that the beam is circular, $w_{0,x} = w_{0,y} = w_0$ and a TEM_{00} Gaussian beam, that the detuning is large, and it ignores terms of $\mathcal{O}(r^4, z^4)$, as well as vector light shifts. A good resource for exploring these approximations is located in [22]. In our experiment we have slightly elliptical beams. This changes $1/2m\omega_r^2 r^2 \rightarrow 1/2m\omega_x^2 x^2 + 1/2m\omega_y^2 y^2$. Also, if the atoms move around sufficiently within the trap, then they can experience the non-harmonic terms $\mathcal{O}(r^4, z^4)$. This can happen if the atoms get too hot, and can also occur if an external force 'pushes' them around, as in section 6.4. The addition of gravity generally lowers the trap depth by "tipping" the ODT potential as seen in 5.3.

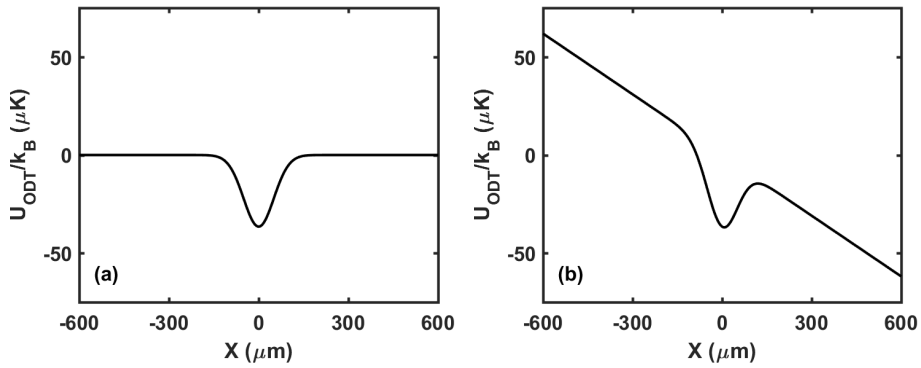

FIG. 5.3: ODT potential energy vs. position. Full calculation using equation 5.6 with $\omega_{0,x} = 101$ μm, $\omega_{0,y} = 154$ μm, laser power = 6 W for the ground state of an ^{87}Rb atom. (a) Shows the trapping potential of just the ODT. The inclusion of gravity in (b) lowers the trap depth from 36 to 22 μK.

5.2 ODT in the MOT Cell with Lasersaurus

Now that we have explored the theory of ODTs we will delve into how we have created them in our apparatus. This section contains information about the installation of the 1064 nm Spectra Physics 3800 ND:YAG laser aka lasersaurus and the creation of an ODT in the MOT cell. Here I discuss methods used to align the ODT to the MOT cell magnetic trap, which should be of use to future students. The challenges of using the direct free-space laser beam out of the lasersaurus are discussed and the section finishes with ways to improve the MOT cell ODT.

The lasersaurus is a laser built in 1988 with a Krypton arc lamp which pumps a neodymium-doped yttrium aluminum garnet (ND:YAG) crystal. We thank Charles Sukenik from Old Dominion University for loaning us the laser. The laser cavity itself is about 7 feet long and the power supply weighs about 400 pounds. The nominal power output for a TEM_{00} mode beam at 1064nm is 10W, though powers as high as 13W are possible with a fresh arc lamp. Lasersaurus was a workhorse of the experiments conducted in chapters 6 and 7 and has run with only minor hiccups since its installation in 2012. However, lasersaurus has a couple of drawbacks that will be discussed shortly: there are significant power fluctuations, $\pm 5\%$ or more

peak-to-peak, as well as pointing instabilities.

The initial motivation for installing an ODT in the MOT cell was to create a second location for cold atom experiments while the chip cell was being used for other graduate student experiments. Some of the experiments that we discussed trying in the MOT cell ODT are: velocity dependent Feshbach resonances, four wave mixing, and gradient magnetometry with trapped atoms. The MOT cell ODT could also, in theory, be used as a second path to BEC should the atom chip malfunction.

5.2.1 Initial alignment

There were many late nights spent in the lab building different iterations of the lasersaurus optical path. The final optical setup included optics and opto-mechanics to collimate the initial beam, send the beam through a 40 MHz acousto-optic modulator (AOM), make the beam round after the AOM, collimate it, and send it through a focusing lens and into the MOT cell to create an atom trap. Acousto-optic modulators are discussed in section 5.2.4. Figure 5.4 shows a block diagram of the optical set-up used to take free space light from the lasersaurus and direct it into the MOT cell to create an ODT.

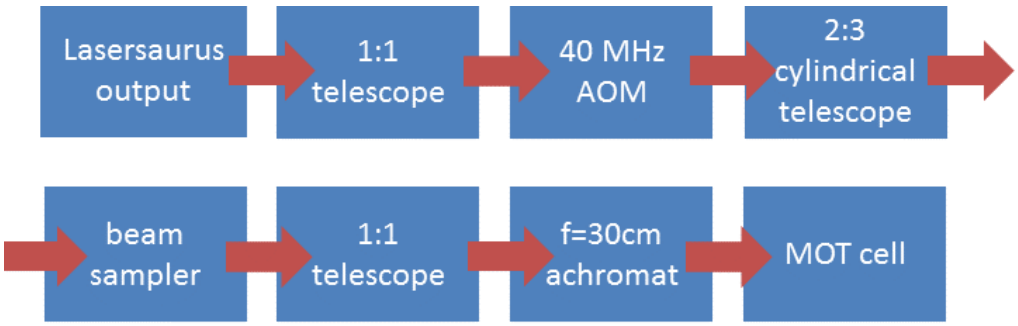

FIG. 5.4: Block diagram of the main features of the MOT cell ODT. The beam going into the achromat lens was not round even with the cylindrical telescope. The waist radius for the collimated beam going into the converging achromat lens was vertical (horizontal) direction was $w_{lens} = 1.01(0.66)$ mm, giving a size at the focus of $w_0 = 101(154)\mu$m.

The next task was to take this light and properly align it to the magnetic trap

in the MOT cell. Getting the alignment correct from scratch involved a significant time investment. The initial rough alignment was done by imaging the MOT using a camera on the opposite side of the vacuum cell to the ODT beam path. Two irises were installed in a line with the MOT position and used as targets to get rough alignment of the ODT to the MOT. After getting the rough alignment, we attempted to load atoms directly from the MOT into the ODT. This procedure worked after randomly walking the pointing mirrors until we got a signal. We then used the overhead CCD camera to align the resulting ODT to the location of the magnetic trap. This was good enough for an initial load from the magnetic trap, discussed later in the section. However, the laser alignment shifted on a day-to-day basis and could move far enough over the course of a week that there was no atomic signal to optimize. This quick degradation in the alignment of the ODT made finding a better alignment method a necessity.

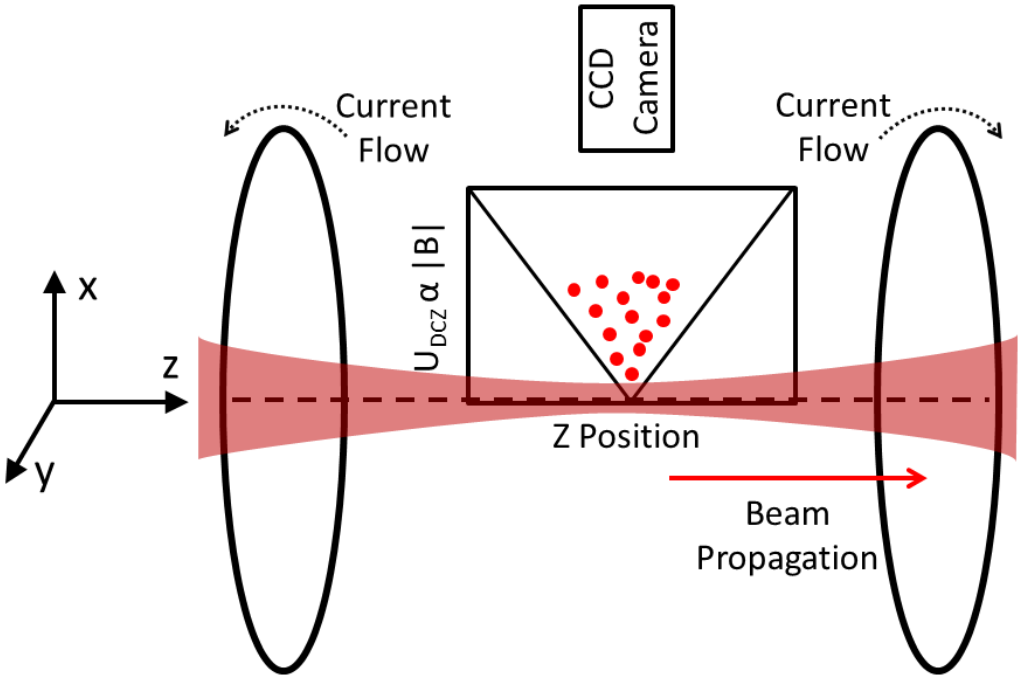

FIG. 5.5: Schematic of the MOT cell magnetic trap with beam alignment. The U_{DCZ} potential shown is that of the magnetic trap only. The beam pictured can be either the 'hole poke' beam or the ODT beam. The images in figure 5.6 were taken with the overhead CCD camera shown here.

After a decent amount of experimentation, we found a shortcut to significantly reduce the amount of time required for alignment. This procedure started by using a flipper mirror to align a resonant 'probe' beam at 780 nm along the ODT beam path. This beam was resonant on the $\left|5S_{1/2}, F = 2\right\rangle \rightarrow \left|5P_{3/2}, F' = 2\right\rangle$ transition. Rough alignment could be done by continuously running a MOT with a 75% laser power reduction and looking for atom loss in the MOT as the alignment was changed. The 'probe' beam removed atoms from the $\left|5S_{1/2}, F = 2\right\rangle \rightarrow \left|5P_{3/2}, F' = 3\right\rangle$ cycling transition and caused the MOT to shrink when properly aligned. The next step in the alignment process was to use the 'probe' beam to poke a hole in the magnetic trap by de-pumping the trapped atoms as seen in Figure 5.6. Using an RF sweep to evaporate atoms and make the magnetic trap physically smaller aided in the alignment process. Centering the atom depletion region on the magnetic trap was typically good enough to start trapping atoms in the ODT, then the trapped atom number could be used for further alignment adjustments.

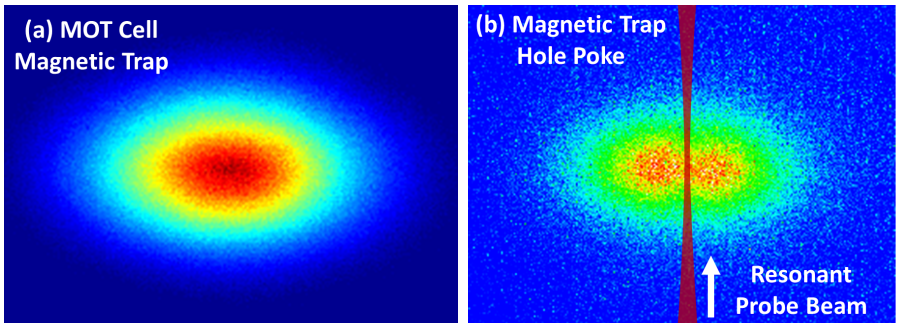

FIG. 5.6: MOT-Cell magnetic trap hole poke. (a) Fluorescence image from above of the MOT-Cell magnetic trap. (b) A hole poke in the magnetic trap with resonant light used as an aid for aligning the ODT. The ODT is aligned when the atom signal loss is maximized (vertical alignment) and the hole is centered in the cloud (horizontal alignment). The two images in (a,b) have different atom numbers and imaging parameters and should only be used for qualitative comparison.

This new alignment procedure aided in positioning of the beam with respect to the atoms, but the beam path also drifted with respect to its optics. Over the course of about a week the pointing of the laser would drift enough that a complete

realignment of the entire beam path in figure 5.4 was necessary. This was a large time sink and lead to a slowdown in experimental progress. I implemented a daily alignment procedure to correct small pointing changes before they became larger. This procedure took between 15-20 minutes and is listed below.

- Align beam to last iris before AOM
- Optimize optical power in the first order of the AOM by adjusting the last mirror before AOM and the AOM angle. The horizontal angle had the most effect by far.
- Align to the two irises after AOM
- Measure optical power out of the lasersaurus, before the AOM, and after the AOM in the first order.

This procedure was followed daily until the optical power output of the lasersaurus dipped below 10 W at which point we changed the Kr arc lamp. The lamps lasted about a month each when running every day.

5.2.2 Load from Magnetic trap to ODT

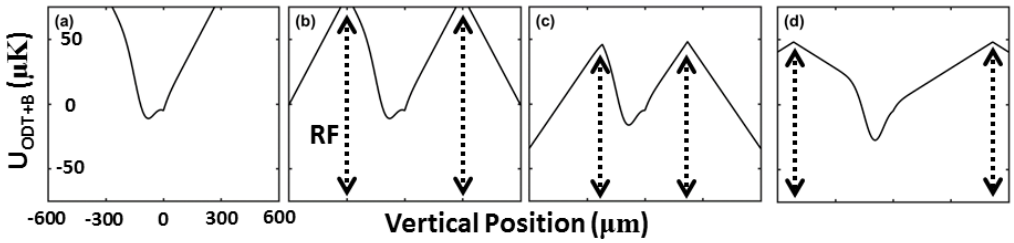

FIG. 5.7: Loading from the magnetic trap into the ODT through with RF evaporation. (a-d) correspond to **Compression**, **RFA**, **RFB**, and $\boldsymbol{I_B}$ **down**, respectively. The location of the RF knife is shown for (b-c). These calculations were done for $w_0 = 101(154)\mu$m of a single beam ODT with 6 W of power. I assume a weak-axis magnetic field gradient of: $dB/dz = 1/2(0.864)$ G/cm/A.

Once the ODT was aligned to the location of the MOT cell magnetic trap, we used a procedure pioneered in [76] to 'evaporate' the atoms from the magnetic trap

into the ODT using an RF knife. This procedure starts the same as every other procedure: $MOT \rightarrow Optical Molasses \rightarrow Optical Pumping \rightarrow Magnetic Trap$. After a short wait to allow the magnetic trap to settle, the ODT loading procedure is as follows:

1. **Compression:** Increase the current in the MOT quadrupole coils to $I_B = 97$ A in 500 ms, turn on ODT.

2. **RFA:** Turn on RF field and ramp from 10 MHz→3.5 MHz in 4 seconds.

3. **RFB:** Ramp down I_B from 97 A → 75 A and simultaneously ramp down RF from 3.5 MHz→2 MHz in 1 second.

4. I_B **down:** Ramp down I_B from 75 A → 32 A in 200 ms while leaving the RF on at 2 MHz.

This process is shown graphically in figure 5.7. Here the combined potential energy of the magnetic trap and the single beam ODT, neglecting gravity, is plotted as a function of vertical position. The ODT is aligned slightly below the location of the magnetic trap zero (to the left in figure 5.7) to reduce unwanted spin-flips. Figure 5.7(a) corresponds to **Compression**; (b,c) correspond to **RFA,B** and have the location of the RF knife displayed; as the RF knife is lowered, the atoms are cooled into the ODT potential; (d) shows the final stage of $\boldsymbol{I_B}$ **down** where the RF knife value is kept constant while the value of dB/dz is lowered to 14 G/cm, lower than the value of 15 G/cm needed to counteract gravity for the $|2,2\rangle$ state. The magnetic trap can be left on to provide axial confinement for the $|2,2\rangle$ state, or it can be turned off to have atoms trapped only by the ODT.

We can get a measure for how well the loading process worked by analyzing the atom number, temperature, and phase space density of atoms in the combined magnetic and optical trap. Figure 5.8 shows a temperature measurement of atoms

loaded into the 'retro-reflected' ODT, explained in subsection 5.2.3, just after the magnetic confinement is turned off. In this data set there were $N \approx 4.3 \times 10^6$ atoms at a temperature of $T \approx 6\mu$K. When analyzing the atom images, the data were fit to the Gaussian function below which has a factor of 2 difference in σ_0 compared to the w_0 in equation 5.6. Here the cloud is centered on y_0 and the fit along $\hat{y}$ has an amplitude N_0.

$$N = N_0 e^{\frac{(y-y_0)^2}{2\sigma_y^2}} \tag{5.15}$$

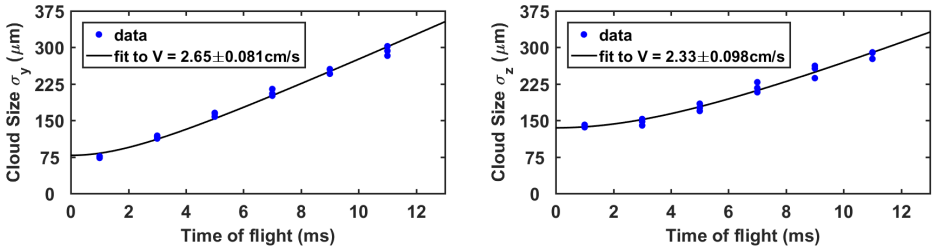

FIG. 5.8: Temperature measurement in the ODT. The left plot shows the measured size in the $\hat{y}$ direction and the right plot shows the same along $\hat{z}$. The data are fit to: $\sigma(t) = \sqrt{\sigma_0^2 + (vt)^2}$ where σ_0 is the initial cloud size, t is the time of flight, and v is the expansion velocity. The temperature can be approximated as: $T(\mu K) = 1.05v^2(cm/s) \approx 6\mu$K for ^{87}Rb in the ODT, see equation 4.2. Data taken on 18 July 2013 in Spectra Physics Lab Book 2, pg. 105.

We can use the initial size of the cloud and the measured temperature to make an educated guess of the trapping frequencies in the ODT, even though they were not independently measured. Using the Virial Theorem and assuming a harmonic trap we start by equating the time average of the kinetic energy of the atoms KE with the time average of the potential energy PE. The time average is denoted by the brackets $\langle\rangle$.

$$\langle KE \rangle = \langle PE \rangle \tag{5.16}$$

We can now plug in the definitions of the KE and PE in one dimension for an atom with mass m, velocity v, and position y in a harmonic trap with trapping frequency

ω_{trap} centered on $y = 0$.

$$\frac{1}{2}m\langle v^2\rangle = \frac{1}{2}m\omega_{trap}^2\langle y^2\rangle \tag{5.17}$$

Now we assume that the v is the expansion velocity and $\langle y^2\rangle = \langle \sigma_0^2\rangle$ that we get from the fit in figure 5.8.

$$\omega_{trap} = \sqrt{\frac{\langle v^2\rangle}{\langle \sigma_0^2\rangle}} \tag{5.18}$$

Using the values from figure 5.8 we get trapping frequencies of $\omega_{trap,y} = (2\pi)54$ Hz and $\omega_{trap,z} = (2\pi)27$ Hz. If we assume that the trapping frequency along $\hat{x}$ is equal to the trapping frequency along $\hat{y}$ then we can arrive at a phase space density in the ODT of $PSD = 1.47 \times 10^{-4}$.

5.2.3 Retro-Reflection

The atom cloud quickly expands axially in a single beam ODT once the magnetic confinement is ramped off. This happens because there is very little axial confinement in the single beam configuration. We selected the ODT to have a relatively large beam waist so that pointing fluctuations of the lasersaurus would have a correspondingly smaller effect on the loading, but this choice also leads to a very weak axial trapping frequency. Using a power of 6 W in equation 5.12, the axial trapping frequency should be $w_z \approx (2\pi)1$ Hz compared to the 'radial' trapping frequency of $\omega_{trap,y} = (2\pi)54$ Hz and the axial trapping frequency of the retro-reflected hybrid magnetic-optical trap of $\omega_{trap,z} = (2\pi)27$ Hz measured in the previous section.

This axial confinement problem can be solved by recycling the beam that crosses through the MOT cell and folding it back along the same path, with a small angular deviation, to create a crossed ODT. The beam paths are shown schematically in Figure 5.9(b), though not to scale. The beam is originally incident from the left and is sent back through the MOT cell at a small angle to create the retro-reflected

ODT in Figure 5.9(c). Folding the 'retro' beam back onto the original beam creates a trapping potential with more axial confinement.

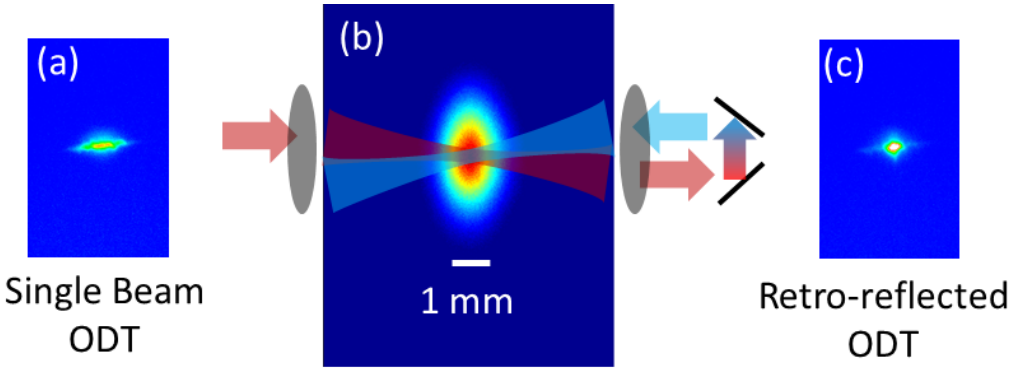

FIG. 5.9: Normal and retro-reflected beam ODT Schematic. (a) ODT created with a single beam. (b) MOT cell magnetic trap with cartoon overlays of first-pass beam in red and 'retro' beam in blue. The colors do not represent an actual wavelength change and are used only as a visual aid. (c) image of the ODT created with the retro-reflected beam setup.

Folding the laser beam back on itself has the potential to create an optical lattice. Optical lattices can be used for many interesting physics applications, but they are generally detrimental to cooling a cloud to quantum degeneracy because of their ability to fracture the single cloud into smaller non-interacting clouds. In order to determine if this was a problem in our setup we used a Michelson interferometer setup to make a measurement of the coherence length of the lasersaurus. The coherence length is roughly defined as the path length difference in the interferometer over which a laser will still create an interference pattern with itself. This is also the length over which the beam can travel while still being able to create an optical lattice. We were hoping for as short a coherence length as possible in order to minimize the chances that we had inadvertently created an optical lattice.

Figure 5.10 shows the 'fringe visibility' data as a function of the path length difference (PLD) in the interferometer. I have the quotes around the 'fringe visibility' to emphasize that this was not a complete measurement of the fringe visibility. The method used in this experiment was to jiggle one of the mirrors of the interferometer

and look at the corresponding noise as measured by the photodiode. Despite our quick experiment, we were able to find regions of PLD where the 'fringe visibility' was good (close to 0) and bad (close to 1).

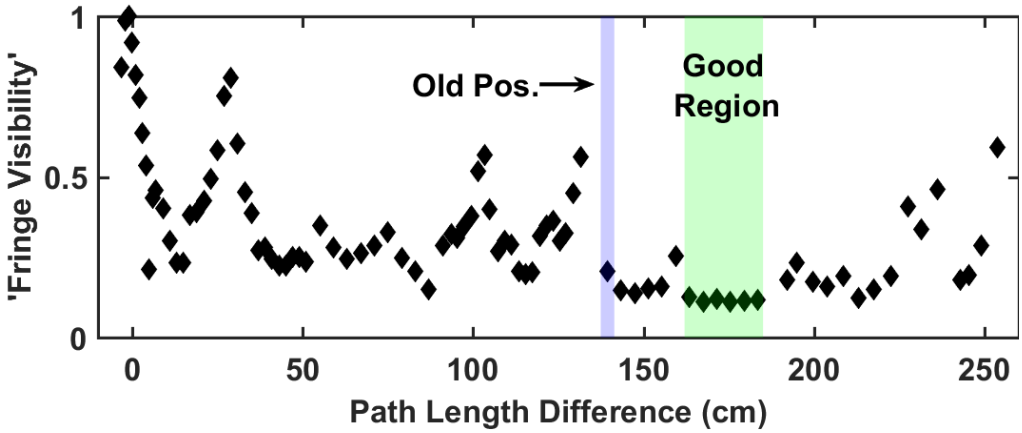

FIG. 5.10: Plot of 'fringe visibility' in a Michelson interferometer to assess the coherence length of the lasersaurus. This was not a strict fringe visibility measurement, but nonetheless gave qualitative guidance that we should position in the green 'good region'. The previous position is highlighted in blue.

The first setup of the 'retro' beam , which we used to take the data in Figure 5.9, did not have the benefit of this information. However, we lucked out and were in the blue region of Figure 5.10. We determined that there was a relatively wide region with low 'fringe visibility' shaded in green and moved the setup to have a PLD centered in this region at 175 cm.

Figure 5.11 shows a qualitative picture of a harmonic trapping potential with a superimposed lattice potential. The ideal scenario has a purely harmonic potential shown in (a). The first setup with a PLD of 139 cm (blue region in Figure 5.10) is shown in (b) while the better green green region is shown in (c). Introducing a $\lambda/2$ waveplate into the path of the 'retro' beam can create a $lin- \perp -lin$ lattice. This would change the interference pattern from an intensity to a polarization lattice that the atoms are much less sensitive to [22]. The predicted trapping potential for this configuration is shown in (d). We moved on to other experiments in chapter 6

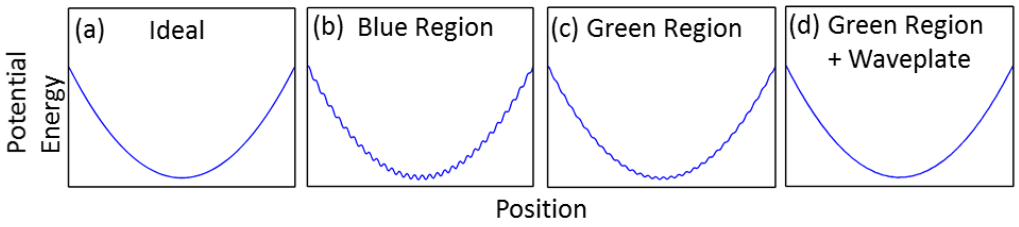

FIG. 5.11: Qualitative lattice roughness. Plot of trapping potential energy created by the ODT with an unwanted lattice potential from the 'retro' beam. (a) Shows the ideal case with no lattice, (b,c) shows the blue, green, regions of Figure 5.10. (d) shows what we predict the intensity lattice to be if we add a $\lambda/2$ waveplate to the 'retro' beam to change to a $lin- \perp -lin$ lattice. The lattice amplitude is to scale between the figures, but not to scale with the harmonic trapping potential.

before getting a chance to install the waveplate.

5.2.4 40 MHz AOM Driver

The power stability of the light coming out of the lasersaurus, $\pm 5\%$ was too large to run reliable experiments. To address this issue, we installed a 'noise eater' system. This system worked by first measuring the optical beam power of light reflected from a beam sampler (roughly 1% reflection) incident on a photodiode. This photo-diode converted the optical power to an electronic signal, which was then used as the input to a PI feedback circuit. The requested power could be set by an analog output on the ADwin sequencer. The PI feedback box compares the requested power to the measured power and uses the difference between the two to output a signal used to keep the laser power constant. The output of the PI locking system is sent to a VVA inside the 40 MHz AOM driver that controls the amount of laser power in the first order beam that was sent to the experiment. This system was able to reduce the optical power noise in the laser beam to a value consistent the noise on the measuring photodiode without any incident light. These measurements put an upper limit on the laser power optical noise of $\pm 0.5\%$ peak-to-peak. Figure 5.12 shows a block diagram of the entire feedback system including the laser, beam sampler, photodiode, ADwin computer control, AOM RF driver, and 40 MHz AOM.

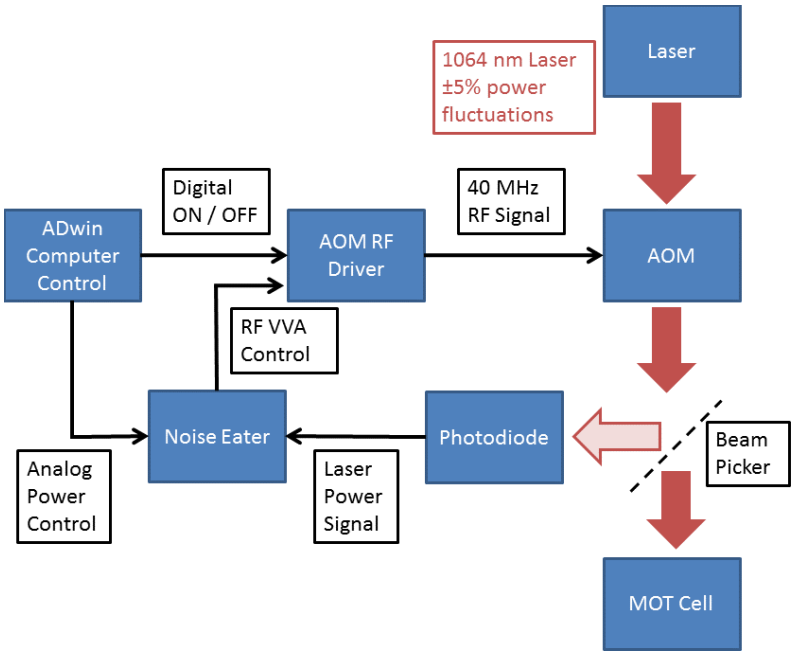

FIG. 5.12: Noise eater block diagram. Block diagram of noise eater setup used to reduce the power fluctuations in the lasersaurus from ±5% to ±0.5% Most optical elements are omitted here for clarity. The Adwin sequencer can be used for digital control of the AOM driver as well as analog control of the power set point in the noise eater PI feedback box.

A large piece of this noise eater control circuit is the electronics box used to generate and control the RF power sent to the acousto-optic modulator (AOM). Figure 5.13 shows a block diagram of the AOM RF driver. An AOM is a crystal

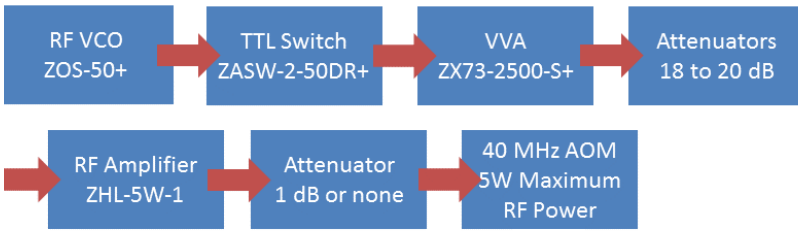

FIG. 5.13: Block diagram of the 40 MHz AOM driver. The RF signal originates with the voltage controlled oscillator and finishes with the 40 MHz AOM that can handle a maximum of 5 W of RF power. The parts numbers are from Mini-Circuits. The RF amplifier (ZHL-5W-1) occasionally changes its gain for no apparent reason.

that uses RF acoustic waves to diffract incident light [77]. AOMs in ultracold atom experiments are typically used for fast control of the power of lasers by the much easier control of the RF electronics used to power the acoustic waves in the AOM. In

this experiment, the light diffracted by the acoustic waves (first order) was directed at the MOT cell and the un-diffracted light (zeroth order) was directed to a beam dump. The RF power level dictates the proportion of the incident optical power output into each path. Figure 5.14 shows how this ratio of output powers changes with a change in RF power.

I built and tested an AOM driver box to output a maximum power of 5W at 40 MHz to the AOM, as seen in Figure 5.13. The RF power can be turned off quickly with a digital control signal sent to the 'TTL Switch'. The switching time $(10-90\%)$ on this specific unit is quoted at 10 ns. The RF power can also be controlled with an analog signal to the voltage-variable attenuator (VVA). This device passes minimum RF power (maximum attenuation) at an input voltage of 0 V and passes maximum RF power (minimum attenuation) at an input voltage of 17 V. There is a voltage doubling circuit built in to double the input analog voltage from 0-10 V to 0-20V to access the full range of attenuation. The output from the PI feedback box was used as the voltage control of the VVA.

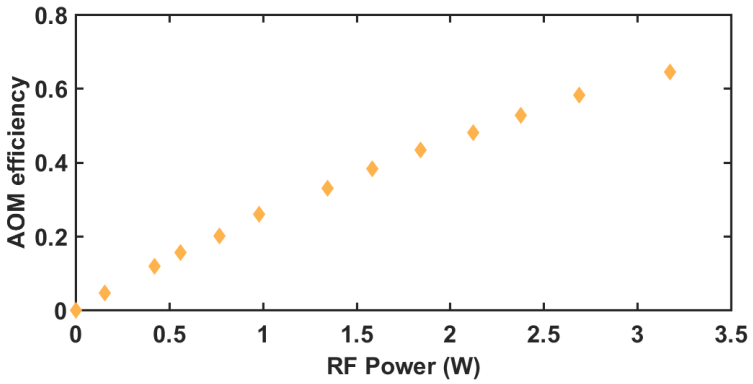

FIG. 5.14: AOM efficiency vs. 40 MHz RF power. The AOM efficiency is given by the ratio of power in the first order beam out of the AOM to the total optical power input $Eff. = P_1/P_{total}$. This data set has a maximum value at $Eff. = 65\%$ at an RF power of 3.2 W.

This RF signal is sent through a 5 W amplifier before reaching the AOM. This amplifier has been shown to change its gain over time and the exact cause is not known. For example, the amplifier gain changed from 45 dB to 49 dB from 16-23

February 2016. Too much RF power can damage the AOM. Both too much and too little power can cause a drop in usable optical power in the first order of the AOM. This issue can be diagnosed by measuring the optical efficiency of the AOM as shown in figure 5.14. The AOM efficiency is given by the ratio of optical power in the first order beam out of the AOM to the total optical power input $Eff. = P_1/P_{total}$. Not measured in this data set is a dip in AOM efficiency if the power is too high. We did not want to run the risk of damage to the AOM by running more RF power when taking these data.

5.3 Fiberization

One of the main limitations of using the lasersaurus in a free space configuration is that it has significant pointing fluctuations on both long (days) and short time scales (sub-second). These fluctuations required a realignment of the ODT in the MOT cell on a daily basis despite a relatively large magnetic trap and beam focus of $w_{0,x} = 101$ μm for the vertical direction and $w_{0,y} = 154$ μm for the horizontal direction. Experiments in the chip cell use a much smaller magnetic trap and have a correspondingly much smaller tolerance for alignment drifts.

We purchased a 1.5 W 1064 nm single frequency, single mode fiber laser from NovaWave to create an ODT near the chip and mitigate any alignment drift issues. This laser worked sporadically for a year and then died, thus necessitating an alternate solution to keep running experiments with an ODT near the chip. The solution that we came up with was to take the existing lasersaurus and direct its light into a high power fiber. This process of fiberization takes the pointing fluctuations from the lasersaurus and turns them into fluctuations in the coupling efficiency into the fiber which then manifest themselves as fluctuations in the output power from the fiber. Luckily, we already had a system in place to correct laser power fluctuations.

Figure 5.15 shows a block diagram of the fiberized setup before and after the high power fiber. The top of the diagram is very similar to the original noise eater diagram in Figure 5.12. We changed some optics before the fiber to mode-match the input beam to the fiber with a collimated beam waist of $w = 1.45$ mm in the vertical direction and $w = 1.28$ mm in the horizontal direction. When the lasersaurus is operated with an output power of about 8 W, then it is reduced to about 4 W before making it to the input coupler of the high power fiber. The rule-of-thumb for fiber coupling is that 50% of the incident power will make it through. This is pretty standard in our experiment - we can get as high as 60%, but this efficiency

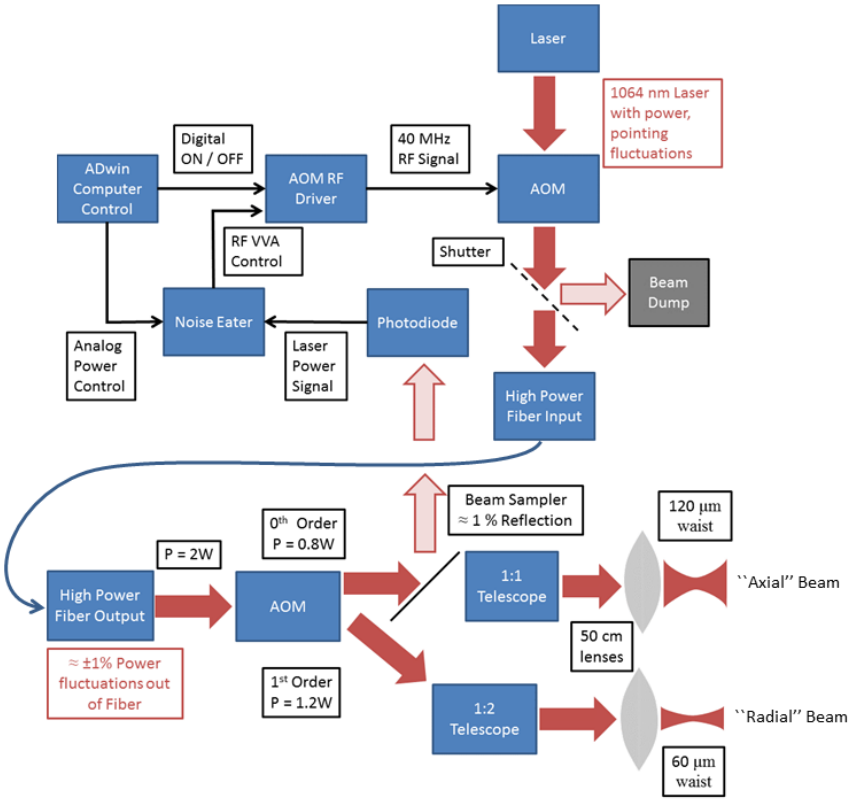

FIG. 5.15: ODT fiberization setup and beam path to chip cell. (Top) Schematic of experimental control of 1064 nm ND:YAG 'lasersaurus'. There is both digital and analog control of the pre- and post-fiber AOMs, as well as digital control of the laser shutter. There is initially 8 W of laser power with power and pointing fluctuations. The noise eater uses the laser power through the fiber to correct for both the initial power fluctuations and the pointing fluctuations, which turn into power loss out of the fiber. There are $\approx \pm 1\%$ power fluctuations through the fiber. The radial ODT beam has a final waist of 60 μm, while the axial beam has a final waist of 120 μm.

degrades as the alignment of lasersaurus drifts. Typically, we get an output power of 2W, just pushing the upper power limits of the fiber.

The key to good power stability out of the fiber is to to measure the power after the fiber with a beam sampler and photodiode: any pointing fluctuations from lasersaurus that result in a change in power out of the fiber can be corrected by increasing the power out of the AOM before the fiber. We measure an upper limit on the power stability out of the fiber of $\pm 1\%$. This noise level was limited by the photodiode and scope used to measure the power.

5.4 Crossed ODT at chip

The goal of introducing an ODT near the chip was to create an atom trap that was spin-independent and did not affect the atoms when turned off quickly. An ideal ODT would be located as close as possible to the chip wires and confine the atoms in as small a space as possible. This positioning allows the the atoms to experience the largest AC magnetic field gradients possible, which leads to large ACZ forces. The tight confinement ensures the atoms experience (mostly) the same AC magnetic field and gradient and thus the same ACZ force.

We installed an initial beam, called the 'radial' beam, with waist radius at its focus of $w_0 = 60$ μm using a 50 cm converging lens, as shown in figure 5.16 (note the change in coordinates). This focus size was chosen to minimize the waist of the beam at a distance $z = 1$ cm from the focus where it could be clipped by the atom chip. We calculate that 5% of the power is clipped by the chip if the beam is perfectly horizontal. We aligned the beam at a small angle to avoid clipping the beam before the focus.

We ran into the same problem with axial confinement with the ODT installed near the chip that we did with the ODT in the MOT cell. With only the radial beam, the confining force along the beam ($\hat{z}$) is very weak and the atoms spread out from a size ≈ 200 μm to the size of the axial camera CCD ≈ 2 mm of over the course of ≈ 100 ms. To combat this issue, we add a laser along $\hat{x}$, the 'axial' beam, to provide confinement along $\hat{z}$. This beam has a waist radius of 120 μm and has to be tilted 'up' towards the atom chip so that it does not get clipped before reaching the atom cloud. This can be seen in figure 5.16. The axial beam is pictured propagating from left to right. The radial beam propagates into the page and is tilted up, though not as much as the axial beam. After reaching the atom cloud, most of the axial beam is blocked by the chip and cannot be imaged. This configuration results in a

crossed ODT with trap frequencies $\omega_{(x,y,z)} = (2\pi)(172, 178, 28)$ Hz and a calculated trap depth of 23 μK.

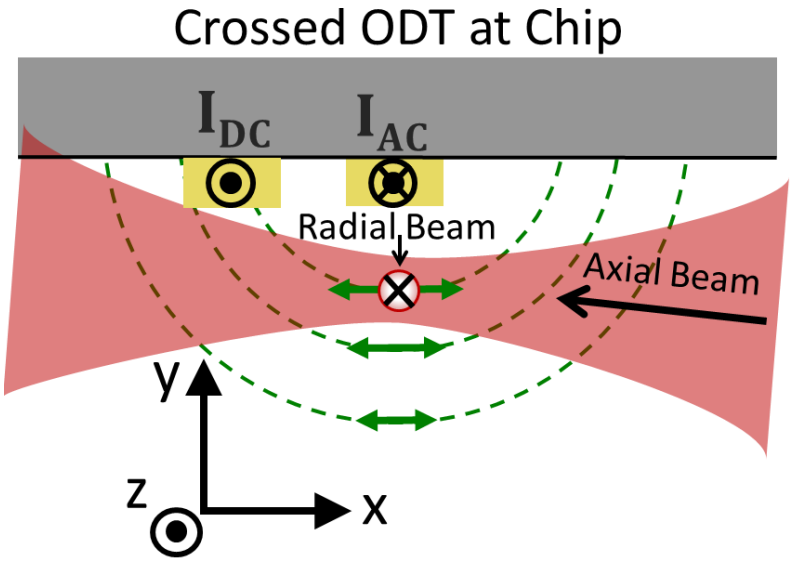

FIG. 5.16: Crossed ODT under atom chip. The 1064nm beams attracts the atoms to the region with the highest-intensity, the focus. The radial beam has a 60μm waist radius beam and goes into the page. The axial beam propagates from left to right and has a waist radius of $\omega_0 = 120\mu$m. Both beams are angled 'up' to prevent clipping before reaching the atoms, though the axial beam at a larger angle.

The bottom half of figure 5.15 shows how we obtain two beams (radial and axial) from a single output of the fiber. The first order of the 80 MHz AOM is used for the radial beam, while the zeroth order of the beam is used for the axial beam. The two beams come out of the AOM at different horizontal angles. Installing a f=20 cm lens at a distance z = 20 cm from the AOM turns this angle difference into a position difference at its focus. A D-shaped mirror then picks off the zeroth order beam without clipping the first order beam. The beams then travel a distance z=40 (20) cm before being collimated with a f=40 (20) cm lens for the first (zeroth) order beams. This factor of 2 difference in telescopes makes the collimated radial beam 2 times larger which accounts for the factor of 2 difference in the ultimate focus waists of $w_0 = 60$ (120) μm for the radial (axial) beams from the first (zeroth) order of the 80 MHz AOM; a larger collimated beam gives a smaller waist radius at the focus.

The alignment procedure for the radial beam starts by aligning it with the radial probe beam used to image atoms in the chip cell. One must also ensure that the beam is level by following its path after going through the chip cell. These steps should be sufficient to see the beam on the radial camera, which can be used to overlap the beam with the in-trap atom cloud position. A word of warning: the ODT beam has more than enough power to damage the camera. Align at low power and use sufficient filters in the beam so that the camera is not damaged. When running at full power a dichroic mirror is used to reflect the 1064 nm ODT beam to a beam dump and allow the 780 nm imaging light through to the camera. A high-pass filter (780 nm passed and 1064 nm blocked) is used in addition to prevent any ODT power bleed-through that could affect the imaging.

Using the camera to overlap the ODT beam with the in-trap atom cloud position is often good enough to load some atoms into the ODT. One should operate the DC chip trap to about the 'RF6' column on the Adwin sequencer, and then turn on the ODT. Quickly ramp off the DC chip trap in 10 ms, then do a short hold in the ODT (10 ms) before imaging. Often there is a trail of atoms falling out of the ODT along $+\hat{y}$ so that a hold time of longer than 10 ms leads to a weak atomic signal in the ODT. From here the alignment can be fine-tuned by looking at the loading efficiency into the ODT.

If this procedure does not work (i.e. there are no atoms in the ODT after initial alignment), then another method that can be used is to turn on the ODT during the time of flight of a hot cloud released from the DC chip trap. The 'RF1' column from section 4.5 is a good place to start. The ODT will distort the travel of the atoms and this distortion can be seen on the CCD camera iamges. The alignment of the ODT can be tuned by moving this distortion to overlap with the in-trap location of the atoms in the DC chip trap. This is generally good enough to load some atoms into the ODT; from here, the earlier described fine tuning can be used.

Aligning the axial beam is similar to the radial beam. The procedure starts by aligning the axial beam to the axial probe beam used to image the atoms along $\hat{x}$ in figure 5.16. One then images the radial ODT at short hold time on the axial camera. This gives information about where the atom cloud is in the $\hat{z}$ direction in figure 5.16. The axial beam can then be moved until it is horizontally aligned along $\hat{z}$ by imaging it on the axial camera. When properly aligned, the axial beam hits the chip and cannot be seen on the axial camera. Vertical alignment of the axial beam is completed by tilting it 'up' along $-\hat{y}$ and watching its effect on the atoms held in the crossed ODT at long hold times. With poor alignment, the atoms will spread out along $\hat{z}$. With the beam properly aligned, the atoms will remain constrained along $\hat{z}$ by the axial beam.

CHAPTER 6

AC Zeeman Force Measurement

The main result of this thesis is contained within this chapter; we were able to measure a spin-dependent force produced from the AC Zeeman effect that is stronger than gravity and is consistent with theoretical predictions. We leveraged the large AC magnetic field gradient possible in the near-field regime close to a current carrying wire on an atom chip to increase the ACZ force and thus expand upon previous work [26, 27]. ^{87}Rb atoms were released from a trap close ($d \approx 100$ μm) to a wire carrying microwave current at a frequency of $f \approx 6.8$ GHz. The ACZ force imparted a velocity impulse to the atoms during a short microwave pulse which was turned into a change in position after a time of flight. This change in position can then be used to calculate the average force experienced by the atoms.

This chapter is organized roughly chronologically. Section 6.1 describes the initial measurements that we made of the AC Zeeman force by releasing the atoms from a DC magnetic trap underneath the chip U-wire containing the microwave current. A discussion follows about troubleshooting the experiment and further attempts at getting atoms released from a DC chip trap to experience a force larger than gravity. Section 6.2 presents the primary force measurement results which were

obtained by releasing atoms from a crossed ODT instead of a DC magnetic trap. This section also contains a demonstration of the spin-selective nature of the ACZ force, including a force applied to the $|2,0\rangle$ state that is insensitive to first order DC Zeeman shifts. The chapter finishes with a discussion of sloshing experiments using the ACZ force conducted both in the DC chip trap and the ODT in section 6.4.

6.1 Time-of-flight - Chip Trap

The first measurements that we made of the AC Zeeman force were conducted by positioning the atom cloud underneath the U-wire containing the microwave current using a DC chip trap. Figure 6.1(a) contains the experimental set-up for the 'standard' DC chip trap beneath the Z-wire where the atoms get loaded from the magnetic transport and cooled by RF evaporation (see also figure 4.12). Figure

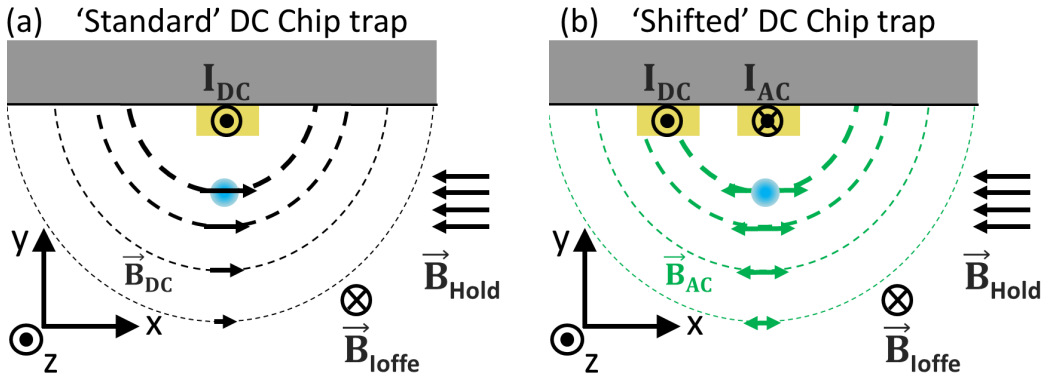

FIG. 6.1: DC Chip Trap Shift Under U-Wire (a) Shows the 'standard' DC chip trap under the Z-wire where the atoms are loaded from the magnetic transport and cooled using RF evaporation. A vertical trim field (not shown) was applied to shift the cloud center horizontally in (b). The green lines now show the AC magnetic field generated by the U-wire. The experimental parameters were as follows: $B_{Hold} = 5.2$ G, $B_{V.trim} = -5.4$ G, I_z =0.45 A, $I_{Ioffe} = 5.1$ G. Gravity is oriented down along $-\hat{y}$ for both cases.

6.1(b) shows the 'shifted' DC chip trap located beneath the U-wire where the ACZ force measurements were conducted. The addition of a vertical magnetic field (not shown) shifts the trap location horizontally under the U-wire in figure 6.1(b). The diagram is not to scale; the gold coated silver wires are 3 μm tall, 50 μm wide, and

100 μm center-to-center. When shifted, the atom cloud is located at a distance $d \approx$ 90 μm underneath the U-wire. The plan for the first experiment was to release the atoms from the DC chip trap by doing a fast turn off of all of the power supplies used to create the trap, then apply the ACZ force to the atoms. The microwave field targets the $|e\rangle$=$|2,2\rangle \leftrightarrow |g\rangle$=$|1,1\rangle$ transition, and the atoms are initialized into the $|e\rangle$=$|2,2\rangle$ state.

I will first give a brief refresher on the ACZ theory from chapter 3 before delving into the experimental results. Equation 3.10, repeated below for convenience, gives the expected force from the energy shift due to the ACZ effect in equation 3.6.

$$F_{ACZ\pm} = -\frac{d}{dr}U_{ACZ} = \mp\frac{\hbar}{2}\frac{\Omega}{\Omega'}\frac{d\Omega}{dr} \tag{6.1}$$

This equation assumes that the detuning of the applied field from the atomic resonance δ has no spatial dependence. The Rabi frequency is proportional to the strength of the applied AC magnetic field component that drives the targeted transition, i.e. $\Omega \propto B_{AC}$. If we assume the thin-wire limit then Ampère's law gives the scaling of the Rabi frequency with respect to the distance from the chip d: $\Omega \propto B_{AC} \propto 1/r$. Section 3.2 gives more detail on calculating the Rabi frequency. The ACZ force in our experiment comes from the large AC magnetic field gradient produced by in the near-field regime of a current carrying wire.

The $\pm$ in equation 6.1 corresponds to the $|\pm\rangle$ eigenstates discussed in section 3.1.3. For atoms in $|e, N-1\rangle$, a red-detuned field ($\delta < 0$) corresponds mostly to the $|+\rangle$ state, which is a weak-field seeker. Similarly, a blue-detuned field ($\delta > 0$) corresponds mostly to the $|-\rangle$ state, which is a strong-field seeker for atoms initially in $|e, N-1\rangle$. For an on-resonance field ($\delta = 0$), the $|e, N-1\rangle$ state is an equal superposition of both the $|+\rangle$ and $|-\rangle$ states.

6.1.1 First Attempt - Push Pull

The first attempt at measuring the ACZ force using atoms released from the DC chip trap was a qualitative success. The experiment was conducted by performing a fast turn-off of the DC chip trap, waiting 3 ms, then executing a fast turn-on of the microwave field at a set experimental detuning of δ_{exp} from the $|e\rangle \leftrightarrow |g\rangle$ transition at a DC magnetic field of $B_{DC} = 5.1$ G. The DC magnetic field was provided by the Ioffe field, oriented along $-\hat{z}$ in figure 6.1, unless otherwise noted. The microwave current was turned on and left at full power (3.3 W) for 2 ms to impart a velocity impulse to the atoms. There was then a 9 ms time of flight to transform this velocity impulse to a change in position which was measured by taking a picture of the atom cloud using absorption imaging. The results followed the qualitative predictions that the red-detuned microwaves with $\delta_{exp} < 0$ pushed the atoms away from the chip and blue-detuned microwaves with $\delta_{exp} > 0$ pulled the atoms toward the chip as shown in figure 6.2.

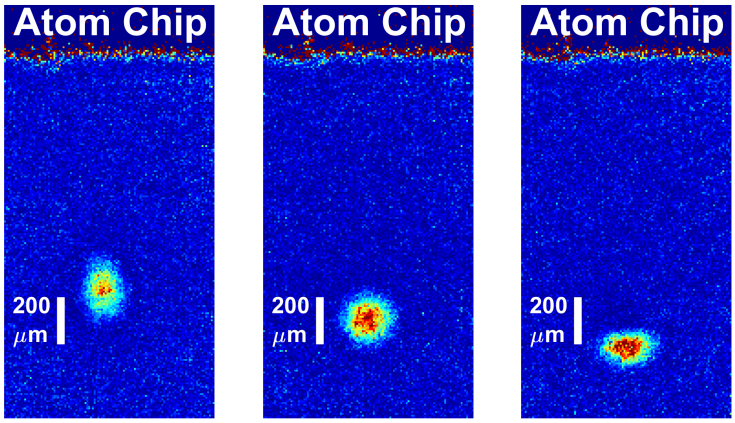

FIG. 6.2: False color absorption images of the first attempt successful at using the ACZ force. From left to right: 6845.50 MHz (red-detuned), control without microwaves, 6846.0 MHz (blue-detuned). The transition resonance for $B_{DC} = 5.1$ G is at 6845.7 MHz. The microwave pulses were 2 ms long and were applied 3 ms after doing the fast turn-off of the DC chip trap. There was then a 9 ms time-of-flight after the microwave pulse.

These measurements was repeated 5 times at varying microwave frequencies

roughly centered on the resonant frequency of 6845.7 MHz to get a more quantitative picture of how the ACZ force changed with detuning. The results are plotted in figure 6.3. Data were taken without a microwave pulse so that we could extract the change in the center of the cloud. Each atom cloud was fit to a Gaussian to find the center location, which was then compared to the control center taken without a microwave pulse to get the change in y center Δy. Each data point is an average of 5 measurements and the error bars represent the standard deviation of the measurements.

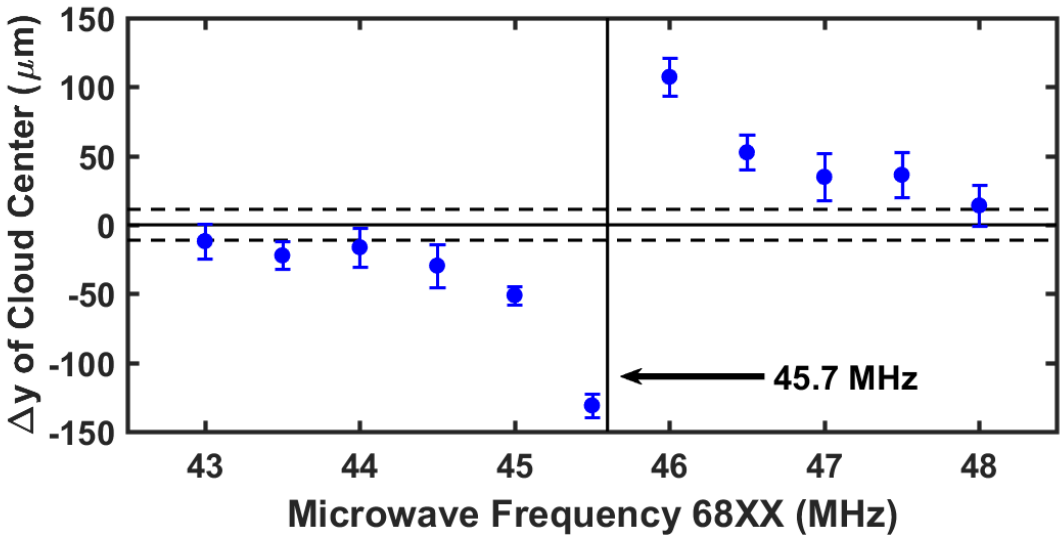

FIG. 6.3: First push/pull with AC Zeeman force. The y center of the cloud was measured by fitting to a Gaussian and compared to the y center of a control without microwaves. Each point is an average of 5 measurements and the error bars represent the standard deviation of the 5 measurements. The horizontal dashed lines represent the standard deviation in measuring the control y center. The atomic resonance occurs at approximately 6845.7 MHz.

6.1.2 Initial Analysis

While the first measurement of the the ACZ force was a qualitative success, it had some major issues that needed to be addressed. One of these issues was that the cloud splits into two when the force was applied on resonance, $\delta_{exp} = 0$. This scenario simultaneously produced the high-field seeking state $|-\rangle$, which was

pulled up toward the chip and the low-field seeking state $|+\rangle$, which was pushed down away from the chip, as shown in figure 6.4. It turns out that this is exactly what should happen. Figure 3.5 shows that, for an applied field on resonance with $\delta_{exp} = 0$, the $|e, N-1\rangle$ state is an equal superposition of $|-\rangle$ and $|+\rangle$ states. The atom cloud, initialized in $|e, N-1\rangle$, is split equally into the $|-\rangle$ and $|+\rangle$ states when the microwave field is applied on resonance. The imaging light is targeted

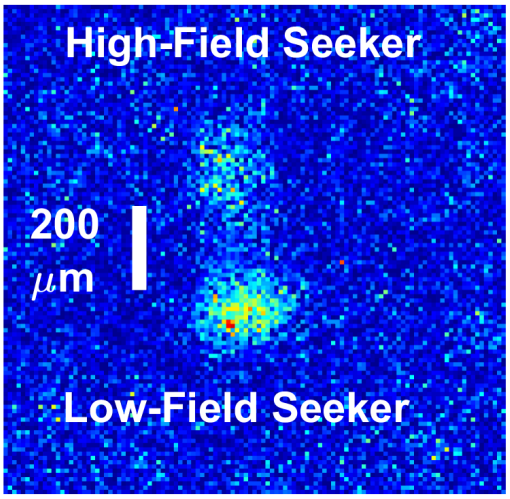

FIG. 6.4: On-resonance ACZ force. Applying a microwave field on resonance splits the atom cloud into a high-field seeking state that gets pulled towards the chip and a low-field seeking state that gets pushed away from the chip. There is 1 ms wait time between the turn-off and a 0.5 ms microwave pulse at a maximum power of 3.3W, followed by 12 ms time-of-flight before absorption imaging.

to image only the $|e\rangle$=$|F = 2, m_F = +2\rangle$ state, so there is a factor of 2 less in the imaging signal, leaving each cloud with only 1/4 of the original signal with no microwaves. This is why the clouds in figure 6.4 look faint compared to those in 6.2. This cloud splitting can be eliminated by performing an Adiabatic Rapid Passage (ARP), introduced in section 3.1.3, to maintain the atom cloud in only one of the $|\pm\rangle$ states. This ARP sweep is performed by turning on the microwave field sufficiently off resonance ($|\delta_0| \gg |\Omega|$) and rapidly sweeping the microwave frequency to the desired experimental detuning δ_{exp}, thus keeping the atoms in a single eigenstate.

The second major issue was that the maximum measured force in the initial

measurements (figure 6.3) was weaker than gravity. The applied ACZ force was extracted by using Newton's Third Law that states that the force F is the time derivative of momentum, p.

$$F = \frac{dp}{dt} = \frac{m\Delta v}{t_{pulse}} = \frac{m\Delta y}{(tof)t_{pulse}} \tag{6.2}$$

Here the Δv is the change in velocity of the atom cloud, m is mass of a ^{87}Rb atom, t_{pulse} is the microwave pulse duration, tof is the time of flight, and Δy is the change in y center of the cloud. The maximum force applied in figure 6.3 was for a microwave frequency of 6845.5 MHz, which resulted in a $\Delta y = -131$ μm and a force of $F = -0.74$ mg where g is the acceleration due to gravity.

There are two convenient assumptions that are needed when using Equation 6.2 to calculate the $F = F_{ACZ}$. The first assumption is that the atom cloud experiences a constant force, or rather that it does not move much, during the microwave pulse time. We can calculate the distance that the atom cloud moves, y_p, during the $t_{pulse} = 2$ ms microwave pulse application time, using simple kinematics equations:

$$y_p = v_0 t_{pulse} + \frac{1}{2} a t_{pulse}^2 \tag{6.3}$$

Here $a = g + F_{ACZ}/m$ is the acceleration that atoms with mass m experience. The initial velocity v_0 can be calculated by: $v_0 = g t_{wait}$ where $t_{wait} = 3$ ms is the wait time between the turn-off of the DC magnetic trap and turn-on of the microwave pulse. Plugging in all of the values gives a cloud movement during the microwave pulse of Δy= 93 (64) μm for the red (blue)-detuned cases that add to (subtract from) gravity. The atoms start at a distance $d \approx 90$ μm from the chip. Assuming a scaling of $\Omega \propto 1/d$, and $F_{ACZ} \propto \frac{1}{d^2}$ for $\delta = 0$, this leads to a change in the on-resonance force by a factor of 2 during the pulse time for the red-detuned case.

Experiments performed after we gained this knowledge started with atoms at rest and had a shorter microwave pulse time to mitigate the movement of the atoms during the microwave pulse.

The second assumption in Equation 6.2 is that the F_{ACZ} is constant over the cloud size, or that the cloud is small compared to the spatial variation of the microwave field. The shape of the cloud after the force is applied can be used as a diagnostic tool to test this assumption; if the assumption is valid, then the atom cloud will have the same shape with and without a microwave pulse. Figure 6.2 shows that this assumption is not valid: the 'blue-detuned' case on the left shows a vertically elongated cloud, while the 'red-detuned' case on the right shows a vertically squished cloud, compared to the cloud in the middle taken without a microwave pulse.

This change in cloud shape is most likely due to the strength of the microwave field varying over the size of the atom cloud. The closer the atoms are to the chip wire carrying the microwave current, the larger the Rabi frequency and the larger the Rabi frequency gradient, which leads to a larger force. This spatially varying force then leads to the misshapen cloud. The cloud size (Gaussian radius) is calculated to start at 2 μm when the atoms are first released and then grows to 15 μm when the microwave are turned on, 3 ms after the trap is turned off. Using equation 6.1 and assuming $\Omega \propto 1/r$, this finite atom cloud size leads to a force change of $\pm 20\%$ for atoms that are ± 1 Gaussian width away from the center of the cloud.

6.1.3 Time-of-flight Frequency Scans

One of the experimental parameters that we tried, unsuccessfully, to change is the time between releasing the atoms from the DC chip trap and turning on the microwave field. Ideally, this time should be as short as possible to increase the

Rabi frequency experienced by the atoms. A short wait time also limits the initial velocity of the atoms, as well as the initial size of the cloud. It turns out that the 3 ms we guessed at for the initial experiment was the best value for this parameter. For shorter wait times, a spurious magnetic field (probably due to residual eddy currents formed from quickly turning off the DC chip trap) has not died out yet. This spurious, but short lived, magnetic field creates a cascade of issues in our experiment, starting with a transient B_{DC} which changes the resonant microwave frequency, causing the δ_{exp} to change during the first 3 ms after turn-off of the chip trap. This changing δ_{exp} in turn would cause a time-varying ACZ force.

The method used to diagnose this problem was to measure the $|2,2\rangle \leftrightarrow |1,1\rangle$ microwave resonance at various times of flight (tof) between the turnoff of the DC chip trap and the application of a short microwave pulse at a set frequency. As described in section 3.2.1, the atoms will Rabi flop back and forth between $|2,2\rangle$ and $|1,1\rangle$ centered about a value determined by the detuning from the atomic resonance. In our system, the amplitude of the Rabi flopping quickly decays to the central value. This is most likely due to the finite size of the cloud in the trap so that there are many different Rabi frequencies sampled that quickly dephase to the atomic population value that we measure. By measuring this population as a function of microwave frequency we can map out the atomic resonance. These data were taken with an experimental sequence of: T ms tof $\rightarrow$ 0.5 ms microwave pulse at variable frequency $\rightarrow$ (13-T) ms tof $\rightarrow$ absorption image. The microwave pulse was done at a power of 250 mW to balance between quickly Rabi flopping the atoms and limiting the ACZ force. Figure 6.5 shows plots of the total atom number in the $|2,2\rangle$ state as a function of microwave frequency for various times of flight. We started at $T =$ 1 ms and continued to increase T until the center and width of the plot stopped changing, using this as a signal that the spurious magnetic fields have died down. We see that at $T = 3$ ms tof the center has settled at approximately 6845.5 MHz.

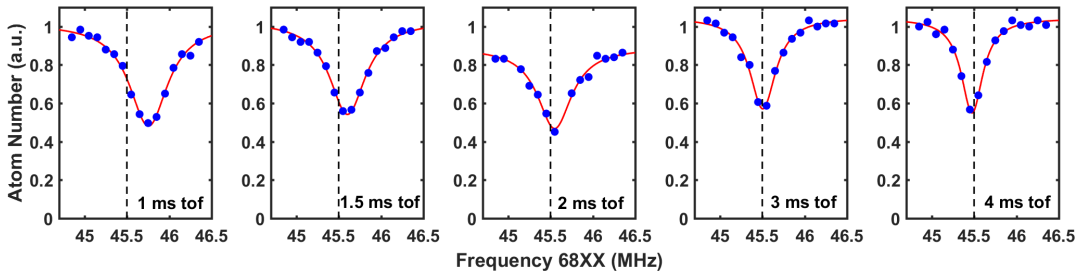

FIG. 6.5: Time-of-flight frequency scans. The plots are relative $|2,2\rangle$ atom number vs. microwave frequency at time of flight values (T) ranging from 1 ms to 4 ms. The reference line is at 6845.5 MHz, roughly the resonance value for 3 and 4 ms time of flight after the spurious magnetic fields have died down.

We lucked out in our first test with T = 3 ms, as having gone any faster and we would have run into the spurious magnetic fields.

6.1.4 Second Try - Push Pull with ARP

We used an 0.1 ms ARP sweep from an initial detuning of $\delta_0 = \pm 6$MHz to constrain the atoms to one of the $|\mp\rangle$ states in our second attempt at measuring the ACZ force. This experiment was made at a full microwave power of 3.3 W. This enabled us to maximize the force by operating on resonance, $\delta_{exp} = 0$ MHz, without sacrificing out atomic cloud imaging signal. Figure 6.6 shows the results of this second try by applying the ACZ force on resonance. At this point we had not figured out that it was important to limit the microwave pulse duration to maintain a constant ACZ force, and so t_{pulse} was left at 2 ms. The long t_{pulse} caused the misshapen cloud in figure 6.6, because the atoms sampled a large change in the ACZ force depending on where they were in the cloud. The measured ACZ force for the data in figure 6.6 only increased to $F_{ACZ} \approx 0.87\ mg$ (using equation 6.2 with the measured Δy).

On this attempt, we hit the limits of the apparatus: the ACZ force was limited by the 44 μm that the atoms fall during the 3 ms it takes for the eddy currents to

die down. On resonance, the ACZ force scales like

$$F_{ACZ} \propto \frac{d\Omega}{dr} \propto \frac{1}{r^2} \tag{6.4}$$

where Ω is the Rabi frequency and r is the distance between the atoms and the chip wire. This scaling assumes that the $|B_{AC}|$ generated by the chip wire follows a $1/r$ dependence. Increasing r from 90 μm to 90 μm+44 μm= 134 μm decreases the ACZ force by a factor of 2.2. In order to get the atoms to experience a force

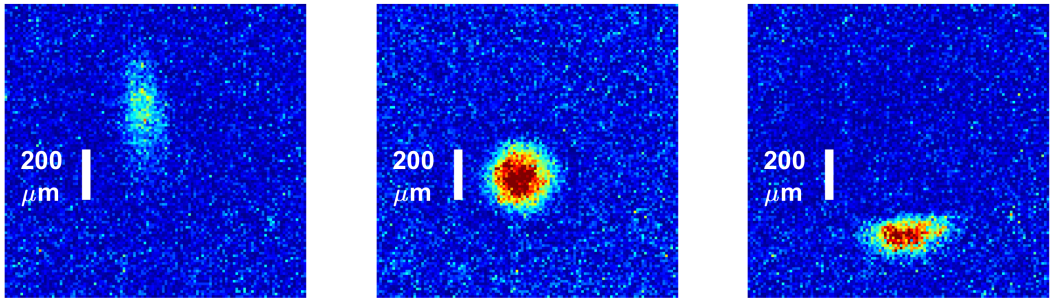

FIG. 6.6: False color absorbtion images of the second attempt at pushing and pulling atoms using the ACZ force. From left to right: $\delta_0 = +2.5$ MHz, control without microwaves, and $\delta_0 = -2.5$ MHz. Both microwave pulses started with a 0.1 ms ARP sweep from δ_0 to $\delta_{exp} = 0$ MHz and were 2 ms long. The initial tof before the ARP sweep was 3 ms after doing the fast turn-off of the DC chip trap. There was then a 9.9 ms time-of-flight after the microwave pulse.

stronger than gravity they need to be closer to the chip wire than 144 μm. For that to happen we need to shorten the wait time between turning off the trap and applying the microwave pulse. This is not possible with the DC chip trap because of the spurious magnetic field issues discussed in section 6.1.3. The only option left is to invest the time in positioning an ODT as close as possible to the chip U-wire so that we can get around the eddy current problem. It is not possible to shift the DC magnetic trap closer to the U-wire because the force from the vertical DC magnetic field gradient is not sufficient to cancel gravity.

6.2 Successful Approach: Time-of-flight with ODT at Chip

The solution to the aforementioned issues with releasing atoms from the DC chip trap was to install a $\lambda = 1064$ nm optical dipole trap (ODT) as close to the atom chip as possible. This crossed ODT is described in detail in chapter 5. The main advantage of this change in trap is that rapidly turning off an ODT does not create any spurious magnetic fields; the microwave pulse can be applied immediately after the ODT turnoff. This allows the atoms to experience the ACZ force closer to the U-wire, with zero initial velocity, and without any time to expand in size. In addition, the ODT creates the same potential energy for each hyperfine spin state within the $5S_{1/2}$ ground levels of ^{87}Rb, allowing for the spin-dependent force measurements in section 6.3.

This section starts with a brief description of the experimental setup and ODT loading procedure in subsection 6.2.1. More details on this setup can be found in chapter 5. Subsection 6.2.2 contains the main ACZ force measurement for this chapter. Subsection 6.2.3 describes the methods used for the *ab-initio* theoretical predictions of the ACZ force. This is followed by a discussion on experimental complications in subsection 6.2.4. The section concludes with a demonstration of the spin-dependence of the ACZ force in subsection 6.3.

6.2.1 ODT Experimental Setup and Loading Procedure

Figure 6.7 shows the experimental set up for the ODT at the chip. Similar to figure 6.1, figure 6.7 is mostly not to scale, but the two optical beam waists are on the same scale. The radial beam shown in the center has a $w_0 = 60$ μm waist radius at the focus, optical power of $P = 1.2$ W, and is directed along $\hat{z}$. The radial beam is

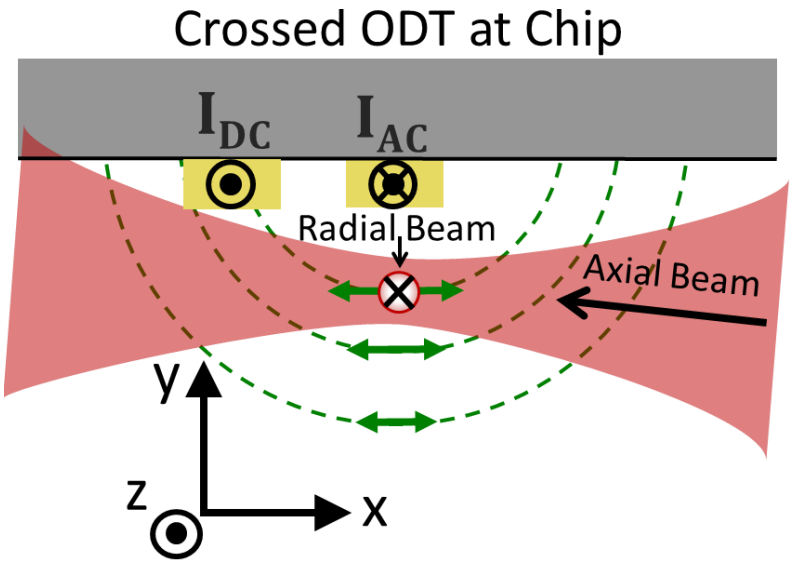

FIG. 6.7: Crossed ODT under the atom chip. The 1064nm beams attract the atoms to the region with the highest-intensity, the focus. The radial beam has a 60 μm waist radius beam and goes into of the page. The axial beam propagates from left to right and has a waist radius of $w_0 = 120$ μm and is angled 'up' to prevent clipping before reaching the atoms.

positioned approximately $d \simeq 100$ μm below the U-wire containing I_{AC}. The atom chip measures 2 cm along $\hat{z}$ and 3 cm along $\hat{x}$. The radial beam is angled slightly up along $\hat{y}$ to prevent it from being clipped by the chip surface before reaching the atoms. The gold rectangles in figure 6.7 show the Z-wire that provides the DC chip trap potential and the U-wire containing the AC microwave current. The green dashed lines represent the resulting B_{AC}. The green arrows represent the direction of $\vec{B}_{AC}$ directly beneath the U-wire.

With only the radial beam, the confining force along the beam ($\hat{z}$) is very weak and the atoms spread out from a initial size of ≈200 μm to 2 mm, the size of the axial camera screen of over the course of ≈100 ms. To combat this issue, we add another laser, the axial beam to provide confinement along $\hat{z}$. This axial beam has a waist radius $w_0 = 120$ μm, optical power $P = 0.8$ W and is directed primarily along $\hat{x}$. The axial beam has to be tilted 'up' along $-\hat{y}$ so that it does not get clipped before reaching the atom cloud. After reaching the atom cloud, most of the beam

is blocked by the chip and cannot be imaged. Upon adding this beam, the atoms were confined to the overlap region in the ODT. We measure a lifetime in this trap configuration of $\tau = 9$ seconds, see figure 7.10(d).

The ODT loading procedure starts with the normal chip loading and evaporation procedure described in section 4.5. Depending on the desired experimental parameters, the chip evaporation path can be can be stopped earlier or later to provide a hotter cloud with more atoms or a colder cloud with fewer atoms. Two common stopping points are 'RF6' and 'RF8'. 'RF6' stops at an RF knife value of 3.44 MHz and loads N $\approx 1.5 \times 10^5$ atoms with a temperature of T $\approx$ 370nK in the ODT. 'RF8' stops at an RF knife value of 3.385 MHz which loads N $\approx 5 \times 10^4$ atoms with a temperature of T $\approx$ 150nK in the ODT. The atoms loaded from the DC chip trap are mostly spin-polarized in the $|F = 2, m_F = +2\rangle$ state. A small fraction of atoms are in the $|2, 1\rangle$ state, and are selectively removed from the chip trap with a low power (P = 250 mW) microwave 'clean sweep' that targets the $|2, 1\rangle \leftrightarrow |1, 0\rangle$ transition.

Once the atoms are evaporatively cooled to the desired level, the ODT is turned on with a radial beam power of $P \approx 550$ mW. This low power ODT only hold atoms against gravity where the radial and axial beams intersect. The DC chip trap is then adiabatically moved from under the Z-wire to under the U-wire, where it is co-located with the ODT. Then, the currents driving the DC chip trap are simultaneously ramped down in 50 ms to finish the hand-off from DC chip trap to ODT. Once the atoms are loaded into only the 'crossed' region of the ODT, the radial beam power is then ramped up over 200 ms to a maximum optical power of 1.2 W to create a trap with trap frequencies $\omega_{(x,y,z)} = (2\pi)(172, 178, 28)$ Hz and a calculated trap depth of 23 μK.

6.2.2 ODT-based ACZ Force Measurement

We chose to load from 'RF8' for a colder cloud with less atoms for the time of flight ACZ force measurements: the atom number is N $\approx 5 \times 10^4$, and the temperature is T $\approx$ 150nK. The value of $B_{DC} = 5.1$ G is constant throughout the experiment. The experimental sequence starts by loading atoms into the ODT, followed by a short hold time in the ODT of 25 ms to allow imaging shutters to open. Next, the ODT laser power is turned off with the digital and analog control for both AOMs, and the ODT laser shutter is closed. Immediately after the ODT turnoff, the microwaves were turned on at full power, $P = 3.3$ W, targeting the $|2,2\rangle \leftrightarrow |1,1\rangle$ transition: first, a $t_{ARP} = 0.1$ ms ARP sweep is applied from $\delta_0 = \pm 13$ MHz to a variable detuning δ_{exp}, to keep the atoms in the $|\mp\rangle$ eigenstate: second, the microwaves are left on for a duration of $t_{pulse} = 0.5$ ms at δ_{exp} to impart a velocity impulse to the atoms. After the t_{pulse} time the microwave power is turned off and there is a time of flight of $tof = 12.25$ ms before absorption imaging targeting the $|2,2\rangle$ state.

The data in figure 6.8 show representative false color images taken during the force measurement experiment. The two images on the left show images taken without microwaves, as a control. The white box in the left-most image represents the zoom-in region used for the other four images. The three images on the right show the results of applying a 0.5 ms microwave pulse on-resonance, i.e. with $\delta_{exp} = 0$ MHz. The middle image shows the result of applying the microwave pulse without the ARP sweep: the cloud is split into two; the $|+\rangle$ state gets pushed down and the $|-\rangle$ state gets pulled up. The two 'Push(Pull)' images on the right have a 0.1 ms ARP sweep, at full microwave power $P = 3.3$ W, from an initial detuning of $\delta_0 = -(+)13$ MHz before the application of the 0.5 ms microwave pulse. In the two right-most images all of the atoms are either pushed down or pulled up. Each

image is the result of averaging five separate images.

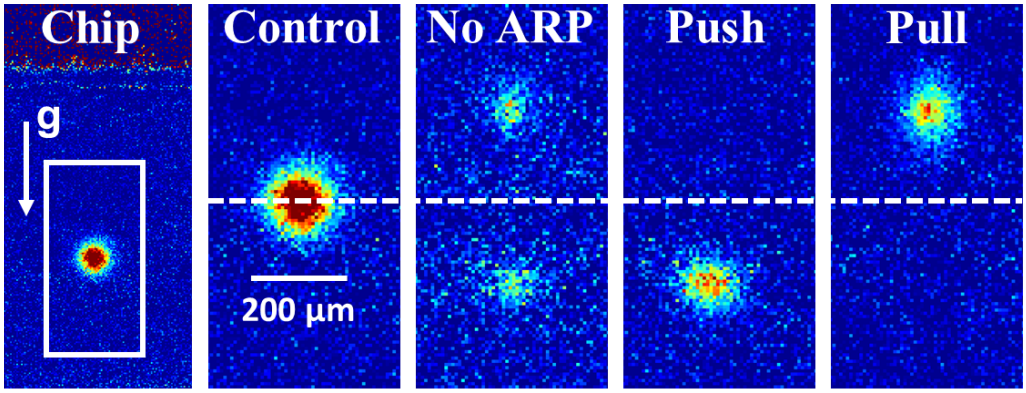

FIG. 6.8: False color images of ACZ force measurements. The images are the result of applying a 0.5 ms microwave pulse to atoms immediately after release from an ODT. The image on the left shows gravity directed down away from the chip (top of the image). The white rectangle shows the zoom-in region for the the 4 images on the right, which share the same scale bar. The data are the result of averaging 5 separate images.

The force measurement experiments shown in figure 6.8 were repeated at different values of δ_{exp} to map out the ACZ force as a function of detuning. Figure 6.9 summarizes these measurements and analysis, and is the main results of this thesis. Figure 6.9(a) shows the results of fitting the center of the clouds as a function of microwave detuning δ_{exp}. The points shown are the average of five separate data sets and the error bars represent the standard deviation of the mean. The black squares represent data taken without an ARP sweep. In this case the cloud splits into a low-field seeking state $|+\rangle$ and a high-field seeking state $|-\rangle$. When the field is tuned far off-resonance, only one of these states is visible. When the field is tuned close to resonance, both states are visible and can be fit independently. The red(blue) triangles represent data taken with the ARP sweeps to keep all of the atoms in the $|+\rangle(|-\rangle)$ states. The three open triangles near resonance have low atom number, and so the five images were averaged together before fitting. The two black lines are *ab-initio* theoretical prediction of the ACZ-induced change in position, Δy, including the contribution from the ARP sweep, based on the measured Rabi frequency and Rabi frequency gradient. The shading represents a 1σ confidence interval on the

predictions. The right-hand y-axis plots the ACZ force from the measured Δy using equation 6.2. This is exact for the 'no ARP' case (black squares) and approximately correct for the 'with ARP' cases (red and blue triangles).

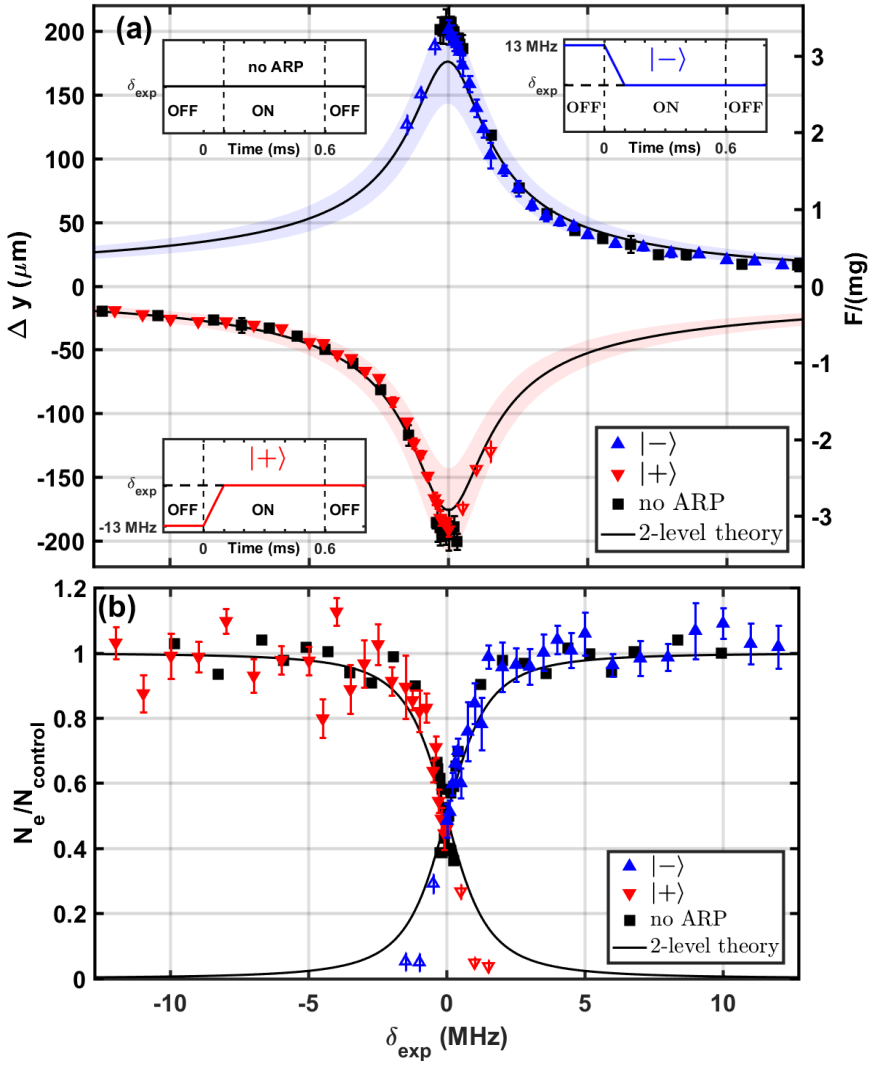

FIG. 6.9: AC Zeeman Force Measurements. (a) Atom cloud displacement Δy vs. microwave detuning δ_{exp}. The data include measurements with no ARP sweep (black squares) and with an ARP sweep initiated from $\delta_0 = \pm 13$MHz to constrain atoms in the$|\mp\rangle$ state (red and blue triangles). The right axis shows the ACZ force applied by a 'no ARP' microwave pulse; this axis is approximately correct for ARP sweep data. The black curves are *ab-initio* theory predictions with 1σ shading, not fits. Timing sequences for each case are shown as insets. (b) Measured atom number in $|e\rangle$ vs. δ_{exp} normalized to the average atom number without a microwave pulse. All data are taken with *tof*=12.25 ms and $B_{DC} = 5.1$ G. Data points are averages of 5 measurements. Error bars give the standard deviation of the mean. The data plotted with open triangles had low atom numbers and were analyzed differently by averaging the five images and then performing fits.

The ARP sweep imparts to the atom cloud a small velocity impulse whose contribution to the total $\Delta y \propto \Delta v$ varies from 20% for $\delta_{exp} = \delta_0 = \pm 13$ MHz to 5% for $\delta_{exp} = 0$ MHz on resonance. The ARP sweep contribution, Δy_{ARP}, is simple to calculate for the case where the experimental detuning does not change from the initial detuning, $\delta_{exp} = \delta_0$. In this case the force is constant in time and the formula is given below.

$$\Delta y_{ARP} = \frac{F_{ACZ}(tof)t_{ARP}}{m} = \mp\frac{\hbar}{2}\frac{\Omega}{\Omega'_{exp}}\frac{d\Omega}{dr}\frac{(tof)t_{ARP}}{m} \tag{6.5}$$

Here $\Omega'_{exp} = \sqrt{\delta^2_{exp} + \Omega^2}$ is the generalized Rabi frequency using the experimental detuning δ_{exp}. Finding the Δy_{ARP} for the case when the detuning, and thus force, vary in time involves integrating the force over the application time. This case shown below in equation 6.6, but is only valid for $\delta_{exp} - \delta_0 \neq 0$

$$\Delta y_{ARP} = \frac{tof}{m}\int_0^{t_{pulse}} F_{ACZ}\, dt = \mp\frac{tof}{m}\frac{\hbar}{2}\Omega\frac{d\Omega}{dr}\frac{t_{ARP}}{\delta_{exp} - \delta_0}\ln(\frac{\delta_{exp} + \Omega'_{exp}}{\delta_0 + \Omega'_0}) \tag{6.6}$$

Here $\Omega'_0 = \sqrt{\delta^2_0 + \Omega^2}$ is the generalized Rabi frequency using the initial detuning $\delta_0 = \pm 13$ MHz.

The experimental data for the ACZ force measurement in figure 6.9(a) agree with the *ab-initio* theoretical predictions to within the error bars for all values of δ_{exp}. However, we do observe a systematic deviation from the theory prediction: off resonance, $\delta_{exp} > 2$ MHz, the measured force for the $|+\rangle$ state undershoots the theoretical prediction; near resonance, $|\delta_{exp}| > 2$ MHz, both states overshoot the prediction.

In addition to measuring the ACZ force, the experimental data taken to produce figure 6.9(a) can also give information about the eigenstates of the system. Figure 6.9(b) plots the relative population in the excited state as a function of the detuning,

δ_{exp}. The measured atom number was normalized to control data taken without a microwave pulse. The black lines are *ab-initio* theoretical predictions based on the measured Rabi frequency. The expected relative population in the excited state $|e\rangle$ is given by equation 3.15, repeated here,

$$|\langle e, N-1|\pm\rangle|^2 = \frac{1}{2}(1 \mp \frac{\delta_{exp}}{\Omega'_{exp}}) \tag{6.7}$$

Most of the data in figure 6.9(b) match well with the theory lines in black. However, the three pairs of points with open triangles farthest past resonance for both red and blue detuning are lower than predicted. The signal-to-noise ratio is quite low for these points; 5 different images had to be averaged together to get a measurable signal. This drop in signal-to-noise makes it difficult to get a reliable measurement of their relative population.

6.2.3 Theoretical Predictions

The theoretical prediction for the ACZ force in one dimension was made by independently measuring the Rabi frequency Ω and the spatial derivative of the Rabi frequency $d\Omega/dr$. The ACZ force in one dimension is then given by equation 3.10 for the, $|\pm\rangle$ states, repeated here,

$$F_{ACZ} = \mp\frac{\hbar}{2}\frac{\Omega}{\sqrt{\delta^2+\Omega^2}}\frac{d\Omega}{dr} \tag{6.8}$$

The first step towards an accurate theoretical prediction of F_{ACZ} was to make an accurate measurement of the resonance frequency of the targeted transition. The resonant frequency of the $|2,2\rangle \leftrightarrow |1,1\rangle$ transition for atoms held in the ODT with $B_{DC} = 5.1$ G was measured to be 6845.434 MHz $\pm$ 0.003 MHz, as shown in figure 6.10. These data were taken by abruptly turning on the microwave field at low

power, $P = 20$ mW, at different δ_{exp} and letting the atoms Rabi flop for a time of 1 ms while held in the ODT. As discussed in section 6.1.3, the atom state population ratio quickly converges on a value dictated by the detuning from resonance. The populations of the two states $|g\rangle$=$|1,1\rangle$ and $|e\rangle$=$|2,2\rangle$ were measured separately to get a more accurate measurement of the atom population ratio, N_e/N_{total}. This was done by applying a brief DC magnetic gradient pulse, commonly called a 'Stern-Gerlach' (SG) pulse, to spatially separate the two spin states before imaging and is discussed in more detail in chapter 7, section 7.1.

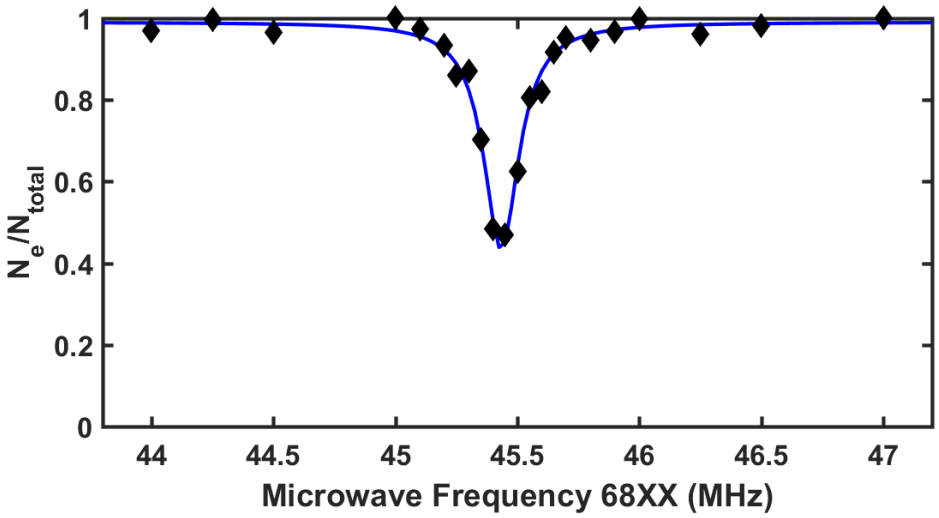

FIG. 6.10: Resonance plot for the $|2,2\rangle \leftrightarrow |1,1\rangle$ at $B_{DC} = 5.1$ G. This data was collected the same day as the 'no ARP' data in Figure 6.9. The data (black diamonds) were fit to: $\frac{N_e}{N_{total}} = A - \frac{D}{\pi}\frac{\frac{1}{2}\Gamma}{(f-f_0)^2+(\frac{1}{2}\Gamma)^2}$ (blue line) where f is the applied microwave frequency. The fit gives a center position $f_0 = 6845.434 \pm 0.003$ MHz and a width of $\Gamma = 0.174 \pm 0.010$ MHz.

Next, the Rabi frequency Ω was measured. This measurement was done by abruptly turning on the microwave field at the newly measured resonant frequency at low power ($P = 20$ mW) to atoms initialized in $|e\rangle = |2,2\rangle$ in the ODT. The microwaves are left on for a variable amount of time during which the atoms Rabi flop between states $|e\rangle$ and $|g\rangle$ as described in section 3.2.1. After this flop time, the atoms are released from the ODT and a DC Stern-Gerlach pulse is applied to measure both the $|e\rangle$ and $|g\rangle$ populations. Figure 6.11 shows the results of the

Rabi flopping measurements. The atoms start in $|e\rangle$ at t=0, then proceed to 'flop' back and forth between states with increased microwave time. The data points for each Rabi frequency measurement were randomized to limit the effects of apparatus drift. Each measurement was conducted twice as a way to test the reproducibility of the measurement. The Rabi frequency for the 'normal' ODT in figure 6.11(a) was measured to be $\Omega_N = (2\pi)123.9 \pm 0.6$ kHz, while the Rabi frequency for the 'sag' ODT (discussed below) in figure 6.11(b) was measured to be $\Omega_S = (2\pi)109.8 \pm 2.5$ kHz. Here the uncertainty was taken as the spread of the two measurements.

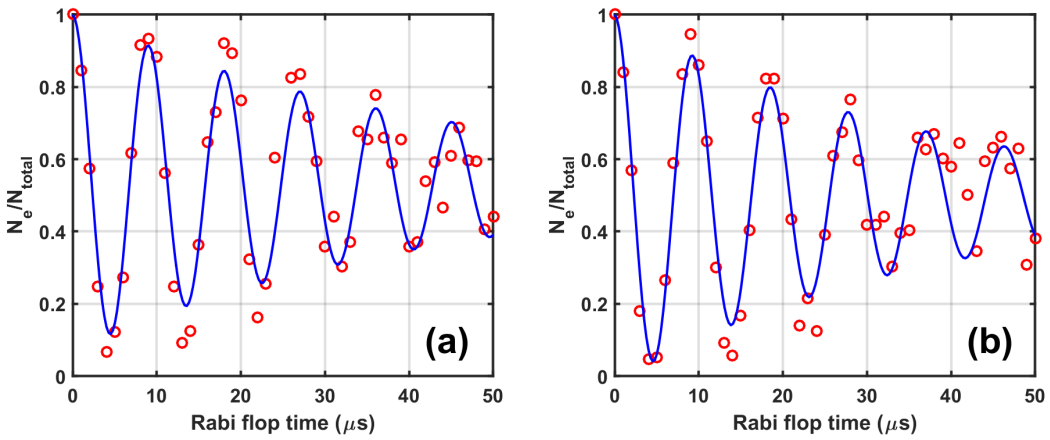

FIG. 6.11: Rabi flopping on the $|2,2\rangle \leftrightarrow |1,1\rangle$ transition at $B_{DC} = 5.1$ G (a) has atoms in the 'normal' ODT while (b) has atoms in the lower power 'sag' ODT (see figure 6.12) that is shifted down away from the chip due to gravity. This data was collected the same day as the 'no ARP' data in figure 6.9. The data (red circles) are fit to a cosine function with decaying amplitude (blue line): $\frac{N_e}{N_{total}}(t) = Ae^{-t/\tau}cos((2\pi f)t) + (1 - A)$. This function enforces $\frac{N_e}{N_{total}}(t = 0) = 1$.

The amplitude of the oscillations in figure 6.11 decay on a timescale of tens of μs. A possible explanation for this short decay time is that the atoms experience slightly different Rabi frequencies depending on their relative position. Over time the peaks and troughs of these different frequencies 'de-phase' and lower the oscillation amplitude. Previous attempts at Rabi flopping with atoms loaded from 'RF6' had a much faster decay time. These atoms were hotter and thus had a larger in-trap volume, potentially sampling a larger range of Rabi frequencies, and decaying faster.

The last piece of equation 6.8 needed to predict the ACZ force is the spatial derivative of the Rabi Frequency, $d\Omega/dr$. This was measured by moving the ODT a distance dr and re-measuring the Rabi frequency to get the resulting difference $d\Omega$. In order to reproducibly move the ODT, we decided to implement a 'sag' ODT by lowering the laser power. The weaker laser power leads to a downward shift of trap center due to the proportionally larger gravitational force on the atoms. The resulting shift was $dr = 11.36 \pm 0.83$ μm, as shown by the gray column in figure 6.12. The Rabi frequency measured in this 'sag' trap was $\Omega_S = (2\pi)109.8 \pm 2.5$ kHz (see figure 6.11(b)). This gives a change in Rabi frequency of $d\Omega = (2\pi)14.1 \pm 2.6$ kHz.

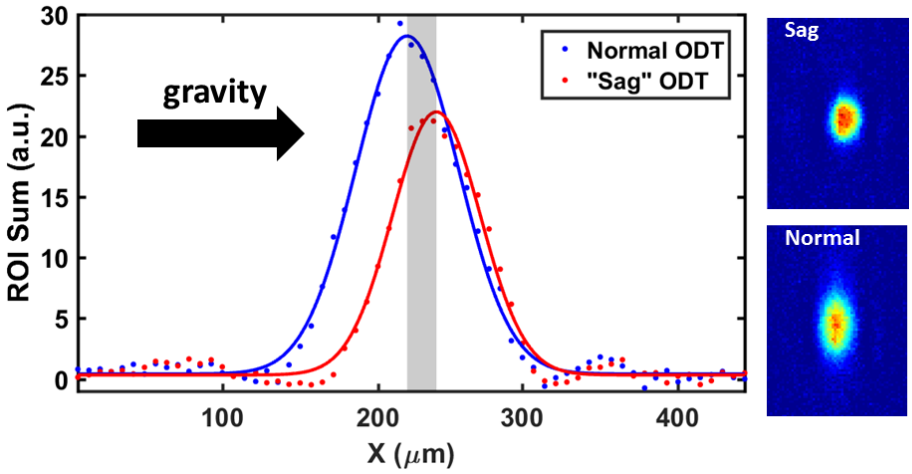

FIG. 6.12: 'Sag' ODT position measurement. Each measurement is an average of 20 images. There is a 1/3 atom loss in the 'sag ODT'. The measured change in cloud centers is $dr = 11.36 \pm 0.83$ μm (gray band). The time of flight for both cases was 4.25 ms to allow the atoms to fall out of a dark fringe in the absorption imaging beam. The false color images are on the right are for the 'sag' (top) and 'normal' (bottom) ODTs.

The measured values and their relative uncertainty used in predicting the ACZ force are compiled in table 6.1. The uncertainty in δ_{exp} is given by the linewidth of the microwave source and is negligible compared to the uncertainty in Ω_N, Ω_S, and $d\Omega$. The largest uncertainty, by far, comes from measuring the Rabi frequency in the 'sag' ODT, Ω_S, and its effect on the uncertainty in measuring the change in Rabi frequency $d\Omega$. The 2% uncertainty in measuring Ω_S turns into a 19% uncertainty

in measuring $d\Omega$ and dominates the uncertainty in the overall ACZ force prediction in figure 6.9(b).

Quantity	Measured Value	Relative Uncertainty
'Normal' Rabi Freq. Ω_N	$(2\pi)1.2626 \pm 0.0057$ MHz	4.5×10^{-3}
'Sag' Rabi Freq. Ω_S	$(2\pi)1.123 \pm 0.025$ MHz	2.2×10^{-2}
Rabi Freq. Diff. $d\Omega$	$(2\pi)0.139 \pm 0.026$ MHz	1.9×10^{-1}
Position Change dr	$11.81 \pm 0.47\mu$m	4.0×10^{-2}
$\Delta\Omega/\Delta r = d\Omega/dr$	$(2\pi)1.18 \pm 0.22 \times 10^{10}$ Hz/m	1.9×10^{-1}

TABLE 6.1: ACZ force error propagation. This table shows the measured value for each quantity that goes into the ACZ force prediction and its relative uncertainty. The error in the force is dominated by the error in $d\Omega$ which can be traced back to the error in the 'Sag' Rabi frequency.

By using the data in table 6.1 combined with equation 3.17 it is possible to extract the amplitude of microwave magnetic field as well as its spatial gradient. A measured Rabi frequency of $(2\pi)1.26$ MHz on the $|2,2\rangle \leftrightarrow |1,1\rangle$ transition gives a measured microwave magnetic field amplitude of

$$|B_-| = \frac{2\hbar}{\mu_B\sqrt{3}}\Omega = 1.04\,\mathrm{G} \tag{6.9}$$

. If we assume that the microwave field is polarized along $\hat{x}$, then this gives a microwave magnetic field with amplitude $|B_x| = 2|B_-| = 2.08$ G. If we further assume the thin-wire approximation and that the ODT is located a distance d= 100 μm from the microwave U-wire, then this microwave field is the result of an RMS current of $I = 0.037$ A. We can also use the measured Rabi frequency spatial gradient of $d\Omega/dr = (2\pi)1.18 \times 10^{10}$ to derive the spatial gradient of the microwave magnetic field amplitude.

$$|\frac{dB_x}{dr}| = 2\frac{|}{dB_-}dr| = 2\frac{2\hbar}{(\mu_B\sqrt{3})}\frac{d\Omega}{dr} = 1.95\ \frac{\mathrm{T}}{\mathrm{m}}195\ \frac{\mathrm{G}}{\mathrm{cm}} \tag{6.10}$$

We can use this value to test our earlier assumption of the atom-wire distance

the thin wire limit. Ampère's law to derive a microwave magnetic field amplitude gradient of $|dB_x/dr| = \mu_0 I/(2\pi r^2) = 209$ G/cm. This value is well within the $\pm 18\%$ uncertainty in the measurement of $d\Omega/dr$.

Data were taken to measure the ACZ force as a function of microwave power during the same experimental run as the data in figure 6.9. These data include measurements with an ARP sweep from $\delta_0 = -13$MHz to $\delta_{exp} = 0$ and $\delta_{exp} = -1$ MHz as well as data without an ARP sweep for $\delta_{exp} = -5$ MHz. These data are shown in figure 6.13. The left-hand axis plots the measured Δy as a function of the microwave power. The right-hand axis plots the measured force derived from the measured Δy from Equation 6.2. As discussed previously, this axis is exact for the 'no ARP' case and is approximately correct for the 'with ARP' cases. The shaded line plots the *ab-initio* theoretical prediction with 1σ uncertainty for the ACZ force ('no-ARP'). This prediction assumes $\Omega \propto \sqrt{P}$, where P is the power of the microwave field. The measured force tends to overshoot the prediction. At maximum power, the force increases as we get closer to resonance, $\delta_{exp} \to 0$, just as we see with the data in figure 6.9.

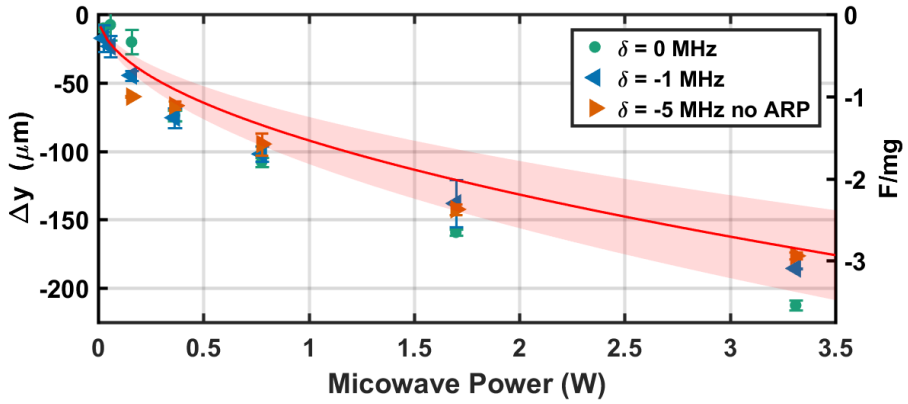

FIG. 6.13: Measured ACZ force vs. microwave power. The experimental procedure was the same as figure 6.9 for the red-detuned $|+\rangle$ case. The green circles and blue triangles had an ARP sweep, while the orange triangles did not have an ARP sweep. The off-resonant data were scaled by a factor $\sqrt{1+(\delta/\Omega)^2}$ with $\Omega = 1.263 \pm 6$MHz and $d\Omega/dr = (2\pi)1.18 \pm 0.22 \times 10^8$Hz/m. The theory line plots the expected Δy including the ARP pulse, similarly to the line in figure 6.9. The shaded region represents the uncertainty in the theory prediction.

6.2.4 Experimental Complications

The ACZ force produced a force along $\hat{x}$ in addition to that along the desired $\hat{y}$ direction. Careful attention was paid to properly locating the atoms directly underneath the microwave current U-wire. The positioning of the atoms can be verified and changed, if needed, by applying a large ACZ force and minimizing the change in x position, Δx, of the cloud. The horizontal force was much smaller, and the effects on the x-center of the atoms were only noticeable near resonance. We can use $\theta = \tan^{-1}(\Delta x/\Delta y)$ to find that the microwave force is off from the vertical by $\theta = \tan^{-1}(15\mu m/196\mu m) \approx 5°$. Here, Δx and Δy are the change in the center of the atom cloud for the on-resonance case in figure 6.9. Taking the $\cos(5°) = 0.9962$ we find that the force as measured only along $\hat{y}$ differs from the total force less than 0.4%.

In this iteration of the experiment, we sought to act on the atom cloud with a more constant force, as determined by the microwave field and field gradient. The microwave pulse started with the atoms at rest immediately after the ODT turnoff and was decreased in length from 2 ms to 0.5 ms. While it is infeasible to directly image the microwave field, a good metric for the 'constancy' of the applied force is the cloud size along the direction that the force is applied. If the force is constant and there is no microwave field curvature, then the entire cloud will experience the same force and the size will not change. If, however, there is microwave field curvature, then the atoms experience a different force depending on their position. In this case, the cloud size will change with the applied force. Figure 6.6(left and right) are good examples of atoms experiencing a microwave field curvature. It is more difficult to reliably tell by eye if the clouds changed shape in figure 6.9, so the Gaussian width from the fits was used as a quantitative measure. We chose to measure the widths of the clouds for the largest force at $\delta_{exp} = 0$ MHz. Without a

microwave pulse the cloud had a width of $\sigma_y = 47 \pm 4\mu$m. The cloud size for the push(pull) was $\sigma_y = 44 \pm 4(52 \pm 9)\mu$m. These data suggest that the red-detuned clouds that experienced a 'push' away from the chip were slightly squished, while the blue-detuned clouds that experienced a 'pull' were slightly elongated by ≈10%, much less than the first two iterations. To limit the microwave effects of the field curvature further, one could reduce the atom cloud size (i.e. temperature) or the microwave pulse time at the cost of lower signal-to-noise when measuring the resulting change in cloud center.

6.2.5 Fitting ACZ Force vs. Microwave Detuning

This subsection presents the process of fitting the measured change in cloud center vs. microwave detuning in figure 6.9 to determine if there is a different set of parameters for the Rabi frequency Ω and its spatial gradient $d\Omega/dr$ that better represent the measured data. The data in figure 6.9 show that the measured near-resonance ($|\delta_{exp}| < 1$ MHz) position change Δy is systematically above the *ab-initio* theory line shown in black. This shift occurs for both the data taken with an ARP sweep, shown in blue and red triangles for the $|-\rangle$ and $|+\rangle$ states, as well as for the data taken without an ARP sweep, shown in black squares. The data without the ARP sweep follows the same shape as that with the ARP sweep. The data taken farther off resonance is close to the prediction for the $|+\rangle$ state with $\delta_{exp} < -1$ MHz. However, the data taken for the $|-\rangle$ state with $\delta_{exp} > +1$ MHz is systematically under the prediction. This discrepancy motivates fitting these two data sets independently.

The data will be fit using contributions to the total position change of the center of the cloud (Δy) from the t_{ARP}= 0.1 ms ARP sweep (Δy_{ARP}) and from the t_{pulse}=

0.5 ms microwave pulse at constant frequency (Δy_{pulse}) as shown below:

$$\Delta y = \Delta y_{ARP} + \Delta y_{pulse} = (\Omega \frac{d\Omega}{dr})(\frac{tof}{m})(\frac{\hbar}{2})[\frac{t_{ARP}}{\delta_{exp} - \delta_0} \ln(\frac{\delta_{exp} + \Omega'_{exp}}{\delta_0 + \Omega'_0}) + \frac{t_{pulse}}{\Omega'_{exp}}] \quad (6.11)$$

In equation 6.11, $tof = 12.25$ ms is the time of flight, m is the mass of a ^{87}Rb atom, $\hbar$ is the reduced Planck's constant, $\delta_0 = \pm 12.45$ MHz is the initial microwave detuning of the ARP sweep for the $|\mp\rangle$ state, δ_{exp} is the experimental detuning, and the generalized Rabi frequencies are $\Omega'_0 = \sqrt{\delta_0^2 + \Omega^2}$ and $\Omega'_{exp} = \sqrt{\delta_{exp}^2 + \Omega^2}$.

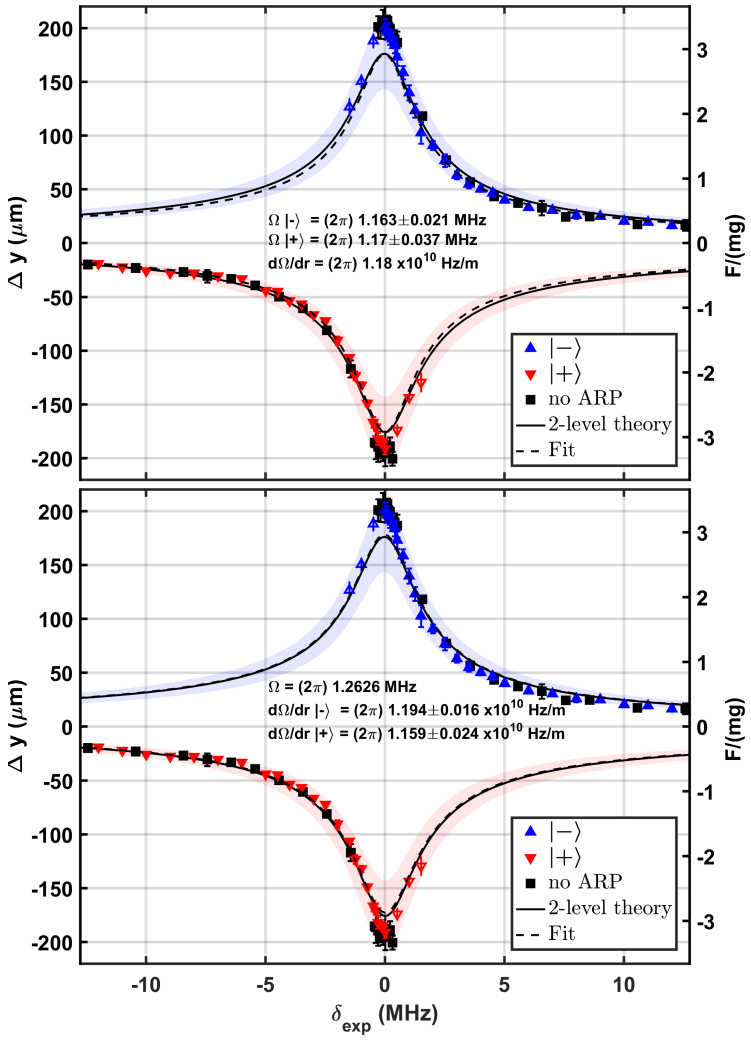

FIG. 6.14: Fit to ACZ force vs. detuning for one parameter. (top) Fit to Ω only. (bottom) Fit to $d\Omega/dr$ only. The fits are conducted for the $|+\rangle$ state (initial red-detuning) and for the $|-\rangle$ state (initial blue-detuning) data independently. The data are fit to equation 6.11.

The individual points are weighted by a factor w equal to the inverse of the variance of the point, $w = 1/\sigma^2$, where σ is the uncertainty in the measurement. The plotted error bars have length σ above and below the points. Figure 6.14 shows the results of fitting the data in figure 6.9 to either Ω or $d\Omega/dr$, using the data in table 6.1 to define the non-fitted parameter. Fitting to only one parameter in figure 6.14 does not lead to much change in the shape of the fitted curve (dashed line) from the *ab-initio* predictions (solid line). The fitted Rabi frequencies Ω (top of figure 6.14) and Rabi frequency spatial gradients $d\Omega/dr$ (bottom of figure 6.14) differ by only a few percent from the values in table 6.1 and do not address the overshoot near-resonance or the undershoot off-resonance for the $|-\rangle$ state.

If both Ω or $d\Omega/dr$ are used as free parameters, as shown in figure 6.15, then the fits match the measured data much more closely. The fitted values vary from

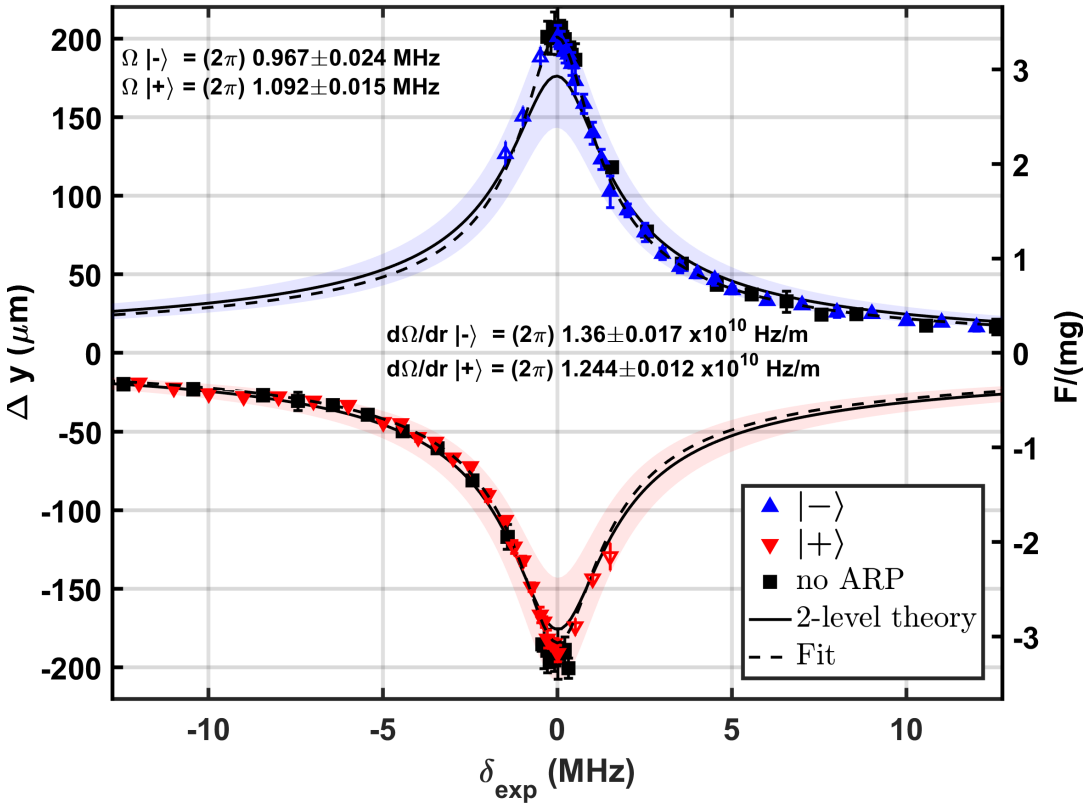

FIG. 6.15: Fit to ACZ force vs. detuning for the two parameters, Ω and $d\Omega/dr$. The fits are conducted for the $|+\rangle$ state (initial red-detuning) and for the $|-\rangle$ state (initial blue-detuning) data independently. The data are fit to equation 6.11.

the independently measured values by more than 10%, and are different between the $|+\rangle$ and $|-\rangle$ states. The two parameter fit is much closer to the data points near-resonance than either the *ab-initio* theory or the one parameter fits in figure 6.14. In addition, the two parameter fit for the $|-\rangle$ state does a better job at matching the 'undershoot' of the off-resonance data.

The fitted values in figure 6.15 change from the independently measured values in table 6.1 in the same direction for both of the $|\pm\rangle$ states. The fitted Ω is smaller, and the $d\Omega/dr$ larger, than the independent measurements. Reconciling the fitted values takes changing at least two of the previous measurements. If the measured 'Normal' Rabi frequency is decreased to match the fit, then the value of $d\Omega/dr$ will decrease. The 'Sag' Rabi frequency will have to be lowered, and more than the 'Normal', or the position change dr will have to be lowered to account for the increase in the fitted value of $d\Omega/dr$. A close look at the data for the 'Sag' ROI Sum, red points in figure 6.12, suggests that the center of the 'Sag' ODT may be closer to the 'Normal' ODT, leading to a smaller dr than was reported. Changing the value of dr by as little as 1.1 μm would cause a 10% change in its value.

The fitted values in figure 6.15 differ for the $|+\rangle$ and $|-\rangle$ states. The fit for the $|-\rangle$ state has a larger $d\Omega/dr$, but a smaller Ω than that for the $|+\rangle$ state. This conflicts with the assumption that the Rabi frequency is monotonic. Using the approximation of a single thin-wire in the near-field limit where the AC magnetic field strength follows the DC magnetic field strength as $B_{AC} \approx B_{DC}\,(\mathrm{e}^{i\omega_{AC}t})$, we expect the AC magnetic field strength to be inversely proportional to the distance from the wire r by $B_{AC} \propto 1/r$. Since the Rabi frequency is proportional to the AC magnetic field strength we expect $\Omega \propto 1/r$ and $d\Omega/dr \propto 1/r^2$, leading to a monotonic decrease in both with increasing r. The $|-\rangle$ state gets pulled closer to the chip wire by the ACZ force so if there were a change in Rabi frequency between the two, then we would expect the $|-\rangle$ state to experience a larger Ω and a larger

$d\Omega/dr$. We instead see a smaller Ω and a larger $d\Omega/dr$, which suggests that the AC magnetic field strength is not monotonic. This could be due to capacitive or inductive coupling between the targeted wire and adjacent wires, which are on the order of 100 μm away.

6.2.6 ACZ Force Measurement at 39 G

An ACZ force measurement was conducted at a DC magnetic field value of B_{DC} = 39 G in addition to the previously discussed measurement at B_{DC} = 5 G from section 6.2.2. These data are shown in figure 6.16. This measurement used the same

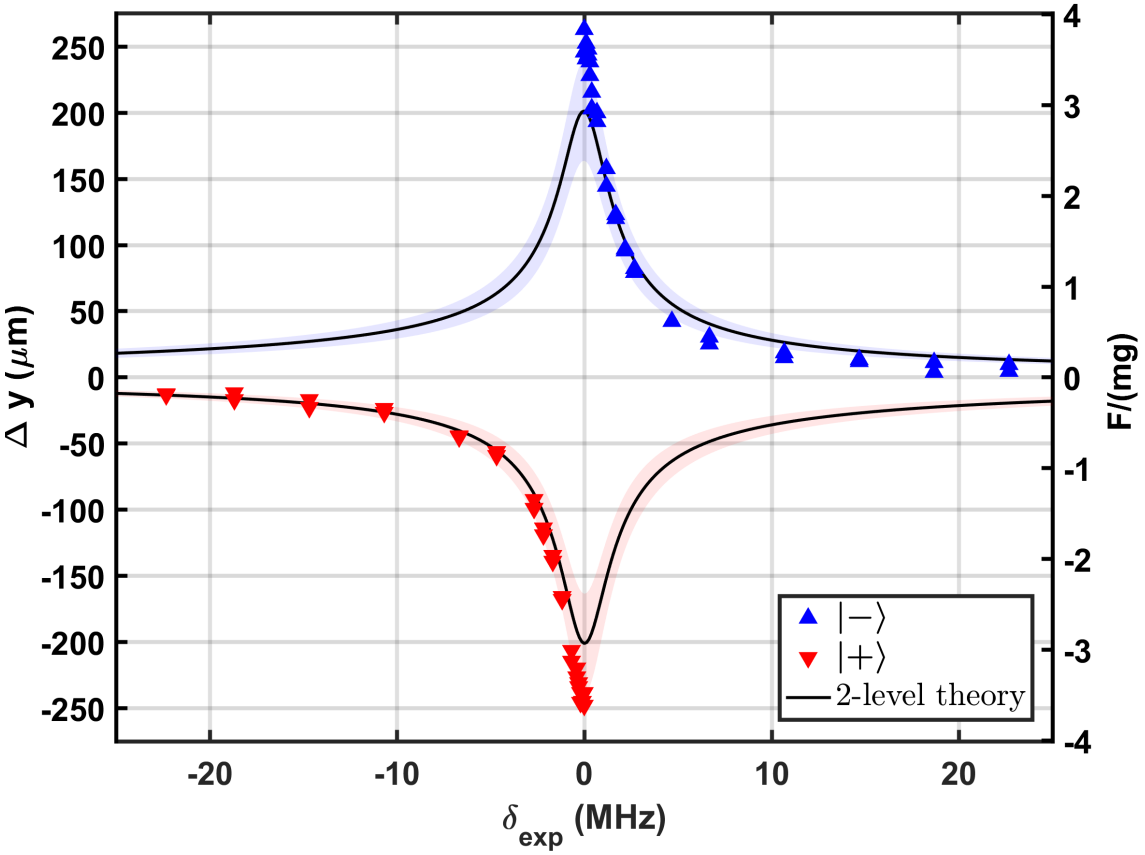

FIG. 6.16: ACZ Force vs. Detuning with B_{DC} = 39 G. The experimental sequence was similar to that for the data in figure 6.9. Here, the time of flight is 14 ms and the ARP sweeps start from $\delta_0 = \pm$ 23 MHz. Note the change in x- and y-axis scaling between this figure and 6.9. This data was taken on 28 Oct, 2015, months before the data taken on 03 and 05 Feb 2016 in figure 6.9.

experimental method previously described in section 6.2.2, with two differences. The first difference is that the time of flight between the microwave pulse and imaging here is 14 ms instead of the 12.25 ms used in the previous section. The second difference is that these measurements were taken with initial detunings for the ARP sweep of $\delta_0 = \pm 23$ MHz for the $|\mp\rangle$ states instead of $\delta_0 = \pm 13$ MHz.

The data collection for this measurement was not taken as rigorously as in section 6.2.2. There were only two data points collected for each detuning and the scatter is plotted instead of the mean with error bars. There was no measurement taken without an ARP sweep. There was also no independent measurement of Ω or $d\Omega/dr$ to make an accurate comparison with theoretical predictions. We can, however, make an educated guess that the Ω and $d\Omega/dr$ were similar to those in table 6.1 and use these values as a way to compare the measured force between the two data sets. The black line and shaded regions in figure 6.16 plot the *ab-initio* theoretical predictions for the change in cloud center Δy as a function of microwave detuning based on the measured data in table 6.1.

The measured data for Δy in figure 6.16 exhibit the same general behavior where it overshoots the expected value for the near-resonance case ($|\delta_{exp}| < 1$ MHz). The measured position change for the $|-\rangle$ state undershoots the prediction off-resonance, just like the experiment with $B_{DC} = 5$ G. This undershoot for the $|-\rangle$ state off resonance combined with the overshoot for both states near-resonance at DC magnetic field values of $B_{DC} = 5$ G and $B_{DC} = 39$ G suggest that these features are not dependent on the DC magnetic field. This, in turn, suggests that it is unlikely that these features are due to a contribution from a third atomic level. If this were the case, then an increase of almost an order of magnitude in the DC magnetic field value would have shifted this third level significantly out of resonance, leading to a smaller force deviation.

6.3 Spin-specific ACZ Force

One of the main selling points of the ACZ force as an experimental tool is that it is spin-specific, i.e. that the force can be selectively applied to one spin state and not others. A specific M1 hyperfine transition can be targeted by selecting the frequency of the microwave field. With a sufficiently large B_{DC}, the other transitions between the hyperfine manifolds are sufficiently off resonance that the ACZ force is negligible. In addition to the frequency, the polarization of the microwave field can be used to select specific transitions to target, though this is more experimentally challenging.

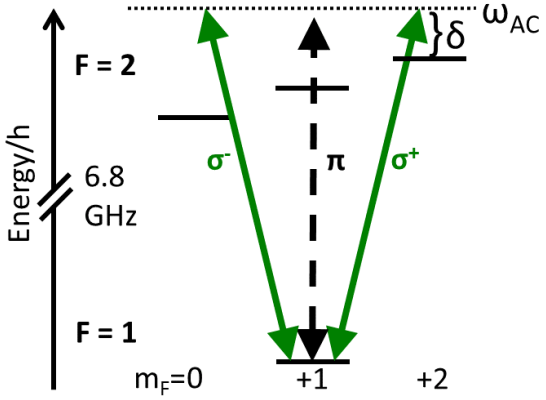

FIG. 6.17: Simplified energy level diagram with B_{AC} polarization. This diagram shows for the electronic ground state for alkali atoms with nuclear spin $I = 3/2$, e.g. ^{87}Rb. The microwave AC magnetic field's frequency ω_{AC} and polarization $(\sigma^+, \sigma^-, \pi)$ can be used to selectively target transitions.

To perform this experiment we used the spin-independent nature of the ODT that was previously installed to make a quantitative measurement of the ACZ force [22]. The spin-independence of the ODT is, oddly enough, a critical piece of this experiment. This spin-independent potential allows for the experimental time necessary to initialize the atom cloud into a spin mixture before turning off the ODT and applying the targeted ACZ force. We used an ARP-based method to create an approximately equal spin-mixture of atoms, loaded from 'RF8', in the $|F = 2, m_F = 0, 1, 2\rangle$ states. Figure 6.18 and Table 6.2 show the method used

to create this roughly equal spin mixture within the ODT from atoms initially in the $|F = 2, m_F = +2\rangle$ state. The sweeps using $\Delta m_F = \pm 1$ using the $\sigma^{\pm}$ polarized

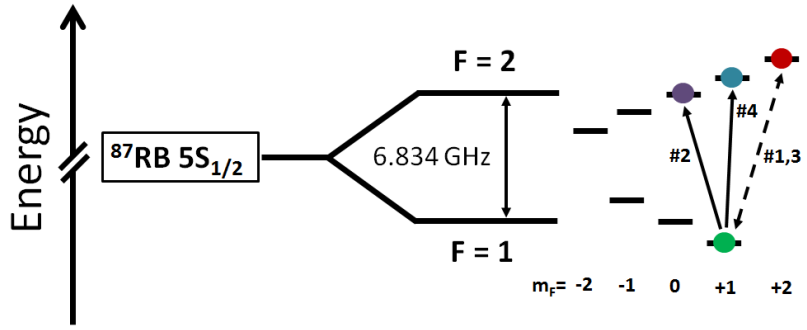

FIG. 6.18: Preparation of spin mixture for spin-dependence demonstration. The atoms are initialized into $|2, 2\rangle$. ARP1 takes 1/3 of the initial $|2, 2\rangle$ population into $|1, 1\rangle$. ARP2 takes all of the population of $|1, 1\rangle$ and transfers it into $|2, 0\rangle$. ARP3 takes half of the remaining atoms from $|2, 2\rangle$ into $|1, 1\rangle$. ARP4 takes all of the atoms from $|1, 1\rangle$ into $|2, 1\rangle$. This produces a final atomic sample in the ODT that is a roughly equal mixture of $|2, 0\rangle$, $|2, 1\rangle$, and $|2, 2\rangle$.

microwaves were done at a microwave power of 20 mW (ARP1,2,4). The ARP3 sweep with $\Delta m_F = 0$ used the π polarized microwaves and had an increased microwave power of 200 mW. The microwave power was increased for this ARP sweep because there was much less relative microwave power in the π polarization due to the orientation of the DC magnetic field.

Name	Transition	f_0 (MHz)	f_F (MHz)	δ_0 (MHz)	δ_F (MHz)	P (mw)
ARP1	$\|2, 2\rangle \leftrightarrow \|1, 1\rangle$	6956.53	6944.29	11.90	-0.33	20
ARP2	$\|1, 1\rangle \leftrightarrow \|2, 0\rangle$	6859.30	6883.30	-13.20	10.80	200
ARP3	$\|2, 2\rangle \leftrightarrow \|1, 1\rangle$	6956.53	6944.06	11.90	-0.56	20
ARP4	$\|1, 1\rangle \leftrightarrow \|2, 1\rangle$	6895.91	6919.91	-12.65	11.35	20

TABLE 6.2: ARP procedure for spin mixture. The sweeps start at f_0 and end at f_F. The detuning from the targeted resonance is also given for convenience. The $|2, 2\rangle \leftrightarrow |1, 1\rangle$ and $|2, 0\rangle \leftrightarrow |1, 1\rangle$ transition frequencies were measured. The $|2, 1\rangle \leftrightarrow |1, 1\rangle$ transition frequency is an estimate based on $B_{DC} = 52$ G. The generated spin-mixture was used to test the spin-dependence of the ACZ force in figure 6.20. The procedure starts with atoms in $|2, 2\rangle$ and makes a roughly equal mixture of $|F = 2, m_F = 0, 1, 2\rangle$

Once the atoms are in a spin mixture we need a way to tell which spin state is which when imaging. The traditional tool of a DC Stern-Gerlach (SG) pulse is well suited to his purpose (see also section 6.2.3) . We normally apply a DC magnetic

field gradient using current running through the chip Z-wire to spatially separate the atomic states. We ran into problems with this method when applying it in combination with the ACZ force due to the curvature in the DC magnetic field, $\frac{d^2|B_{DC}|}{dy^2}$. An ACZ force that 'pulled' the atoms closer to the chip felt a stronger 'push' from the DC SG pulse. Similarly, an ACZ force that 'pushed' atoms farther away from the chip reduced the push that the atoms felt from the DC SG pulse. This feedback mechanism made it difficult to adequately separate the spin states and show a spin-specific force on the atom cloud.

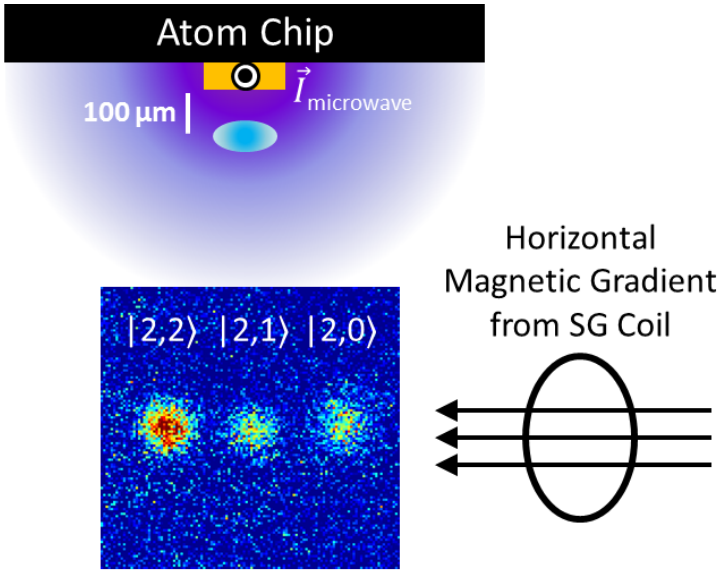

FIG. 6.19: Cartoon schematic of the horizontal Stern-Gerlach set up. The coil producing the horizontal magnetic field gradient was located just outside of the vacuum cell wall. Atoms were released from the trap, the ACZ force was applied for 0.5 ms, then the magnetic gradient SG coil was turned on for 12 ms before absorption imaging to spatially separate the spin states in the horizontal direction.

The solution to this problem was to add a magnetic field coil as seen in figure 6.19. We installed a N≈50 turn coil just outside of the chip-cell that provided a DC magnetic field gradient predominantly in the horizontal direction, perpendicular to the ACZ force in the vertical direction. This new DC magnetic field gradient also had much less curvature, so the atoms experienced a force that did not depend as much on their position. This new 'SG' coil effectively removed the feedback

mechanism between the microwave and DC magnetic field pulses.

The data shown in figure 6.20 were taken with a similar procedure to the initial force measurement. The spin mixture was released from the ODT, then a 0.1 ms ARP sweep was applied at full microwave power (3.3 W) on the targeted transition from $\delta_0 = \pm 13$ MHz, followed by a 0.5 ms hold at δ_{exp}. The +(-) refer to atom clouds that are pushed(pulled). Next, a second ARP from δ_{exp} to $\delta_F = \pm 13$ MHz was applied to drive all of the atoms back to the original spin state. There was the same 12.25 ms time of flight after the microwave pulse. This second ARP sweep returned the atom cloud to the original state and allowed a factor of 2 more atomic signal in the targeted state compared to the single ARP method. This was needed for this experiment specifically because there was an initial reduction by 1/3 in the atomic signal by splitting the cloud into 3 different spin states. Each of the images in figure 6.20 are averages of 5 individual frames of data.

We can extract useful quantitative information in figure 6.20 in addition to the qualitative data that the targeted spin state moved and the other ones did not. This quantitative data is obtained in the same manner as the data in figure 6.9. The 3 spin state clouds are spatially separated and can be fit independently. Using the relation between the measured movement of the cloud center Δy and the ACZ force in equation 6.2 we can extract the applied force for each spin state. The results are is shown in table 6.3 and agree reasonably well with the predicted on-resonance force in equation 6.8 using the measured microwave gradient (i.e. $d\Omega/dr = (2\pi)1.18 \pm 0.22 \times 10^{10}$ Hz/m for the $|2,2\rangle \leftrightarrow |1,1\rangle$ transition).

The Rabi frequency, and its gradient, are proportional to the matrix element of the targeted transition from equation 3.17 and table 3.1. The first two rows of figure 6.20(a,b) were taken at $B_{DC} = B_{Ioffe} = 52$ G using σ^+ (σ^-) microwave transitions.

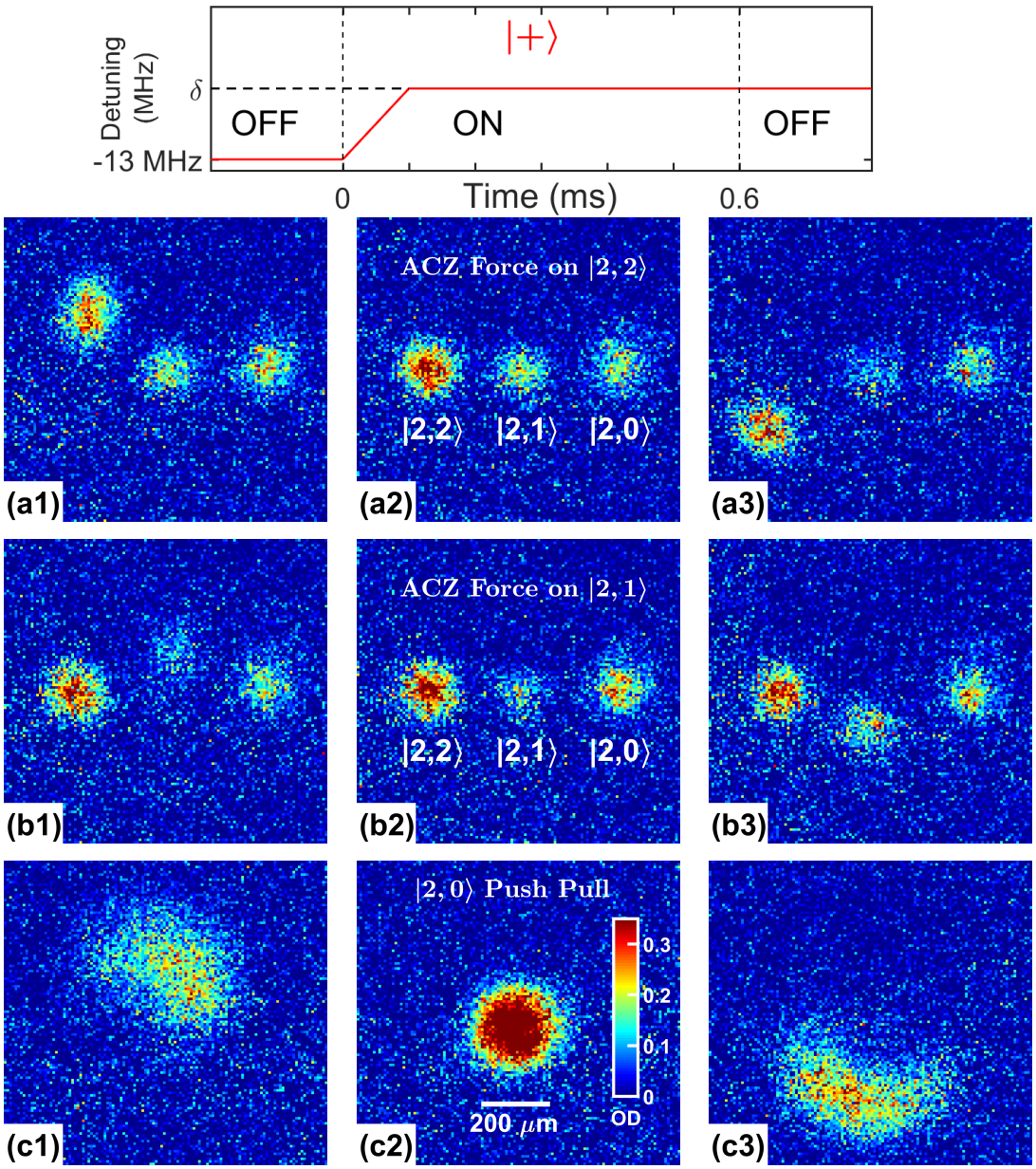

FIG. 6.20: Demonstrations of spin selectivity. The timing diagram on top shows detuning vs. time for a pushing force with $\delta_0 = -13$ MHz. (a) Spin-specific targeting of the ACZ force to $|2, 2\rangle$ (see (a2) for spin assignment) using a similar procedure to that for figure 6.9. The ACZ force pulls up (a1), is off (a2), and pushes down $|2, 2\rangle$ (a3). The spins are spatially separated after the ACZ force is applied. (b) Spin-specific targeting of the ACZ force to $|2, 1\rangle$ The ACZ force pulls up (b1), is off (b2), and pushes down $|2, 1\rangle$ (b3). (c) A resonant ACZ force acts on a cloud of $|2, 0\rangle$ atoms using a π transition instead of the standard $\sigma^{\pm}$ transitions. The ACZ force pulls up (c1), is off (c2), and pushes down $|2, 0\rangle$ (c3). All the false color images share the same length scale and optical depth-to-color conversion scale (max. OD=0.35), which are given in (c2). The ACZ force is produced with a microwave power of 3.3 and W applied for 0.5 ms at $B_{dc} = 52$G. The chip is located above the images, and gravity is down. The atoms are imaged after a time of flight of 12.25 ms.

The applied microwave field is oriented along $B_x = 1/2(B_+ + B_-)$ for DC quantization field along $\hat{z}$ in figure 6.1, assuming the thin-wire limit and no capacitive or inductive coupling between neighboring wires. With these assumptions, the microwave magnetic field amplitude gradient was previously calculated as $|dB_x/dr| = 195$ G/cm in section 6.2.3. In figure 6.20(c), however, the quantization field was rotated by ramping down the B_{Ioffe} to 0 G and ramping up the B_{Hold} to 46 G simultaneously before releasing the atoms from the ODT. The new $B_{DC} = B_{Hold} = 46$ G is oriented along $\hat{x}$ in figure 6.1 so that the microwaves polarized along B_x drove the $\Delta m_F = 0$ π transitions. The π transition had a much larger matrix element for the $|2,0\rangle$ state than the $\sigma^{\pm}$ transitions, as shown in table 3.1.

Transition	Freq. (MHz)	Mat. Elem. ($\hbar/4$)	$F_{th.}$ (mg)	F_{exp} (mg)
$\|2,2\rangle \leftrightarrow \|1,1\rangle$	6944.62	$\sqrt{12}$	2.76±0.5	2.79±0.04
$\|2,1\rangle \leftrightarrow \|1,0\rangle$	6872.50	$\sqrt{6}$	1.95±0.4	1.77±0.09
$\|2,0\rangle \leftrightarrow \|1,0\rangle$	6835.72	$\sqrt{16}$	3.19±0.6	3.21±0.04

TABLE 6.3: Spin-specific forces. The first two columns show the targeted transition and resonance frequency for the rows of images in figure 6.20. The third column shows the relative matrix elements for the targeted transitions from table 3.1. The fourth and fifth columns show experimental and theoretical ACZ forces. These predictions use equation 6.8 and the data in table 6.1. The Rabi frequency, and its gradient, are proportional to the matrix element found in equation 3.17.

We were also able to selectively remove spin states from the ODT by applying an ACZ force to trapped atoms, as shown in figure 6.21. The experimental procedure

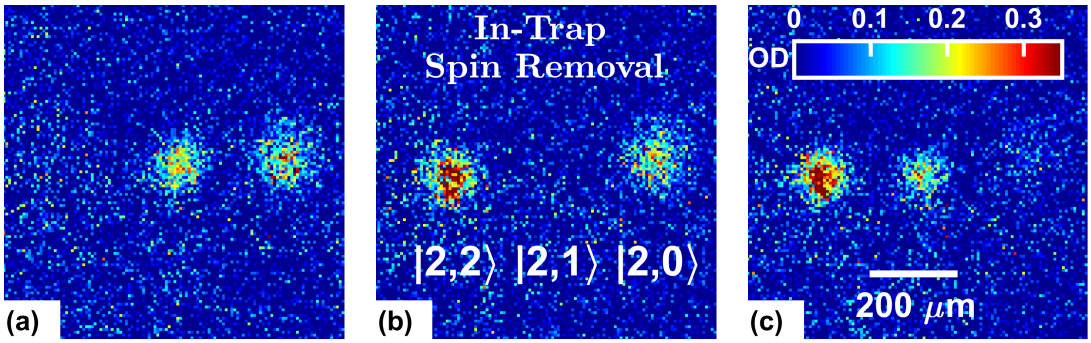

FIG. 6.21: Spin Selective Atom Removal from ODT. (a-c) show selective removal of spin states $|2,2\rangle$, $|2,1\rangle$, and $|2,0\rangle$, respectively, from the ODT. The ACZ force was applied for 5 ms to selectively eject the atoms from the ODT.

started with the same spin mixture preparation as in the free-space push/pull in figure 6.20. The DC quantization field was rotated from $B_{DC} = B_{Ioffe} = 52$ G to $B_{DC} = B_{Hold} = 46$ G for the $|2,1\rangle$ and $|2,0\rangle$ states in figure 6.21. After this, the microwave field was turned on at full power and a detuning of $\delta_0 = -13$MHz with atoms trapped in the ODT. A 1 ms ARP sweep to resonance ($\delta_{exp} = 0$) was applied first, followed by a hold of 5 ms to push the selected spin state out of the trap. The atoms were then released and the horizontal SG spin-separation procedure was applied. We were able to successfully remove each of the $|F = 2, m_F = 0, 1, 2\rangle$ states without disturbing the other spin states.

This spin-selective atom removal can be useful for performing sympathetic cooling where one atom species (or spin) is targeted for forced evaporation by removal from the atom trap. The un-targeted species (or spin) is then cooled through collisions [78, 79]. This sympathetic cooling has been shown to work in magnetic traps where forced evaporation is possible by applying an RF field to spin-flip the targeted state [78, 79]. However, this procedure requires preparation of atoms in the higher-energy magnetically trappable states, which can flip into the lower-energy anti-trappable states through inelastic collisions [80]. Performing sympathetic cooling in an optical dipole trap with the ACZ force would allow for atom clouds prepared in an arbitrary spin-state and could mitigate this inelastic spin-flipping.

6.4 In trap sloshing

In addition to time of free-space based push-pull measurements of the ACZ force in the previous sections, we were able to use the ACZ force to induce mechanical oscillations, i.e. sloshing, of trapped atoms in both a DC chip trap and an ODT. The oscillatory motion served as an independent method to observe the ACZ force on ultracold ^{87}Rb. This data shows a measured force larger than gravity in both the ODT and the DC magnetic trap. However, interpreting these data to get an accurate force measurement is more challenging than the free-space based approach. Furthermore, These measurements were not conducted with the same independent measurements of Ω and $d\Omega/dr$ for comparison with *ab-initio* theory.

6.4.1 DC Chip Trap Sloshing with ACZ effect

We performed experiments with atom sloshing in the DC chip trap using the ACZ effect before we installed the ODT at the chip. These experiments were an to attempt to measure a force stronger than gravity without having to go through the effort of installing an ODT at the chip.

The experimental procedure started with the usual DC chip trap and evaporative cooling. The chip trap position was then slowly moved to create a trap directly beneath the U-wire as seen in figure 6.1(b). Next, the microwaves were turned on at full power (P=3.3 W) and $\delta_0 = \pm 11.5$ MHz. A slow ARP sweep was applied by ramping the frequency to δ_{exp} in 20 ms. This ARP sweep served two functions. First, this ARP kept all of the atoms in the same eigenstate. Second, the ARP slowly increased the ACZ force, akin to slowly drawing back a slingshot.

Figure 6.22 shows a schematic of this slingshot method for a harmonic trap with potential energy $U_0 = \frac{1}{2}m\omega^2 y^2$ where ω is the trapping frequency, m is the mass of the atom and y is the distance from the trap center. Slowly applying

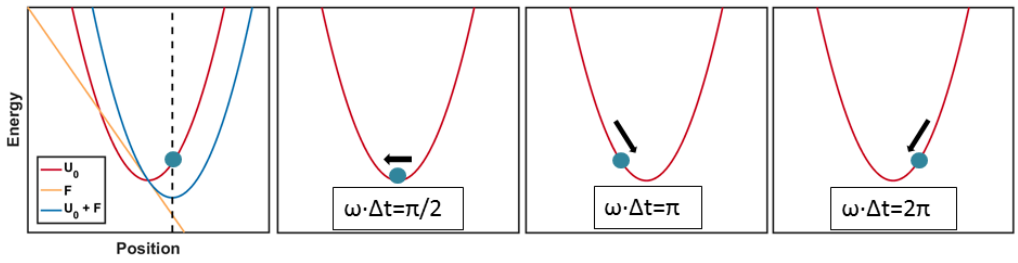

FIG. 6.22: Graphical representation of the slingshot method. The atoms are originally trapped with the potential in red (left). A force is gradually applied in orange which displaces the center of the trap (blue potential). Quickly turning off the force causes the atoms to experience the original potential in red and begin to slosh with frequency ω in the three images to the right.

the force moves the center of the cloud a distance of $\delta y = F/(m\omega^2)$ where F is the applied force. When the applied force is quickly turned off, the atoms experience the original potential and start to slosh with a maximum velocity of $v_{max} = F/(m\omega)$ and frequency ω. Forces with opposite polarity should lead to opposite initial positions and subsequently opposite sloshing velocities (π out of phase sloshing).

The position change of the atoms while in the trap is typically small compared to the imaging resolution of our system. Instead of measuring the in-trap position, we measure the sloshing velocity. The trapping potential is turned off after a set 'slosh time'. Then, a time of flight of duration Δt converts the sloshing velocity v_y into a measurable change in position Δy by $\Delta y = v_y \times \Delta t$. This Δy can be tens of pixels on the imaging camera, which has a typical uncertainty in measuring the position of $\pm \approx 0.3$ pixels. The in-trap sloshing velocity v_y can then be calculated by $v_y = \Delta y/\Delta t$.

We performed this sloshing experiment in the DC chip trap at various experimental detunings, δ_{exp}. Figure 6.23 shows the in-trap sloshing velocity as a function of slosh time as an example of these results for $\delta_{exp} = \pm 10$ MHz. Table 6.4 shows the values of the fit from figure 6.23. The red and blue-detuned sloshing is exactly π out of phase, which demonstrates the bipolarity of the applied ACZ force. Both data sets also have the exact same sloshing frequency, ω. This is evidence that the

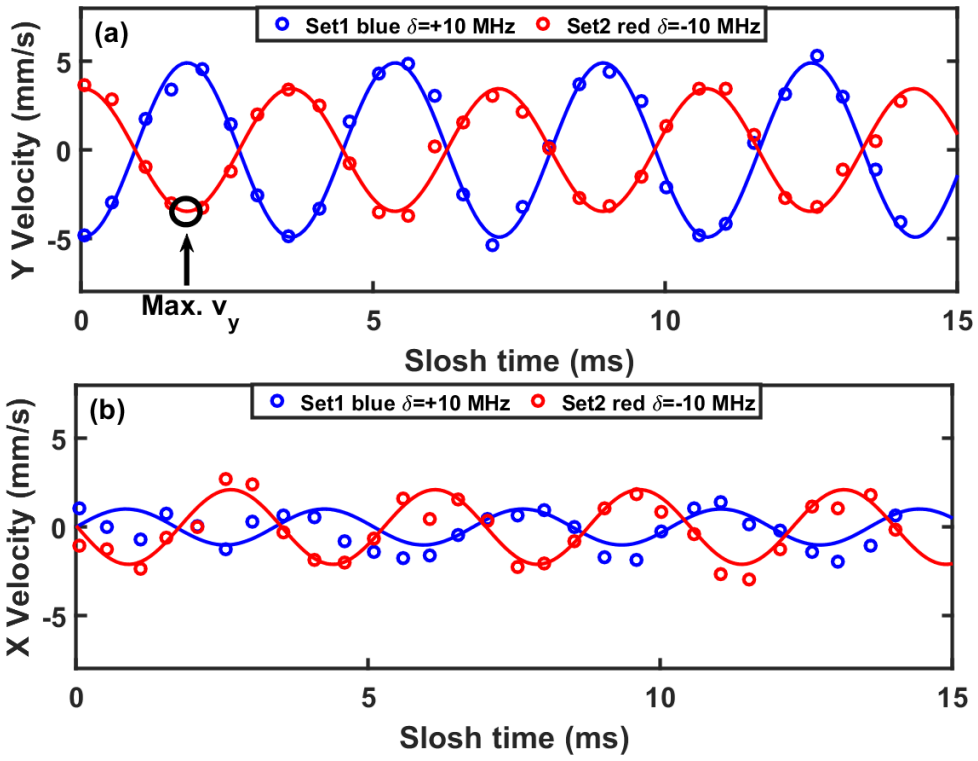

FIG. 6.23: DC chip trap sloshing with ACZ force. (a) shows the sloshing velocity $v_y = \Delta y/tof$ along $\hat{y}$ with $t_{slosh} = 1.65$ ms highlighted as the maximum of $|v_y|$ (b) shows the sloshing along $\hat{x}$. The time of flight (tof) was 14.25 ms, $B_{DC} = 5.1$ G, $P = 3.3$ W, and the experimental detuning was $\delta_{exp} = \pm 10$ MHz. There was a 1 ms slosh time before data collection started. The data (circles) was fit to $v = Asin(\omega t + \phi)$ (solid lines). Table 6.4 shows the fit values.

atoms stayed within the harmonic region of the trapping potential. The mixing of the eigenstates of the trapped $|e\rangle$ state and the anti-trapped $|g\rangle$ state during the application of the ACZ force did not lead to atom number loss from the DC magnetic chip trap at the measured sloshing times.

In figure 6.23, the blue-detuned sloshing has a larger amplitude than the red detuning case. This could be due to the curvature of the microwave field. The blue detuned microwave field pulls the cloud closer to the chip where the force is greater, vice-versa for the red-detuned field. The expected in-trap shift is 3μm. For $\delta_{exp} \gg \Omega$ the ACZ force scales like $\Omega(d\Omega/dr) \propto 1/r^3$. A 3μm shift leads to a $\pm$ 10% shift in the force for red and blue for a distance $d \simeq 90$ μm from the chip.

The atoms also sloshed in the $\hat{x}$ direction in addition to the $\hat{y}$ direction, as

Data Set	A (mm/s)	ω (rads.)	$\Delta\phi$ (units of π rads.)
set1-blue x	1.15 ± 0.16	$(2\pi)273 \pm 5$	-0.52 ± 0.09
set1-blue y	4.92 ± 0.12	$(2\pi)281 \pm 1$	0.00 ± 0.02
set2-red x	2.11 ± 0.15	$(2\pi)286 \pm 3$	1.00 ± 0.04
set2-red y	3.46 ± 0.11	$(2\pi)281 \pm 1$	0.49 ± 0.02

TABLE 6.4: Fit values from figure 6.23 for sloshing in the chip trap. The data was fit to the equation $v = Asin(\omega t + \phi)$ for the data collected in figure 6.23. The phase is reported relative to the second row, set1-blue y, and is in units of π radians. Data was taken on 30 April 2015 at a detuning of $\delta_{exp} = \pm 10$MHz. Book 7 pg. 96

shown in figure 6.23(b). Table 6.4 shows the fit parameters from the sloshing in both directions. In general, the $\hat{x}$ sloshing is smaller than the $\hat{y}$ sloshing, with roughly the same trap frequency. The blue(red) detuned cases have relative y-x phases of $\approx -(+)\frac{\pi}{2}$. A likely explanation for this behavior is that there is a small undesired ACZ force along $\hat{x}$ in addition to the larger targeted force along $\hat{y}$. This could be produced if the atom trap were not directly underneath the U-wire, or if there were microwave fields with gradients along $\hat{x}$.

By selecting the time that gives the maximum sloshing velocity ($t_{slosh} = 1.65ms$) we can extract the ACZ Force as a function of detuning, δ_{exp}, in figure 6.24. The force can be found from the maximum change in cloud position Δy, the time of flight Δt, and thus the maximum oscillation velocity Δv to be

$$F = \Delta v/(m\omega) = \Delta y/(\Delta t m\omega) \tag{6.12}$$

for a trapping frequency ω and atoms with mass m. Using this method and the oscillation frequency extracted from the experiment in figure 6.23, we are able to use one experimental sequence to measure the ACZ force on the atoms in the chip trap.

There are some limitations with the data in figure 6.24. First, when the microwave frequency is tuned close to the atomic resonance, the adiabatic potential

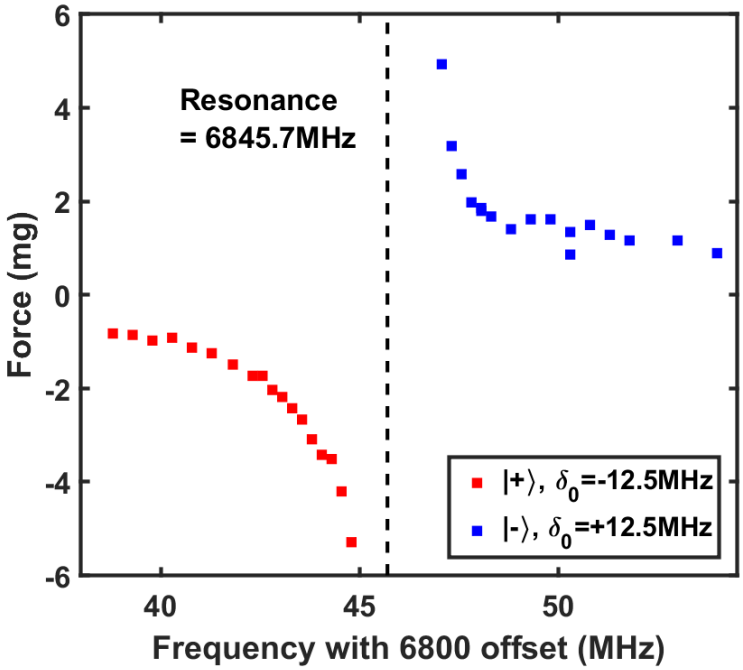

FIG. 6.24: DC chip trap sloshing with the ACZ Effect. The in-trap oscillation time was $1 + 1.65$ ms, denoted as the maximum v_y in figure 6.23. The δ_{exp} was varied and the change in y-center of the cloud was measured after a time of flight. The applied force can be calculated by using equation 6.12.

created by the addition of the microwave field and the DC magnetic field can start to contribute to the measured force [46, 81, 82]. Second, the curvature of the microwave field can lead to differing forces as the clouds are pushed farther away from the chip (red) or pulled closer to the chip (blue). Last, the ACZ force may be pushing the atoms out of the harmonic trapping region of the DC chip trap. These effects would lead to a breakdown in equation 6.12 if the trapping potential was no longer harmonic. These limitations could contribute to the asymmetry seen in figure 6.24. The data in this section demonstrate that the ACZ force can be used for chip-trapped atoms, as shown previously in [83, 34].

6.4.2 In trap sloshing - ODT at Chip

Once the ODT was installed we performed sloshing experiments similar to those conducted in the DC chip trap. The ODT does not suffer from the limitation of the

adiabatic potential that the DC chip trap does [46, 81, 82]. However, the limitation of the microwave field curvature and moving past the harmonic region of the trapping potential are still present.

Figure 6.25 shows the results of the slingshot method of sloshing atoms using the ACZ effect in the ODT. The microwave power was ramped up from 20 mW to 480 mW in 1.5 ms. Next, a 20 ms ARP frequency ramp was applied from $\delta_0 = +14$ MHz to $\delta_{exp} = +4$ MHz. The value of $B_{DC} = 39$ G was held constant. Each sloshing time was taken twice, and the scatter is plotted. The amplitude of the oscillations

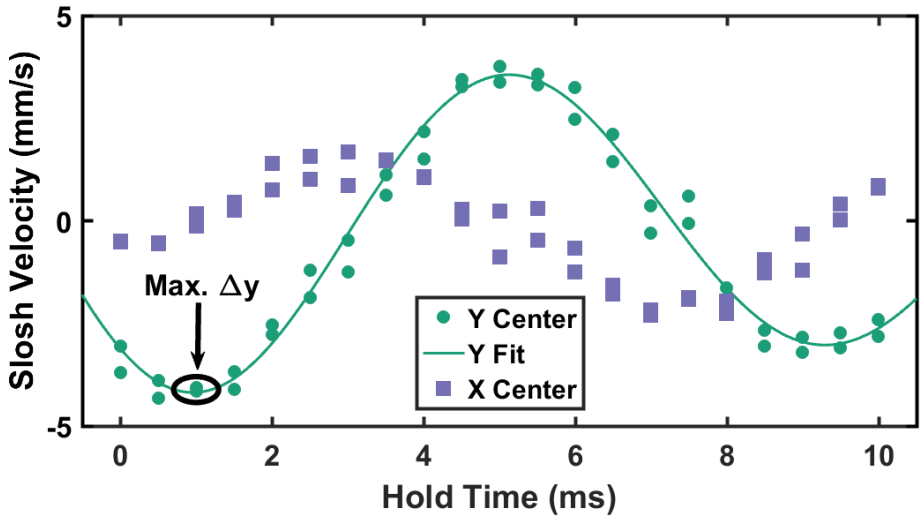

FIG. 6.25: Sloshing with ACZ force in ODT. Sloshing velocity versus slosh time is plotted. There was a 0.5 ms hold time before data collection started. The fit uses $v_y = Aexp^{-\frac{t}{\tau}}cos(2\pi ft + \phi)$ with A = 62 um, $\tau = 26$ ms, f = 120 Hz, $\phi = 3/4\pi$. The data was taken on 23 Oct 2015 in Book #8, pg. 53.

dampen much faster in the ODT than in the DC chip trap. This sloshing experiment in the ODT was conducted before its final iteration with a strong crossing beam, which may help explain the sloshing amplitude decay. Once the initial oscillations were recorded, the value of the maximum Δy (and thus V_y) was found to be at 1 ms of slosh time.

The slosh time was 'parked' at this maximum value of sloshing velocity and the detuning, δ_{exp} was varied, and the cloud position was measured. This gives the ACZ

force as a function of detuning in figure 6.26. The measured force was intentionally

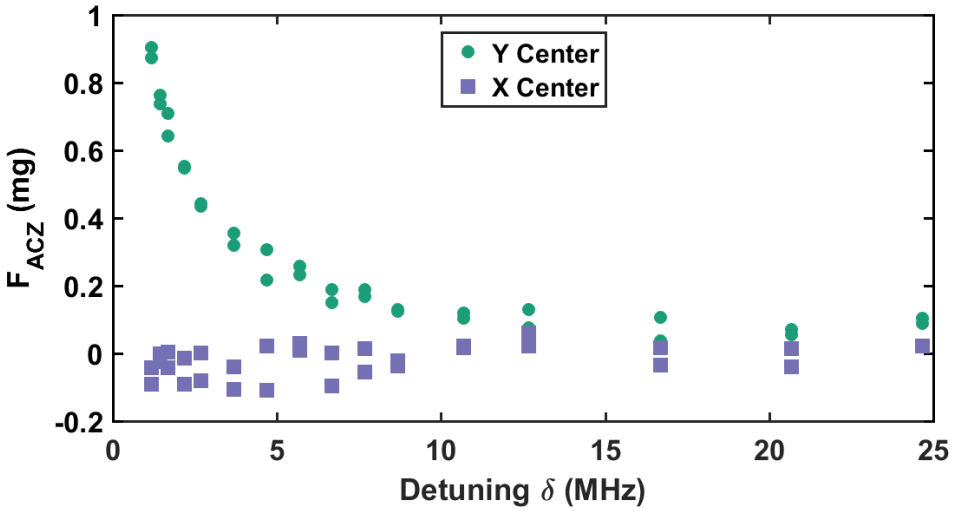

FIG. 6.26: ODT Slosh with ACZ Force vs. δ_{exp}. The hold time was parked at 1 + 0.5 ms to give the maximum v_y and the δ_{exp} was varied. Otherwise, the same procedure was used as in figure 6.25. Data was taken on 23Oct2015, Book #8, pg.54.

kept low, P = 480 mW, in order to minimize the in-trap displacement and limit the effect of the microwave field curvature. The power reduction also helped to keep the atoms close to the harmonic region of the ODT trapping potential. If we assume that the Rabi frequency scales like $\Omega \propto \sqrt{P}$, then the on-resonance force scales similarly. Increasing the microwave power from 480 mW to a maximum of 3.3 W should increase the force at $\delta = +0.1MHz$ from $F_{ACZ} = 0.88$ mg to $F_{ACZ} = 2.33$ mg.

CHAPTER 7

Microwave Dressed State Stability

This chapter describes experiments conducted to investigate the time evolution of the eigenstates of atoms subject to a microwave field gradient. The time dependence of dressed-atom eigenstates is a critical piece to determining whether an atom trap based on the ACZ force is practical and has been difficult to theoretically predict [26]. In this chapter, we investigate whether this time dependence is due to single particle physics or due to multi-particle physics (e.g. collisions between atoms). We find that the eigenstate of atoms subject to a microwave field gradient change over time and that the exact behavior of the eigenstates depends on the DC magnetic field, the detuning of the microwave field from atomic resonance, and the exact dressed-atom eigenstate that the atoms are initialized in (i.e. $|-\rangle$ or $|+\rangle$).

In the experiments in this chapter, we take an exploratory approach to investigating the time dependence of the eigenstate. This first step characterizes the behavior of the states and how this behavior changes with easily changed experimental parameters like the DC magnetic field and the detuning from resonance as a guide for future work with the ACZ effect. The second step, yet to be done, will be to develop a physics model that explains the observed data. To test this with

an experiment, we prepared atoms in either $|\pm\rangle$ with an ARP sweep and left a low-power microwave field on for a set time. We then reversed the ARP sweep and counted the number of atoms remaining in the 'correct' state and those that flipped to the 'wrong' state. This information about the time evolution of the eigenstates of the system, but does not give other information like the coherences between the $|+\rangle$ and $|-\rangle$ states during the hold time.

This chapter is organized as follows. Section 7.1 presents the experimental method and data collection process. Section 7.2 describes the stability of the dressed states as a function of DC magnetic field B_{DC} and section 7.3 studies this stability as a function of experimental detuning δ_{exp}. Section 7.4 covers the effects of atomic density on the time dependence of the eigenstates. Section 7.5 presents the atom number decay and heating experienced in some of the experiments as well as the effect of varying the microwave linewidth. Section 7.7 discusses the stability of the $|+\rangle$ state and how its behavior is different than the $|-\rangle$ state. The chapter finishes with section 7.8 which lists remaining questions and avenues for future experimentation.

7.1 Experimental Method

This experiment was conducted with atoms held in the crossed ODT with a trap depth of 23 μK located a distance $d \approx 100$ μm under the U-wire. The atoms were loaded by stopping the evaporation path at 'RF6', see section 4.5. There were about N=1.5×10^5 atoms loaded at a temperature of T=320 nk. We chose to load more, hotter, atoms in order to be able to measure smaller changes in the atom number more accurately.

In this experiment, we wanted to suppress the possibility of spin-dependent evaporation from the ODT due to the ACZ force (see e.g. section 6.3) in order to

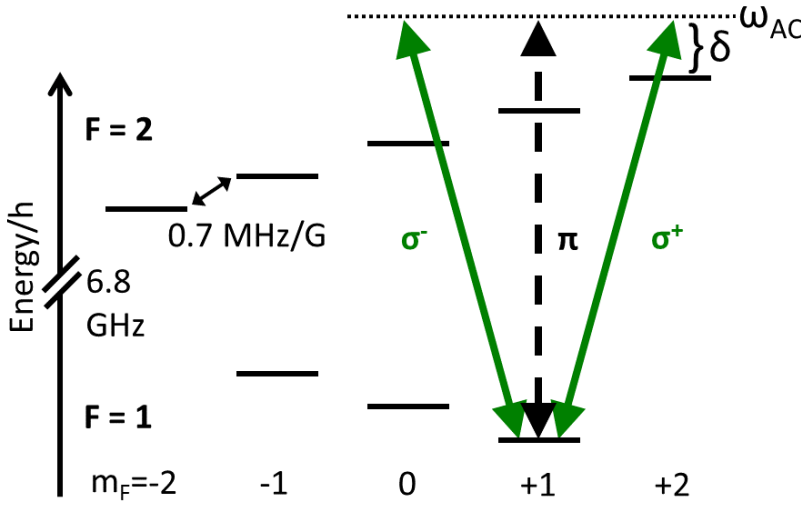

FIG. 7.1: Hyperfine level diagram with applied microwave fields. This figure shows how the m_F levels split with applied DC magnetic field. The green arrows show $\sigma^{\pm}$ microwaves and the dashed black arrow shows a π polarized microwave field. Unless otherwise noted, we apply a microwave field that is an equal superposition of σ^+ and σ^-. Atoms are initialized in $|F = 2, m_F = +2\rangle$. ARP1 and ARP2 are on the $|F = 2, m_F = +2\rangle \leftrightarrow |F = 1, m_F = +1\rangle$ transition. ARP3 is on the $|F = 1, m_F = +1\rangle \leftrightarrow |F = 2, m_F = +0\rangle$ transition.

focus on the stability of the dressed atom states. We conducted the experiment at 20 mW of microwave power, the lowest power supported by our system: this resulted in a predicted Rabi frequency of $\Omega = (2\pi)100$kHz. We calculate that the on-resonance ACZ force for this microwave power alters the trap depth by 2 μK. The experimental sequence is shown graphically in Figure 7.2 and described below.

1. The B_{DC} is linearly ramped from 5 G to the experimental value (5 - 52 G) in 10 ms.

2. The microwaves are turned on at a detuning of $\delta_0 = \pm$ 13 MHz for the $|\mp\rangle$ state.

3. ARP1: The detuning is swept to δ_{exp} over the course of 20 ms.

4. Hold time: The microwave are left on at δ_{exp} for a variable hold time.

5. ARP2: The detuning is swept back to $\delta = \pm$ 13 MHz over the course of 20 ms. Atoms in the original eigenstate (step 2) are mapped onto the $|e\rangle$ state while

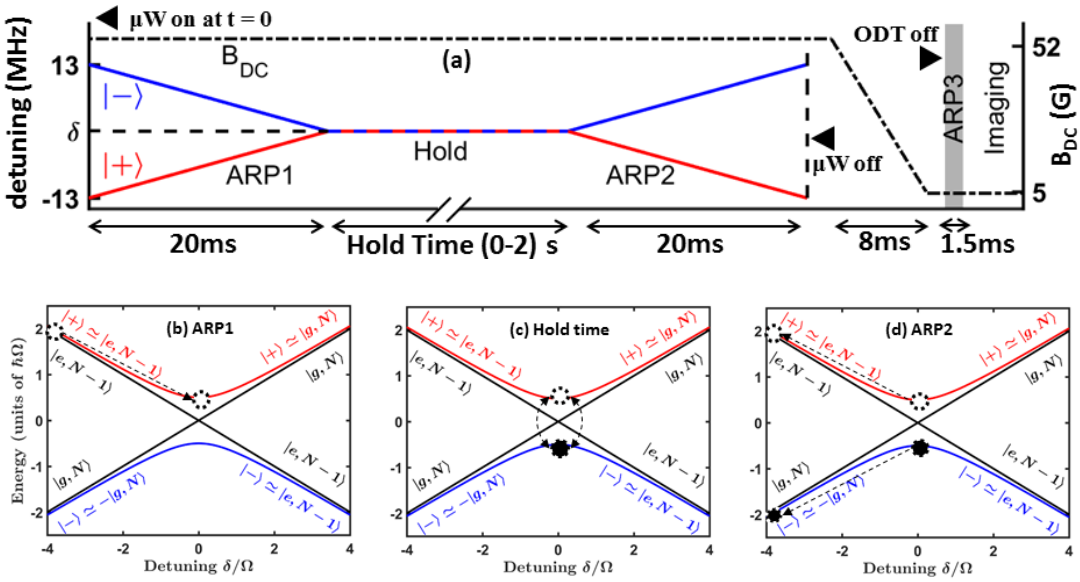

FIG. 7.2: Timing diagram for the time-dependence measurements with avoided level crossing cartoon. In the timing diagram in (a) The microwave power is turned on at t = 0. ARP1 lasts for 20 ms, then there is a variable hold time followed by the 20 ms ARP2. Next, the microwaves are turned off, and there is a 2 ms wait time before B_{DC} is ramped down to 5 G for imaging. The ODT is turned off, then ARP3 is performed on $|1,1\rangle \leftrightarrow |2,0\rangle$. Finally, a DC Stern-Gerlach pulse is applied during the time-of-flight to spatially separate the two states before absorption imaging. This figure shows an experimental value of $B_{DC} = 52$ G, though B_{DC} was operated over the range 5-52 G. The images in (b-d) are adaptations from figure 3.1 showing the initial eigenstate (white circle) and spin-flipping to the other eigenstate (black circle) during the hold time.

atoms that have 'flipped' to the other eigenstate are mapped onto the $|g\rangle$ state.

6. The microwave power is turned off, followed by a 2 ms wait time, then B_{DC} is ramped down to 5 G in 8 ms.

7. The ODT power is turned off followed by a 1.5 ms wait time.

8. (ARP3) is applied to transfer $|1,1\rangle \rightarrow |2,0\rangle$ for easier imaging.

9. DC magnetic field gradient applied to spatially separate $|2,0\rangle$ and $|2,2\rangle$ states.

10. 0.1 ms 'trap' and 'repump' pre-pulse to optically pump $|2,0\rangle$ into $|2,2\rangle$.

11. Absorbtion imaging to count atoms.

Figure 7.3 shows a representative false color absorption image for data collected in this experiment. A DC magnetic field gradient is applied, called a Stern-Gerlach pulse, to spatially separate the two spin states. The dark region at the top is where the atom chip blocks the imaging light. The atom cloud on top, labeled $|g\rangle$, is the $|2,0\rangle$ state and is insensitive to the Stern-Gerlach pulse to first order. This state represents population in the $|1,1\rangle$ state transfered by ARP3 to $|2,0\rangle$, see figures 7.2 and 7.1. The 'squished' cloud at the bottom is the $|e\rangle = |2,2\rangle$ state. The DC Stern-Gerlach pulse 'squishes' the $|e\rangle$ atom cloud due to the curvature in the Stern-Gerlach magnetic field.

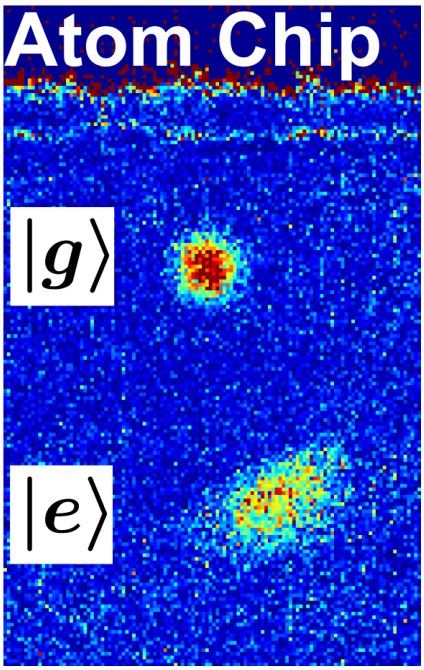

FIG. 7.3: An example false color image showing the Stern-Gerlach imaging of the $|g\rangle$=$|1,1\rangle$ and $|e\rangle$=$|2,2\rangle$ states. This image was taken for 75 ms of hold time in the $|+\rangle$ state, $B_{DC} = 52$ G and $\delta_{exp} = -0.4$ MHz. The image is 1.5 mm x 0.9 mm.

Our measurement method gives us the atom number in the $|e\rangle$ and $|g\rangle$ states, N_e and N_g, respectively, as well as the total atom number $N_{total} = N_e + N_g$. The fraction of atoms in $|e\rangle$ is given by $\eta = N_e/N_{total}$ and represents the fraction of atoms remaining in the original eigenstate, which is selected in step 2 of the timing

sequence by the sign of δ_0. This chapter focuses on the time evolution of $\eta(t)$ and how it is affected by various experimental parameters such as the DC magnetic field B_{DC} and the microwave detuning δ_{exp}. Notably, our experimental method is not sensitive to the coherence between the $|+\rangle$ and $|-\rangle$ eigenstates over the course of the 'flipping'. In other words, the measurement cannot distinguish between a quantum superposition of the $|+\rangle$ and $|-\rangle$ states and a statistical mixture.

The results of this experiment are different depending on whether the atoms are initialized in the $|+\rangle$ or $|-\rangle$ state. If the atom cloud is initialized in the $|+\rangle$ state there is significant atom loss from the ODT over time. This effect is mitigated if the atoms are in the $|-\rangle$ state. I focus the bulk of the analysis on the $|-\rangle$ state because it limits the possible causes of the observed spin flipping and the time evolution can be studied on a longer time scale.

7.2 Dressed State Stability - DC Magnetic Field

In this section, we study the stability of the $|-\rangle$ eigenstate as a function of the DC magnetic field B_{DC}. We measure the populations in the $|e\rangle$ and $|g\rangle$ states as a function of hold time, and then plot the fraction of atoms in $|e\rangle$. Figure 7.4 shows an example of data collected for the $|-\rangle$ state at $B_{DC} = 5$ G and $\delta_{exp} = 0$ MHz. The data shown is the ratio of atom number in the 'correct' state to the total atom number N_{total}: $\eta(t) = N_e/N_{total}$. This data can roughly be described by the following formula:

$$\eta(t) = Ae^{t/\tau} - \beta t + \eta_F \tag{7.1}$$

The ratio starts at $\eta(t = 0) \simeq 1$ and exhibits a fast exponential decay with amplitude A and time constant τ to a value η_F followed by a slow linear decay with slope $-\beta$. In this case, the spin ratio decays quickly to a roughly equal ratio of spins with

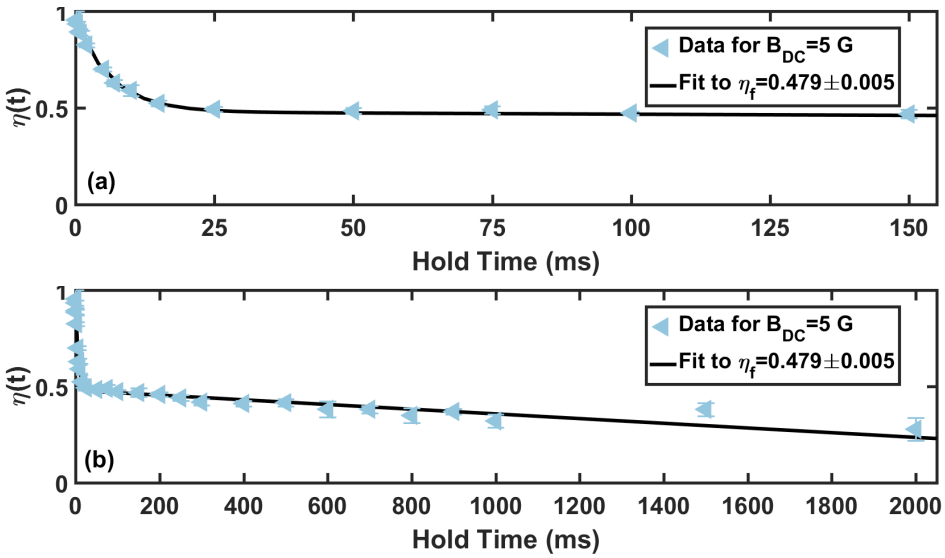

FIG. 7.4: Hold time data for $\eta(t)$ at$B_{DC} = 5$ G and $\delta_{exp} = 0$ MHz. The data (blue triangles) are fit to equation 7.1 (black line). (a) Shows a zoom-in on the $t = 0 \rightarrow 150$ ms region with the quick exponential decay and (b) shows the full data set. This is an average of 4 data sets and error bars represent the standard deviation.

$\eta_F = 0.479 \pm 0.005$ followed by a linear decay with slope $-\beta$.

One of the important results of this chapter is that we find that the time evolution of $\eta(t)$ depends strongly on the magnitude of the magnetic field, B_{DC}. Figure 7.5 shows the results of $\eta(t)$ measurements taken at 5 different values of B_{DC}, all on-resonance with $\delta_{exp} = 0$ MHz. The data in this figure show a couple of interesting trends. First, the atoms tend to stay in the correct eigenstate ($\eta(t)$ is larger) for increasing value of B_{DC}. For $B_{DC} = 5, 12, 26$ G the ratio $\eta(t)$ quickly decays to a value of 0.5, before taking on a slow linear decay with slope $-\beta$. The $B_{DC} = 39$ G case is interesting as it features revivals in the value of $\eta(t)$ for $t = 50, 250, 700$ ms. None of the other B_{DC} studied showed these revivals. The $\eta(t)$ for $B_{DC} = 52$ G has some scatter generally centered around $\eta(t) \simeq 0.95$, but does not decay much over time. The gray band in Figure 7.5 represents the value of $\eta(t)$ measured without microwaves turned on for ARP1 and ARP2. The microwaves were left on for ARP3 to ensure any atoms that got into $|1, 1\rangle$ through collisions, or another spin-flop process not related to the microwaves, got transfered into $|2, 0\rangle$

for imaging. The gray band represents one standard deviation above and below the average measured value of $\eta(t)$ for the 26 data points collected for $t = 0.1 \rightarrow 2000$ ms. Leaving ARP3 on for this test could be an issue. If for example there was somehow a leakage of microwaves into the chip during the hold time, then it could account for some spin flips. A different test would be to run with the microwave system completely turned off and see if there were any spin flips.

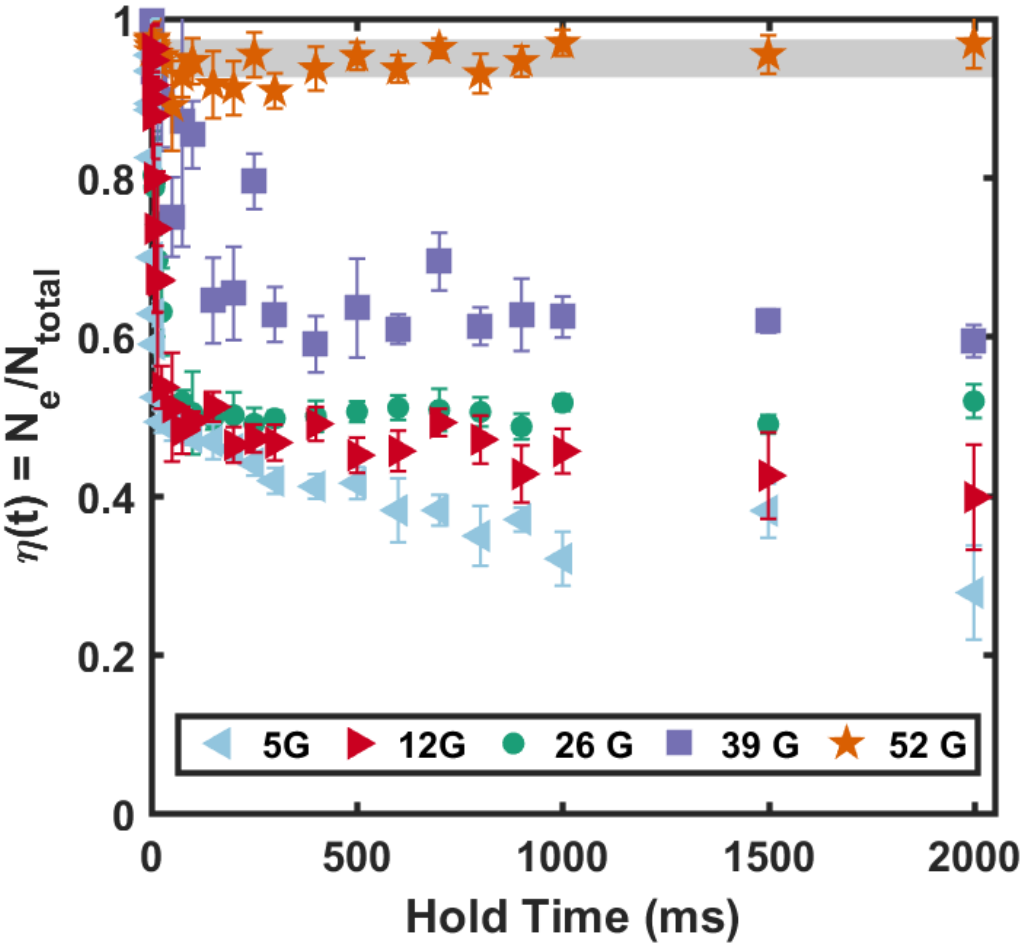

FIG. 7.5: Hold time results with five different B_{DC}. This plots the ratio of atoms in the 'correct' state to the total atom number, $\eta(t) = N_e/N_{total}$. The results are all taken on resonance with $\delta_{exp} = 0$ MHz. There is a relatively fast exponential decay to η_F followed by a slow linear decay. The gray band shows the results with the microwave turned off for ARP1, the hold time, ARP2, but on for ARP 3 with $B_{DC} = 52$ G.

There are some important pieces of information to note about the data in figure 7.5. First, these data were collected over the course of 5 non-consecutive

days. Four data sets were collected over the first three 'data days' of 13 April, 14 April, and 18 April 2016. These four data sets represent the entire data collected for $B_{DC} = 5, 12, 39$ G and are also present in the $B_{DC} = 26, 52$ G data. The fourth 'data day' was 22 April, 2016 and consisted of collecting data only with $B_{DC} = 26$ G, but with varying detunings δ_{exp}. One of these data sets is contained within the average plotted, the other is not. The omitted data set decayed more slowly to a larger value of η_F. This data set was taken while setting up the system and changing around the initial detuning. It is possible that I made an error and had the initial or final detuning set wrong, but I cannot say for sure. We also discarded one of the data sets for $B_{DC} = 52$ G. We collected 2 of 3 good data sets on 27 Apr, 2016. One of the data sets displayed strange behavior inconsistent with the other 5 and was discarded.

In order to determine the cause of the spin flips in Figure 7.5 we plot the measured atom number in each state as a function of time for varying values of B_{DC} in figure 7.6. The data plotted represents the absolute atom number measured in the 'correct' $|e\rangle$ state and the 'wrong' $|g\rangle$ state. The total atom number in the apparatus can drift by a factor of 2 day-to-day. In order to compare data sets taken a few days apart we normalized the atom number to an average of the total atom $N_{total} = N_e + N_g$ number in the first four images $t = 0.1, 0.3, 0.7, 1$ ms and then averaged the different data sets together. The results plotted in figure 7.6 represent these averages and the error bars represent the standard deviation of the mean.

The data in figure 7.6 for $B_{DC} = 26$ G show that the mechanism for the initial fast decay of $\eta(t)$ is a spin-flip between states. The atom cloud starts in $|-\rangle$ at t = 0.1 ms. After $t \simeq 50ms$ half of the cloud spin flips to the $|+\rangle$ state. Over the course of the next 2 seconds, there is overall atom number loss, but the ratio remains the same. The data in figure 7.6 for $B_{DC} = 39$ G show that the revivals in $\eta(t)$ for $t = 50, 250, 700$ ms correspond to some sort of spin-flip as well; the decrease in $|g\rangle$

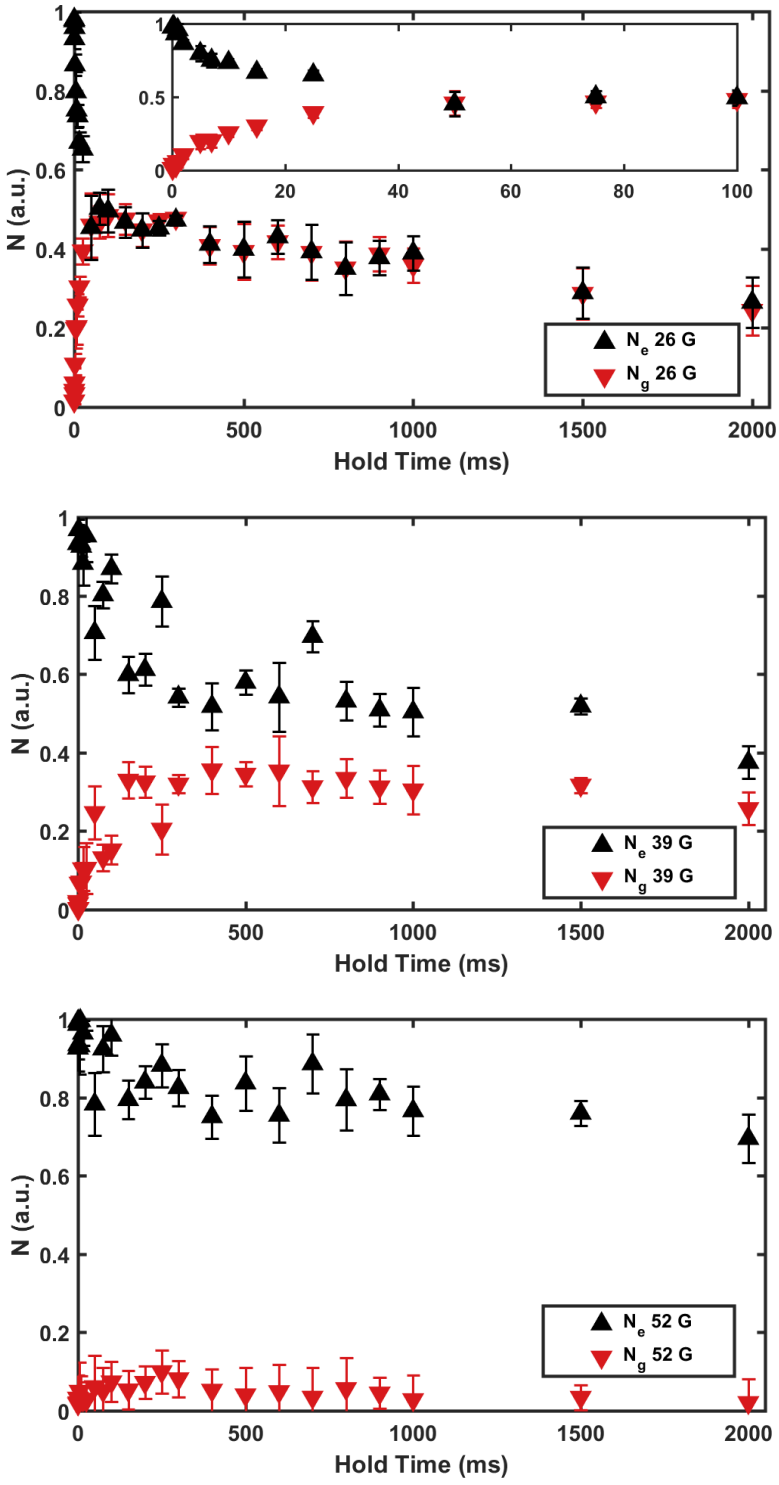

FIG. 7.6: Atom number in $|e\rangle$ and $|g\rangle$ vs. time for an initial state $|-\rangle$. The three plots show the atom number measured in each of the $|e\rangle$, $|g\rangle$ states as a function of time. The data are an average of 5, 4,and 6 sets for $B_{DC} = 26, 39, 52$ G, respectively. The error bars represent the standard deviation of the mean. Each data set was normalized to the initial total atom number, (the average of $N_{total} = N_e + N_g$ for $t = 0.1, 0.3, 0.7, 1$ ms) so that sets starting with different atom numbers could be compared.

corresponds to an increase in $|e\rangle$. This points to overall atom number being conserved, which is a comforting thought. The data in figure 7.6 for $B_{DC} = 52$ G show that there is a small dip in the N_e corresponding to a small rise in the N_g around t = 200 ms. In all three plots, the total atom number decreases as t increases to 2 seconds. This is discussed in more detail in subsection 7.5.

There are 4 different fit parameters than can be obtained from the fitting equation in 7.1, each with their own merits. We will focus on η_F as it is the easiest to quantify and tends to have the greatest effect on the eigenstate at the times of interest. An ideal, practical AC Zeeman force would have a value as close to $\eta_F = 1$ as possible. The value of A is generally dictated by η_F as $A \simeq 1 - \eta_F$ for atom clouds starting with $\eta(t = 0) = 1$. Since these two are so closely linked, it behooves us to focus on only one of the quantities. Some of the data in figure 7.5 show a linear decay and some do not. The $B_{DC} = 5$, 12 G data shows linear decay at long time scales, but the data for $B_{DC} = 26$, 39 G do not. While this term does contribute to the behavior of $\eta(t)$ for the $B_{DC} = 5$, 12 G measurements, η_F has a stronger effect on the overall value of $\eta(t)$, even at long hold times. The time constant for the exponential decay, τ, is an interesting quantity, but its value does not directly dictate the value of $\eta(t)$ like η_F and the slope $-\beta$ do.

Figure 7.4 is a good example of data that are well described by the value of η_F. This case was chosen because it settles to a value of η_F quickly and the linear decay given by $-\beta$ occurs on a much longer time scale. This behavior leads to a value of η_F that is easy to quantify and separate from the linear decay. This was not always the case for every iteration of B_{DC} and δ_{exp}, but we found that the value η_F gives the most practical measure of how much spin-flipping occurs in the experiment of any single parameter.

Figure 7.7 represents the main result of this section and shows the values of η_F obtained from fitting the data in figure 7.5. These values of η_F increase from

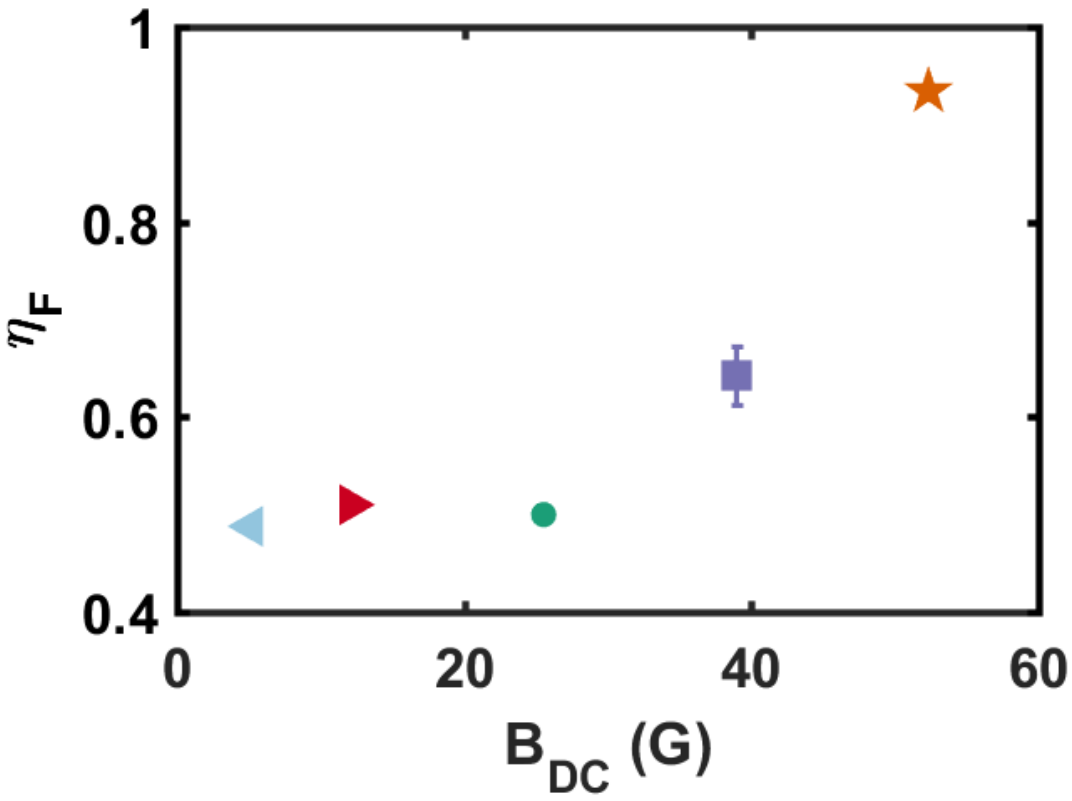

FIG. 7.7: η_F for different B_{DC} as defined in Equation 7.1. Error bars represent 1σ from the fit and are often smaller than the markers. The colors and symbols correspond to figures 7.5 and 7.8.

$\eta_F \simeq 0.5$ to $\eta_F \simeq 0.95$ as B_{DC} increases from 5 G to 52 G. It is not immediately clear why increasing B_{DC} would decrease the rate of spin-flips, however we can make an informed guess why this would happen. Increasing the value of B_{DC} increases the energy splitting between the different m_F levels within a hyperfine level. This larger energy splitting could decrease the rate of spin-flips if the line width of the microwave field somehow drove other transitions, like the $|1,1\rangle \leftrightarrow |2,0\rangle$ transition for example. More experiments and modeling are necessary before any definitive statements can be made on why a larger B_{DC} is associated with less spin-flipping. For example, an experiment could be conducted with an microwave antenna external to the vacuum cell to test the effects of adding the microwave field without the associated microwave gradient generated by using the atom chip.

7.3 Dressed State Stability - Detuning

The stability of the eigenstates varies with the detuning δ_{exp} similarly to the DC magnetic field B_{DC}. In much the same way that increasing B_{DC} was good for keeping atoms in the 'correct' state, increasing the value of δ_{exp} also kept more atoms in the 'correct' state. Figure 7.8 shows that η_F increases as the detuning δ_{exp} is increased for atoms initialized in $|-\rangle$. The Rabi frequency in this measurement was $\Omega = (2\pi)100$ kHz and sets the scale for the effect of varying the detuning δ_{exp} on η_F.

While in general increasing δ_{exp} increased η_F, there is also an interplay between the DC magnetic field and the detuning. At lower B_{DC} of 26 and 39 G, η_F increases from about 0.5 to 0.95 as the detuning changes from 0 MHz to 0.4 MHz. At a slightly larger B_{DC} of 52 G there is a slight dip in η_F from 0.95 to 0.80 only for a detuning of -0.1 MHz.

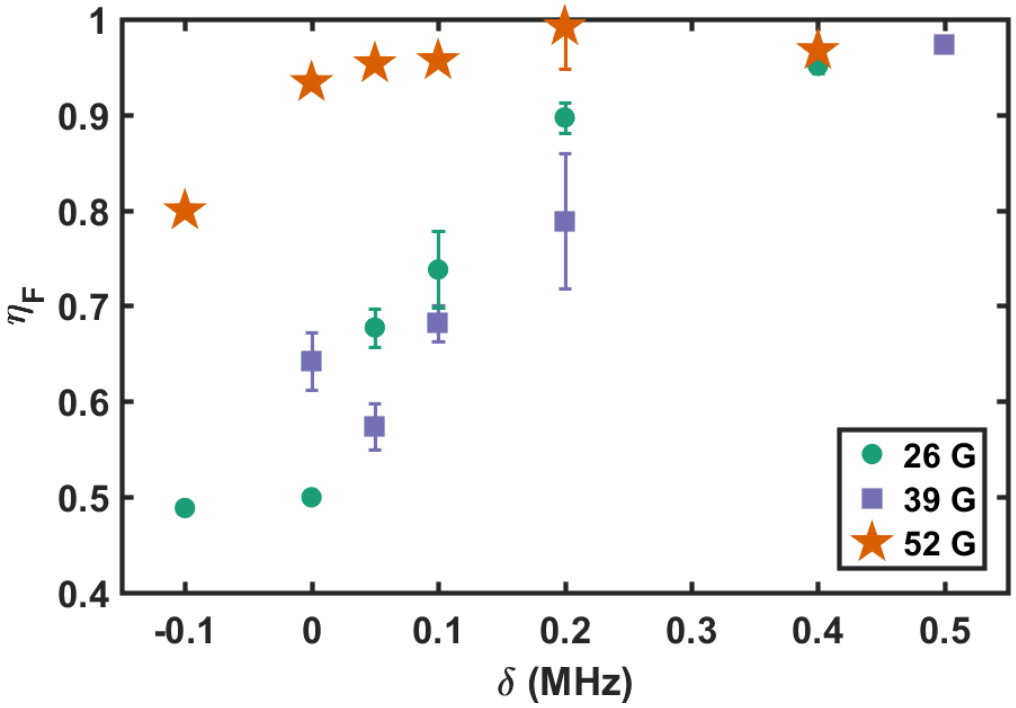

FIG. 7.8: η_F versus δ_{exp} for three different B_{DC}. Error bars represent 1σ from the fit. The colors and symbols are consistent with those in figures 7.5 and 7.7

There are a few interesting pieces of Figure 7.8 that are worth highlighting. First, there is only a dip for $B_{DC} = 52$ G for a detuning of $\delta_{exp} = -0.1$ MHz. There is no corresponding dip for $B_{DC} = 26$ G. This may point to a spin-flip mechanism that is more active as the atoms go more into the $|g\rangle$ state as the detuning is swept from an initial detuning of $\delta_0 = +13$ MHz past resonance to an experimental detuning of $\delta_{exp} = -0.1$ MHz. This also points to a spin-flip mechanism that drives the two eigenstates toward equilibrium where $\eta_F = 0.5$, otherwise we would have seen η_F decrease for $\delta_{exp} = -0.1$MHz for $B_{DC} = 26$ G. Second, there is a dip for $B_{DC} = 39$ G at a detuning of $\delta_{exp} = +0.1$ MHz. The best explanation that I can come up with, other than scatter, is that the data for η_F with ($\delta_{exp} \neq 0$) were all taken on one day where the data for $\delta_{exp} = 0$ were taken on other days.

7.4 Density Dependence

We have performed measurements of the measured ratio, $\eta(t)$, at different atomic densities and collision rates to help determine the mechanism for the change of eigenstate. The two different atomic densities were created by loading the ODT from different points along the RF evaporation path (see section 4.5). The lower density was created by evaporating all the way to 'RF8', while the higher density was created by stopping the evaporation at 'RF6'. The 'RF6' load had more atoms that were hotter that lead to an increased collision rate, while the 'RF8' ODT load had fewer atoms that were colder, with a lower collision rate. The collision rate is calculated as $k = n\sigma v$ where n is the atomic density, v is the average velocity of the atoms, and $\sigma = 8\pi a$ is the cross section for elastic collisions with the scattering length a [47].

We performed a repeated measurement at the longest hold time of 2 seconds, where we expected the greatest change in $\eta(t)$ to be. This measurement was per-

formed on the $|-\rangle$ state and the different densities were interspersed every apparatus cycle, about every 40 seconds. This was done to combat the slow drift in atom number in our apparatus that occurs on an approximately 1 hr time scale. The results of this measurement are shown in Table 7.4. They show that there is no measurable

	$\eta(t) = 2$ s (Fit)	$\eta(t) = 2$ s (P.C.)	N	Temp. (nK)	k (Hz)
RF6	0.901 ± 0.010	0.897 ± 0.011	9.58×10^4	278	35
RF8	0.910 ± 0.016	0.913 ± 0.020	4.05×10^4	184	22

TABLE 7.1: Measurements of $\eta(t = 2s)$ for different atomic collision rates at B_{DC}=52 G. These data were taken for the $|-\rangle$ state. 20 frames were averaged together and then fit. The atom number, temperature, and collision rate k were measured using interspersed control data sets without microwaves or a DC Stern-Gerlach pulse.

difference in the $\eta(t = 2s)$ for the different collision rates. These data were taken by averaging together 20 frames, then measuring the atom number by either fitting the cloud or doing a simple count over every pixel (P.C.). This allowed for better counting of the smaller atom numbers in the 'RF8' case by increasing the signal-to-noise ratio.

Figure 7.9 plots $\eta(t)$ for two different atomic densities and collision rates, k, for both the $|-\rangle$ state and the $|+\rangle$ state. Note the different y-scale in figure 7.9(a) and figure 7.9(b). The apparatus had little atom number drift for taking the $|+\rangle$ data in Figure 7.9(b). However, the overall atom number drifted down by a factor of 2 over the course of the 2 hours it took to take the data for the $|-\rangle$ state in Figure 7.9(a). The 'RF6' data went from $1.55 \times 10^5 \rightarrow 6.6 \times 10^4$ total atoms and the 'RF8' drifted from $1.01 \times 10^5 \rightarrow 4.8 \times 10^4$. This limited the difference in the collision rates that we could access in the experiment. For each experiment, the 'RF6' and 'RF8' data were alternated every other run to limit the effect of the slow atom number drift and the data within the sets, for different hold times, was randomized. These data runs lasted about 20 minutes each.

There is no statistically significant difference in $\eta(t)$ for different collision rates,

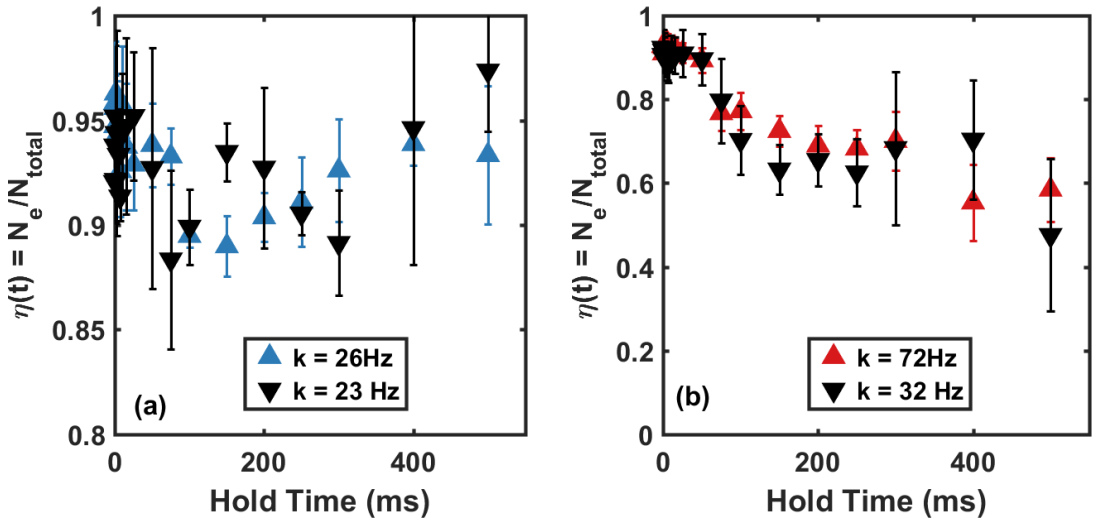

FIG. 7.9: $\eta(t)$ density dependence. Both (a) and (b) were taken for $\delta_{exp} = 0$ MHz and $B_{DC} = 52$ G. (a) shows $\eta(t)$ for the $|-\rangle$ state for $\delta_0 = -13$ MHz. (b) shows $\eta(t)$ for the $|+\rangle$ state for $\delta_0 = +13$MHz. There was significant total atom number loss in (b) for $t > 500$ ms, see section 7.7. There was a approx. 50% loss in initial atom number while taking the $|-\rangle$ data in (a), which lead to the 'RF6' case (blue upwards triangles) having only a slightly higher collision rate than the 'RF8' case. Note the different scales on the y axes for the two plots.

given their error bars, in any of the experiments listed in figure 7.12 or in table 7.4. This suggests that the cause for the change in eigenstate is related to single-atom physics rather than collisions between atoms.

7.5 Atom Number Decay and Heating

One of the complications that arose when analyzing the data for $\eta(t)$ vs. hold time is that the overall atom number decreases over time, as shown figure 7.10. The atom number decrease depends stongly on the initial eigenstate of the atoms, the value of B_{DC}, and the detuning, δ_{exp}. The general trends are that more atoms stay in the ODT for the $|-\rangle$ state, for larger B_{DC}, and for detunings δ_{exp} farther from resonance.

Figure 7.10 shows the total atom number $N = N_e + N_g$ as a function of hold time for the same data as the ratio results in figure 7.5. Each data set was fit to

$N(t) = N_0 e^{-t/\tau}$ to find the effect of applying the microwave on the trap lifetime, τ. Here N_0 represents the initial value of N(t). Figure 7.10(d) shows a lifetime measurement (i.e. total atom number vs. time) conducted in the ODT at a $B_{DC} = 5$

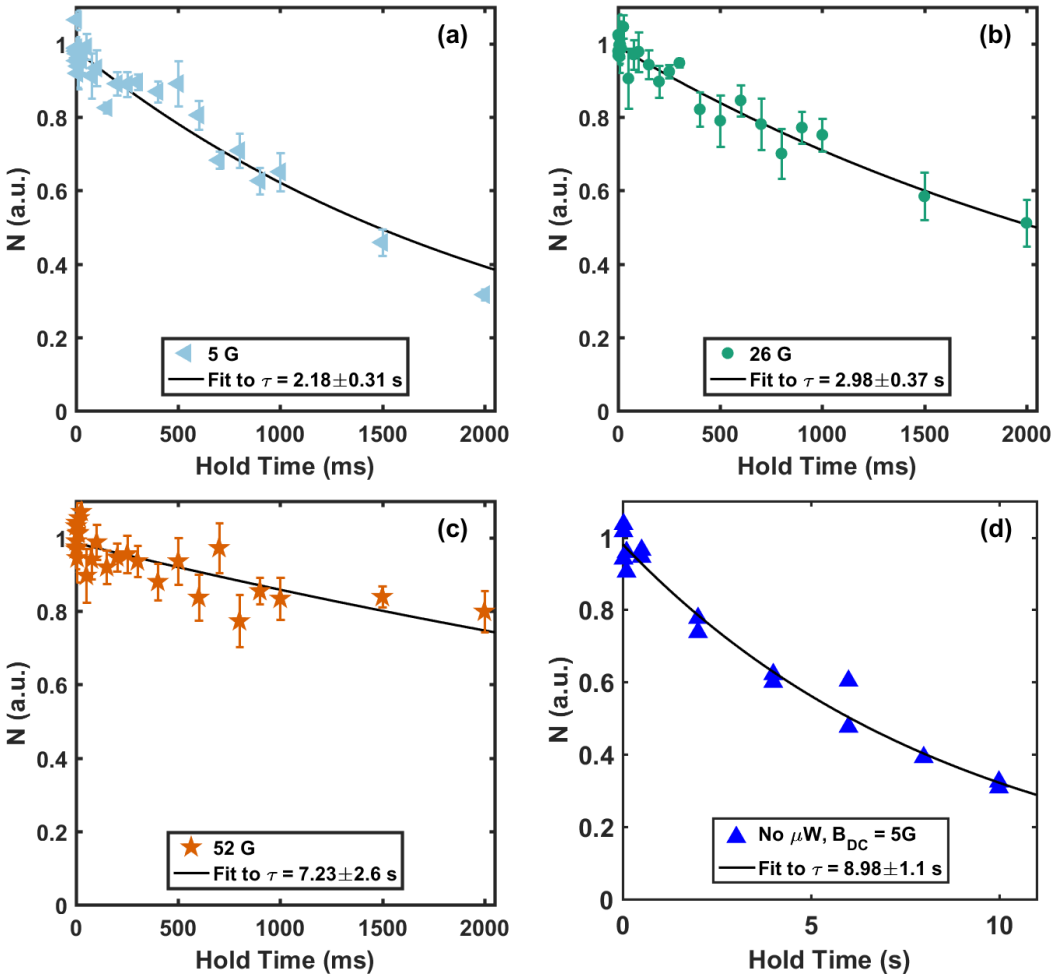

FIG. 7.10: Total atom number versus hold time for atoms held on the crossed ODT. (a-c) Shows data for the $|-\rangle$ state, $\delta_{exp} = 0$ MHz, and $B_{DC} = 26, 39, 52$ G. The starting atom number varied $\simeq 15\%$ for each data run. In order to average the data together the first 4 atom numbers for t = 0.1 $\rightarrow$ 1 ms were averaged and used as a control for the rest of the set. The relative atom number remaining at each time was then averaged together to get the data shown above. The errorbars represent 1 standard deviation in measuring the relative atom number. (d) shows a separate test without microwaves or a DC Stern-Gerlach pulse for comparison at $B_{DC} = 5$. There were two measurements per point and both are plotted.

G without applying any microwaves as a control: the lifetime without microwaves is $\tau = 9.0 \pm 1.1$ s. Figure 7.10 shows that applying the microwaves decreases the trap lifetime of the atoms held in the ODT to $\tau = 2.2 \pm 0.3$, 3.0 ± 0.4, and 7.2 ± 3.0 seconds

for the $B_{DC} = 5, 26$, and 52 G cases, respectively. The data taken with microwaves was only taken out to a time of $t = 2s$ so it is difficult to claim knowledge of the lifetime past this time. What I can say is that there is the most atom loss at $t = 2s$ for $B_{DC} = 5$ G, followed by $B_{DC} = 26$ G, and $B_{DC} = 52$ G.

The measured value of the trap lifetime clearly depends on the value of B_{DC}. We can speculate about possible explanations for the dependence of the lifetime on the magnetic field. One possible explanation for this is that the Ioffe coils that produce the B_{DC} have a small amount of magnetic field curvature that can act to compress atoms along the axial direction ($\hat{z}$ in figure 6.7). This compression only occurs for the low-field seeking state $|e\rangle$=$|F = 2, m_F = +2\rangle$ and acts to decompress the trap for the high-field seeking state $|g\rangle$=$|F = 1, m_F = +1\rangle$. Larger values of B_{DC} require increasing the current in these coils, which increases this curvature, and thus the axial confinement for the $|e\rangle$ state and decreasing it for $|g\rangle$. This extra confinement would tend to keep the $|e\rangle$ state within the 'crossed' region where the two ODT beams overlap and the trap depth is the largest. A larger trap depth means the atoms can stay around longer and could lead to the increased trap lifetimes that we see.

If there was a mechanism that heated the atoms, like the microwave field, then we would expect to see atom number loss as the temperature of the atoms approached $\simeq 1/10$ of the trap depth. In this scenario, the atoms could heat up enough to escape the 'crossed' portion of the ODT and leak out along the axial direction of the beam to a region where the trap depth is smaller, and then leave the trap. The net effect of all of this is that the lifetime of the ODT would increase with increasing B_{DC}.

Figure 7.11 shows the measured temperature of the cloud as a function of hold time. There are no microwaves applied in figure 7.11(a) and the temperature slowly increases past 500 nK over the course of a 2 second hold with a $B_{DC} = 52$ G. In

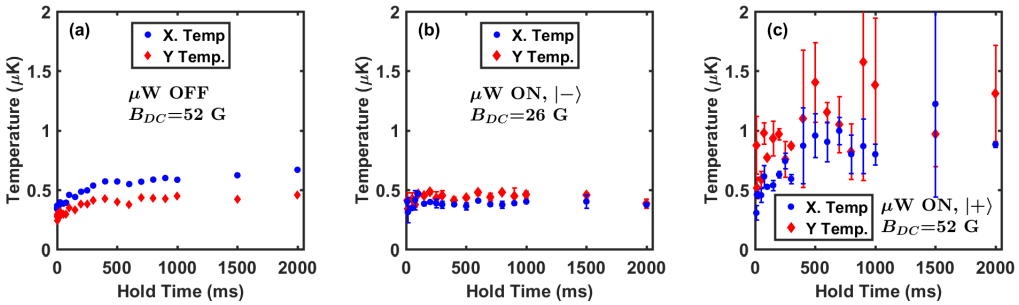

FIG. 7.11: Heating in the ODT with and without microwaves. (a) Was taken without microwaves at B_{DC}=52 G. (b) Has B_{DC}=26 G and was in the $|-\rangle$ state (c) Has B_{DC}=52 G and was in the $|+\rangle$ state. In the case of (a) no microwaves, the temperature was measured after 10.9 ms time-of-flight and each data point was measured once. For (b) and (c) 'with microwaves', there was a DC Stern-Gerlach pulse applied, and the temperature was measured by the atoms in the $|2,0\rangle$ state. The data points in (b) and (c) represent averages of 2 and 3 data sets per point, respectively. The error bars represent one standard deviation.

Figure 7.11(b), however, the microwave field is applied on resonance ($\delta_{exp} = 0$ MHz) at $B_{DC} = 26$G for the $|-\rangle$ state and temperature never gets above 500 nK. The lifetime for the no microwave measurement in (a) is $\tau = 9.6 \pm 5.2$ seconds while the lifetime for the measurement in (b) is $\tau = 3.0 \pm 0.4$ seconds. This combination of heating without loss in (a) and no heating plus loss in (b) lends credence to the idea that something is heating the atoms and that B_{DC} acts as a mechanism to increase the trap depth. Figure 7.11(c) shows the heating for data collected with the $|+\rangle$ state at $B_{DC} = 52$ G and $\delta_{exp} = 0$ MHz. These data show large error bars because of rapid atom number loss ($\tau = 0.8 \pm 0.1$ s), discussed in more detail in section 7.7. Nevertheless, it shows that the temperature can increase to a value of more than 500 nK when the value of B_{DC} is increased from 26 to 52 G.

7.5.1 Microwave Linewidth

The linewidth of the applied microwaves has an effect on the time constant of the exponential decay, τ, of $\eta(t)$ (see equation 7.1). The line width does not affect η_F, however. Figure 7.12 shows the decay of $\eta(t)$ for the SynthNV microwave source

clocked by the HP8657B signal generator and by the lab-built DDS system. Details

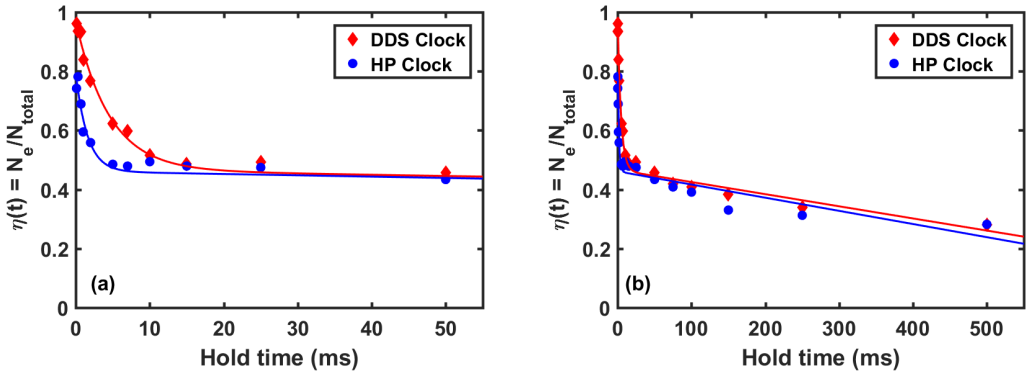

FIG. 7.12: $\eta(t)$ for different microwave line widths. $\eta(t)$ is shown for both the DDS (red) and HP (blue) clock sources for the SynthNV. (a) shows a zoom-in for short hold times and (b) shows the full time during which the data were collected. These data were taken for $B_{DC} = 5$ G and $\delta_{exp} = 0$ MHz and the $|-\rangle$ state. The data taken with the two clock sources have different time constants for the initial decay: τ_{HP}= 1.4 and τ_{DDS}= 5 ms. The data also show different initial values of $\eta(t = 0.1ms) \simeq 0.80$ for the HP clock and $\eta(t = 0.1ms) \simeq 0.95$ for the DDS. The values of η_F and the slope $-\beta$ are roughly equal for the two clocks.

of these systems can be found in section 4.6 The exponential decay constant, τ, is somewhat faster in the case of the HP source ($\tau = 1.4$ ms) compared to the DDS source ($\tau = 5$ ms). Both of the exponential decays go to the same value of η_F after about 20 ms and have approximately the same linear decay rate, $-\beta$. The second difference in the two plots on figure 7.12 is that η starts at different values. For the DDS clock, the atoms start almost all in the correct eigenstate, $\eta(t = 0.1ms) \simeq 0.95$. However, for the HP clock, the atoms do not start all in the correct eigenstate with $\eta(t = 0.1ms) \simeq 0.8$. We suspect that the linewidth of the applied microwave field may be a factor in this discrepancy.

Figure 7.13 shows the microwave linewidth broadcast from the chip U-wire using the HP and DDS clocks for the SynthNV. Both sources resulted in the same overall microwave power that was fed into the TerraSat amplifier, whose output was then sent to the chip wire. We had a 'sniffer' coil attached to a Spectrum Analyzer (Anritsu MS2038c). The HP clock had to a much broader microwave linewidth than

the DDS clock.

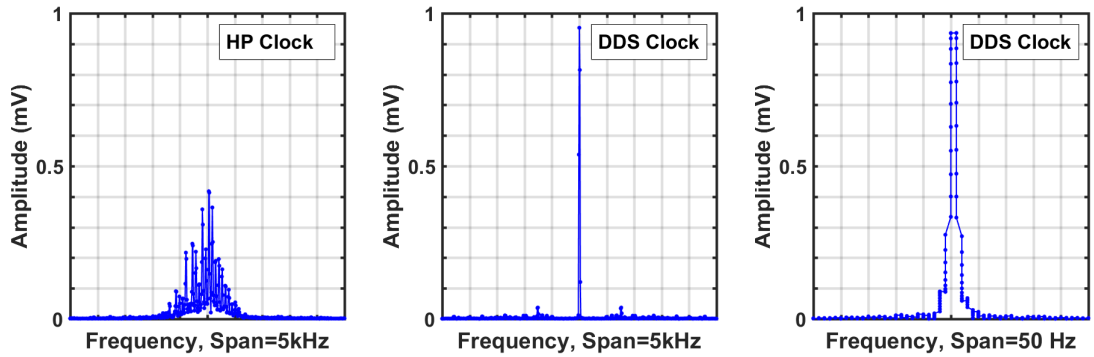

FIG. 7.13: Microwave line width at 6.845 GHz measured with a spectrum analyzer (Anritsu MS2038c) for different sources clocking the SynthNV. The clocks were run at 106.96072 MHz to generate a center frequency of 6845.501854 MHz for the HP clock and 6845.486154 MHz for the DDS. The difference in center frequency suggests that the DDS clock and HP clock differ by 2 parts in 10^6. The test was conducted with a 'sniffer' coil outside of the vacuum cell picking up microwaves broadcast from the chip wire.

This difference in the linewidth of the microwaves generated by the two clock sources must be the difference in the measured $\eta(t)$ values. The line width difference also suggests an explanation for the different initial values of the atom sample: the HP clock could 'skip' to a random phase and break the continuity of the microwave magnetic field sine wave during the initial ARP1 and get atoms to flip to the wrong eigenstate. Assuming a FWHM linewidth of 1 box = 0.5 kHz gives a phase 'skip' time of 2 ms for the HP clock spectrum in Figure 7.12. A 'skip' time of 2 ms is on par with the ARP1 time of 20 ms as well as the time constant of the exponential decay $\tau = 1.4$ ms. The DDS clock has a much narrower linewidth, FWHM ≈ 1.25 Hz and only 'skips' phase approximately once every second. This would keep the atoms in the correct eigenstate during ARP1, and lead to a larger $\eta(t = 0)$. These data suggest that the initial exponential decay could be related to the microwave linewidth in some manner, however there is probably another mechanism responsible for the $\tau = 5$ ms time constant decay for the DDS clock, which occurs on a much shorter timescale than the dephasing time of the DDS-based microwave system.

7.6 Microwave Power

A brief study was conducted on the effect of varying the microwave power on the time stability of the ACZ eigenstates. The experimental results are shown in figure 7.14. These data were taken on-resonance ($\delta_{exp} = 0$ MHz) with a DC magnetic field value of $B_{DC} = 39$ G. Only one set of data were taken for each different microwave power. The standard microwave power used in the other measurements in this chapter is 20 mW.

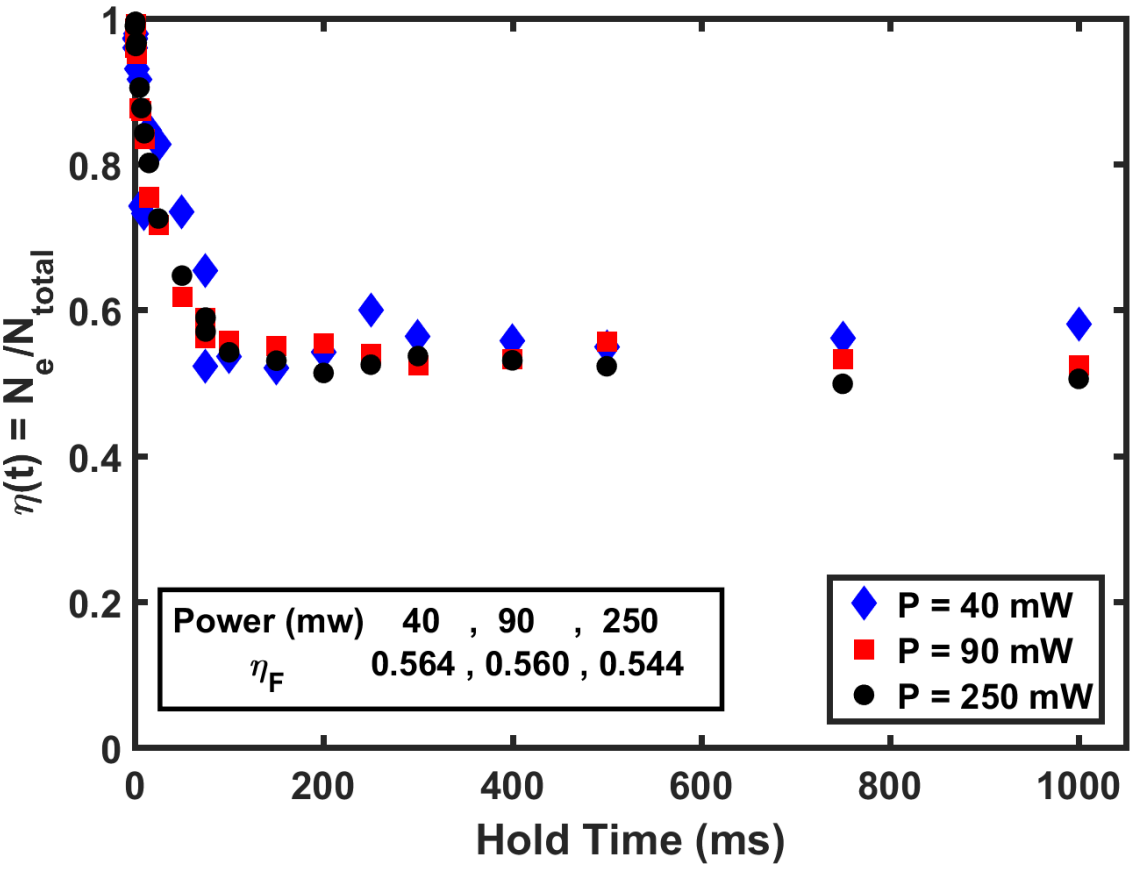

FIG. 7.14: Behavior of $\eta(t)$ vs. Microwave Power. These data were taken on-resonance ($\delta_{exp} = 0$ MHz) at a DC magnetic field $B_{DC} = 39$ G. There is no significant change in η_F with a change in microwave power.

The data in figure 7.14 demonstrate that varying the microwave power by about an order of magnitude does not appreciably alter the short term or long term behavior of the dressed atom eigenstates. Each of the data sets shows the same behavior

with an exponential decay with time constant $\tau \approx 25$ μK to a value of $\eta_F \approx 0.55$. The values of η_F do not vary by more than a few percent. There is a small difference in the values of the linear slope for the three data sets, $\beta = 0$, 3.9, 4.6 $\times 10^{-5}$ 1/ms for P = 40, 90, 250 mW, but not enough to make a large difference in the overall behavior.

7.7 Red-detuned $|+\rangle$ case

The behavior of the $|+\rangle$ eigenstate, produced with an ARP from $\delta_0 = -13$MHz, is given in figure 7.15 and is qualitatively similar to the decay of the $|-\rangle$. The value of η_F increases for increasing B_{DC}, but there is no clear relation for increasing δ_{exp}. In addition, the overall atom number decays much more quickly than the $|-\rangle$ state case: see figure 7.16. This atom number loss leads to the large error bars at t=1500, 2000 ms seen in figure 7.15. This atom number loss is much greater than for the $|-\rangle$ case in Figure 7.10 and suggests that the $|+\rangle$ state is behaving qualitatively differently than the $|-\rangle$ state.

The data in figure 7.15 shows $\eta(t)$ for $B_{DC} = 26$ G for different values of δ_{exp}. This was done because data was only collected for $B_{DC} = 26$ G and 52 G for the $|+\rangle$ case. This data shows roughly the same relation between η_F and δ_{exp} as that in section 7.3 for the $|-\rangle$ state. The $\eta_F = 0.20 \pm 0.11$ is smallest for $\delta_{exp} = 0$ MHz and increases to $\eta_F = 0.484 \pm 0.006$ for $\delta_{exp} = -0.1$ MHz and $\eta_F = 0.44 \pm 0.09$ for $\delta_{exp} = -0.4$ MHz. This is also a good example of the limitations of using η_F as a single metric to describe the data. The $\eta(t)$ for $\delta_{exp} = -0.1$ MHz is clearly lower than for $\delta_{exp} = -0.4$ MHz, but the linear decay term $-\beta$ allows for the difference in η_F. The values of the linear decay term are $-\beta = -0.0675 \pm 0.015$ for $\delta_{exp} = -0.1$ MHz and $-\beta = +0.09 \pm 0.1$ for $\delta_{exp} = -0.4$ MHz. The large uncertainty for $\delta_{exp} = -0.4$ MHz is a good example of the problems that arise when trying to decouple the

exponential and linear decay terms when they occur at similar time scales.

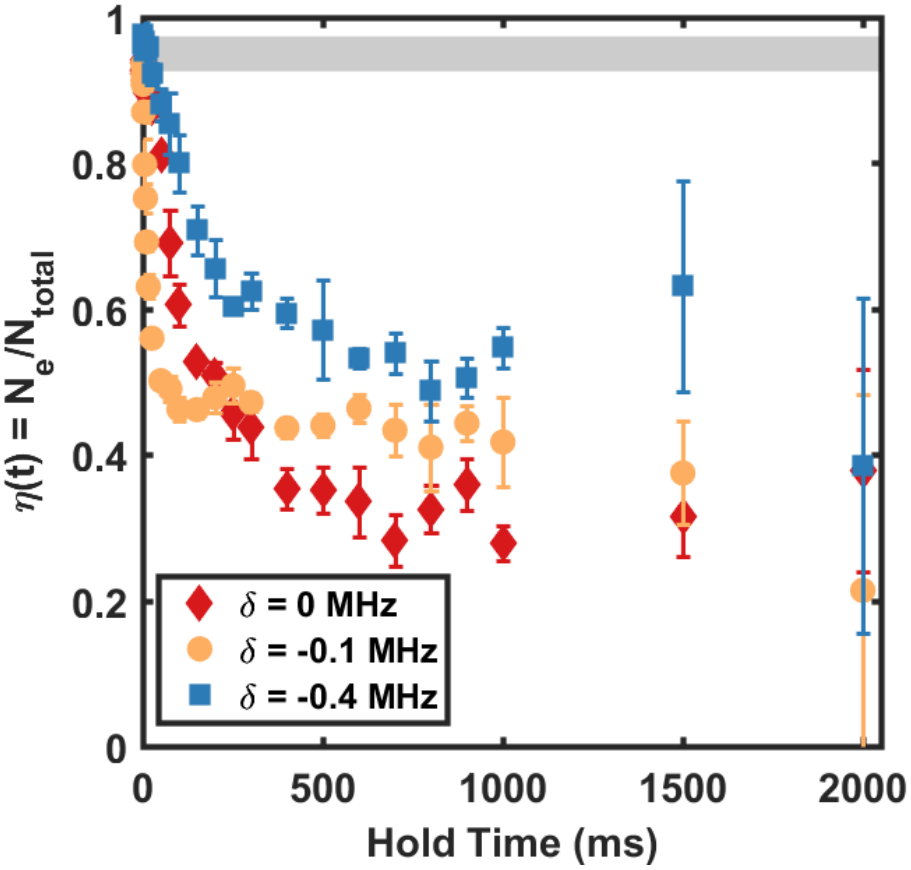

FIG. 7.15: Red-detuned $|+\rangle$ $\eta(t)$ behavior. These data were taken at $B_{DC} = 26$ G for varying δ_{exp}. The $|+\rangle$ state shows the same general behavior for $\eta(t)$ as the $|-\rangle$ state with more atoms left in the 'correct' state for larger values of $|\delta_{exp}|$. However, there is much more atom loss for the $|+\rangle$ case which leads to the large error bars for $t = 1000, 2000$ ms.

One possible explanation for the large atom number loss seen in Figure 7.16 is that the microwave field is causing more heating for the $|+\rangle$ case. This extra heating would then lead to the increased atom number loss. Figure 7.11(c) shows that the atoms in the $|+\rangle$ case heat much more quickly than the case without microwaves and the $|-\rangle$ case. I do not have a good explanation for why the $|+\rangle$ state would heat up more than the $|-\rangle$ state. In addition to the heating, the ACZ force for the $|+\rangle$ case 'pushes' in the same direction as gravity with a magnitude $F_{ACZ} \approx 0.25\ mg$ for the low-current that we use for this experiment. We calculate that this lowers the trap depth from 23 μK to 21 μK. A good experiment to do to test this scenario

is to use a 'flat' microwave field produced by an antenna outside of the vacuum cell to determine whether the ACZ force itself is responsible for the differences between the $|+\rangle$ and $|-\rangle$ cases.

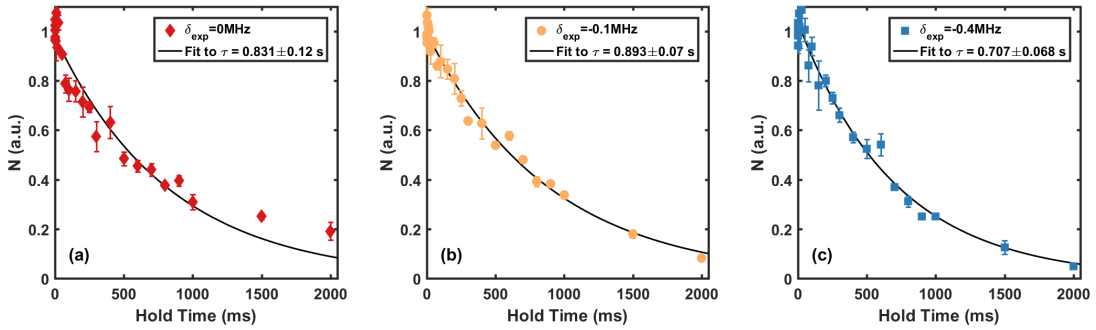

FIG. 7.16: Red-detuned $|+\rangle$ atom number vs. time. (a-c) are taken with $B_{DC} = 26$ G and with $\delta_{exp} = 0, -0.1, -0.4$ MHz. Each data set is normalized to its starting value before averaging. Atoms are lost much more quickly for the $|+\rangle$ than for the $|-\rangle$ state and at comparable rates for each δ_{exp}.

Another possible cause for the rapid atom loss for the $|+\rangle$ case is that the atoms are transitioning to a different state that we do not image with the current DC Stern-Gerlach setup. There is a greater chance that this is the case for the $|+\rangle$ case because the initial ARP sweeps from $\delta_0 = -13$ MHz are much closer to, and sometimes overlap, other hyperfine transitions, depending on the value of B_{DC}.

Prior to imaging, we applied a DC Stern-Gerlach pulse to spatially separate the $|2,0\rangle$ and $|2,2\rangle$ states. This worked well to count atoms in these two states separately. However, this DC Stern-Gerlach pulse scheme only allows us to image low-field seeking states. If the atoms were somehow driven into a high-field seeking state when the DC Stern-Gerlach pulse was applied, they would be pulled up near the chip Z-wire and would probably not have been imaged.

As an example, suppose that the atoms were driven from $|2,2\rangle \rightarrow |1,1\rangle \rightarrow |2,0\rangle$ during the 'hold time' before they were released from the ODT. The microwave field strength driving the $|1,1\rangle \leftrightarrow |2,0\rangle$ transition, $B_- = B_x - iB_y$, has just as much power as that driving the $|2,2\rangle \leftrightarrow |1,1\rangle$, $B_+ = B_x + iB_y$, from the applied AC magnetic

field along $\hat{x}$. The atoms in $|2,0\rangle$ would then be transferred into the $|1,1\rangle$ state by ARP3 and pulled up to the chip by the DC Stern-Gerlach pulse, and thus would not have been imaged. This process would have shown up as a loss in the total atom number.

Tests were conducted to measure whether any atoms were pumped into $|2,0\rangle$ by the microwave field by running the normal procedure without an ARP3 pulse driving the $|1,1\rangle \leftrightarrow |2,0\rangle$ transition. These tests did not measure any atoms in $|2,0\rangle$. However, these tests were only conducted at two different parameter pairs (B_{DC}, δ_{exp}) and were conducted with a DC Stern-Gerlach pulse, which would have pulled away any atoms in high-field seeking states like $|F=2, m_F=-2,-1\rangle$. In the future, a better way to investigate this phenomenon would be to select a couple of values of B_{DC} and δ_{exp} that give large atom number loss and perform the experiments without any DC Stern-Gerlach pulse to determine if there is true atom number loss or if some of the atoms are just getting pumped to a state that we do not image. Another good option for the future is to use the horizontal Stern-Gerlach coil described in section 6.3.

Figure 7.17 shows the measured atom number in $|e\rangle$ and $|g\rangle$ as a function of hold time, and is similar to figure 7.6. The time evolution of $\eta(t)$ shows the same qualitative features as for the $|-\rangle$ case in figure 7.6: a quick spin-flip from $|e\rangle$ to $|g\rangle$ followed by total atom number decay. For the $|+\rangle$ state here, however, the total atom number decay is much faster. Also, the data in figure 7.17(a) for $B_{DC} = 26$ G and $\delta_{exp} = 0$ MHz have a quick decay of the $|e\rangle$ state population that does not stop at an equal mixture of the $|+\rangle$ and $|-\rangle$ states as occur (i.e. η_F=0.5) in figure 7.6(a).

It would be useful to investigate if the atoms are truly leaving the trap and, how it is happening. A useful experiment to run would be to image the atom cloud *in-situ* using the axial camera to determine whether the cloud is escaping the 'crossed' part of the ODT. This could then be correlated with different values of B_{DC} and

δ_{exp} as an additional tool to diagnose what is causing the atom loss that we measure.

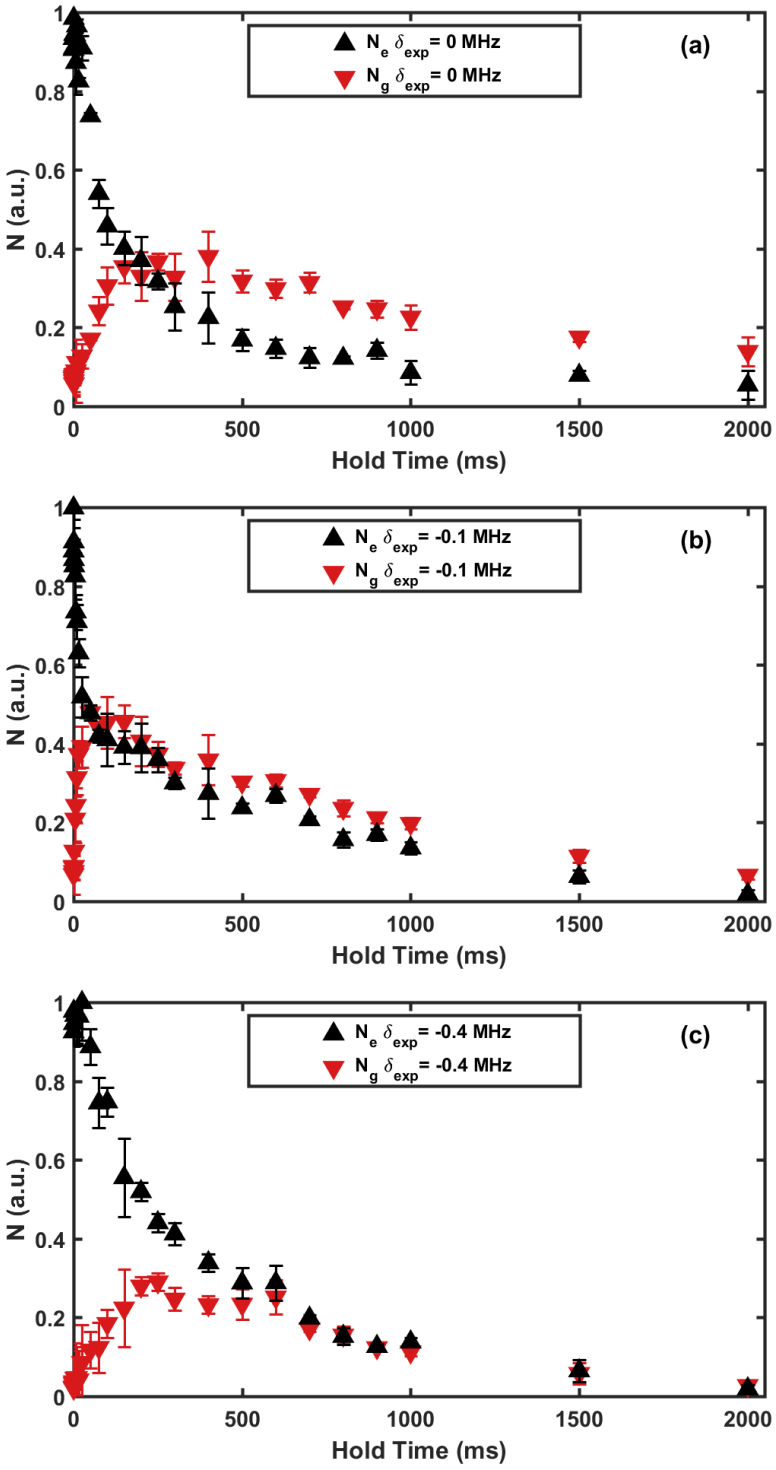

FIG. 7.17: Red-detuned $|+\rangle$ behavior. Atom number vs. hold time for each spin state for $B_{DC} = 26$ G and $\delta_{exp} = 0, -0.1, -0.4$ MHz for (a-c). In all three images there is a spin-flip process from $|+\rangle$ to $|-\rangle$ followed by rapid atom number loss.

7.8 Remaining Questions - Future Exploration

There is much more to learn about the time-dependent behavior of the dressed atom eigenstates and this avenue of exploration is far from fully explored. Here I have listed some questions that we are still trying to answer:

1. Is the force from the ACZ effect contributing to the time evolution of the states that we measure? A future avenue of exploration would be to employ microwave antenna (just outside the vacuum system) to have a comparable Rabi frequency but a small gradient to limit the force applied.

2. Why are there revivals in the 39 G data for the $|-\rangle$ state? This could be a manifestation of an oscillating spin-flip process with different frequencies dephasing and re-phasing. It would be interesting to explore with a denser time step near the revival times.

3. What is the starting ratio for different B_{DC} and why does it differ?

4. Why does the no-microwaves case have anything in the 'wrong state'?

5. Why do atoms leave the trap and why is the escape rate much larger for the red detuned case?

6. Are the atoms leaving or are they transfered to a state that we do not image?

CHAPTER 8

Building Atom Chips

Atom chips are small circuit boards with wire traces that are used to produce magnetic fields for trapping and manipulating cold atoms [31]. Atom chips are an essential technology for running experiments with a practical AC Zeeman effect because of their ability to position atomic clouds very close ($d < 100$ μm) to the current carrying wires, well within the microwave near-field ($d \ll \lambda$) they produce. However, a major drawback of using atom chips in an experiment is that the wire patterns cannot be changed once the chip is made. Furthermore, the manufacturing process is costly and time-consuming. As experiments with the ACZ effect move forward it is inevitable that the chip designs will be optimized and changed with the new information.

This chapter describes work that I completed during the summer of 2015 at the Air Force Research Laboratory (AFRL) in Albuquerque, New Mexico trying to solve this problem. The cold atom group there is developing a new technique using a commercial laser mill to pattern wire traces onto direct-bond copper (DBC) substrate to create atom chips. This technique should be able to produce the smaller wire sizes necessary for ACZ experiments while being must faster and cheaper than

traditional atom chip manufacturing techniques.

This chapter is organized as follows: section 8.1 goes further into the motivation for manufacturing new atom chips for use in future ACZ experiments. Section 8.2 describes material choices for both the current-carrying wires and the substrates that hold them. Section 8.3 describes the laser-milling process and gives an example of a finished atom chip. Section 8.4 describes the outlook of the laser milling process and initial of work done with thinner metalizations.

8.1 Laser Milling Motivation

Using atom chips as a tool for ultracold atom experiments has been around since 2001 [31]. DC magnetic traps created by atom chips typically have high collision rates due to their tight confinement and can evaporatively cool to BEC more quickly than other techniques [31]. Atom chips also benefit from their ability to change the shape and position of the DC magnetic trap they produce. This flexibility allows for optimizing the loading of atoms from a traditional DC magnetic trap to an ACZ-based trap by matching the size and shape of the traps. The wires on atom chips are closely spaced, which allows for a trapping potential to be created with neighboring wires with modest power requirements (P<10W). Atom chips also have good heat-sinking capabilities and have been used with DC currents as large as 100A for 2 seconds [84].

One of the major technical challenges of building the next generation of atom chips capable of supporting ACZ experiments is the ability to properly impedance match the chip wire 'load' to the microwave source. The atom chip in our apparatus was not designed for operation at 6.8 GHz and just happened to allow enough microwave current to flow on the chip wire to produce an ACZ force stronger than gravity. We measured a Rabi frequency of $\Omega = (2\pi)1.3\text{MHz}$ on the $|2,2\rangle \leftrightarrow |1,1\rangle$

transition at a distance of $r = 100\mu$m from a single wire. Using the definition of the Rabi frequency in equation 3.17 and Ampère's law with the thin wire approximation, this Rabi frequency is the result of an RMS microwave current of 37 mA. With perfect 50 Ω impedance matching, the microwave current would be 260 mA from a P=3.3W microwave source. If we were able to do this impedance matching, then the on-resonance ACZ force would increase by a factor of 7. If we can then decrease the wire wire impedance, then we can drive even more microwave current and produce stronger near-field $|B_{AC}|$. This impedance matching effort will most likely require a significant amount of trial and error in building and testing new chip designs before we settle on one to put into an experiment.

The traditional methods of manufacturing atom chips via lithography are expensive, time consuming, and require specialized facilities. Only recently have experimentalists been able to manufacture atom chips in-house via chemical etching of DBC substrates [84]. This was done by the AFRL cold atom group at shortly before their move to Albuquerque, NM. This technique allows for cheap and fast in-house manufacturing of atom chips. The drawback to chemical etching of DBC is that the smallest feature size is limited to wire traces that are about 175 μm wide and 125 μm tall, with a 500 μm center-to-center spacing for neighboring traces. These center-to-center feature sizes are too large to be compatible with most practical ACZ near-field experiments. We would like to have wires that are at most 10 μm tall, 25 μm wide and 25 μm center-to-center. This small wire size would limit how the skin effect at 6.8 GHz affects the shape of B_{AC} and the short center-to-center distance would allow for more compact trapping potentials, or less microwave power. These wire feature sizes, like most things, will have to be tested with trial and error to ensure that they can handle the required microwave power.

8.2 Chip and Wire Materials

Most atom chip manufacturing starts by manufacturing the atom chip wafer on a custom basis by either evaporative deposition or electroplating. Evaporative deposition is more expensive and time consuming than electroplating but tends to create smoother metallic layers and the metal thickness can be more finely tuned. Once the wafers are produced, the wire traces are cut into the outer metal layer of the chip by lithographic techniques. This process includes ordering a custom-made lithography mask for each new chip, adding to the cost and turn-around time. There is generally a thin, high conductivity, metallic wire layer (thickness $t < 20\mu$m) of Gold, Silver, or Copper attached to a thicker layer of substrate such as Si, Al_2O_3, or AlN to provide mechanical stability and power dissipation. Atom chips manufactured with these thin wires, $t < 20$ μm, typically cannot handle high currents, $I > 2$ A, depending on the width of the wire. These chips also tend to be mechanically fragile and easy to damage during manufacturing, processing, and installation. The first chip in our apparatus broke during installation. The replacement chip currently used in the apparatus is limited by overheating to a Z-wire current of $I = 1$ A.

Each wire and substrate material has its own advantages and drawbacks, including electrical conductivity, thermal conductivity, adhesion between wire and substrate, and coefficient of thermal expansion (CTE) match between wire material and substrate. Listed in Tables 8.1 and 8.2 are properties of commonly used wire and subtrate materials. Sapphire (Al_2O_3) is transparent and is commonly used for high resolution imaging applications that image atoms through the chip. Si is a staple of the semiconductor industry and has many established manufacturing processes. AlN provides excellent thermal conductivity and mechanical rigidity at the cost of being somewhat brittle. Other materials that have been used in atom chip

construction are GaAs and alumina [85].

Material	Cu	Ag	Au
Electrical Conductivity (x10^7 S/m at 20 C)	5.96	6.30	4.10
Coefficient of Thermal Expansion (10^{-6}/°K)	17	18	14

TABLE 8.1: List of electrical conductivities and coefficients of thermal expansion for various wire materials

Material	AlN	Si	Sapphire
Thermal Conductivity (W/m· K at 20 C)	170	156	25
Coefficient of Thermal Expansion (10^{-6}/°K)	4.5	3	5.3

TABLE 8.2: List of thermal conductivities and coefficients of thermal expansion for various chip substrate materials

An alternative to the current atom chip manufacturing processes is direct-bond copper (DBC). DBC is an inexpensive commercially available off-the-shelf metalized substrate that is commonly used in power electronics applications. It is created by heating a thin ($100 - 200$ μm) layer of copper and thicker layer of AlN (130 μm to 1 mm) to bond the two materials. The DBC bond is mechanically strong and can withstand significant stress during atom chip manufacturing and installation. DBC atom chips can also withstand large currents (10A steady state, 100A pulsed) [86], which could allow for creating ACZ traps about $d \approx 500$ μm away from the wire surface for sufficient microwave current. This high current capability allows for placing DBC atom chips outside of the vacuum chamber. In this geometry, the atom chip is placed as close as possible to a thin (≈ 200 μm) membrane so that the atoms can be trapped from a few mm to 500 μm from the chip [87]. Atom chips mounted outside of the vacuum chamber allow for quick changes in atom chips due to damage, defect, improvement or new experimental design [87]. Exterior atom chips also allow for much easier heat sinking, air- or liquid-based, and electrical

connections without putting mechanical stress on a fragile vacuum cell.

8.3 Laser Milling Process

The process of manufacturing an atom chip using laser milling of DBC substrates starts with designing the chip and its wires in a two-dimensional model. This can be done in either a free software like Inkscape or with a commercial software like AUTOCAD. In either case, the end result is a 'Drawing Exhange Format' (*.dxf*) file that contains the drawing of the chip and its wires in dimensions of mm. The lab-built conversion software assumes the units of the *.dxf* to be in mm. Figure 8.1 shows the complete cycle of designing and manufacturing a new atom chip from idea to finished product. Figure 8.2 shows a 2D CAD drawing used to manufacture atom chips on the laser mill that is based on the current chip in our apparatus.

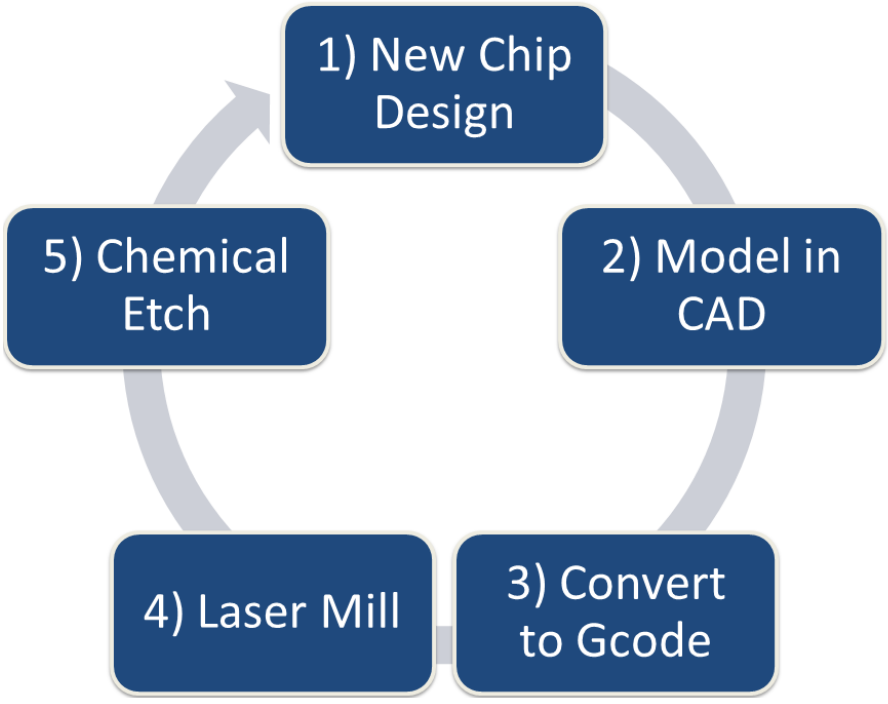

FIG. 8.1: Laser milling process flow chat. This process skips the custom manufacturing process of substrates by using commercially available DBC. The entire process from initial idea through finished product can be completed in-house in less than 24 hours. The parts for a 3 cm x 2 cm chip cost less than $25.

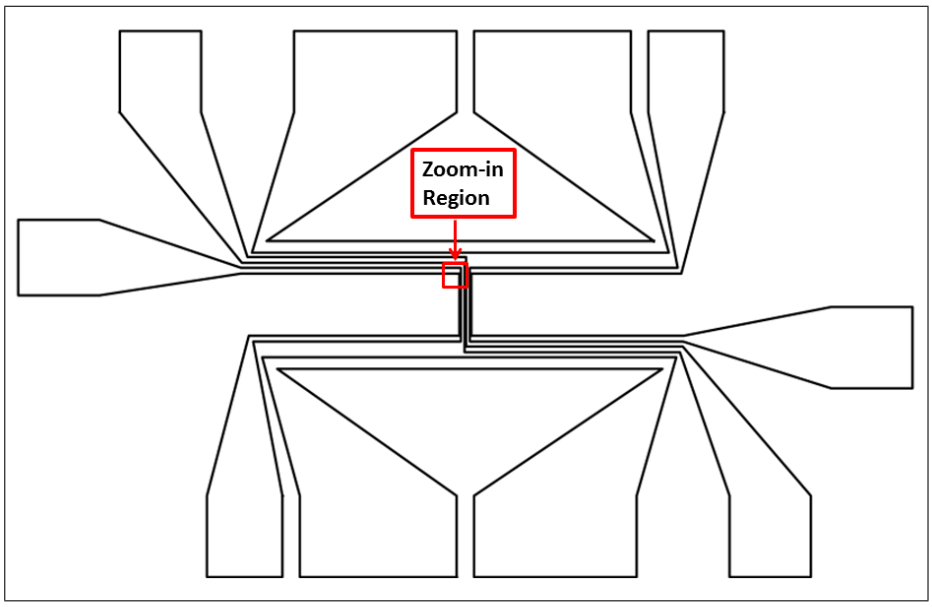


```
30 G0 X22.381174 Y12.205000
31 CALL BLASTAWAY
32 G1 X16.279631 Y16.571538
33 G1 X16.265000 Y16.600000
34 G1 X16.265000 Y19.400000
35 G1 X16.300000 Y19.435000
36 G1 X21.700000 Y19.435000
37 G1 X21.735000 Y19.400000
38 G1 X21.735000 Y16.604654
39 G1 X23.041274 Y11.779145
40 G1 X23.007490 Y11.735000
41 G1 X8.651312 Y11.735000
42 G1 X8.617788 Y11.780055
43 G1 X10.065000 Y16.605136
```

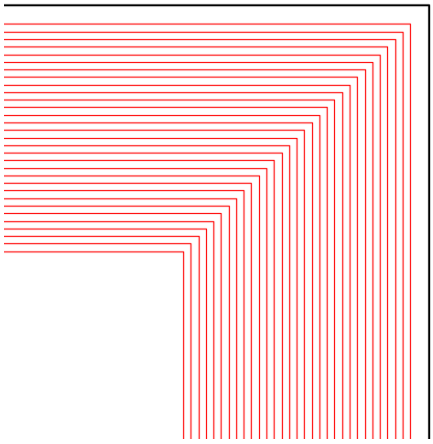

FIG. 8.2: Design of atom chip and wire cuts. (top) CAD drawing of a simplified backup atom chip. The red square represents the zoom-in region shown on the bottom right. The chip measures 3 cm x 2 cm. The three central wires, Z and 2 U wires, are the only ones used for the ACZ force measurement experiment. The top and bottom larger U wires were left as spare wires. (bottom right) Zoom in on a corner showing laser cut traces in red. The red lines have a total combined width of $w \approx 60$ μm and represent where the laser cuts will be. The single black line represents the edge of the wire trace. (bottom left) GCode example that the laser mill can interpret to make cuts. Each G1 command tells the laser mill to move the different X and Y coordinates while firing the laser beam. These commands were snipped from the top of the file and do not represent the cuts shown at the bottom right.

Once the new atom chip has been designed, a lab-made conversion software helps to convert the polygons and circles drawn in the *.dxf* engineering file into useful commands that the laser mill can interpret. The laser mill can interpret a

rudimentary language called G-Code, as seen in Figure **??**, that specifies where the mill should move while using the laser to make cuts.

The quality of the wire traces in DBC atom chips depend significantly on the laser machining process used to create them. This conversion software includes control over the various aspects of the cutting process needed to make high quality cuts. The real challenge to making high quality wire traces is to use the conversion software to control how wide the cuts are, how to space the individual passes, if and how many times to repeat the cuts, and in what order the make the cuts.

Some of the obstacles to making clean cuts are: 1) not cutting through the copper layer leaving spurious electrical connections, 2) cutting into and damaging the AlN substrate leading to decreased power dissipation, and 3) waste copper slag sticking to the remaining copper wire leading to wire roughness and spurious connections. Occasionally, the copper being cut is not completely ejected by the laser pulses and sticks around as unwanted slag. This can cause problems with faulty connections between wires or wires and ground planes. The un-ejected copper can also cause issues with distorting the wire shapes, leading to a distortion in the produced magnetic fields. This would distort the trapping potential experienced by the atoms and could cause issues like cloud fragmentation.

The overall width of the cut is defined as the width of copper intended to be removed around the wire traces. The standard width is 150 μm and can be made arbitrarily wider, and as low as 30 μm, depending on how closely drawn the wires are for a specific application and copper thickness.

The user can decide how often to fire laser pulses and whether to fire them based on distance traveled or time elapsed. The 'time elapsed' method consists of firing a laser pulse at a set repetition rate regardless of where the laser mill is. We have found that using 2 kHz works well. This method can lead to uneven cutting when maneuvering around complicated shapes that requires the translation stages

to slow down. This leads to removing extra material in these slow-moving sections and can damage the substrate material. Another method is to fire a pulse after the laser mill has moved a certain distance. We have found that using a distance of 17 μm works well. This method gives more consistent cuts, but requires the purchase of an additional piece of software from the laser mill manufacturer.

The spacing between adjacent cut traces is important in determining how smooth the cuts from the laser mill are. We have found that a 2 μm spacing works well for a mill beam with waist radius $w_0 \approx 10\mu$m. This allows sufficient overlap between the cut traces to allow smoothing between locations where the beam has fired a pulse and where it has not.

There are roughly 70 cut traces around any given wire path and the quality of the final product depends on the time order in which the cuts are made. We have found that using a mix of cut order methods works the best to mitigate the unwanted copper slag formation. The recipe for cutting copper with thickness $t = .005" = 127$ μm is as follows:

1. Draw cut paths with an overall width of 150 μm and a spacing of 2 μm.

2. Have the CNC mill trace out beam paths and fire the laser pulses after moving 17 μm.

3. Perform these cuts with the middle-to-edges then the edges-to-middle methods (described below).

4. Repeat the last step 3 times before stepping the Z value of the laser focus down by 100 μm.

5. Repeat step 4 four times to go down by total a distance of 400 μm.

8.3.1 Cut patterns

Outside-to-inside

The 'outside-to-inside' method of cutting traces works by cutting the trace that is on the outside and continuing with the next most outside trace until reaching most the inside trace. The 'inside-to-outside' method is just the opposite: start at the inner most trace and work outwards.

Middle-to-Edges

The middle to edges cut method works by starting at the center of the cut paths and working outwards as listed below.

1. Start at the cut path to the left of center
2. Move to the path just right of center
3. Move to a path second left of center
4. Move to a path second right of center
5. Continue in this manner until reaching the outer most edges of the cut pattern

The 'edges-to-middle' is similarly the opposite method of 'middle-to-edges'.

8.3.2 Chemical Etching

Once the laser mill has finished cutting the traces in the copper there is a good chance that there are some unwanted connections between wires and pads that are a result of either incomplete cutting or the ejected copper slag. The last step in manufacturing a chip is to clean up the traces with some chemical etching to ensure electrical isolation. There are two types of chemical etching that can be effective

when cleaning up the traces. The first method requires a simple aqueous solution of HCl that specifically targets the unwanted slag that is a by product of the milling process. This slag is largely already oxidized and can be removed via the following reaction:

$$2HCl_{aq} + Cu_s^{1+} = H_{2(g)} + CuCl_{2(aq)} \tag{8.1}$$

This method of chemical etching has the distinct advantage that it only removes previously oxidized copper from the chip and poses no risk to damaging the unoxidized wires on the chip. Figure 8.3 shows a before and after view of this method of chemical etching on an atom chip made in the summer of 2015.

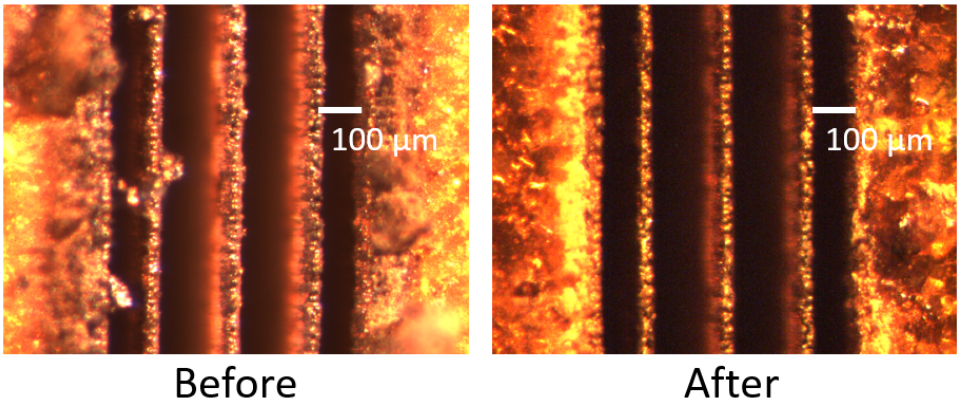

FIG. 8.3: Zoom-in view showing the central region of the chip where the Z- and 2 U-wires meet in the middle. The copper slag in the left image is an unwanted by-product of the laser milling process. The simple chemical etch in equation 8.1 removes this copper slag in the image on the right.

Chemical etching with just the above method may not be sufficient to ensure electrical isolation of the wires. If the above process does not electrically isolate the wires, then we can apply another chemical etching step that etches normal, unoxidized, copper. The reaction time must be limited in order to fully remove the unwanted copper slag while minimize the etching of the wires themselves. The chemical reaction for etching solid copper is as follows:

$$CuCl_{2-aq} + Cu_s \rightarrow 2CuCl_{aq} \tag{8.2}$$

The aqueous $CuCl_2$ in the above equation, or Cu^{2+} ions, get depleted and converted to $CuCl$, or Cu^{1+} ions. At a certain point the etchant needs to be regenerated by converting the Cu^{1+} ions to Cu^{2+} ions. This is completed by capturing the leftover etchant and performing a regeneration process by adding dissolved oxygen, via a bubbling hose in the liquid, and HCl. The etchant regeneration reaction is:

$$4HCl_{aq} + 4CuCl_{aq} + O_{2-g} \rightarrow 4CuCl_{2-aq} + 2H_2O \tag{8.3}$$

The extra water that comes from the reaction can be simply boiled off, leaving a new batch of etchant recycled from the old, reducing chemical waste.

8.3.3 Finished Product

Figure 8.4 shows side-on views using an optical microscope of wires cut with varying widths using laser milling of DBC. The widths of the wires and the spacing between them are $50, 100$, and 150 μm from left to right. As the wires get smaller, they become less rectangular and more trapezoidal. This shows the limitation of the beam width of the laser. The laser waist radius is nominally 10 μm at the focus. As the beam passes over the same location over and over the adjoining copper gets removed, leading to the trapezoidal wire shapes. These images were taken without

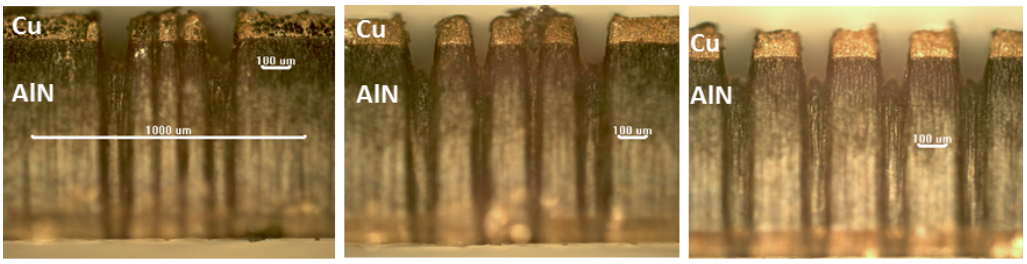

FIG. 8.4: Side view of DBC substrate and wire traces. The width of the wires, and the spacing between them is $50, 100, 150$ μm from left to right. The copper thickness is 127 μm.

any chemical etching. The copper slag can be easily seen in the middle image. These

images also show that the wire cutting process goes a little too far and cuts into the AlN substrate by about 100 μm. This could lead to poor heat-sinking in an operational chip. In the future, fewer laser passes should be made in order to limit the amount of substrate removed.

A finished chip is shown in Figure 8.5. The surface of the chip is covered in Kapton tape as a layer of physical protection during handling. The visible holes were created by an ohmmeter probe used to ensure the electrical isolation between wires.

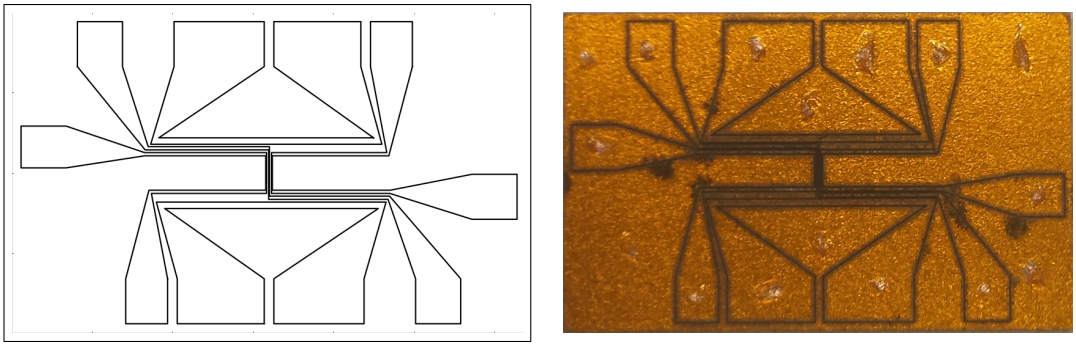

FIG. 8.5: (left) Initial CAD drawing of atom chip. (right) Microscope image of finished product after laser milling the chip on a DBC substrate. The DBC chip still has the protective layer of Katpon tape. There are small pricks in the tape made to measure the resistance between adjacent wires. This chip measures roughly 3 cm wide x 2 cm, and is 1 mm thick.

8.4 Outlook

Laser milling of DBC substrates holds promise as a method for manufacturing atom chips cheaply, quickly, and with commercially available substrates. This process is well suited for manufacturing prototype atom chips to test microwave impedance matching. This manufacturing method creates atom chips that are capable of running high currents (I=10 A continuous, I=100A for 2 seconds) [86] that can be used outside of the vacuum cell and swapped without breaking vacuum.

The roughness of the wires made with this process needs to be investigated

further before they are a good option for an operational atom chip inside a vacuum cell. One method that can be used to make smoother wires is to start with a smoother, and thinner substrate. Near the end of my summer tenure, I received samples of samples of 330μm AlN substrates with a 0.1 μm layer of Nichrome and a 2μm layer of copper. I am not certain, but I believe that these substrates are made using either electroplating or evaporative deposition. Figure 8.6 shows profilometry measurements of the samples taken before laser machining. These measurements suggest that the roughness of the samples is on par with the thickness of the 2μm copper layer.

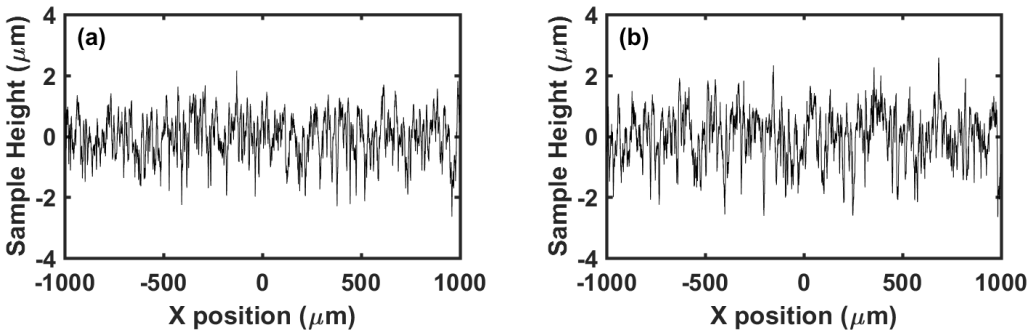

FIG. 8.6: Profilometry measurements of thin copper layer sample. Measurements were taken on the four corners of the sample. (a) shows the Top-Right corner and (b) shows the Bottom-Left corner. The samples had a 330μm thick AlN substrate with a 0.1 μm layer of Nichrome and a 2μm layer of copper.

CHAPTER 9

Conclusion

In the introduction to this thesis, I stated that we would demonstrate a practical AC Zeeman force produced by a microwave magnetic near-field, generated by an atom chip, that was spin-dependent, stronger than gravity, and consistent with theoretical predictions. Chapter 6 demonstrates that we were able to do just this: we measured an ACZ force that is consistent with two level dressed atom theory originally described more than 25 years ago [26]. This technique for ultracold neutral atom manipulation was dormant since it was first shown to weakly spatially constrain cesium atoms with a large circulating power (P $>$ 1 kW) [27]. We measured a maximum force over three times the strength of gravity with an applied microwave power of 3.3 W at 6.8 GHz targeting the M1 hyperfine transition $|F = 2, m_F = +2\rangle \leftrightarrow |F = 1, m_F = +1\rangle$ in the $5S_{1/2}$ electronic ground level of ^{87}Rb. We also showed the ability to selectively target the ACZ force to atoms in one and only one spin state within a spin mixture of $|F = 2, m_F = 0, +1, +2\rangle$.

We studied the stability of the dressed atom eigenstates in an applied microwave field in chapter 7. This experiment showed some interesting and unexpected behavior where the atoms did not all stay in the correct spin eigenstate over time. There

measured stability of the eigenstates was not the same between the $|-\rangle$ and $|+\rangle$ states and depended on the values of the applied DC magnetic field and the microwave detuning from resonance. This is worthy of more experimental investigation. There are questions listed at the end of the chapter that can be addressed with a relatively modest experimental effort.

Chapter 8 discusses another avenue of future work: building new atom chips using laser etching of direct-bond copper substrates. This is an interesting research avenue in its own right and could also lead to improvements in future ACZ experiments. The atom chip used in the experiments in this thesis was designed and constructed (by D. Jervis, U. of Toronto) before we had the ACZ experiments in mind. During its construction and integration into the apparatus no efforts were made to make it compatible for operation with AC currents at the GHz level. From our experiments measuring the force in chapter 6, we can estimate that a microwave power of 3.3 W drives an RMS current of $I = 37$ mA. If we were able to properly impedance match the chip wire with the 50 Ω microwave source, then we would drive a current of $I = 257$ mA, roughly 7 times higher. This would result in an increase in the on-resonance ACZ force of a factor of 7 and the far-off resonance force by a factor of $7^2 = 49$. Even larger microwave currents are possible if the impedance of the microwave source plus chip wire system can be lowered from 50 Ω. Increasing the efficiency in driving microwave current would allow for traps using the ACZ effect to more tightly confine the atoms at a given microwave power.

Creating an atom trap using only the ACZ force is the most interesting continuation of this work. A trap created in this manner would have the benefits of a traditional DC chip trap, e.g. tight confinement and forced evaporation, while allowing for operation at arbitrary DC magnetic fields, to tune atom-atom interactions with a magnetic Feshbach resonance, similar to an optical dipole trap. An ACZ-based atom trap would also be inherently spin-dependent and would open the

door for new applications of cold atom systems. A trapped atom interferometer using the ACZ force should allow for precise measurements of acceleration without the need for a large apparatus like those required for free-space interferometers.

It is my hope that this thesis proves useful to those who come after me. Chapters 2 and 3 should be a useful reference for me and other graduate students in the laboratory when we inevitably forget equations. Chapters 4 and 5 were written with an emphasis on passing my institutional knowledge on to future students in the laboratory. Chapter 6 describes the demonstration of a practical, spin-dependent ACZ force. There is still more work to do by trapping atoms with only the ACZ effect, and using the effect to work with K atoms in addition to Rb atoms. There is also more work to be done with the time evolution measurements in Chapter 7. Building new atom chips to expand upon the work in Chapter 8 is more of an effort, but could pay dividends in driving larger microwave current through future atom chips to operate traps using the ACZ effect.

BIBLIOGRAPHY

[1] N. Hinkley, J. A. Sherman, N. B. Phillips, M. Schioppo, N. D. Lemke, K. Beloy, M. Pizzocaro, C. W. Oates, and A. D. Ludlow, "An Atomic Clock with 10ˆ(18) Instability," *Science (80-.).*, vol. 341, no. 6151, pp. 1215–1218, 2013.

[2] A. Peters, K. Y. Chung, and S. Chu, "High-precision gravity measurements using atom interferometry," *Metrologia*, vol. 38, no. 1, pp. 25–61, 2003.

[3] S. M. Dickerson, J. M. Hogan, A. Sugarbaker, D. M. S. Johnson, and M. A. Kasevich, "Multiaxis inertial sensing with long-time point source atom interferometry," *Phys. Rev. Lett.*, vol. 111, no. 8, pp. 1–5, 2013.

[4] S.-Y. Lan, P.-C. Kuan, B. Estey, P. Haslinger, and H. Müller, "Influence of the Coriolis Force in Atom Interferometry," *Phys. Rev. Lett.*, vol. 108, no. 9, p. 090402, 2012.

[5] P. Berg, S. Abend, G. Tackmann, C. Schubert, E. Giese, W. P. Schleich, F. A. Narducci, W. Ertmer, and E. M. Rasel, "Composite-Light-Pulse Technique for High-Precision Atom Interferometry," *Phys. Rev. Lett.*, vol. 114, no. February, pp. 1–5, 2015.

[6] I. Dutta, D. Savoie, B. Fang, B. Venon, C. L. Garrido Alzar, R. Geiger, and A. Landragin, "Continuous Cold-Atom Inertial Sensor with 1 nrad/sec Rotation Stability," *Phys. Rev. Lett.*, vol. 116, no. 18, pp. 1–5, 2016.

[7] D. Jaksch and P. Zoller, "The cold atom Hubbard toolbox," *Ann. Phys. (N. Y).*, vol. 315, no. 1, pp. 52–79, 2005.

[8] S. Murmann, F. Deuretzbacher, G. Zürn, J. Bjerlin, S. M. Reimann, L. Santos, T. Lompe, and S. Jochim, "Antiferromagnetic Heisenberg spin chain of few cold atoms in a one-dimensional trap," *arXiv Prepr.*, vol. 215301, no. NOVEMBER, pp. 1–17, 2015.

[9] B. Kasch, H. Hattermann, D. Cano, T. E. Judd, S. Scheel, C. Zimmermann, R. Kleiner, D. Koelle, and J. Fortágh, "Cold atoms near superconductors:

atomic spin coherence beyond the Johnson noise limit," *New J. Phys.*, vol. 12, no. 6, p. 65024, 2010.

[10] A. Bonnin, N. Zahzam, Y. Bidel, and A. Bresson, "Characterization of a Simultaneous Dual-Species Atom Interferometer for a Quantum Test of the Weak Equivalence Principle," *arXiv*, vol. 023626, pp. 1–16, 2015.

[11] A. E. Leanhardt, T. A. Pasquini, M. Saba, A. Schirotzek, Y. Shin, D. Kielpinski, D. E. Pritchard, and W. Ketterle, "Cooling Bose\hyphen Einstein condensates below 500 picokelvin," *Science (80-.).*, vol. 301, no. SEPTEMBER, pp. 1513–1515, 2003.

[12] P. Medley, D. M. Weld, H. Miyake, D. E. Pritchard, and W. Ketterle, "Spin gradient demagnetization cooling of ultracold atoms," *Phys. Rev. Lett.*, vol. 106, no. 19, pp. 1–4, 2011.

[13] W. Muessel, H. Strobel, D. Linnemann, D. Hume, and M. Oberthaler, "Scalable Spin Squeezing for Quantum-Enhanced Magnetometry with Bose-Einstein Condensates," *Phys. Rev. Lett.*, vol. 113, no. 10, p. 103004, 2014.

[14] D. Frese, B. Ueberholz, S. Kuhr, W. Alt, D. Schrader, V. Gomer, and D. Meschede, "Single atoms in an optical dipole trap: towards a deterministic source of cold atoms," *Phys. Rev. Lett.*, vol. 85, no. 18, pp. 3777–3780, 2000.

[15] W. Alt, D. Schrader, S. Kuhr, M. Mueller, V. Gomer, and D. Meschede, "Single atoms in a standing-wave dipole trap," *Phys. Rev. A - At. Mol. Opt. Phys.*, vol. 67, no. 3, p. 8, 2002.

[16] C. Weitenberg, M. Endres, J. F. Sherson, M. Cheneau, P. Schauss, T. Fukuhara, I. Bloch, and S. Kuhr, "Single-spin addressing in an atomic Mott insulator.," *Nature*, vol. 471, no. 7338, pp. 319–24, 2011.

[17] F. K. Fatemi, K. M. Jones, and P. D. Lett, "Observation of optically induced Feshbach resonances in collisions of cold atoms," *Phys. Rev. Lett.*, vol. 85, no. 21, pp. 4462–4465, 2000.

[18] T. L. Nicholson, S. Blatt, B. J. Bloom, J. R. Williams, J. W. Thomsen, J. Ye, and P. S. Julienne, "Optical Feshbach resonances: Field-dressed theory and comparison with experiments," *Phys. Rev. A - At. Mol. Opt. Phys.*, vol. 92, no. 2, pp. 1–15, 2015.

[19] E. Tiesinga, A. J. Moerdijk, B. J. Verhaar, and H. Stoof, "Conditions for Bose-Einstein condensation in magnetically trapped atomic cesium," *Phys. Rev. A*, vol. 46, no. 3, pp. 1–4, 1992.

[20] P. Courteille, R. S. Freeland, D. J. Heinzen, F. A. van Abeelen, and B. J. Verhaar, "Observation of a Feshbach Resonance in Cold Atom Scattering," *Phys. Rev. Lett.*, vol. 81, no. 1, pp. 69–72, 1998.

[21] C. Chin, R. Grimm, P. S. Julienne, and E. Tiesinga, "Feshbach resonances in ultracold gases," *Rev. Mod. Phys.*, vol. 82, no. 2, pp. 1225–1286, 2010.

[22] R. Grimm, M. Weidemüller, and Y. B. Ovchinnikov, "Optical dipole traps for neutral atoms," *Adv. At. Mol. Opt. Phys.*, vol. 42, p. 95, 2000.

[23] N. Lundblad, M. Schlosser, and J. V. Porto, "Experimental observation of magic-wavelength behavior of Rb87 atoms in an optical lattice," *Phys. Rev. A - At. Mol. Opt. Phys.*, vol. 81, no. 3, pp. 3–5, 2010.

[24] C. Y. Park, J. Y. Kim, J. M. Song, and D. Cho, "Optical Stern-Gerlach effect from the Zeeman-like ac Stark shift," *Phys. Rev. A*, vol. 65, no. 3, p. 033410, 2002.

[25] O. Mandel, M. Greiner, A. Widera, T. Rom, T. W. Hänsch, and I. Bloch, "Coherent Transport of Neutral Atoms in Spin-Dependent Optical Lattice Potentials," *Phys. Rev. Lett.*, vol. 91, no. 1, p. 010407, 2003.

[26] C. C. Agosta, I. F. Silvera, H. Stoof, and B. J. Verhaar, "Trapping of neutral atoms with resonant microwave radiation," *Phys. Rev. Lett.*, vol. 62, no. 20, pp. 2361–2364, 1989.

[27] R. J. C. Spreeuw, C. Gerz, L. S. Goldner, W. D. Phillips, S. L. Rolston, C. I. Westbrook, M. W. Reynolds, and I. F. Silvera, "Demonstration of neutral atom trapping with microwaves," *Phys. Rev. Lett.*, vol. 72, no. 20, pp. 3162–3165, 1994.

[28] M. Bloom and K. Erdman, "The Transverse Stern-Gerlach Experiment," *Can. J. Phys.*, vol. 40, no. 2, pp. 179–193, 1962.

[29] M. Bloom, E. Enga, and H. Lew, "Observation of the Transverse Stern-Gerlach Effect in Neutral Potassium," *Can. J. Phys.*, vol. 45, no. 4, pp. 1481–1495, 1967.

[30] C. Ospelkaus, U. Warring, Y. Colombe, K. R. Brown, J. M. Amini, D. Leibfried, and D. J. Wineland, "Microwave quantum logic gates for trapped ions," *Nature*, vol. 476, no. 7359, pp. 181–184, 2011.

[31] P. Hommelhoff, T. W. Hänsch, and J. Reichel, "Bose-Einstein condensation on a microelectronic chip," *Nature*, vol. 413, no. October, pp. 4–7, 2001.

[32] U. Warring, C. Ospelkaus, Y. Colombe, K. R. Brown, J. M. Amini, M. Carsjens, D. Leibfried, and D. J. Wineland, "Techniques for microwave near-field quantum control of trapped ions," *Phys. Rev. A*, vol. 87, no. 1, p. 013437, 2013.

[33] P. Böhi, M. F. Riedel, J. Hoffrogge, J. Reichel, T. W. Hänsch, and P. Treutlein, "Coherent manipulation of Bose-Einstein condensates with state-dependent microwave potentials on an atom chip," *Nat. Phys.*, vol. 5, no. 8, p. 9, 2009.

[34] C. F. Ockeloen, R. Schmied, M. F. Riedel, and P. Treutlein, "Quantum metrology with a scanning probe atom interferometer," *Phys. Rev. Lett.*, vol. 111, no. 14, pp. 1–5, 2013.

[35] R. Geiger, V. Ménoret, G. Stern, N. Zahzam, P. Cheinet, B. Battelier, A. Villing, F. Moron, M. Lours, Y. Bidel, A. Bresson, A. Landragin, and P. Bouyer, "Detecting inertial effects with airborne matter-wave interferometry," *Nat. Commun.*, vol. 2, pp. 474–477, 2011.

[36] F. X. Esnault, N. Rossetto, D. Holleville, J. Delporte, and N. Dimarcq, "HORACE: A compact cold atom clock for Galileo," *Adv. Sp. Res.*, vol. 47, no. 5, pp. 854–858, 2011.

[37] M. H. Anderson, J. R. Ensher, M. R. Matthews, C. E. Wieman, and E. A. Cornell, "Observation of Bose-Einstein Condensation in a Dilute Atomic Vapor," *Science (80-.).*, vol. 269, no. 5221, pp. 198–201, 1995.

[38] K. B. Davis, M. O. Mewes, M. R. Andrews, N. J. Van Druten, D. S. Durfee, D. M. Kurn, and W. Ketterle, "Bose-Einstein condensation in a gas of sodium atoms," *Phys. Rev. Lett.*, vol. 75, no. 22, pp. 3969–3973, 1995.

[39] E. A. Salim, J. De Natale, D. M. Farkas, K. M. Hudek, S. E. McBride, J. Michalchuk, R. Mihailovich, and D. Z. Anderson, "Compact, microchip-based systems for practical applications of ultracold atoms," *Quantum Inf. Process.*, vol. 10, no. 6, pp. 975–994, 2011.

[40] T. van Zoest, N. Gaaloul, Y. Singh, H. Ahlers, W. Herr, S. T. Seidel, W. Ertmer, E. Rasel, M. Eckart, E. Kajari, S. Arnold, G. Nandi, W. P. Schleich, R. Walser, A. Vogel, K. Sengstock, K. Bongs, W. Lewoczko-Adamczyk, M. Schiemangk,

T. Schuldt, A. Peters, T. Könemann, H. Müntinga, C. Lämmerzahl, H. Dittus, T. Steinmetz, T. W. Hänsch, J. Reichel, E. A. Cornell, C. E. Wieman, W. Ketterle, G. Stern, A. Peters, K. Y. Chung, S. Chu, I. Ciufolini, E. C. Pavlis, S. Fray, C. A. Diez, M. Weitz, S. Dimopoulos, P. W. Graham, J. M. Hogan, M. A. Kasevich, S. Rajendran, A. E. Leanhardt, A. Vogel, W. Hänsel, P. Hommelhoff, J. Reichel, R. Folman, P. Krüger, J. Schmiedmayer, J. Denschlag, C. Henkel, J. Fortágh, C. Zimmermann, Y. Kagan, E. L. Surkov, G. V. Shlyapnikov, Y. Castin, R. Dum, P. Storey, M. Olshanii, G. Nandi, R. Walser, W. P. Schleich, T. A. Pasquini, J. Billy, and G. Roati, "Bose-Einstein condensation in microgravity.," *Science*, vol. 328, pp. 1540–3, jun 2010.

[41] A. Kubelka-Lange, S. Herrmann, J. Grosse, C. Lämmerzahl, E. M. Rasel, and C. Braxmaier, "A three-layer magnetic shielding for the MAIUS-1 mission on a sounding rocket," *Rev. Sci. Instrum.*, vol. 87, no. 6, 2016.

[42] T. Schuldt, C. Schubert, M. Krutzik, L. G. Bote, N. Gaaloul, J. Hartwig, H. Ahlers, W. Herr, K. Posso-Trujillo, J. Rudolph, S. Seidel, T. Wendrich, W. Ertmer, S. Herrmann, A. Kubelka-Lange, A. Milke, B. Rievers, E. Rocco, A. Hinton, K. Bongs, M. Oswald, M. Franz, M. Hauth, A. Peters, A. Bawamia, A. Wicht, B. Battelier, A. Bertoldi, P. Bouyer, A. Landragin, D. Massonnet, T. Lévèque, A. Wenzlawski, D. J. Heinzen, P. Windpassinger, K. Sengstock, W. von Klitzing, C. Chaloner, D. Summers, P. Ireland, I. Mateos, C. F. Sopuerta, F. Sorrentino, G. M. Tino, M. Williams, C. Trenkel, D. Gerardi, M. Chwalla, J. Burkhardt, U. Johann, A. Heske, E. Wille, M. Gehler, L. Cacciapuoti, N. Gürlebeck, C. Braxmaier, and E. Rasel, "Design of a dual species atom interferometer for space," *Exp. Astron.*, vol. 39, no. 2, pp. 167–206, 2015.

[43] J. Rudolph, W. Herr, C. Grzeschik, T. Sternke, A. Grote, M. Popp, D. Becker, H. Müntinga, H. Ahlers, A. Peters, C. Lämmerzahl, K. Sengstock, N. Gaaloul, W. Ertmer, and E. M. Rasel, "A high-flux BEC source for mobile atom interferometers," *New J. Phys.*, vol. 17, no. 6, p. 065001, 2015.

[44] G. Rosi, F. Sorrentino, L. Cacciapuoti, M. Prevedelli, and G. M. Tino, "Precision measurement of the Newtonian gravitational constant using cold atoms.," *Nature*, vol. 510, no. 7506, pp. 518–21, 2014.

[45] J. M. Mc Guirk, G. T. Foster, J. B. Fixler, M. J. Snadden, and M. A. Kasevich, "Sensitive absolute-gravity gradiometry using atom interferometry," *Phys. Rev. A - At. Mol. Opt. Phys.*, vol. 65, no. 3, pp. 1–14, 2002.

[46] T. Schumm, P. Krüger, S. Hofferberth, I. Lesanovsky, S. Wildermuth, S. Groth, I. Bar-Joseph, L. M. Andersson, and J. Schmiedmayer, "A double well interferometer on an atom chip," *Quantum Inf. Process.*, vol. 5, no. 6, pp. 537–558, 2006.

[47] H. J. Metcalf and P. van der Straten, *Laser Cooling and Trapping*. Springer, 1999.

[48] J. Dalibard and C. Cohen-Tannoudji, "Dressed-atom approach to atomic motion in laser light : the dipole force revisited," *J. Opt. Soc. Am. B*, vol. 2, no. November, pp. 1707–1720, 1985.

[49] H. Young and R. Freedman, *University Physics*. Addison-Wesley, 12 ed., 2006.

[50] J. Dalibard and C. Cohen-Tannoudji, "Laser cooling below the Doppler limit by polarization gradients: simple theoretical models," *J. Opt. Soc. Am. B*, vol. 6, no. 11, p. 2023, 1989.

[51] D. A. Steck, "Rubidium 87 D Line Data." 2015.

[52] T. Bergeman, G. Erez, and H. J. Metcalf, "Magnetostatic trapping fields for neutral atoms," *Phys. Rev. A*, vol. 35, no. 4, 1987.

[53] W. Wing, "On Neutral Particle Trapping in Quasistatic Electromagnetic Fields," *Prog. Quant. Elect.*, vol. 8, no. 181, 1984.

[54] J. F. Sherson, C. Weitenberg, M. Endres, M. Cheneau, I. Bloch, and S. Kuhr, "Single-atom-resolved fluorescence imaging of an atomic Mott insulator.," *Nature*, vol. 467, no. 7311, pp. 68–72, 2010.

[55] S. Aubin, "Private Communications." 2016.

[56] I. I. Rabi, "Space quantization in a gyrating magnetic field," *Phys. Rev.*, vol. 51, no. 8, pp. 652–654, 1937.

[57] L. Yatsenko and H. J. Metcalf, "Dressed-atom description of the bichromatic force," *Phys. Rev. A - At. Mol. Opt. Phys.*, vol. 70, no. 6, pp. 1–12, 2004.

[58] X. Hua, C. Corder, and H. J. Metcalf, "Simulation of laser cooling by the bichromatic force," *Phys. Rev. A - At. Mol. Opt. Phys.*, vol. 93, no. 6, pp. 1–6, 2016.

[59] L. Aldridge, S. E. Galica, and E. E. Eyler, "Simulations of the bichromatic force in multilevel systems," *Phys. Rev. A - At. Mol. Opt. Phys.*, vol. 93, no. 1, pp. 1–14, 2016.

[60] E. Tiesinga, B. J. Verhaar, and H. Stoof, "Threshold and resonance phenomena in ultracold ground-state collisions," *Phys. Rev. A*, vol. 47, no. 5, pp. 4114–4122, 1993.

[61] M. K. Ivory, A. R. Ziltz, C. T. Fancher, A. J. Pyle, A. Sensharma, B. Chase, J. P. Field, A. Garcia, D. Jervis, and S. Aubin, "Atom chip apparatus for experiments with ultracold rubidium and potassium gases.," *Rev. Sci. Instrum.*, vol. 85, no. 4, p. 043102, 2014.

[62] S. Groth, P. Krüger, S. Wildermuth, R. Folman, T. Fernholz, J. Schmiedmayer, D. Mahalu, and I. Bar-Joseph, "Atom chips: Fabrication and thermal properties," *Appl. Phys. Lett.*, vol. 85, no. 14, pp. 2980–2982, 2004.

[63] M. K. Ivory, *Experimental Apparatus for Quantum Pumping with a Bose-Einstein Condensate*. PhD thesis, College of William and Mary, 2016.

[64] A. R. Ziltz, *Ultracold Rubidium and Potassium System for Atom Chip-based Microwave and RF Potentials*. PhD thesis, College of William and Mary, 2015.

[65] S. Aubin, "Aubin Cold Atom Lab," 2016.

[66] A. Keshet and W. Ketterle, "A Distributed GUI-based Computer Control System for Atomic Physics Experiments," *arXiv:1208.2607*, pp. 1–6, 2012.

[67] P. B. Wigley, P. J. Everitt, A. V. D. Hengel, J. W. Bastian, M. A. Sooriyabandara, G. D. Mcdonald, K. S. Hardman, C. D. Quinlivan, P. Manju, C. C. N. Kuhn, I. R. Petersen, A. Luiten, J. J. Hope, N. P. Robins, and M. R. Hush, "Fast machine-learning online optimization of ultra-cold-atom experiments," *Nat. Publ. Gr.*, vol. 6, no. April, pp. 1–6, 2015.

[68] P. T. Starkey, C. J. Billington, S. P. Johnstone, M. Jasperse, K. Helmerson, L. D. Turner, and R. P. Anderson, "A scripted control system for autonomous hardware timed experiments," *Rev. Sci. Instrum.*, vol. 23, no. April, p. 11, 2013.

[69] B. P. Anderson and M. A. Kasevich, "Loading a vapor-cell magneto-optic trap using light-induced atom desorption," *Phys. Rev. A - At. Mol. Opt. Phys.*, vol. 63, no. 2, pp. 1–6, 2001.

[70] V. Bagnato, D. E. Pritchard, and D. Kleppner, "Bose-Einstein condensation in an external potential," *Phys. Rev. A*, vol. 35, no. 10, pp. 4354–4358, 1987.

[71] K. L. Corwin, "A Circularly-Polarized Optical Dipole Trap and Other Developments in Laser Trapping of Atoms," pp. 1–136, 1999.

[72] R. Chicireanu, K. D. Nelson, S. Olmschenk, N. Lundblad, A. Derevianko, and J. V. Porto, "Differential light-shift cancellation in a magnetic-field-insensitive transition of Rb87," *Phys. Rev. Lett.*, vol. 106, no. 6, pp. 1–4, 2011.

[73] A. Ashkin, "Acceleration and Trapping of Particles by Radiation Pressure," *Phys. Rev. Lett.*, vol. 24, no. 4, pp. 156–159, 1970.

[74] J. D. Miller, R. A. Cline, and D. J. Heinzen, "Far-off-resonance optical trapping of atoms," *Phys. Rev. A*, vol. 47, no. 6, 1993.

[75] E. Hecht, *Optics*. Addison-Wesley, 4th ed., 2001.

[76] Y.-J. Lin, A. Perry, R. Compton, I. B. Spielman, and J. Porto, "Rapid production of R87b Bose-Einstein condensates in a combined magnetic and optical potential," *Phys. Rev. A*, vol. 79, p. 063631, jun 2009.

[77] E. I. Gordon, "A Review of Acoustooptical Deflection and Modulation Devices," *Proc. IEEE*, vol. 54, no. 10, pp. 1391–1401, 1966.

[78] S. Aubin, S. Myrskog, M. H. T. Extavour, L. J. LeBlanc, D. McKay, A. Stummer, and J. H. Thywissen, "Rapid sympathetic cooling to Fermi degeneracy on a chip," *Nat. Phys.*, vol. 2, no. 6, pp. 384–387, 2006.

[79] C. Myatt, E. Burt, R. Ghrist, E. Cornell, and C. Wieman, "Production of Two Overlapping Bose-Einstein Condensates by Sympathetic Cooling," *Phys. Rev. Lett.*, vol. 78, no. 4, pp. 586–589, 1997.

[80] M. Lara, J. L. Bohn, D. E. Potter, P. Soldán, and J. M. Hutson, "Cold collisions between OH and Rb: The field-free case," *Phys. Rev. A - At. Mol. Opt. Phys.*, vol. 75, no. 1, pp. 1–19, 2007.

[81] M. White, H. Gao, M. Pasienski, and B. DeMarco, "Bose-Einstein condensates in rf-dressed adiabatic potentials," *Phys. Rev. A*, vol. 74, p. 023616, aug 2006.

[82] O. Zobay and B. Garraway, "Two-Dimensional Atom Trapping in Field-Induced Adiabatic Potentials," *Phys. Rev. Lett.*, vol. 86, pp. 1195–1198, feb 2001.

[83] M. F. Riedel, P. Böhi, Y. Li, T. W. Hänsch, A. Sinatra, and P. Treutlein, "Atom-chip-based generation of entanglement for quantum metrology.," *Nature*, vol. 464, no. 7292, pp. 1170–1173, 2010.

[84] M. B. Squires, J. A. Stickney, E. J. Carlson, P. M. Baker, W. R. Buchwald, S. Wentzell, and S. M. Miller, "Atom chips on direct bonded copper substrates," *Rev. Sci. Instrum.*, vol. 82, no. 2, 2011.

[85] V. Vuletic and J. Reichel, *Atom Chips*. Wiley-VCH, 2011.

[86] M. B. Squires, J. A. Stickney, E. J. Carlson, P. M. Baker, W. R. Buchwald, S. Wentzell, and S. M. Miller, "Atom chips on direct bonded copper substrates Atom chips on direct bonded copper substrates," *Rev. Sci. Instrum.*, vol. 023101, no. 2011, 2014.

[87] M. B. Squires, S. E. Olson, B. Kasch, J. A. Stickney, C. J. Erickson, J. A. R. Crow, E. J. Carlson, and J. H. Burke, "Ex Vacuo Atom Chip Bose-Einstein Condensate (BEC)," *Arxiv*, pp. 1–5, 2016.